2012

The use of the bulk properties of gamma-ray burst prompt emission spectra for the study of cosmology

Adam Goldstein

THE USE OF THE BULK PROPERTIES OF GAMMA-RAY BURST PROMPT EMISSION SPECTRA FOR THE STUDY OF COSMOLOGY

by

ADAM GOLDSTEIN

A DISSERTATION

Submitted in partial fulfillment of the requirements
for the degree of Doctor of Philosophy
in
The Department of Physics
to
The School of Graduate Studies
of
The University of Alabama in Huntsville

HUNTSVILLE, ALABAMA

2012

In presenting this dissertation in partial fulfillment of the requirements for a doctoral degree from The University of Alabama in Huntsville, I agree that the Library of this University shall make it freely available for inspection. I further agree that permission for extensive copying for scholarly purposes may be granted by my advisor or, in his/her absence, by the Chair of the Department or the Dean of the School of Graduate Studies. It is also understood that due recognition shall be given to me and to The University of Alabama in Huntsville in any scholarly use which may be made of any material in this dissertation.

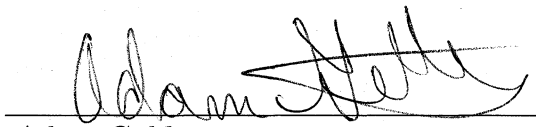

Adam Goldstein

11/1/12

(date)

ABSTRACT

School of Graduate Studies
The University of Alabama in Huntsville

Degree Doctor of Philosophy College/Dept. Science/Physics

Name of Candidate Adam Goldstein

Title The Use of the Bulk Properties of Gamma-Ray Burst Prompt Emission Spectra for the Study of Cosmology

The study of bulk spectral properties of Gamma-Ray Bursts (GRBs) is important to understanding the physics behind these powerful explosions and may even be an aide in studying cosmology. The prompt emission spectral properties have long been studied by a growing community of researchers, and many theories have been developed since the discovery of GRBs. Even though the exact physics of these phenomena is not completely understood, GRBs have been proposed to give insight on other astrophysical phenomena from dark matter to the expansion of the universe. Obviously, using GRBs to study cosmology requires a large sample size to adequately constrain results and provide confident conjectures. For this reason, BATSE and GBM results are paramount to the study of the prompt emission of GRBs. Using results from both instruments, I study the bulk spectral properties of GRBs and describe analysis techniques that can be used to study cosmology.

Abstract Approval: Committee Chair Robert D. Preece 10/29/12
Dr. Robert D. Preece

Department Chair
Dr. Gary P. Zank

Graduate Dean Rhonda Kay Gaede 11/14/12
Dr. Rhonda K. Gaede

DISSERTATION APPROVAL FORM

Submitted by Adam Goldstein in partial fulfillment of the requirements for the degree of Doctor of Philosophy in Physics and accepted on behalf of the Faculty of the School of Graduate Studies by the dissertation committee.

We, the undersigned members of the Graduate Faculty of The University of Alabama in Huntsville, certify that we have advised and/or supervised the candidate of the work described in this dissertation. We further certify that we have reviewed the dissertation manuscript and approve it in partial fulfillment of the requirements for the degree of Doctor of Philosophy in Physics.

Dr. Robert D. Preece	10/29/12 (Date)	Committee Chair
Dr. Massimiliano Bonamente	10/30/12 (Date)	
Dr. Michael S. Briggs	10/30/12 (Date)	
Dr. Jon Hakkila	(Date)	
Dr. Thomas M. Koshut	10/30/12 (Date)	
Dr. Kon-Ichi Nishikawa	10/29/12 (Date)	
Dr. Gary P. Zank	(Date)	Department Chair
Dr. John D. Fix	10/30/12 (Date)	College Dean
Dr. Rhonda K. Gaede	11/14/12 (Date)	Graduate Dean

ACKNOWLEDGMENTS

I am extremely grateful and fortunate to have had the help and support from numerous people over the course of my studies and research. It has been particularly advantageous for me to be welcomed so openly into the *Fermi* Gamma-Ray Burst Monitor team as well as the larger gamma-ray astronomy group at the NSSTC. First and foremost in acknowledgment should be my committee chair and advisor, Rob Preece. His serendipitous discovery of me as graduate research assistant and willingness to introduce me to the study of gamma-ray bursts and high-energy astrophysics provided me with a spectacular, unique opportunity. Without the opportunity to work on gamma-ray bursts as a member of the GBM team, it is likely that this dissertation would not have been so successful. I appreciate the encouragements and many long conversations with him that have helped me through this process. I am also very grateful for the time and effort put forth by every member of my committee: Max Bonamente, for his extremely helpful discussions on model-fitting and statistics as well as cosmology; Michael Briggs, for his extensive knowledge of statistics and gamma-ray detection processes, as well as his ability to point out areas in which I can improve; Jon Hakkila, for discussions on the internal luminosity function of GRBs and its importance to cosmology; Tom Koshut, for his overwhelming scientific, academic, and professional career guidance; and Ken Nishikawa; for his insight into the theoretical processes of gamma-ray bursts and willingness to devote an extensive amount of time to improving this dissertation. I would also like to acknowledge the

GBM senior scientists for recognizing within me qualities befitting of a research scientist: Narayan Bhat, Michael Briggs, Valerie Connaughton, Jerry Fishman, Andreas von Kienlin, Chryssa Kouveliotou, Shiela McBreen, Chip Meegan, Bill Paciesas, Rob Preece, and Colleen Wilson-Hodge. I would also like to thank the other graduate students and post-doctoral students who have worked with me on GBM over the past four years. The many long conversations and shared experience of weathering this storm have been invaluable, both professionally and personally.

I would like to express gratitude, as well, for all of my professors at UAH. Their guidance and attitude have proven that their students are their top priority. I have learned much in my graduate studies, largely due to the patience and diligence of my professors. I would be remiss in neglecting to acknowledge Gary Zank, Chair of the Physics department at UAH. His concern for his students and diligence toward achieving high quality research has contributed to the success of the department, the university, and all of his students. In addition, I would like to acknowledge and thank the NASA Graduate Student Research Program, as this program has funded most of the research presented in this dissertation. Without the financial support from this program, this research, my publications, and my conference presentations would not have been possible.

Some of the most important people whom I must thank are my closest family and friends. My parents have constantly pushed me to believe in myself as they have believed in me over the past twenty years. They have offered unlimited guidance and support and have been integral in every success in my life. The proudest moments of my life are the moments that make them proud to be my parents. I am forever

grateful for their constant love and assurance. All of my family and closest friends have supported me so much throughout this entire process, and during the difficult times, their thoughtfulness and encouragement have made the path seem clear and the obstacles seem small. Last, but certainly not least, is one person who has unwaveringly supported and encouraged me through the good and bad times: Nina Money. She has been with me every step of the way through my graduate studies and doctoral research. She has witnessed the unbelievable highs and lows of such a difficult, yet rewarding, accomplishment. I am eternally grateful for her patience, assurance, encouragement, and all she has done for me over the past several years.

TABLE OF CONTENTS

LIST OF FIGURES

LIST OF TABLES

TABLE PAGE

LIST OF SYMBOLS

SYMBOL	DEFINITION
A	Amplitude of GRB photon model
a	Unitless universe scale factor
B	Magnetic energy density
c	Speed of light in a vacuum; $c \approx 3.0 \times 10^{10}$ cm/s
D_C	Comoving distance
D_H	Hubble distance
d_L	Luminosity distance
E_b	Break energy of the GRB spectrum
E_γ	Collimation-corrected energy release in gamma-rays
E_{iso}	Isotropic energy release in gamma-rays
E_p	Peak energy of the GRB power spectrum
E_{piv}	Photon model pivot energy
F_γ	Observed flux in gamma-rays
f_b	Collimation-correction beaming fraction
G	Gravitational constant
G_L	Ghirlanda limit

H_0	Hubble parameter
h	Planck constant; $h \approx 4.2 \times 10^{-18}$ keV s
K	Cosmological K-correction
k	Cosmological curvature parameter
$\mathcal{L}$	Likelihood
L_γ	Collimation-corrected luminosity in gamma-rays
L_{iso}	Isotropic luminosity in gamma-rays
m_e	Electron rest mass; $m_e \approx 9.11 \times 10^{-28}$ gm
n_p	Circumburst medium particle density
p	Electron distribution power law index
q	Deceleration parameter
$\mathcal{R}$	Likelihood Ratio
R	Universe scale factor
r_e	Classical electron radius; $r_e \approx 2.82 \times 10^{-13}$ cm
S_γ	Observed fluence in gamma-rays
T_{90}	The duration of burst starting at 5% fluence and ending at 95% fluence
t_H	Hubble time
t_j	Observed jet break time
t_L	Lookback time

V_C	Comoving volume
w	Dark Energy equation of state index
z	Redshift
α	Low-energy GRB spectral power law index
β	High-energy GRB spectral power law index
Γ	Bulk Lorentz factor of the GRB outflow
γ_e	Lorentz factor of the electron distribution
Δ	Smoothly Broken Power Law break scale
ΔS	Difference between the low- and high-energy GRB spectral indices
δ	Relativistic Doppler factor
ϵ	Conversion efficiency
Θ	Vector of parameters
θ	Zenith angle
θ_Γ	Relativistic jet half-opening angle
θ_j	Physical jet half-opening angle
θ_v	Angle of observation from the center of the GRB jet
λ	Power law photon model index
μ	Distance modulus
ν	Frequency

ν_c	Synchrotron cooling frequency
νF_ν	Power density spectrum
σ	Standard deviation
σ_T	Thomson cross-section; $\sigma_T \approx 6.65 \times 10^{-25}\text{cm}^2$
ϕ	Azimuthal angle
χ^2	Chi-square goodness-of-fit
Ω_k	Cosmological curvature dependent on total density
Ω_Λ	Cosmological dark energy density parameter
Ω_M	Cosmological matter density parameter

CHAPTER 1

INTRODUCTION

Gamma–Ray Bursts (GRBs) are enigmatic explosive events that are among the most powerful ever detected. These transients are cosmological in origin and exist at high redshifts, distances at which the individual parent objects cannot be spatially resolved. Gamma–Ray Bursts are detectable at these distances only because of the extreme amounts of energy produced in the explosions of their parent object. Because they are high redshift events and have a large spread in redshift, GRBs are long sought after as a means to probe the early universe. Many have endeavoured to turn GRBs into so-called "standard candles," which are idealized objects whose observed properties tightly correlate with their distance or redshift. Unfortunately, these studies have not been fruitful. The fact that observed properties of GRBs have large dispersions; and the fact that the exact physics of the underlying explosions, the parent objects, and the environments in which the parent object exist are all relatively unknown lead to many complications when using observations to estimate the distance to the GRBs. Also an unfortunate circumstance is the relatively low rate of spectroscopic or photometric redshifts available for GRBs. Because they are relatively short transient events that tend to decay rapidly on average, an estimation of the redshift can be

difficult given the time constraint. Additionally, most GRB–triggering instruments are non–imaging and therefore produce less accurate position estimates of the GRB location in the sky. For these reasons, GRBs have not sufficiently produced reliable results concerning the study of cosmology. To advance their role in the study of the universe, we must be able to solve a number of problems first. In this dissertation, I will discuss these problems, a possible solution and its effectiveness, attempt to set GRBs in place along the cosmological distance ladder, and discuss the implications that has on our current knowledge of cosmology.

1.1 The Discovery and Study of GRBs

Gamma–ray bursts are intense flashes of radiation that appear at unpredictable times from random locations on the celestial sphere. They have been studied since their discovery by the *Vela* Satellite Network [3]. The first dedicated experiment to studying GRBs was the Burst and Transient Source Experiment (BATSE) [4] onboard the Compton Gamma-Ray Observatory (CGRO), which was launched in 1991. During its ∼9 years of operations BATSE amassed observations of over 2700 GRBs and led to groundbreaking discoveries that GRBs could not be of galactic origin and that there exists observationally different classes of GRBs. In 1996, *BeppoSax* [5] was launched by the Italian Space Agency to aid in the observation of GRBs into the X-ray regime with fine localization capabilities at arc-minute resolutions. The localizations from *BeppoSax* allowed for follow-up observations from other X-ray, optical, and radio observatories, leading to redshift measurements. In 1997, afterglow observations resulted in the first redshift measurements that have been

paramount to proving that GRBs are indeed cosmological in origin (GRB 970508) [6]. There now exists a few hundred GRBs with confirmed spectroscopic redshifts ranging from 0.0085 (GRB 980425 [7]) to 8.2 (GRB 090423A [8]). Among other instruments that have observed GRBs include the High Energy Transient Explorer (HETE-2), KONUS-Wind [9], and *Suzaku* [10]. Currently, two dedicated missions are in operation to study GRBs. The *Fermi* Gamma-Ray Space Telescope hosts the Gamma-Ray Burst Monitor (GBM) [1], while the *Swift* spacecraft hosts the Burst Alert Telescope (BAT) [11]. These instruments have a complementary relationship similar to BATSE and *BeppoSax*, with GBM filling the role of BATSE and the BAT filling the role of *BeppoSax*.

Although several missions have been dedicated to studying GRBs and despite nearly 40 years of research, the progenitors of these astrophysical phenomena remain largely unknown. Several thousand of these events have been observed to date, and yet the exact nature of these events evade observation. The bulk of the energy emission of GRBs occurs in the X-ray and gamma-ray regime of the electromagnetic spectrum. Their intensities and durations span many orders of magnitude, where the intensity of a burst is usually defined by its peak flux at a specified time resolution and in a specified energy range. Gamma–Ray Bursts appear to be distributed inhomogeneously in space due to the deviation from a -3/2 power law of the flux distribution, and the angular distribution is isotropic over the entire sky [12, 13]. Observations of delayed emission in X-ray and optical band following the prompt gamma-ray emission provide some evidence of the burst mechanism, although much of the evidence is conflicting. Current research in this area is aided by distributing localizations of GRBs observers

for rapid follow-up observations at other wavelengths [14]. This afterglow search has yielded several observations of apparent burst counterparts.

1.2 Dissertation Outline

Because of the complex issues discussed and the breadth of work included, this dissertation is separated into multiple sections. In Chapter 2, I discuss the gamma-ray instruments used in this dissertation to observe GRBs. An overview of the detector descriptions and physics are included as well as a general description of the spacecraft themselves and the conversion of the detected photons into analyzable data. In Chapter 3, I describe the general observed properties of GRBs, including the prompt emission properties observed by gamma-ray detectors as well as the observed properties of the afterglow as observed by X-ray, optical, and radio instruments. Chapter 4 discusses the current theories on the physics of GRB explosions and the parent object (progenitor). Chapter 5 describes the data analysis procedures and results from the prompt emission observations of GRBs. This includes the description of the spectral catalogs used, the parameter distributions, and their potential physical implications. In Chapter 6, I present a number of correlations derived from the parameters and discuss their importance to the estimation of unknown or undetermined quantities that are crucial to GRBs as well as discuss some of the difficulties inherent in using GRBs to study cosmology. Chapter 7 discusses the framework of cosmological theories, the dynamics of cosmology and cosmological models, and important cosmological observations. Chapter 8 discusses a new method to estimating the redshift, distance, and amount of collimation of GRBs as well as using the results to construct

a GRB Hubble diagram. The GRB Hubble diagram is then used to constrain cosmological parameters and the results are presented in Chapter 9. Finally, a discussion on the results and the cosmological implications can be found in Chapter 10 as well as possible future improvements of the methods.

CHAPTER 2

INSTRUMENTS

Two primary instruments have been used in this dissertation: the Burst and Transient Source Experiment (BATSE) onboard the Compton Gamma-Ray Observatory (CGRO), and the *Fermi* Gamma-ray Burst Monitor (GBM). These instruments are composed of multiple detectors to monitor the entire unocculted sky for gamma-ray transients, particularly GRBs. Both instruments comprise detectors that are sensitive in the keV–MeV range and exhibit peak response in the energy range where GRBs emit most of their flux. This chapter is devoted to describing the detectors and detector physics in detail, and then describing each instrument as a whole. Section 2.1.1.1–Section 2.1.1.3 discuss the different absorption processes in gamma-ray detectors, Section 2.1.2 and Section 2.1.3 describe the two types of detectors use by BATSE and GBM, meanwhile Section 2.2 and Section 2.3 describe the spacecraft and instrumentation of BATSE and GBM, and Section 2.4 discusses how the detector response is formulated.

2.1 Gamma-ray Detector Descriptions

Since gamma-rays are high energy photons and GRBs are distributed isotropically over the sky, it is impractical to build a detector that can image a fast transient event like a GRB with a low background as well as have the ability to trigger on a large number of events. For this reason, scintillating crystals attached to photon multiplier tubes (PMTs) are used as light buckets to collect the photons and convert them into electronic counts. There are a number of processes by which gamma-ray photons can interact with scintillating crystals and a number of different types of scintillating crystals that can be used to cover the energy band that GRBs occupy. The following sections discuss the absorption processes and detector types that are used by the BATSE and GBM instruments.

2.1.1 Gamma-Ray Absorption Processes

Gamma-ray photons may interact with a scintillation crystal in a number of ways. In particular, scintillation crystals with high atomic number and density are generally required. The thickness of the crystal also plays an important part; as the thickness increases, the effective stopping power of the crystal increases, and the more likely a photon of a particular energy will be absorbed in the crystal. The following section discusses the processes by which incident gamma–rays deposit energy in the crystal. Three different processes contribute to the absorption, each of which are dominant at different energies.

2.1.1.1 Photoelectric Absorption

Primarily below a few hundred keV photons will interact with the crystal by photoelectric absorption. This process causes the energy of the incident photon to be absorbed by bound electrons through the photoelectric effect, where the electrons are excited and consequently de-excite to produce UV emission through fluorescence. In theory, the photopeak will be a delta function at energy $h\nu$ if the incident photons are monochromatic, but due to energy dispersion from the fluorescence process the photopeak at $E \sim h\nu$ will typically broaden. One particular problem with a typical scintillation crystal, Sodium Iodide (NaI) is what is known as the K-edge. Located at $\sim$ 31 keV, this nonlinearity in the crystal response is the result of the energy of the incident photon being sufficiently high to overcome the K-shell binding energy of the electrons in the iodine atoms. If a photon with an energy slightly less than the K-shell binding energy is incident on an iodine atom, it will have much greater energy than the outer shell electrons and will not interact with them. The reason for this is that the photoelectric effect must conserve momentum, and since the outer shell electrons act much like free electrons compared to the energetic incident photon, there is no mechanism to carry off the excess momentum from the photon. This causes an attenuation in the interaction cross-section unless a photon exceeds the K-shell binding energy and the inner shell electrons then become available for interaction with the incident photons, thereby increasing the interaction cross-section of the crystal at that energy.

2.1.1.2 Compton Scattering

Compton scattering is an interaction process that becomes dominant above a few hundred keV to several MeV. This process is described by an incident photon scattering off of an electron in the crystal and depositing a fraction of its energy in the electron. The amount of energy transferred to the the electron is the difference between the energy of the photon before and after the interaction. The scattered photon energy ($h\nu'$) is dependent not only on the incident photon energy ($h\nu$), but also the angle of scatter (ϕ_s) by using the conservation of momentum;

$$h\nu' = \frac{h\nu}{1 + \frac{h\nu}{m_e c}(1 + \cos\phi_s)}. \tag{2.1}$$

From this equation, it is apparent that a backscattered photon ($\phi_s = 180°$) results in the maximum amount of deposited energy and a collision resulting in no scattering ($\phi_s = 0°$) results in the minimum. Statistically, the scattering angle for Compton interactions are uniform, resulting in a continuous distribution of energy from the minimum to maximum allowed deposition of energy. This distribution can be predicted by the Klein-Nishina cross-section as a function of energy. The cutoff corresponding to the maximum allowable deposited energy is known as the Compton edge,

$$h\nu_{max} = \frac{2(h\nu)^2}{m_e c^2 + 2h\nu}. \tag{2.2}$$

An example of the Compton edge can be found in Figure 2.1.

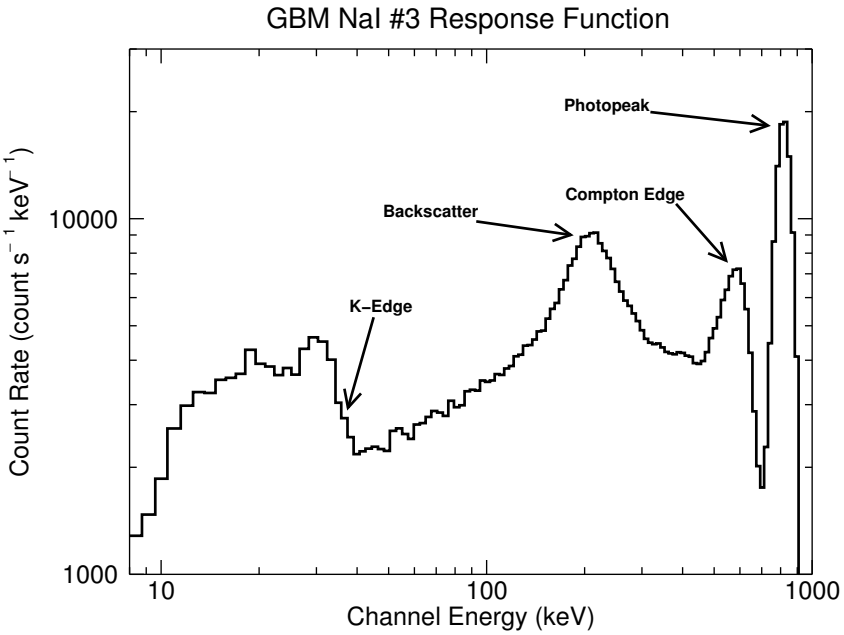

Figure 2.1: NaI response function for simulated photons at 800 keV. The Compton edge is clearly identifiable at ∼600 keV.

2.1.1.3 Pair Production

Incident photons with energy greater than several MeV are dominated by pair production interactions. For this process to start, the incident photon must have a minimum energy of 1.022 MeV since the incident photon energy is to be converted into an electron–positron pair ($2 \times m_e c^2 = 1.022$ MeV). An incident photon at precisely that energy will produce an electron–positron pair with no kinetic energy. Any energy in excess of the minimum energy will be shared by the pair in the form of kinetic energy. Typically the produced positron will interact with an available electron in the crystal, annihilating and producing two photons, each with energy $m_e c^2$. In this case, either or both annihilation photons may escape the detector without further

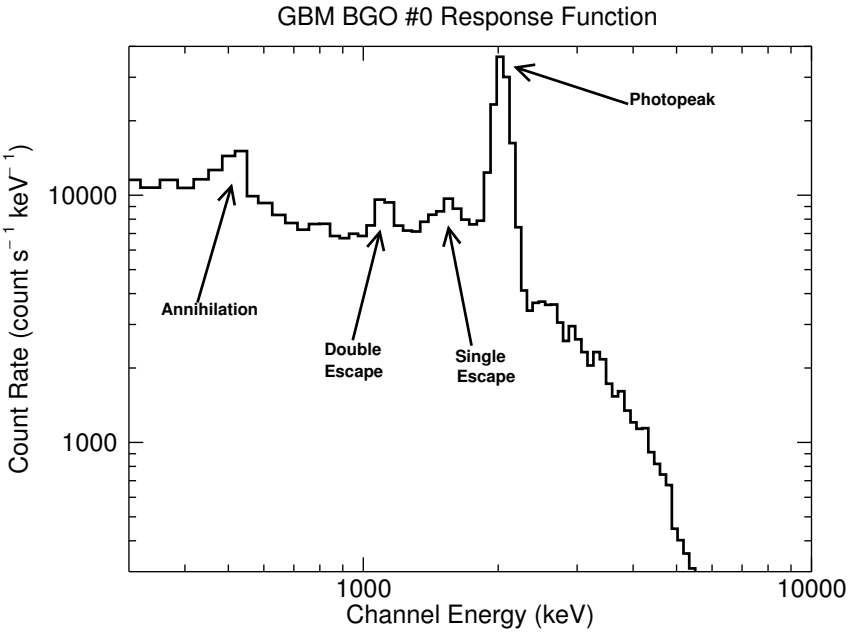

Figure 2.2: BGO response function for simulated photons at 2 MeV. The 511 keV electron–positron annihilation line is clearly identifiable as well as the single (∼1.5 MeV) and double (∼1.0 MeV) escape peaks.

interaction, producing a single escape peak at $h\nu - m_e c^2$ or a double escape peak at $h\nu - 2m_e c^2$ respectively. However, if both photons are unable to escape the detector, they both will contribute to the photopeak. An example of the single and double escape peaks are shown in Figure 2.2.

2.1.2 Sodium Iodide Detectors

Sodium Iodide crystals are of the most ubiquitous type used in high-energy photon photomultiplier tube detectors due to their high efficiency and light yield. Sodium Iodide detectors employ scintillation to send photoelectrons to the PMT. The scintillation process takes all or a part of the energy from an incident photon

on the crystal and transfers it to electrons in the crystal. The electrons absorb the energy and become excited and consequently emit scintillating photons due to to the process of fluorescence as the electrons de-excite. The scintillating photons are then collected by the PMT and are converted to photoelectrons by way of the photoelectric effect. The photoelectrons can then produce a voltage which is then converted into an analog electronic signal. Typically, NaI crystals are doped with thallium (Tl) to activate its scintillation potential.

2.1.3 Bismuth Germanate (BGO) Detectors

Similar to NaI, Bismuth Germanium Oxide (BGO; known as Bismuth Germanate) is a scintillation crystal with high density, high atomic number (Z = 83), making it suitable and efficient at gamma-ray absorption. Bismuth Germanate crystals, however, typically have a lower light yield than NaIs, making them suitable for use with PMT when absorbing photons greater than 1 MeV. The lower light yield is a direct result of the lower efficiency of converting gamma-rays to UV through fluorescence. The energy range of BGO detectors make them more likely to absorb photons due to Compton scattering and pair production methods than through photoelectric absorption, which is the dominant absorption process in NaI crystals. The higher-energy peak response of BGO crystals compared to NaI crystals make them complementary to extend the energy collection range of a multi-detector instrument.

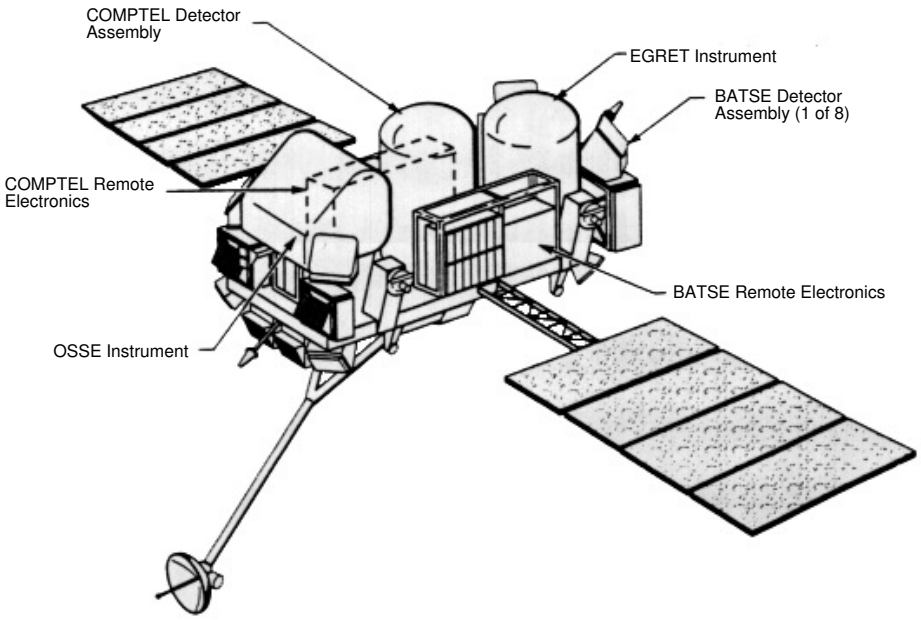

Figure 2.3: Model of CGRO depicting the locations of the different onboard instruments. The BATSE detectors were located on the eight corners of the spacecraft and were oriented for all-sky monitoring.

2.2 The CGRO and BATSE

The Compton Gamma–Ray Observatory (CGRO) was placed into low Earth orbit (∼400 km) by the space shuttle Atlantis in 1991 April. Shown in Figure 2.3 is CGRO and the location and orientation of its instruments. The instruments flown onboard comprised of the Oriented Scintillation Spectrometer Experiment (OSSE), the Imaging Compton Telescope (COMPTEL), the Energetic Gamma-Ray Experiment Telescope (EGRET), and the Burst Alert and Transient Source Experiment (BATSE).

The dedicated GRB mission, BATSE, was an eight-component detector system designed to study the gamma–ray sky in the energy band of ∼10 keV–20 MeV.

Each of the eight modules, mounted on the corners of CGRO, consists of two NaI(Tl) scintillation detectors: a Large Area Detector (LAD), optimized for temporal resolution, and a Spectroscopy Detector (SD), optimized for energy resolution [4]. The configuration of the experiment allowed the maximum unobstructed field of view (approximately 2.6π steradians) for a low Earth orbit satellite.

Each LAD contained a NaI crystal $\sim$51 cm in diameter and $\sim$1.3 cm thick that was uncollimated in the forward hemisphere and passively shielded in the aft hemisphere. The large surface area enabled the collection of a large number of gamma–ray photons as compared to previous orbiting scintillation detectors, thus providing a superior combination of temporal and energy resolution of observed events. The LAD was mounted on the upper part of the module. The planes of the eight LAD faces formed a right–regular octahedron when the modules were in their flight configuration on the CGRO. This ensured that each GRB usually illuminated four detectors (there was a special case where only two detectors were illuminated). The approximate location of a burst could then be determined by comparing the relative count rates in those detectors that observed the burst.

Although most scintillation detectors typically have photomultiplier tubes coupled directly to the crystal, the large surface area of the LADs made this impractical for uniform light collection. The crystal was instead attached to a collection cone that was lined with a light-reflecting barium sulfate-based ($BaSO_4$) coating. Three PMTs collected the scintillation photons and these signals were summed at each detector. The tubes had a minimum quantum efficiency of 26% at 410 nm [15]. The light collection cone was passively shielded up to $\sim$300–400 keV with lead and tin

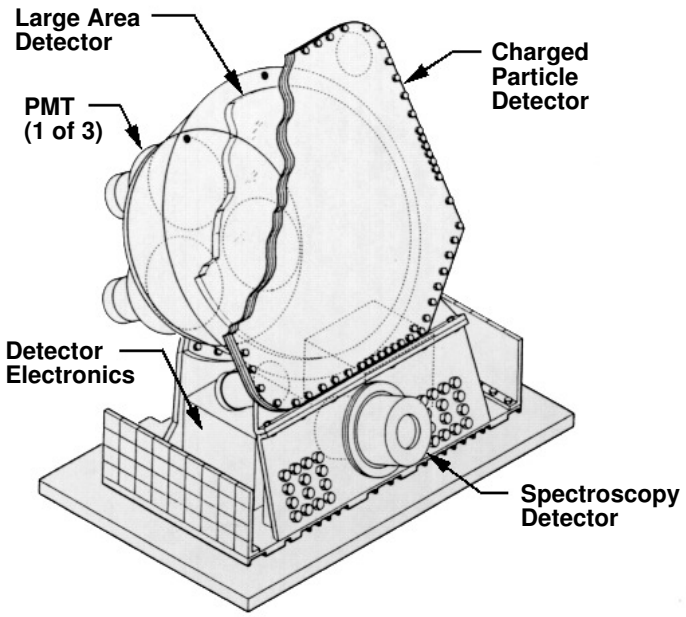

Figure 2.4: One of eight NaI detectors from BATSE consisting of a NaI(Tl) crystal and three PMTs.

layers. The tin layer was designed to absorb the K-shell X–rays produced by gamma interactions in the lead. The front of the crystal was covered by a plastic scintillator whose light was collected by two 5 cm PMTs, the signals of which were also summed at each detector. The purpose of this plastic scintillator, called the Charged Particle Detector (CPD), was to detect particles that entered the LADs. The instrument could be prevented from triggering due to radiation produced by interactions of these particles with the NaI crystal by the detectors' optional coincidence/anti-coincidence circuitry (the instrument operated in anti-coincidence mode for the entire mission). No energy information was available for incident particles; the plastic scintillator was used solely to aid in identification of charged particle events. The threshold energy deposition for the charged particle detector was $\sim$500 keV.

Each LAD was equipped with a system that controlled the high voltages (gain) of the photomultiplier tubes with minimal intervention from controllers on the ground. The Automatic Gain Control (AGC) algorithm computed and executed adjustments to the PMT high voltages so that a feature in the count spectrum remained in a specified energy channel. The background was calculated as a straight line over a specified range of energy channels and was used to produce a background-subtracted count spectrum. The average channel in the range was computed, and if this average was different from a specified average, the high voltage of a single PMT was adjusted to correct the computed value. The PMTs were adjusted cyclically, and the range of voltage adjustment was clamped. If the AGC attempted to change the high voltage to values outside of the specified range, an error was issued. The background feature nominally monitored by the AGC was the 511 keV electron–positron annihilation line that was present in the gamma–ray background. If the line drifted too far from the programmed energy channel, the gains of the PMTs were automatically adjusted $\sim$4 volts higher or lower to move the annihilation line back to the correct energy channel. This procedure, which occurred approximately every 5 minutes, ensured that the eight LADs had nearly equal energies in a given pulse-height channel.

2.3 *Fermi* and GBM

The Gamma–ray Large Area Space Telescope (GLAST) was launched and placed into orbit on June 11, 2008 and was later renamed the *Fermi* Gamma-Ray Space Telescope. Two instruments comprise *Fermi*: the Large Area Telescope (LAT) and the Gamma-ray Burst Monitor (GBM). Shown in Figure 2.5 is a schematic of

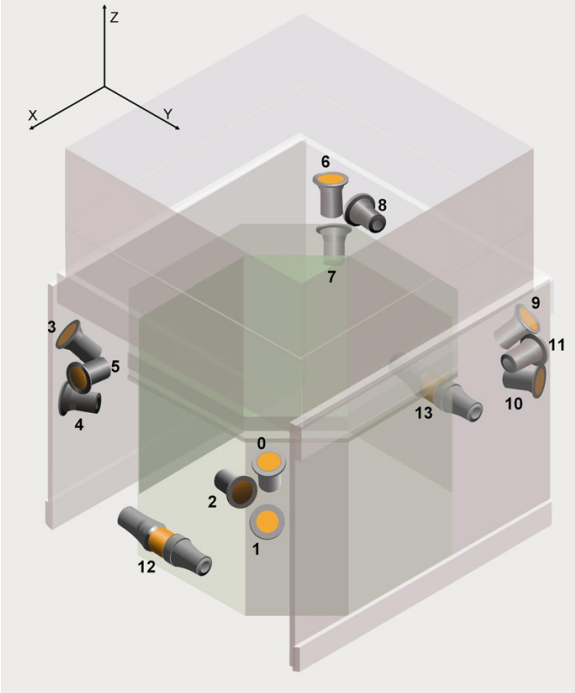

Figure 2.5: Model of *Fermi* depicting the orientation in spacecraft coordinates of the NaI detectors (#0–11) and the BGO detectors (#12 & 13) [1].

Table 2.1: GBM NaI Detector Orientations in Spacecraft Coordinates

Detector #	Azimuth (°)	Zenith (°)
0	45.9	20.6
1	45.1	45.3
2	58.4	90.2
3	314.9	45.2
4	303.2	90.3
5	3.4	89.8
6	224.9	20.4
7	224.6	46.2
8	236.6	90.0
9	135.2	45.6
10	123.7	90.4
11	183.7	90.3

Fermi and the location and orientation of its instruments. The LAT is the primary instrument and works by tracking the source positions and energies of high energy photons that convert to electron-positron pairs within the instrument [16].

The GBM is the secondary instrument on board the *Fermi* Gamma-Ray Space Telescope. The GBM is a 14–detector instrument designed to study the gamma-ray sky in the energy band of ∼8 keV–40 MeV. Twelve of the detectors are NaI(Tl) scintillation detectors, placed in groups of three on the side edges of the spacecraft and pointing at various angles from the *Fermi* Large Area Telescope (LAT) boresight [1]. The pointing angles were chosen by simulations to adequately survey the entire unocculted sky at any time during the orbit and listed in Table 2.1. The other two detectors are each composed of a BGO crystal and are placed on either side of the spacecraft pointing at right angles to the LAT boresight. Photographs of a BGO detector and NaI detector are shown in Figure 2.7 and Figure 2.6 respectively.

The NaI crystals are each 12.7 cm in diameter and 1.27 cm thick and coupled to a single PMT. The NaI detectors cover an energy range from 8 keV–1 MeV. Each BGO crystal has a diameter and thickness of 12.7 cm and coupled to two PMTs to increase the capture of scintillating photons from the crystal. The BGO detectors cover a range of 200 keV–40 MeV [1]. Because of varying orientations and the all-sky coverage of the NaI detectors, the approximate location of a burst can be determined by comparing the relative count rates in the detectors that observed the burst.

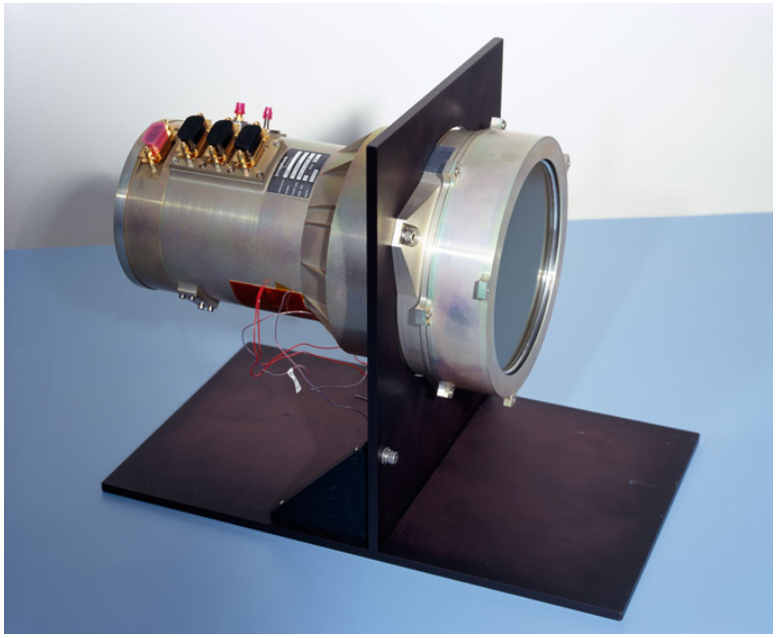

Figure 2.6: One of twelve NaI detectors from GBM consisting of a NaI(Tl) crystal and a PMT [1].

Figure 2.7: One of two BGO detectors consisting of a BGO crystal and two PMTs [1].

2.4 Detector Response Matrices (DRMs)

Detector Response Matrices (DRMs) are mathematical models of the detector's response used to map the observed counts into photons of known energy. Each detector's response is dependent on incident photon energy, the measured detector output energy, and the detector–source angle and the earth–source–spacecraft geometry [17]. This association is dependent on effective area and the angle of the detector to the incoming photons. To do this, DRMs are used to convert the photon energies into detector channel energies. The DRM is a model of the deposition of photon energy in the crystal—a photon that interacts by the photoelectric effect will deposit 100% of its energy, subject to resolution broadening, while a photon that interacts by a single Compton scatter will deposit only a portion of its energy. The energy calibration determines the energy boundaries of the energy deposition channels.

For BATSE, the LAD angular response is, to first order, a cosine function in θ at low energies, where θ is the zenith angle defined with respect to a unit vector normal to the LAD crystal. The response is flatter than a cosine function for energies greater than $\sim$300 keV. The circular configuration and lack of spacecraft interference in the forward hemisphere of each LAD essentially remove any ϕ-dependence of the response function (ϕ is the azimuthal angle with respect to the LAD normal). Figure 2.8 shows an example of a DRM from BATSE LAD detector #6. Unlike BATSE, the DRMs for GBM require a ϕ-dependence since the *Fermi* spacecraft constantly slews and rocks in orbit and the background is not a simple function of time. The source location of a GRB is calculated in spacecraft coordinates and used to estimate the detector–source

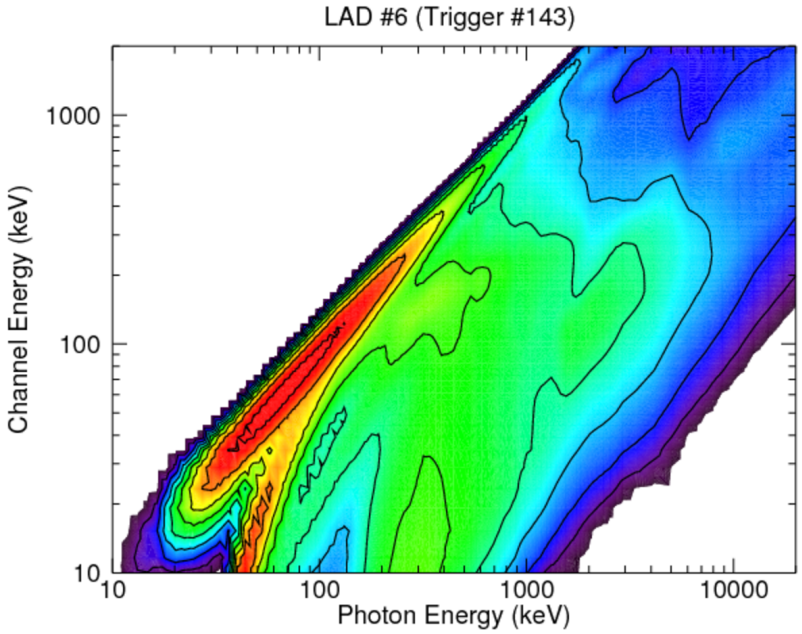

Figure 2.8: The detector response matrix for LAD #6 of BATSE trigger #143 (GRB 910503).

angle. The DRMs record the energy response of the detectors at various angles, which was determined through extensive simulations using the General Response Simulation System (GRESS) [18] and validated by the source survey. The response matrices for all current GRBs were made using GBMRSP v1.9 of the response generator and version 2 of the GBM DRM database, and all responses employ atmospheric response modeling to correct for possible atmospheric interference. Figure 2.9 shows the DRM for a GBM BGO detector and Figure 2.10 shows the DRM for a GBM NaI. In addition, special response files can be generated for GBM, RSP2 files, which contain multiple DRMs based on the amount of slew the spacecraft experiences during the burst. Typically, a new DRM is calculated for every 2° of slew, changing the effective area of each detector based on its angle to the source. These DRMs are then all stored

in a single RSP2 file for each detector. RSP2 response files allow for more accurate spectral analysis of events that are very long, where the angle of the detectors to the source may have changed by a significant amount.

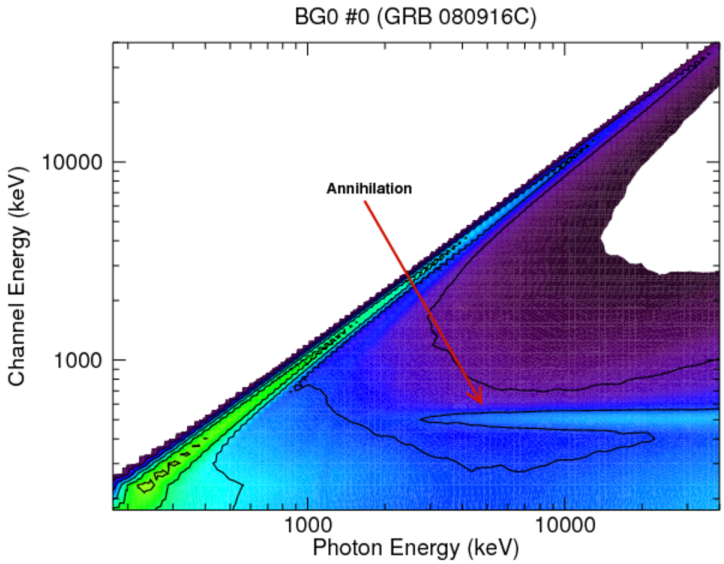

Figure 2.9: The detector response matrix for BGO #0 of GBM GRB 080916C. The 511 keV electron–positron annihilation line is clearly identifiable

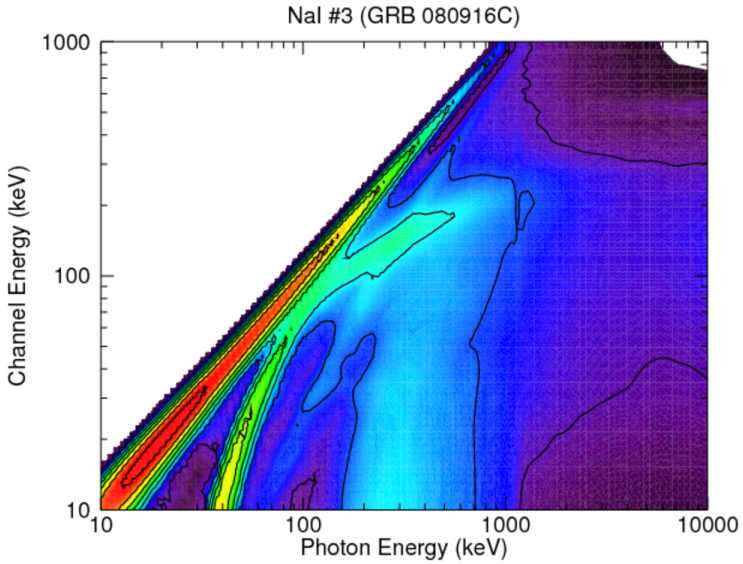

Figure 2.10: The detector response matrix for NaI #3 of GBM GRB 080916C.

CHAPTER 3

OBSERVATIONS OF GRBS

After their accidental discovery by the *Vela* spacecraft, many different instruments have been designed to study the emission of GRBs. A number of instruments are integral in the observations of GRBs. As one of the first deidcated GRB missions, BATSE was awarded a position onboard the Compton Gamma-Ray Observatory, and provides the single largest compendium of burst properties of any instrument. *BeppoSax* came soon after, and contributed to localizing GRBs in the sky. Another particularly important instrument is *Swift*, which, in addition to imaging bursts in the low keV range, can well localize GRBs and study their emission afterglow. Most recently, *Fermi* allows for the study of GRB prompt emission spectra and detection of emission up to hundreds of GeV. Also, there are numerous land-based radio and optical telescoped that help study the burst afterglow. Undoubtedly the observations of both the prompt emission and afterglow phases of the GRBs are important to discerning the physical processes involved.

The first instrument to establish the fact that GRBs are cosmological and non-Galactic was BATSE [12]. As the mission elapsed and an increasing number of GRBs were localized, it became apparent that the distribution was not concentrated

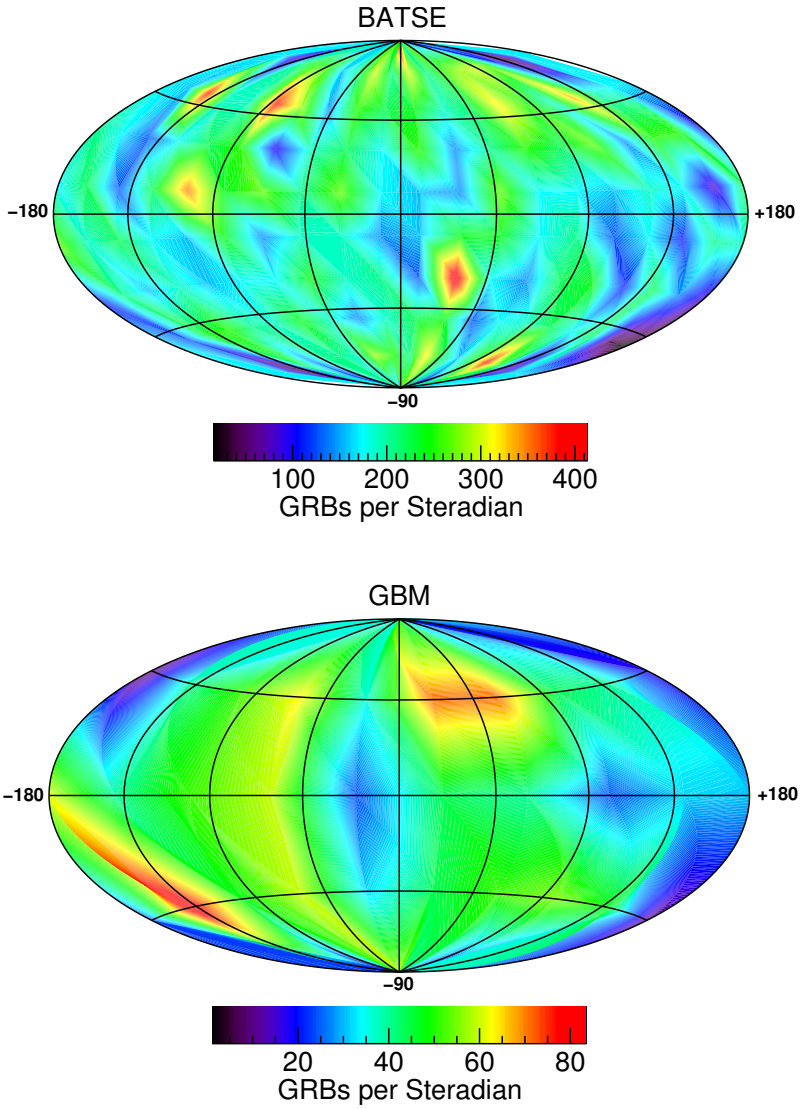

Figure 3.1: [*Top*] The angular distribution of BATSE GRBs on the sky. [*Bottom*] The angular distribution of GBM bursts on the sky covering the first two years of operation.

on the Galactic plane as some had expected, but isotropically distributed over the entire sky. Figure 3.1 displays the differential number of GRBs per steradian for both BATSE and the first two years of GBM. The heat maps display areas of higher and lower concentrations of GRBs, depicting some amount of anisotropy, but no particular concentration about the Galactic plane. Gamma-Ray Bursts were originally studied in the 50–300 keV range, since the peak of their spectrum appeared to generally distribute in that range. A number of GRBs, however, have been discovered to exhibit a peak in spectral emission in the MeV range, such as 990123 [19] and three short GBM GRBs (090227B, 090228, and 090510) [20]. Even the discovery that a number of transients with softer emission, dubbed X-ray Flashes (XRFs), are associated with the same mechanism that produces GRBs leads to the assessment that the GRB prompt emission band could extend down into the keV range [21]. Initially, XRFs were thought to be a different phenomenon, yet their lightcurves are similar to GRB lightcurves and are spectrally similar to GRBs as well. The correlation between the spectral peak (E_p) and luminosity confirmed that they extend the correlation between GRBs to lower E_p and luminosity [21, 22]. The following Section 3.1 describes the observations of the prompt emission, and Section 3.2 discusses the different regimes of afterglow observations.

3.1 Prompt Gamma-ray Emission

The observed properties of the prompt emission of GRBs are largely variable. The duration of such emission typically lasts anywhere from a few tens of milliseconds to hundreds of seconds, and is usually detected in the range from a few keV to about

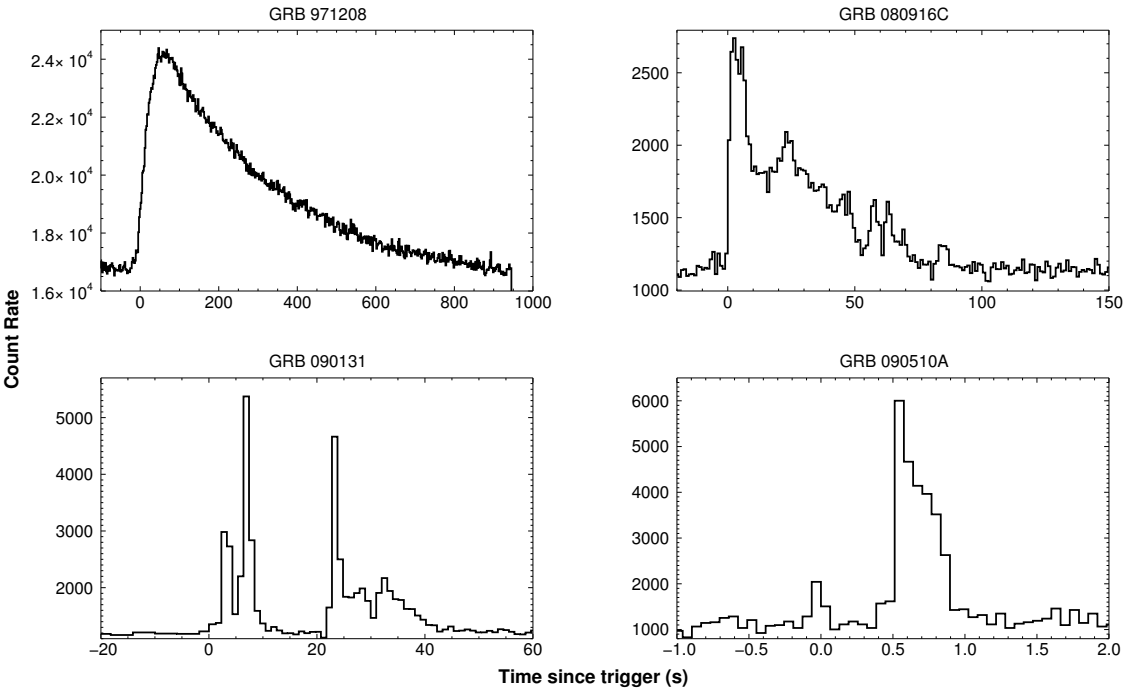

Figure 3.2: The count rate lightcurve of four GRBs before background subtraction. The lightcurves display the varying temporal properties of GRBs

an MeV. The count rate time history of each GRB is unique, rendering classifications based on morphology unsuccessful [23]. The shapes of GRB lightcurves vary widely; they include single-peak and multi-peak events, long duration emission at low intensity, and rapidly rising time profiles with an exponential-like decay phase. Temporal variability on time scales of the order of milliseconds has been observed [24], although smooth light curves with little variability are also observed. Figure 3.2 demonstrates these varying lightcurve characteristics. The durations of bursts span a wide range, with the shortest bursts of the order of tens of milliseconds, and the longest duration bursts lasting for hundreds of seconds. The logarithmic duration distribution of GRBs appears to exhibit two clusters centered at $\sim$0.3 s and $\sim$40 s, with a deficit of

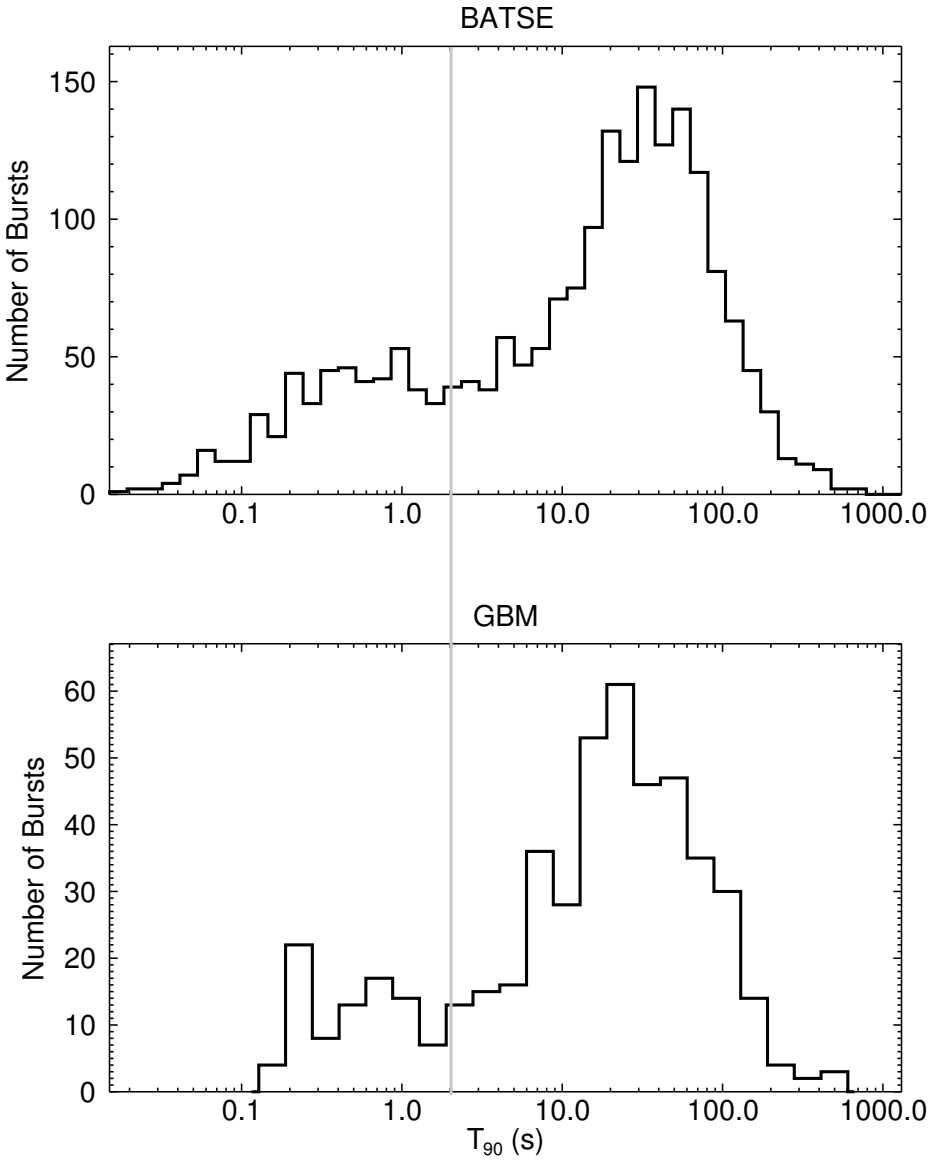

Figure 3.3: [*Top*] The T_{90} duration distribution of 2041 BATSE GRBs. [*Bottom*] The T_{90} duration distribution of 488 GBM GRBs during the first two years of operation. The dividing line at 2 seconds denotes the classical separation between long and short bursts first discovered by BATSE.

bursts of duration ∼2 s dividing the two groups. These two groups exhibit similar angular and intensity distributions [25], indicating they have similar spatial distributions. However, there is evidence for a duration–spectral hardness correlation in which the short duration bursts are spectrally harder than the long bursts [25, 26]. Figure 3.3 shows the BATSE and current GBM T_{90} distributions. The existence of two distributions is apparent, and the distribution of short GRBs contains $\sim 20\%$ of the combined distribution.

In addition to the diverse lightcurve properties of GRBs, they can also exhibit diverse behavior in their spectrum. The spectra of GRBs have been measured (e.g., [27–32]) over a wide energy range (∼10 keV to several GeV). Many burst spectra are consistent with a power law at high energies, showing little or no attenuation of high energy photons, while others exhibit an exponential cutoff at high energies. Spectra at lower energies usually exhibit increasing energy flux at lower energies, with a break between the low and high energy portions of the spectra occurring at approximately 100–300 keV. Most, but not all, gamma–ray bursts exhibit significant spectral evolution, usually evolving from hard to soft. This spectral evolution can make it difficult to ascertain the time–integrated spectrum of the burst. Some bursts display very little spectral evolution, and some display a strong evolution typically from hard to soft energies. Figure 3.4 shows an example of spectral evolution from the GBM-triggered GRB 090926A [33]. The spectral parameters evolve significantly throughout the duration of the burst, and spectral features can entirely disappear and reappear during the different phases of the prompt emission. In the particular case of GRB 090926A, the peak of the spectrum softens but the high-energy power

law hardens, and then an additional exponentially-attenuated power law component becomes evident and eventually hardens into power law component.

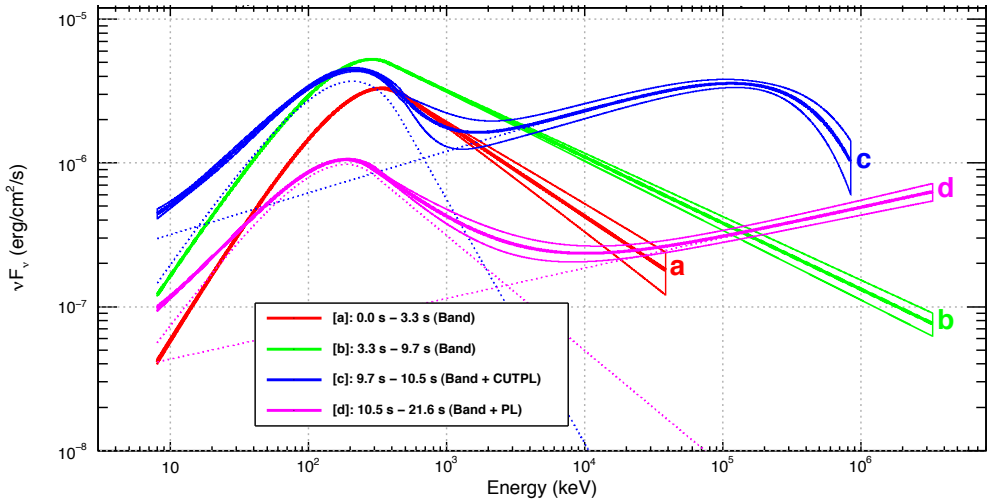

Figure 3.4: Time resolved spectral fits to GRB 090926A with a smoothly broken power law and an additional power law, displaying the evident spectral evolution.

3.2 Multi-chromatic Afterglow Emission

After the prompt emission burst in gamma-rays, an emission counterpart is still visible at lower energies (longer wavelengths), from the X-ray down to the radio. This emission is called the afterglow and can be detectable for days after the prompt emission. Unfortunately, due to the fact that the emission lasts for so long, there are almost no contiguous sets of measurements of the afterglow for GRBs. In fact, in most afterglows there may only be a couple measurements hours or days apart. The afterglow lightcurve is usually much less variable than that of the prompt emission, although can sometimes display variability due to flaring activity from the central engine. In many cases, the afterglow in multiple wavelengths decays in flux as a single power law until the flux has decayed below the detector sensitivity.

With the debut of *BeppoSax*, GRBs were able to be localized with precision and accuracy, and those localizations were rapidly communicated to its onboard X-ray instruments [34] as well as optical and radio telescopes on the ground. The optical observations, in many cases, yield absorption lines that are redshifted from their nominal wavelengths, indicating a redshift for the GRB. In addition, the redshift observation coupled with optical observations of the host galaxy led to identification of GRBs emanating from star-forming regions. Currently, the spectroscopic redshifts number over 250 and span a large range from 0.085 to 8.2 as well as numerous host galaxies identified from which the GRBs originated. Furthermore, the afterglow counterparts to the prompt emission have provided insight into the physics involved during the massive explosion that must result in a GRB and its afterglow. Immediately after

the prompt gamma-ray emission, the observed emission decays in energy and is detectable in the X-ray and then in the optical and eventually in the radio regime. The afterglow can be observed for days, months, or even years after the initial burst of gamma-rays. In many cases the transitions between the different phases of the afterglow is smooth, and even a transition from prompt gamma-ray emission to X-ray afterglow is manifest as a soft gamma-ray tail [35,36]. The following sections describe the characteristics of the afterglow in the different regimes.

3.2.1 X-ray Afterglow

The X-ray afterglow is the most widely detected regime of the afterglow, found in ∼90% of all GRBs. The X-ray lightcurve and spectra usually decays as a power law $F(t,\nu) = t^{\alpha}\nu^{\beta}$, where $\alpha \sim -0.9$ and $\beta \sim -1.4$ [37]. The X-ray lightcurve in reality, however, is often complicated by flaring from what is proposed to be a persistent source created after the initial explosion (see Chapter 4 for details). An example of flaring activity in the X-ray afterglow is shown in Figure 3.5.

3.2.2 Optical Afterglow

The optical afterglow component also tends to decay as a power law with $\alpha \sim -1$ and $\beta \sim -0.7$ initially and then eventually steepens over all optical bands. In some cases, this observed break may be due to the synchrotron or cooling frequency passing through the optical band [38, 39], but in other cases it has been proposed that the break is due to the sideways expansion and deceleration of a relativistic jet [40]. In the case of the latter, the break in the optical lightcurve is termed a

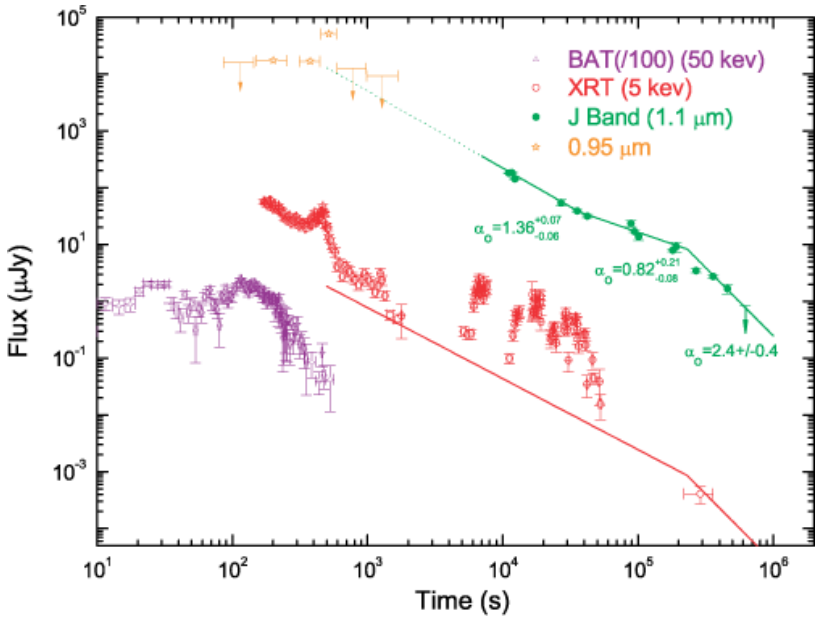

Figure 3.5: An example of late-time X-ray flaring found in the afterglow of GRB 050924 [2]. The X-ray observations appear in red as flaring activity superimposed on the typical power law decay. A jet break is visible at ∼200 ks (2.3 days) in the optical J band.

"jet break," which was a predicted property of the afterglow and an example of an observation is shown in Figure 3.5 at ∼200 ks. The jet break was formulated in the fireball shock model theory and is expected to be achromatic [40]. In the case of this model, GRBs are generally relativistically beamed with a half-opening angle $\theta_\Gamma \approx 1/\Gamma$, where Γ is the bulk Lorentz factor of the outflow. The assumption is that if the geometric collimation, θ_j, is not explicitly dependent on the relativistic collimation, the observed emission would first be from the region covered by the initial θ_Γ and as the ejecta decelerates, Γ decreases, and more of the beam defined by θ_j is accessible for observation. Once Γ has slowed to $\approx 1/\theta_j$, then $\theta_\Gamma \approx \theta_j$ and the observed flux decays faster since there is no longer a transverse addition of the

emission surface to compensate for the decaying brightness. Once the jet break has been detected, the optical lightcurve will continue to decay until it is indistinguishable from the underlying luminosity of the host galaxy, or in some cases, the underlying luminosity of the supernova from which the GRB originated [41–43]. The jet opening angle, and therefore the amount of collimation, can be determined by

$$\theta_j \approx 0.057\left(\frac{t_j}{1\text{ day}}\right)^{3/8}\left(\frac{1+z}{2}\right)^{-3/8}\left(\frac{E_{iso}}{10^{53}\text{ erg}}\right)^{-1/8}\left(\frac{\epsilon}{0.2}\right)^{1/8}\left(\frac{n_p}{0.1\text{ cm}^{-3}}\right)^{1/8} \quad (3.1)$$

where t_j is the time of the jet break in days with respect to the trigger time of the prompt emission, E_{iso} is the isotropic equivalent energy release in gamma-rays, ϵ is the efficiency of converting the kinetic outflow into radiation, normally assumed to be $\sim$0.2 and n_p is the particle density of the circumburst medium [44, 45].

In some cases before or during the smooth optical lightcurve, there will appear an abrupt optical flash. A notable example of this is from GRB 990123 [46] where a bright optical flash was observed during the prompt gamma-ray emission. This suggests that the flash was produced by an entirely different mechanism than the prompt emission [19]. These flashes are described by the theory encompassing reverse shock of the external shock of the blast wave as it impacts the circumburst medium. The direct observations of these optical flashes, therefore, lend credence to a reverse shock in the fireball-shock scenario [44, 47].

In some cases, an optical afterglow is not detected even when an X-ray afterglow is observed, leading these GRBs to be called optically "dark." A possible explanation is that the optical emission is attenuated by dust, which leaves the higher

energy gamma-ray and X-ray emission unabated. Another possibility is that the GRBs are intrinsically weak, and therefore the extrapolated X- ray flux into the optical range is simply below the optical observing threshold. In many cases, the latter explanation appears to be the case, although there appears to exist other optically dark GRBs that should otherwise have observable optical components. [48].

3.2.3 Radio Afterglow

While the prompt gamma-ray emission usually lasts no more than a few hundred seconds, and the X-ray and optical afterglow lasts for a few days or weeks, the radio afterglow can last for months or even years. The radio afterglow does not usually decay like the X-ray and optical but can be variable and exhibit large fluctuations near the start of the emission [49]. It has been suggested that the fluctuation in the radio is due to scattering by the irregularities in the ionized galactic interstellar gas and could be used to constrain the emitting region [50]. For example, GRB 970508 was estimated to have an emission radius of $\sim 10^{17}$ cm at the start of the radio emission [51].

3.2.4 Redshift Measurements

There are two principal methods used to measure the redshift of a GRB from its afterglow. The primary method uses optical spectroscopy to produce a spectroscopic redshift. Initially, spectroscopic redshifts were acquired by emission spectroscopy of the host galaxy, since the host galaxy provided a consistent long-lasting source from which to observe. Many host galaxies, especially distant hosts, are too faint for

reliable spectra, so the early redshift observations were limited. The launch of *Swift* led to the emergence of spectroscopic observations of the optical afterglow. With *Swift*'s rapid and accurate localization of GRBs, the location could be transmitted to any number of large-aperture ground-based telescopes such as VLT, Keck, Lick, and Gemini-S-N, which would then use absorption spectroscopy to determine by how much particular absorption lines are shifted from their usual postion [52].

The secondary technique is used when adequate optical absorption spectra are unavailable and is known as a photometric redshift. This method depends on the observation of the Lyman α absorption break feature through broad filter photometry [53]. Assumptions must be made about the original comoving spectrum, including assumptions about the line-of- sight column density and the amount of dust extinction affecting the observed spectrum [54]. The assumed original spectrum is then boosted into the observed frame for a range of redshifts to determine the most likely redshift. For GRBs in particular, templates are used that incorporate the theoretical emission properties of the afterglow, primarily from synchrotron emission as the expanding jet of the GRB impacts the external medium and converts the kinetic energy of the particles to radiation [55] (see Chapter 4 for more details). Because of the assumptions that are made in the estimation of a photometric redshift, the uncertainties are much larger than the uncertainties of spectroscopic redshifts. This is a primary reason for spectroscopic redshifts to be the method of choice.

CHAPTER 4

THEORETICAL GRB MODELS

The observations of the widely varying properties of GRBs have lead to much insight into the physical workings of GRBs. Certainly there are a number of open questions and uncertainties in the models proposed, but the field of models has been narrowed down to a couple of legitimate models supported by the data. One particular model that describes the initial explosion and expansion is called the fireball model, which relies on Fermi acceleration and a system of internal and external shocks to explain the lightcurve variability and afterglow emission. Additionally, there are a number of viable candidates for GRB progenitors, including collapsing supermassive stars, and merging binary neutron stars. Section 4.1 covers the leading proposed emission mechanisms that produce the observed GRB prompt emission spectra and afterglow. Section 4.2 describes the leading models into the different GRB progenitors.

4.1 GRB Emission Mechanisms

Many models exist on the emission mechanisms of GRBs, though not one single model has been able to adequately explain the diversity of GRB temporal and spectral

properties. I briefly describe the leading model and the support of observations to the theory.

4.1.1 Expanding Fireball Model

The fast variability of typical GRBs implies that the emitting region of the burst must be fairly small, but the photon spectrum and the cosmological distances of GRBs indicates that the high energy photon density is large, which would require a large opacity depth [56]. Reconciling the small emitting region with the large opacity depth required to produce what is observed is referred to as the "compactness problem." If an inordinately large amount of energy were packed into a small emitting region, the optical depth would be small and the emitting region would be opaque to > 1 MeV pair-production photons. This causes an attenuation in the spectrum at high energies that is not typically observed. The solution to this problem is to require that the ejecta be emitted relativistically, thereby causing the observed rapidity of the prompt emission variability by means of the relativistic Doppler shift [57]. In addition, the emitting region as inferred by observation would appear to be smaller than in the comoving frame of the burst because of relativistic beaming. This relativistic material, a combination of gamma-rays and electrons, are referred to as a "fireball," and the theory of the propagation of the initial explosion of the GRB is termed the Expanding Fireball Model.

4.1.2 Internal & External Shocks

In the fireball model, an expanding shell of ejecta impacts the interstellar medium resulting in an external shock front [58, 59]. The ejecta is heated from the shock and slowly cools as the ejecta expands into interstellar space and releases energy most likely via synchrotron processes [60] . This external shock leads to the afterglow and the slow decay in flux that is observed over a wide swath of energies. Efficient energy conversion at the shock fronts seem to explain the smooth seconds–long GRBs [61–63], yet most GRBs do not exhibit a smooth behavior, but instead are highly variable and vary widely in duration. The high degree of variability of many bursts is a cause to question a pure expanding fireball from the initial explosion and emission from the external shock front alone. However, if the fireball is composed of several shells of ejecta that are traveling relativistically but at different Lorentz factors, the shells will impact each other as they expand out from the progenitor and cause shock fronts [60, 64]. These shocks will convert the massive amount of kinetic energy in the explosion into accelerating the particles. The accelerated particles alone could inverse Compton scatter and produce gamma-rays, or with the help of the magnetic field of the progenitor, create gamma-rays through synchrotron radiation [60, 64]. Eventually all the shells will collide, intermix and roughly all the ejecta is moving at the same velocity. At this point, the ejecta impacts the surrounding interstellar medium and produces the aforementioned external shock. This internal–external shock model can adequately explain the high variability and wide range of

durations of the prompt emission via internal shocks, as well as the smooth slow cooling of the afterglow by way of the external shock.

In addition to the traditional model of internal and external shocks, in some cases there may be a reverse shock resulting from the external shock in which the ejecta travels backward from the interstellar medium shock front and again encounters the material in the internal shock. This could possibly lead to bright optical or UV flashes in the afterglow lightcurves [65, 66], which has been observed in a few GRBs [46]. In addition, if the progenitor is not completely destroyed by the initial explosion, it may be able to slowly emit more ejecta after the burst. As this material passes through the series of internal shocks and into the interstellar medium, it can create flares in the afterglow that disrupt the otherwise smoothly decaying afterglow flux. This late-time flaring activity has been observed in a number of GRB afterglows, and namely in afterglows observed by *Swift*.

4.1.3 Acceleration and Emission from Shocks

During the internal shocks, the particles are accelerated and most of the internal energy of the particles must radiate away to produce the observed prompt emission and afterglow. In the fireball model, both the prompt emission and the afterglow are assumed to be produced by Fermi-accelerated electrons. The resulting electron distribution in this case is assumed to be a simple power law. The accelerated particles are also assumed to interact with the magnetic field of the progenitor, causing them to emit most of their energy as synchrotron radiation [67, 68]. In this Synchrotron Shock Model (SSM), synchrotron self-Compton interactions and re-acceleration are

assumed to be negligible and two cases result: fast cooling electrons, which require that the entire electron distribution emit radiation through synchrotron to an energy ν_c; and slow cooling electrons, which is distinguished by only allowing the higher energy electrons to cool to ν_c. Due to the fact that the synchrotron emission power of electrons is

$$P(\gamma_e) = \frac{4}{3}\sigma_T c \beta_v^2 \gamma_e^2 U_B, \tag{4.1}$$

where $\sigma_T = 8\pi r_e^2/3$ is the Thomson cross-section, $\beta_v = v/c$ is the speed of the electrons, γ_e is the Lorentz factor of the electrons, and $U_B = B^2/8\pi$ is the magnetic energy density [69], there is a power dispersion resulting from the cooling electrons. Because of this, the more energetic electrons cool faster than the less energetic electrons. This indicates that the cooling energy ν_c represents the equilibrium energy where the synchrotron cooling timescale balances the cooling timescale due to the adiabatic expansion of the shell. The predicted spectra of the cooling synchrotron emission from the electron distribution for both the fast and slow cooling cases are described by a series of power laws of particular indices that are dependent on the electron distribution index, p.

The high variability of the GRB prompt spectra indicate that the cooling timescale during this phase is short resulting in a fast cooling electron distribution. The afterglow, however, appears to prefer slow cooling since synchrotron cooling should dominate at all energies. Observations of the prompt emission are found to be consistent with the SSM in many cases, although there are still a significant fraction of GRB spectra that cannot be explained by the SSM alone. In addition, it has been

suggested that the particle distributions assumed in the SSM may not be consistent with observed spectra at all [70]. The observed afterglow spectra are more favorable to the SSM because of the small amount of observed polarization, due to the existence of a random magnetic field behind the shocks.

4.2 GRB Progenitors

Although thousands of GRBs have been observed and analyzed, a definite answer to the question of what causes a GRB is still unknown. In the context of the fireball shock model, the central engine progenitor is hidden inside an optically thick region and is not directly observable, although it is expected that the central engine contains $\sim 10^{51}$ erg total energy to accelerate the ejecta to relativistic velocities. Observationally, GRBs seem to be divided into two classes based on the duration and hardness of their prompt emission. Additionally, the short GRBs tend to have smaller redshifts and exist much closer to the current epoch. It has been theorized, mainly on population studies of potential host galaxies, that there exist two primary progenitors. The observations require that the models release an extraordinary amount of energy in a short period of time, and must also reflect the population distribution of the candidate objects. This section describes the two mainstream theoretical progenitors for GRBs.

4.2.1 Long GRBs

Long GRBs are usually associated with the deaths of supermassive stars, particularly with collapsars, supernovae that end with the parent object collapsing into

a black hole [71–74]. The infalling material drives relativistic jets out of the rotational axis to create a shock front [75]. For the core-collapse supernovae scenario to be valid, the star needs to be at least several tens of solar masses, it is likely the star needs to be rapidly rotating for the angular momentum to facilitate the development of collimated beams, and finally the metallicity of the star needs to be low so that the jets can completely break through the collapsing star matter [76–79]. These requirements appear to confirm that long GRBs should emanate primarily from environments that harbor massive stars with low metallicity, environments that existed mainly in the early universe. In fact, the distribution of GRBs with measured redshift appears to peak around 2–3, indicating that these events do indeed originate from the early universe [80, 81]. In addition, several studies have been performed on potential GRB host galaxies to study the environments from which these GRBs originate [82–85]. The findings strongly correlate young and low metallicity galaxies with long GRBs. Long GRBs are usually only found in irregular galaxies or in the arms of spiral galaxies and away from regions of the galaxies where star formation has ceased, indicating that they emanate from massive star populations [86]. In addition, there have a been a few cases where GRBs have been observationally associated with individual supernovae [87–89] . These supernovae tend to be of Type Ib/c which are core-collapse events of low-metallicity massive stars, thus providing further evidence that long GRB progenitors may be primarily formed from collapsars, although more recent GRBs have indicated that there are GRBs without a supernova connection [90].

4.2.2 Short GRBs

While the collapsar model for long GRBs is a fairly well established progenitor model, the progenitor model for short GRBs is somewhat less certain. The leading theory is a merger model of binary neutron stars [91], or a neutron star and formerly supermassive star that collapsed to a black hole [92]. This model assumes that two of the objects in question form a binary pair whose orbits, through gravitational radiation and loss of angular momentum, degenerate until the two objects merge [56,93,94] and form a black hole with a torus of material from the original binary [95]. The process of merging would destroy the neutron star(s) in a violent explosion. The process that the progenitor(s) undergo to create a short GRB is decidedly different than for a long GRB, although the emission mechanisms (synchrotron, inverse Compton) are thought to be the same. Observationally, short GRBs have smaller redshifts and therefore exist much closer than do long GRBs [96]. Short GRBs have been observed to emanate from spiral and elliptical galaxies, although some have been located in regions not corresponding to any particular galaxy. [97, 98]. Rarely are extensive afterglows observed for short GRBs, which supports the merger model of a fast explosion, rather than a slower sustained outflow of ejecta from a collapsar. This lack of afterglow, in fact, may predicate that short GRBs are only loosely collimated. Unfortunately, for a number of short GRBs, X-ray flaring has been observed days after the initial explosion, which complicates the merger model, since the flaring activity is detected long after the merger and explosion should be complete [99].

While the merger scenario is the most preferred for short GRBs, another proposed scenario is caused by flares from magnetars [100]. The flares repeatedly produce bursts of hard X-rays and soft gamma-rays, and because of the temporal and spectral difference from short GRBs, were dismissed as possible progenitor candidates. The magnetar candidate SGR 1806-20, however, produced an extremely bright outburst that caused significant disruptions in the ionosphere [101]. This magnetar was at a distance of $\sim$15 kpc, which is several orders of magnitude closer than typical short GRBs, therefore the luminosity is still much less when compared to a short GRB at $z \sim 1.0$.

CHAPTER 5

GRB SPECTRAL ANALYSIS

This dissertation employs extensive use of the spectroscopy results of GRBs. The analyses performed were intended to be thorough as well as objective by performing an identical analysis on every GRB. The spectral results described herein are formulated in detail in the BATSE [102] and GBM [103] Spectral Catalogs. For completeness, I briefly discuss the analysis methodology in Section 5.1, including the spectral models used in Section 5.1.6 and a short description of each catalog in Section 5.1.7 and Section 5.1.8. Some of the important catalog results are discussed in Section 5.2.

5.1 Analysis Methodology

For both BATSE and GBM bursts, I devised a simple analysis methodology to sufficiently model the spectrum of each GRB. The following sections describe the method with which I used to systematically analyze the spectrum of each GRB. This method produced two different sets of model spectra for each GRB and enables the use of GRB spectra to study cosmology.

5.1.1 Detector Selection

Sodium Iodide detectors from both instruments with source angles of greater than 60° were excluded in all analyses since the response for those detectors were less certain at larger angles. In the case of BATSE, all usable detectors and their corresponding responses for each burst were summed to produce a single file that helped to strengthen the signal of weaker GRB triggers. The detectors for GBM, however, were only summed for the purpose of signal selection and then were jointly fit. One main reason for this difference is the fact that GBM is not zenith-pointed, which was the case for BATSE. Instead, The *Fermi* spacecraft is allowed to slew and every two orbits completes a rocking and barrel roll maneuver to enable full sky survey for the LAT, causing the GBM detector responses to vary independently. Instead, at most the three brightest GBM NaI detectors were selected that had no apparent blockage from other parts of the spacecraft, as well as the closest BGO detector. This set of detectors for each burst were then fit jointly, rather than summed as a single detector and response.

5.1.2 Datatypes

The data type used for the BATSE catalog was 2.048 second resolution CONT data, which provided semi-continuous count rate and 16-channel spectral coverage during the entire BATSE lifetime. Other BATSE datatypes such as HERB or SHERB data provide a much higher energy resolution (128 and 256 channels respectively) at the cost of time resolution. These datatypes provided pre-burst time resolution on the

Table 5.1: GBM Science Datatypes

Name	Maximum Temporal Resolution	Maximum Energy Resolution
CSPEC	1.024 s	128 channels
CTIME	64 ms	8 channels
TTE	2 μs time tags	128 channels

order of ∼300 s, which complicates accurate background subtraction. Additionally, the trigger time resolution can vary depending on the count rate, and in many cases the high temporal resolution and trigger data end before the end of the GRB, further compromising the spectral analysis. Therefore, CONT data were the best choice for time-integrated spectral fitting since they allow the analysis of any precursor or late-time prompt emission that is not covered by other data types.

For GBM, the primary data type used was the time-tagged event (TTE) data, which provide absolute time resolution to 2 μs based on GPS, and high energy resolution of 128 channels (see Table 5.1 for a list of the GBM science datatypes). The TTE data files were binned to 1.024 s for burst durations greater than 2 s and binned to 64 ms for bursts otherwise. The time history of TTE typically starts at ∼30 s before trigger and extends to ∼300 s after trigger. This timespan is adequate for the analysis of most GRBs. For GRBs that have evident precursors or emissions that last more than 300 s after trigger, CSPEC data was used, which extends ∼4000 s before and after the burst. This datatype also has a continuous 128 channel energy resolution which is normally accumulated at 4.096 s temporal resolution that changes to 1.024 s resolution for ∼600 s starting at trigger time.

5.1.3 Energy Selection and Background Fitting

Before spectral analysis could begin, an energy channel range must be selected, and the background must first be modeled so that it can be subtracted from the signal. The entire channel energy range was selected from ∼30 keV–1.8 MeV for BATSE bursts, which excludes the low-energy channel 0 where the instrument response is poor as well as the overflow channel. For GBM, the NaI channel range from ∼8 keV–1 MeV was selected, as well as the BGO channel range from ∼300 keV–38 MeV. With the resulting time series for each burst, a sufficient amount of pre- and post-burst background was selected to model the background and fit a single energy dependent polynomial (choosing up to 4^{th} order) to the background. For each detector the time selection and polynomial order were varied until the χ^2 statistic map over all energy channels was minimized, resulting in an adequate background fit.

5.1.4 Source Selection

For GBM bursts, once the background count rates were determined for each detector for a given burst, the count rates and background models were summed over all NaI detectors to produce a single lightcurve from which objective time selections were made. The background was subtracted, the rates converted to counts, and the signal-to-noise ratio (SNR) for each time history bin was calculated. Only the time bins that contained a SNR greater or equal to 3.5σ were selected as signal. The time selections produced from this criterion were then applied to all detectors for a given burst. This criterion ensures that there is adequate signal to successfully perform a

spectral fit and constrain the parameters of the fit. Similarly, the same 3.5σ SNR selection was performed on the BATSE bursts, although the process was simpler due to the fact that only single summed lightcurve files were used. The SNR selection is termed a "fluence" selection, since the selection is over the entire fluence of the burst. In addition to the fluence selections, a peak flux selection was made for each burst, resulting in a single bin containing the largest background-subtracted signal from the burst. In the case of GBM bursts longer than 2 s, this selection spanned a single 1.024 s bin, otherwise the selection spanned a single 64 ms bin. In the case of BATSE, the time resolution was 2.048 s for all bursts, therefore the brightest 2.048 s bin was selected. This selection was termed the "peak flux" selection.

5.1.5 Spectral Modeling

The spectral analysis of all bursts was performed using RMfit, version 3.4rc1 [104]. RMfit employs a modified, forward- folding algorithm for spectral fitting. This procedure uses each detector response matrix, characterized by the effective collective area, and multiplies them with a model energy spectrum. The result is a model count spectrum, which is then compared to the observed count spectrum by use of a nonlinear least squares minimization algorithm (Levenberg-Marquardt). The Castor C-Statistic, which is a modified log-likelihood statistic based on the Cash parametrization [105] is used in the model-fitting process as a figure of merit to be minimized. This statistic is preferable over the more traditional χ^2 statistic minimization because of the non-Gaussian counting statistics present when studying dim GRBs. Although it is advantageous to perform the spectral fitting using C-Stat, the statistic provides

no estimation of the goodness-of-fit since a standard probability distribution for likelihood statistics does not exist. For this reason, χ^2 was also calculated for each spectral fit performed by minimizing C-Stat. This allows an estimation of the goodness-of-fit of a function to the data even though χ^2 was not minimized. This also allows for easy comparison between nested models.

5.1.6 Spectral Models

Four models were chosen to fit the spectra of GRBs in the GBM catalog and five models were chosen to fit the spectra of GRBS in the BATSE catalog. For both catalogs, these models constitute a simple power law (PL), Band's GRB function (BAND), en exponential cut-off power law (COMP), and a smoothly broken power law (SBPL). In the BATSE Catalog an additional model was fitted, a Log_{10} Gaussian (GLOGE).

5.1.6.1 Power Law

Many astrophysical spectra can by fit by a single power law with two free parameters,

$$f_{PL}(E) = A\left(\frac{E}{E_{piv}}\right)^{\lambda}, \tag{5.1}$$

where A is the amplitude and λ is the spectral index. The pivot energy (E_{piv}) normalizes the model to the energy range under inspection and helps reduce cross-correlation of other parameters. In all cases E_{piv}, a normalization parameter, is held fixed at 100 keV to reduce cross-correlation of the other parameters. While most GRBs exhibit

a spectral break in the GBM or BATSE passband, some weak GRBs are too weak to adequately constrain this break in the fits and therefore we chose to fit these with the PL model.

5.1.6.2 Band's GRB function

Band's GRB function [31] has become a standard spectral form for fitting GRB spectra:

$$f_{BAND}(E) = A \begin{cases} \left(\frac{E}{100\ \text{keV}}\right)^{\alpha} \exp\left[-\frac{(\alpha+2)E}{E_p}\right] & E < \frac{(\alpha-\beta)\ E_p}{\alpha+2} \\ \left(\frac{E}{100\ \text{keV}}\right)^{\beta} \exp(\beta-\alpha)\left[\frac{(\alpha-\beta)E_p}{100\ \text{keV}\ (\alpha+2)}\right]^{\alpha-\beta} & E \geq \frac{(\alpha-\beta)\ E_p}{\alpha+2}. \end{cases} \tag{5.2}$$

The four free parameters are the amplitude, A, the low and high energy spectral indices, α and β, respectively, and the νF_ν peak energy, E_p. This function is essentially a smoothly broken power law with a curvature defined by its spectral indices. The low-energy index spectrum asymptotically becomes a power law.

5.1.6.3 Comptonized Model

This model is an exponentially cutoff power-law which is a subset of BAND in the limit that $\beta \to -\infty$:

$$f_{COMP}(E) = A\ \left(\frac{E}{E_{piv}}\right)^{\alpha} \exp\left[-\frac{(\alpha+2)\ E}{E_p}\right] \tag{5.3}$$

The three free parameters are the amplitude A, the low energy spectral index α and E_p. E_{piv} is again fixed to 100 keV, as for the power law model.

5.1.6.4 Smoothly Broken Power Law

The Smoothly Broken Power Law is a broken power-law characterized by one break with flexible curvature able to fit spectra with both sharp and smooth transitions between the low and high energy spectra. This model, first published in Ryde [106] where the logarithmic derivative of the photon flux is a continuous hyperbolic tangent, has been re-parametrized [107] as:

$$f_{SBPL}(E) = A\left(\frac{E}{E_{piv}}\right)^{b} 10^{(a-a_{piv})} \tag{5.4}$$

where

$$a = m\Delta \ln\left(\frac{e^{q}+e^{-q}}{2}\right), \quad a_{piv} = m\Delta \ln\left(\frac{e^{q_{piv}}+e^{-q_{piv}}}{2}\right),$$

$$q = \frac{\log(E/E_b)}{\Delta}, \quad q_{piv} = \frac{\log(E_{piv}/E)}{\Delta}, \tag{5.5}$$

$$m = \frac{\lambda_2 - \lambda_1}{2}, \quad b = \frac{\lambda_1 + \lambda_2}{2}.$$

In the above relations, the low- and high-energy power law indices are λ_1 and λ_2 respectively, E_b is the break energy in keV, and Δ is the break scale given in decades of energy. The break scale is independent and not coupled to the power law indices as it is with the Band function, and as such represents an additional degree of freedom. However, Kaneko et al. [107] found that an appropriate value for Δ for GRB spectra is 0.3, therefore Δ is fixed at this value.

5.1.6.5 $\mathbf{Log_{10}}$ Gaussian

The Log_{10} Gaussian model is a Gaussian parametrized with logarithmic energies, or GLOGE. The photon model is represented by

$$f_{GLOGE}(E) = \frac{A}{\sqrt{2\pi}s} \exp\left[-\frac{1}{2}\left(\frac{\log_{10} E - \log_{10} E_{cen}}{s}\right)^2\right], \tag{5.6}$$

where E_{cen} is the centroid energy in keV and s is the standard deviation at E_{cen} in decades of keV. This model is identical to the log-parabolic function that is common in investigating BL Lac spectra, and has recently been used to study GRB spectra [108].

5.1.7 BATSE Spectral Catalog

During its entire 3323 days of operation, BATSE triggered on 2704 GRBs, 2145 of which were presented in the catalog. Bursts that were rejected from the catalog include those with a low accumulation of count rates or a lack of spectral/temporal coverage. In some cases the data collected onboard the spacecraft would be corrupted during storage or during transmission to ground. For this reason, many bursts did not have contiguous data and so were not included in the BATSE catalog. In a few cases data were available but contained incomplete time history, either through data corruption or count rate truncation from an extreme number of detected counts. These bursts were also omitted, as were extremely bright detections where the count rates were so large in each energy channel that caused detector saturation, and in some cases pulse pile-up. Each of the models from Section 5.1.6 were fit to each burst and through model comparison, the most preferred model can be selected (described

Table 5.2: BEST BATSE GRB models

PL	SBPL	BAND	COMP	GLOGE
Fluence Spectra				
506 (23%)	124 (6%)	77 (4%)	903 (42%)	535 (25%)
Peak Flux Spectra				
454 (21%)	150 (7%)	65 (3%)	847 (40%)	629 (29%)

in more detail in Section 5.2). The most preferred models are indicated as the BEST model for the GRB. Table 5.2 shows the number of bursts that are best represented by each model (and the percentage of the entire catalog). In both sets of spectra, the COMP model is preferred over the other models. The BAND and SBPL are preferred on a relatively few cases although they are usually considered to be the concordant empirical models to describe GRB spectra.

5.1.8 GBM Spectral Catalog

During the first two years of operation, GBM triggered on 491 GRBs, 487 of which are presented in the GBM catalog. Similar to the BATSE catalog, two GRBs were excluded due to low accumulation rates, and two were excluded because the data coverage was truncated due to the spacecraft entering the South Atlantic Anomaly (SAA). Each of the first four models in Section 5.1.6 were fit to each burst and model comparison yielded the corresponding BEST sample, containing the preferred spectral models. Table 5.3 contains the number of bursts that are best represented by each model (and the percentage of the entire catalog). Again, the fluence spectra tend to prefer the COMP model, although the PL model is most preferred in most

Table 5.3: BEST GBM GRB models

PL	SBPL	BAND	COMP
Fluence Spectra			
112 (23%)	68 (14%)	75 (15%)	232 (48%)
Peak Flux Spectra			
213 (44%)	51 (10%)	69 (14%)	154 (32%)

peak flux spectra. This differs from BATSE, due in large part to the difference in the sensitivity between the two instruments; GBM is less sensitive, therefore in some cases it cannot accumulate enough data to sufficiently support models with more than two free parameters. Figure 5.1 indicates that observably less intense bursts provide less data to support a large number of parameters. This may appear obvious, but it allows us to determine why in many situations a particular empirical function provides a poor fit, while in other cases it provides an accurate fit. For example, the energy spectra of GRBs are normally well fit by two smoothly joined power laws. For particularly bright GRBs, the BAND and SBPL functions are typically an accurate description of the spectrum, while for weaker bursts the COMP function is most acceptable. This is because the PMTs are high-background instruments and the effective area of the detector response is decreasing rapidly at high energy, as shown in Figure 5.2, therefore the high-energy power law cannot be constrained by the data. Similarly, bursts that have signal significance on the order of the background fluctuations do not have a detectable distinctive break in their spectrum and so the power law is the most acceptable function. Although for weaker GRBs a model with more parameters

is not statistically preferred, it is instructive to study the parameters of even the weaker bursts.

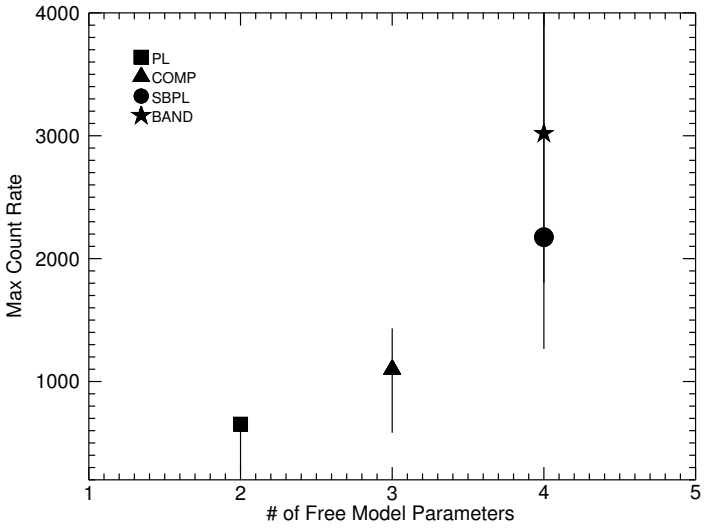

Figure 5.1: Average maximum background-subtracted count rates (as a proxy for intensity) versus the number of degrees of freedom of the BEST model. The error bars shown are the 1σ standard devations of the distributions of maximum count rates for each BEST model.

5.2 Analysis Results

For the purposes of this dissertation, the BEST samples from each catalog is used. The BEST sample for each catalog are defined by compare the goodness-of-fit of all spectral models for each burst and selecting the most preferred model based on the difference in χ^2 per degree of freedom. The criterion for accepting a model with a single additional parameter is a change in χ^2 of at least 6 since the probability for achieving this difference is $\sim$0.01. The BEST parameter sample produces the best estimate of the observed properties of GRBs. By using model comparison, the

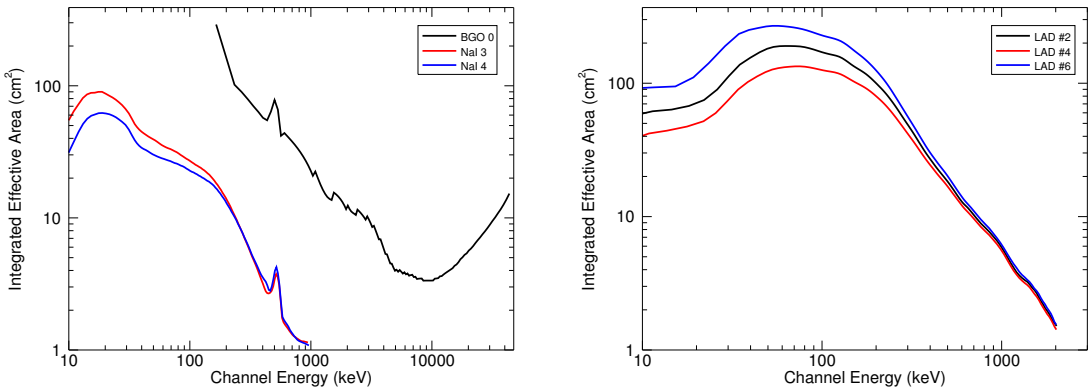

(a) (b)

Figure 5.2: [*Top*] Integrated effective area of the response function for three GBM detectors of GRB 080916C. [*Bottom*] Integrated effective area of the response function for three detectors from BATSE Trigger #143 (GRB 910503).

preferred model is selected, and the parameters are reviewed for that model. The models contained herein and in most GRB spectral analyses are empirical models, based only on the data received; therefore the data from different GRBs tend to support different models.

5.2.1 Parameter Distributions

Distributions of the BEST model parameters from GBM are shown in Figure 5.3 and Figure 5.4. Note that the PL index is statistically an averaging of the low- and high-energy power laws, and that, due to the fact that GBM spectral responses have a peak effective area at lower energies (see Figure 5.2), I have included PL indices in the BEST low-energy index distribution. Although in a number of cases the PL model is statistically preferred over the other models in this catalog, the spec-

tral shape represented by the PL is inherently different from the shape of the other models. Therefore, the PL index is not necessarily representative of either the low- or high-energy indices from the other models. In Figure 5.3(a) and Figure 5.4(a) I show where the distribution of PL indices exists relative to the low-energy index (α) and the high-energy index (β) distributions. The PL index represents 25% of the BEST fluence α distribution and 50% of the BEST peak flux α distribution. The fluence spectra, on the whole, have a steeper measured α and shallower β than the peak flux spectra. The α distribution for the fluence spectra peaks at about -1, while the peak flux low-energy spectral index peaks at about -0.6. Conversely, the β distribution for the fluence spectra peaks at -2.1 and the peak flux high-energy spectral index peaks at -2.4.

Additionally, the E_p (Figure 5.3(b)) distribution differs between the fluence and peak flux spectra, as does the the E_b (Figure 5.4(b)) distribution. The fluence spectra E_p peaks near 200 keV and the E_b peaks at about 150 keV, although the kurtosis of the distribution is much lower than that of the E_p distribution. Meanwhile, the E_p and E_b for the peak flux spectra both peak at about 150 keV. As is shown in Figure 5.3(c) and Figure 5.4(c) the photon flux does not significantly change when widening the energy band from 8 keV–1 MeV to 8 keV–40 MeV. The fluence spectra photon flux peaks around 1.5 photons cm^{-2} s^{-1} and the peak flux photon flux peaks around 4 photons cm^{-2} s^{-1}. Alternatively, the energy flux is greatly affected by expanding the energy band, as is shown in Figure 5.3(d) and Figure 5.4(d). Specifically, the distribution in the 8 keV–1 MeV band peak around a few$\times 10^{-7}$ ergs cm^{-2} s^{-1},

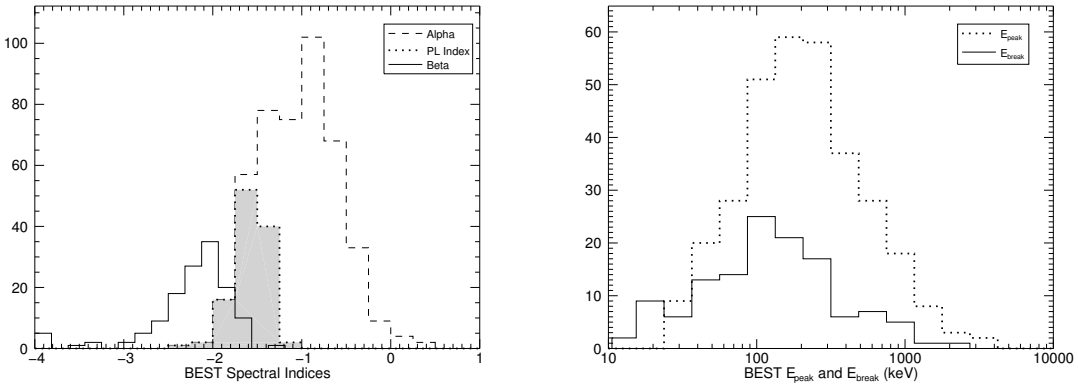

(a)

(b)

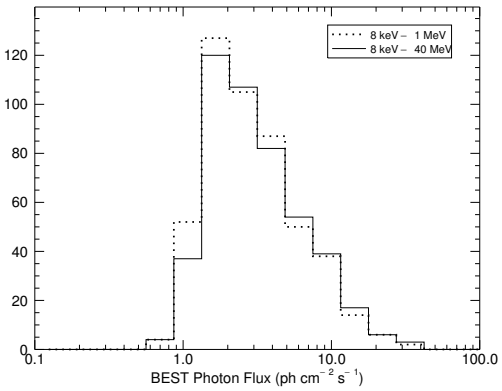

(c)

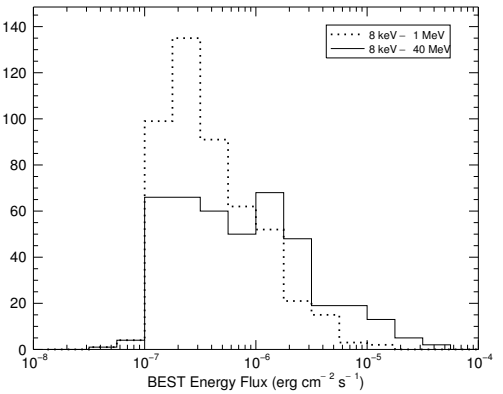

(d)

Figure 5.3: Distributions of the BEST spectral parameters for the GBM fluence spectra. Figure 5.3(a) displays the selection of the BEST low-energy and high-energy spectral indices. The shaded distribution depicts the location of the distribution of the PL index. Figure 5.3(b) shows the selection of the BEST E_p and E_b. Figure 5.3(c) and Figure 5.3(d) show the selection of the BEST photon flux and energy flux respectively.

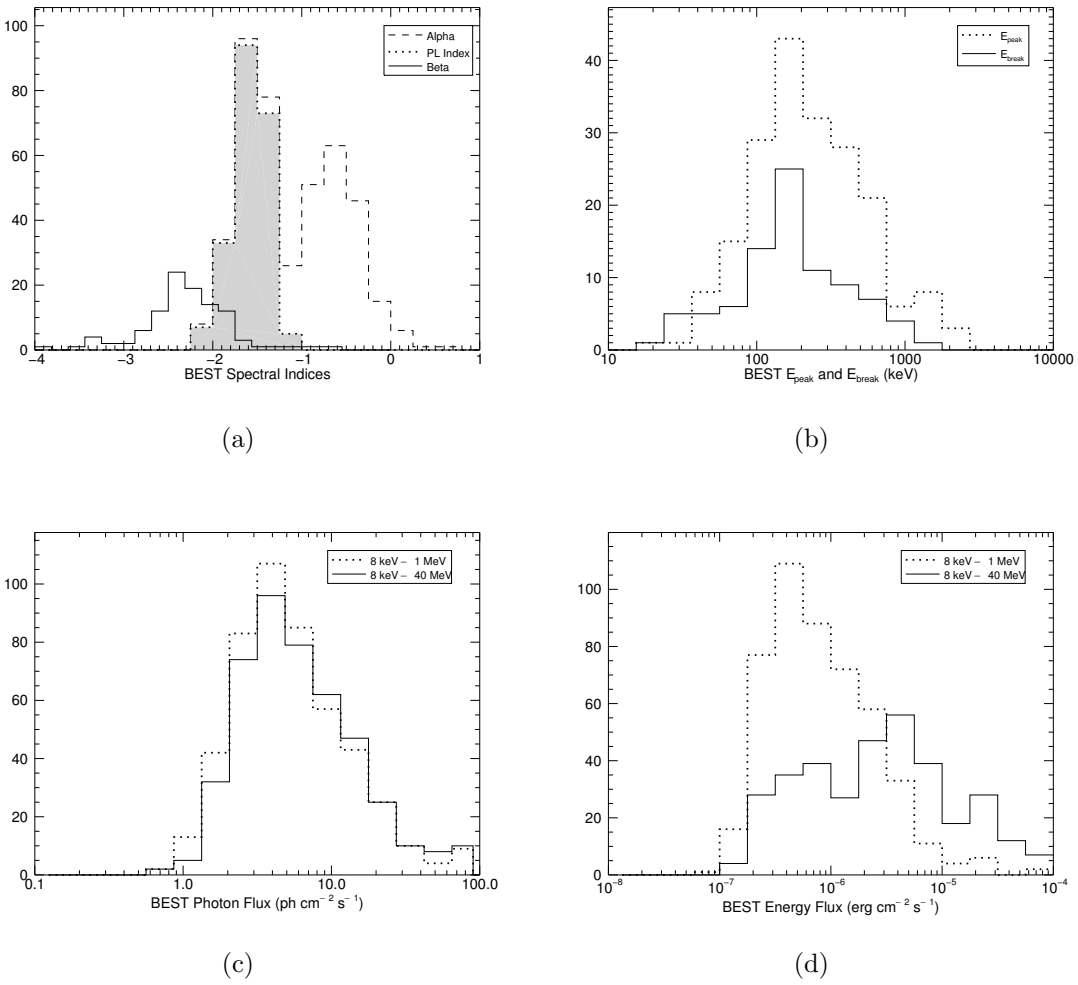

Figure 5.4: Distributions of the BEST spectral parameters for the GBM peak flux spectra. Figure 5.4(a) displays the selection of the BEST low-energy and high-energy spectral indices. The shaded distribution depicts the location of the distribution of the PL index. Figure 5.4(b) shows the selection of the BEST E_p and E_b. Figure 5.4(c) and Figure 5.4(d) show the selection of the BEST photon flux and energy flux respectively.

but in the 8 keV–40 MeV band the distribution broadens significantly and becomes much less peaked, approaching what appears to be a top hat distribution.

Distributions of the BEST model parameters from BATSE are shown in Figure 5.5 and Figure 5.6. Similar to what was found in GBM, the PL index is statistically an averaging of the low- and high-energy power laws; due to the fact that BATSE spectral responses have a peak effective area at $\sim$ 70 keV, (see Figure 5.2) I have included PL indices into the BEST low-energy index distribution. Although in a number of cases the PL model is statistically preferred over the other models in this catalog, the spectral shape represented by the PL is inherently different from the shape of the other models. Therefore, the PL index is not necessarily representative of either the low- or high-energy indices from the other models. In Figure 5.5(a) and Figure 5.6(a) I show where the distribution of PL indices exists relative to the α and beta distributions. The PL index represents 23% of the BEST fluence α distribution and 21% of the BEST peak flux α distribution. The fluence spectra, on the whole, have a steeper measured α and shallower β than the peak flux spectra. The α distribution for the fluence spectra peaks at slightly steeper than -1, while the peak flux low- energy spectral index peaks at slightly shallower than -1. Conversely, the β distribution for the fluence spectra peaks at -2.1 and the peak flux high-energy spectral index peaks at -2.4.

The E_p and E_b distributions are similar between the two spectra, however. The fluence spectra E_p peaks at $\sim$200 keV as does the peak flux spectra E_p and the E_b peaks at more than 200 keV. Note that the E_b distributions are significantly smaller in comparison to the E_p distributions, especially for the fluence spectra,

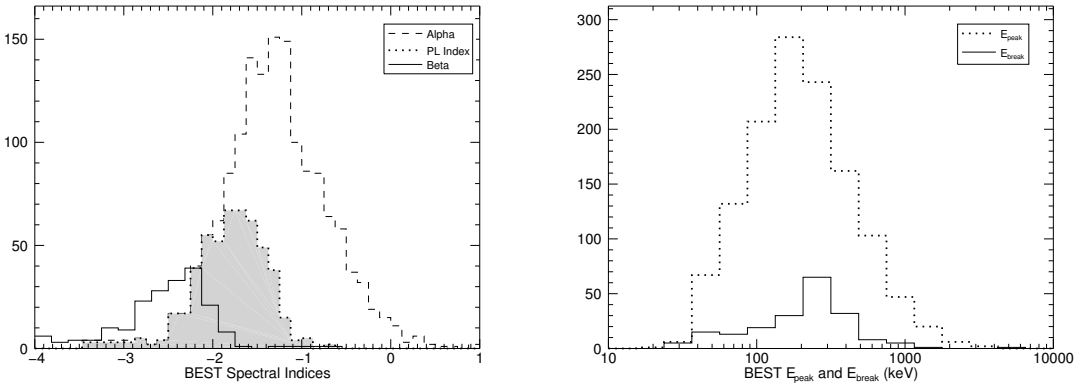

(a)

(b)

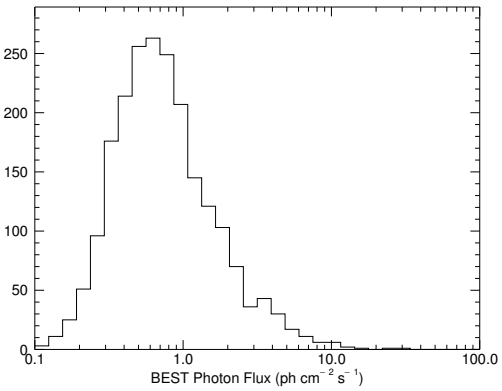

(c)

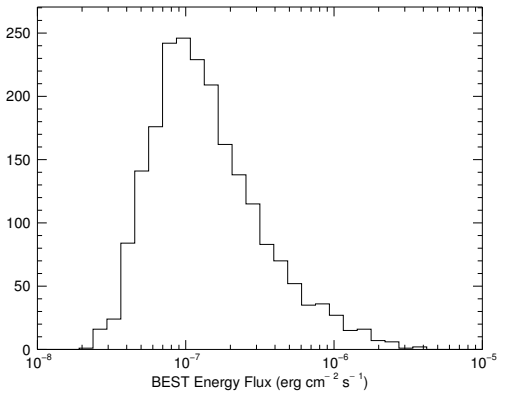

(d)

Figure 5.5: Distributions of the BEST spectral parameters for the BATSE fluence spectra. Figure 5.5(a) displays the selection of the BEST low-energy and high-energy spectral indices. The shaded distribution depicts the location of the distribution of the PL index. Figure 5.5(b) shows the selection of the BEST E_p and E_b. Figure 5.5(c) and Figure 5.5(d) show the selection of the BEST photon flux and energy flux respectively.

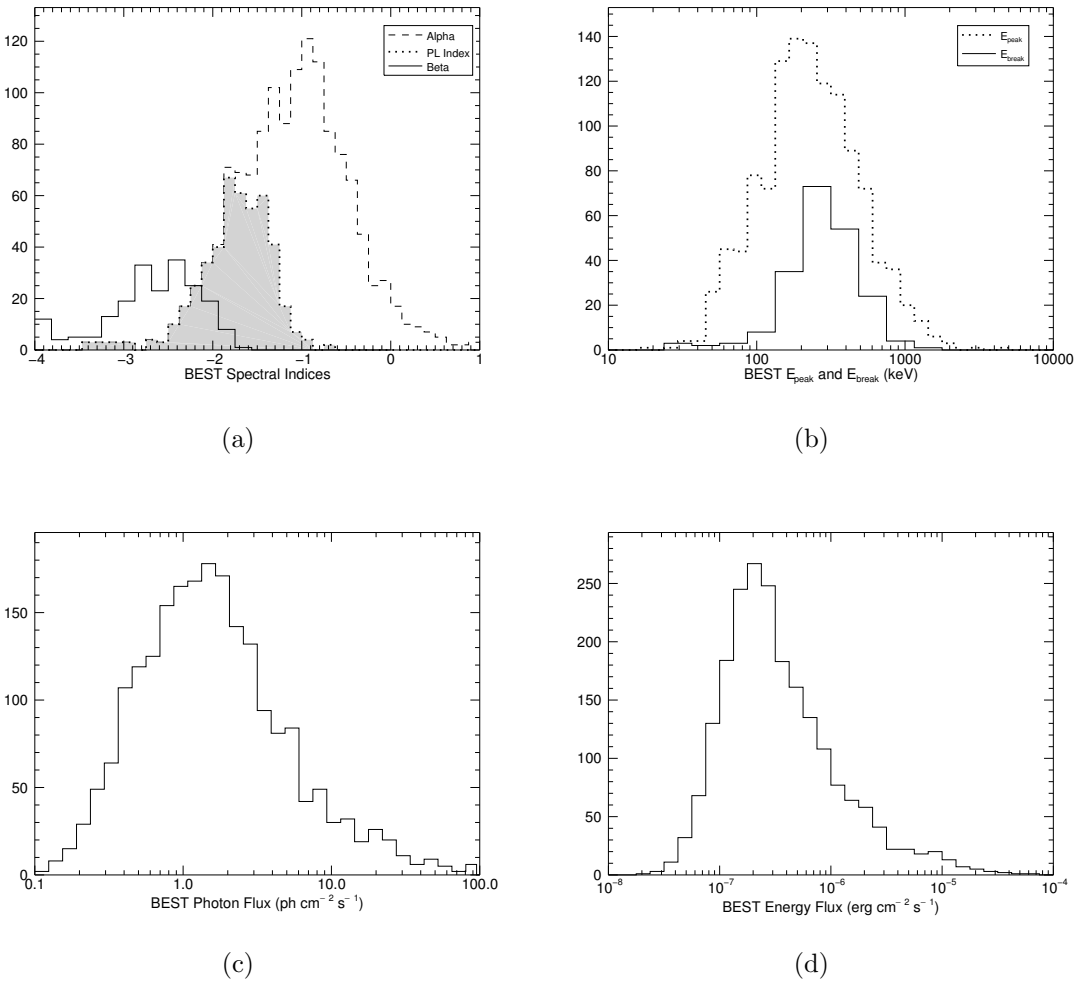

Figure 5.6: Distributions of the BEST spectral parameters for the BATSE peak flux spectra. Figure 5.6(a) displays the selection of the BEST low-energy and high-energy spectral indices. The shaded distribution depicts the location of the distribution of the PL index. Figure 5.6(b) shows the selection of the BEST E_p and E_b. Figure 5.6(c) and Figure 5.6(d) show the selection of the BEST photon flux and energy flux respectively.

simply because the errors are not as well constrained for E_b. As is shown in Figure 5.5(c) and Figure 5.6(c) respectively, the fluence spectra photon flux peaks around 0.6 photons $\mathrm{cm}^{-2}\ \mathrm{s}^{-1}$ and the peak flux photon flux peaks around 1.5 photons $\mathrm{cm}^{-2}\ \mathrm{s}^{-1}$. Comparatively, the fluence energy flux peaks at about 1×10^{-7}erg $\mathrm{cm}^{-2}\ \mathrm{s}^{-1}$, and the peak flux energy flux peaks at 2×10^{-7}erg $\mathrm{cm}^{-2}\ \mathrm{s}^{-1}$, as is shown in Figure 5.5(d) and Figure 5.6(d).

5.2.2 Comparison of Fluence and Peak Flux Spectra

While the fluence spectra are integrated over the entire duration of the prompt emission and display the time-averaged properties of the GRB emission, the peak flux spectra examines each burst at a fiducial snapshot in time and displays the properties of the emission at the most luminous part of the GRB. An important fact of GRB spectra is that there have been observed in many cases significant spectral evolution from hard to soft [31, 109, 110], and therefore the fluence spectra average over this evolution. The fact that the Band function is able to exhibit a large range of curvature allows it to fit the time-integrated spectra as well as fine time spectra, thereby concealing the physical emission process. The evolution of the spectra can significantly change the spectral parameters, and an estimation of the amount of spectral evolution can be shown by comparing the fluence spectral parameters to the peak flux spectral parameters. Figure 5.7 shows the comparison between the low-energy spectral indices from the fluence spectra and peak flux spectra as well as the comparison between the high-energy spectral indices from the fluence spectra and the

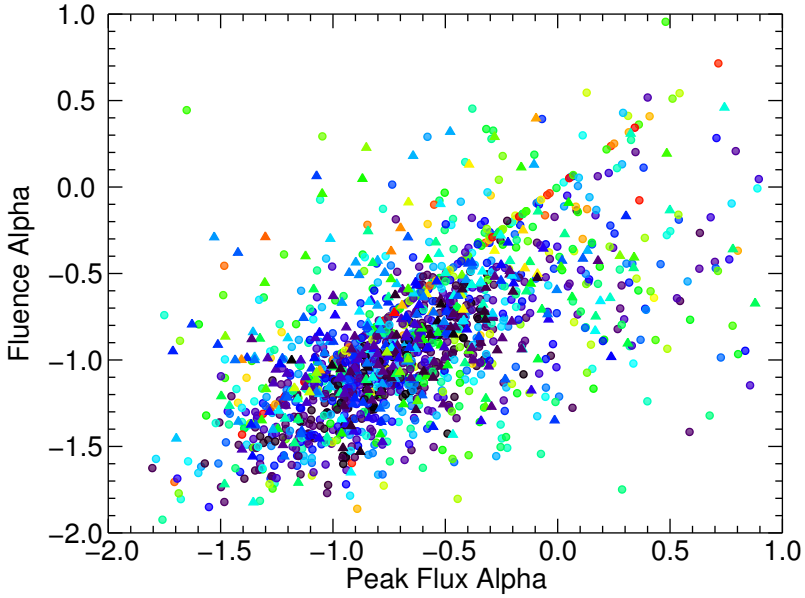

(a) α

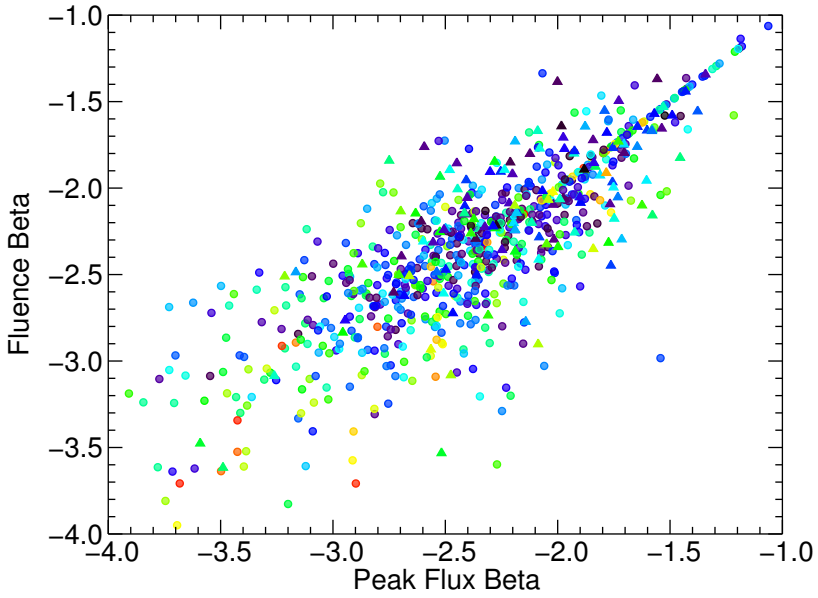

(b) β

Figure 5.7: Comparison of the peak flux to the fluence α and β. The circles represent BATSE spectra and the triangles represent GBM spectra. The color of each point indicates the combined uncertainty from 0.01 (black) to 1.0 (red).

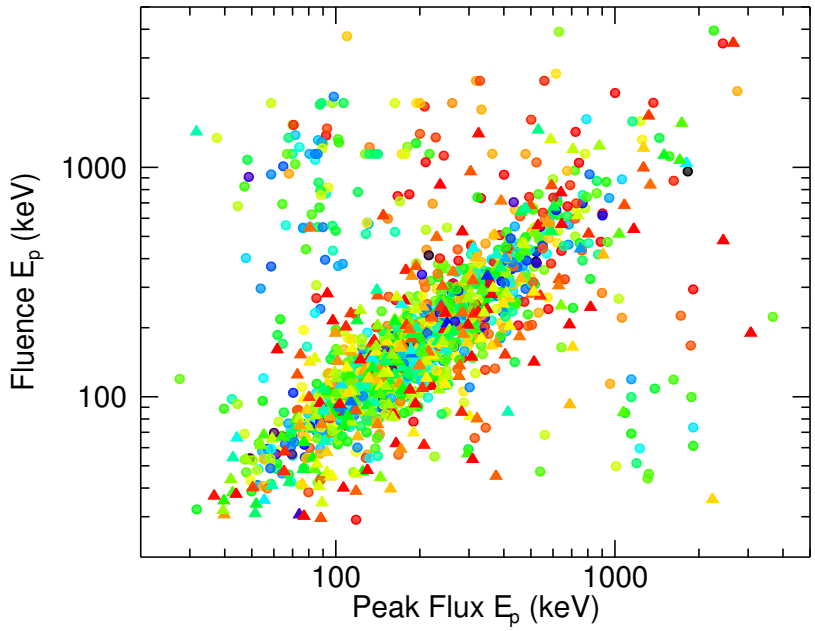

(a) E_p

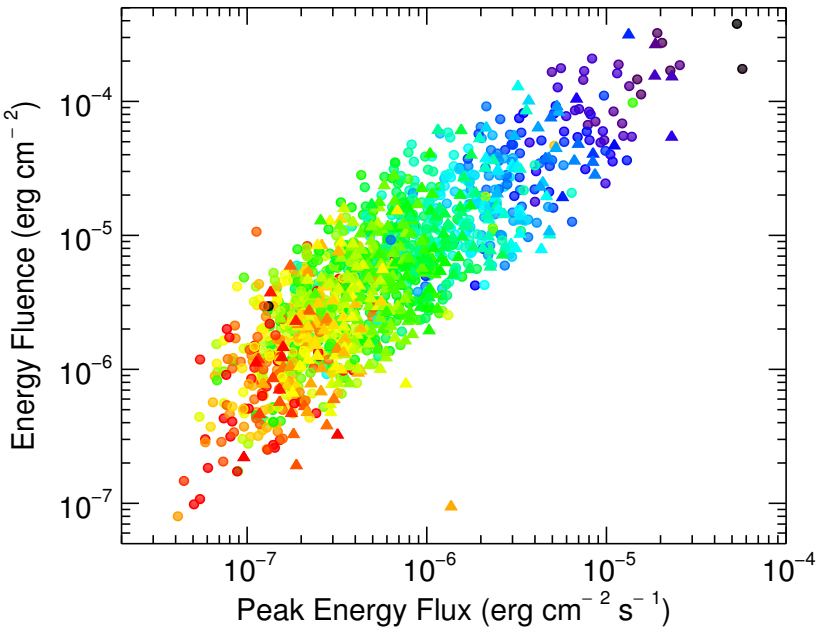

(b) Flux–Fluence

Figure 5.8: Comparison of the peak flux E_p to the fluence E_p and the peak flux to the fluence. The circles represent BATSE spectra and the triangles represent GBM spectra. The color of each point indicates the combined relative uncertainty from 0.01 (black) to 1.0 (red).

peak flux spectra. Shown are spectra from both BATSE and GBM and note that an artifact exists at unity correlation for BATSE GRBs due to the fact that the fluence and peak flux spectra all exist in a single 2 s time bin. There exists a large dispersion for both parameters, although the fluence α is found to be typically softer than the peak flux α. Additionally, the comparison for E_p of the types of spectra and the comparison between the fluence and peak flux are shown in Figure 5.8. A strong correlation exists between the peak flux E_p and fluence E_p, yet there a number of instances where outliers cause significant scatter around the correlation. The peak energy flux and energy fluence show a strong correlation, although fairly broad. The width of the correlation can be explained by the distribution of durations since shorter GRBs will have a fluence that is approximately the same as the peak flux, while the fluence of longer duration GRBs are less representative of the peak flux.

5.2.3 Photon Spectral Indices

An interesting result of the parameter distributions is the $\Delta S = \alpha - \beta$ parameter, the difference between the low- and high-energy spectral indices. This can be an important quantity because current models for the GRB prompt emission mechanism can be broken into two categories: magnetic [111] or internal/external shock [58] driven. Implications about the shock driven case can be drawn directly from ΔS. Sari, Piran, & Narayan [112] presented a model for the prompt emission spectrum where the emission of synchrotron photons by shock accelerated electrons evolves due to radiative and adiabatic losses. A key prediction of this model is a series of relationships between the photon spectral indices above and below the synchrotron

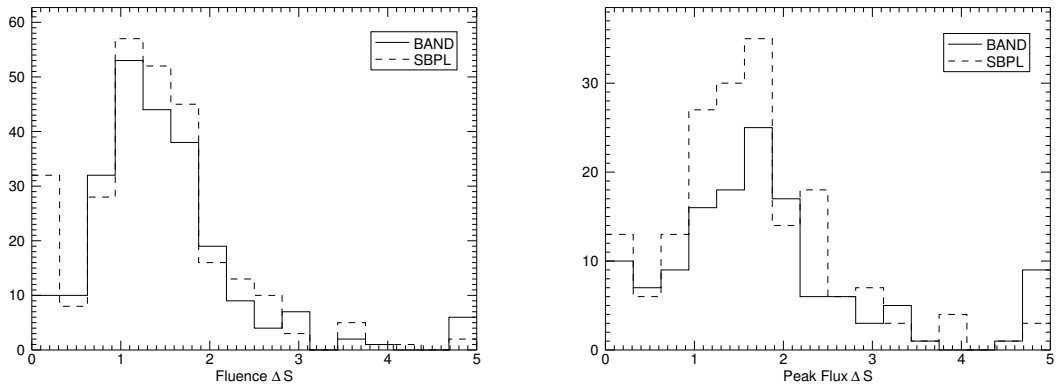

(a) Fluence Spectra

(b) Peak Flux Spectra

Figure 5.9: Distributions of the difference between the low- and high-energy indices from GBM spectra.

peak. Preece et al. [113] found that this relationship can be used to constrain the synchrotron cooling regime of the electrons by looking at the difference of the Band function spectral indices across the νF_ν peak. Therefore, investigating ΔS potentially provides insight into the emission mechanism of GRBs by comparing ΔS to the prediction offered by the synchrotron shock model. Figure 5.9 shows the ΔS distribution for the fluence and peak flux spectra from GBM.

5.2.4 Fitting GRBs with Physical Models

Although the models discussed in the spectral catalogs as well as in most literature are empirical models, several recent studies have aimed to fit GRB spectra with physical models such as synchrotron, synchrotron self-Compton, and inverse Compton radiation [114–116]. While the Band function adequately fits the brightest GRBs, and the Comptonized model is likely preferred in GRBs only when the SNR

is too low to resolve the high energy power law, these empirical models do not reflect the the physical radiation processes of the emission [60]. This is motivation to find a complete physical description of the observed spectrum. Note that while physical modeling of GRB spectra can provide important insight into the radiation process, the overall shape of the spectrum is still well modeled by the Band function. This will prove to be an important point since E_p, representing the peak energy of the νF_ν spectrum, is an important feature that largely remains unchanged when testing GRB spectra with physical models.

CHAPTER 6

PHYSICAL CORRELATIONS OF GRB PROMPT SPECTRAL PARAMETERS

The large spread of values for the observed prompt spectra model parameters have lead to many studies into the correlation between parameters, particularly in relating the rest-frame properties of the bursts [117–120]. In the following chapter, I discuss a number of correlations that have implications for the rest-frame properties of GRBs and their use to cosmographical studies, as well as their pitfalls. In Section 6.1 I discuss a new method to discriminate between classically long and short GRBs, a result derived directly from the BATSE and GBM catalogs. Section 6.2 presents some correlations that have been used as luminosity relations. Section 6.3 takes the discovery from Section 6.1 and the correlations from Section 6.2 to present a new method to estimate the physical jet opening angle of GRBs from the prompt spectra. Finally, Section 6.4 discusses some problems with using the current luminosity relations to study cosmology.

6.1 The E_p–Fluence Ratio

From the BATSE 5B spectral catalog [102], bursts were extracted with a good model fit as determined by a 3σ confidence limit, with the time-integrated E_p and fluence errors for each burst required to be no more than 40% of their respective fitted values. A total of 1121 long bursts and 168 short bursts, classified according to the classical T_{90} cut of two seconds [25], satisfied these criteria. The E_p/fluence energy ratio for each of these bursts were calculated and a histogram plotted of these values. By using a standard nonlinear least-squares fitting algorithm, a single lognormal function was fit to the distribution with the resulting chi-square goodness-of-fit statistic 111 for 32 degrees of freedom. Two log-normal functions were then fit to the distribution with the resulting chi-square statistic of 32 for 29 degrees of freedom. Since the two models are nested, Pearson's χ^2 test was used to show that the large change in χ^2 per degree of freedom results in a chance probability of 5×10^{-17} and that the two log-normals are statistically preferred with a high degree of significance.

From this bimodal distribution an obvious distinction between long and short bursts emerges. Figure 6.1 shows the histogram of E_p/fluence split into two histograms to show that it correlates with the T_{90} duration. A K-S test comparing the long and short burst distributions of the energy ratio to the best fit log-normal functions of the T_{90} distributions, however, finds the correlations to be statistically marginal with 2% and 0.6% respective probabilities that each distribution in Figure 6.1 is drawn from their respective best fit log-normal functions. The energy ratio distribution for short bursts is narrower compared to that of long bursts and is shifted

to higher energies, resulting from the fact that short bursts are generally harder than long bursts. It appears the energy ratio values are a good discriminator between the classical definition of long and short bursts by merging two known discriminators into one quantity, and their relative overlap can be well estimated. Only 4% of long GRBs overlap the 1σ core of the short burst distribution, and 2% of short bursts overlap the the 1σ core of the long burst distribution. Similarly, the overlap for the 2σ cores is 11% and 23%, respectively. Comparatively, for our sample, the classical T_{90} overlap of long bursts onto the 1σ (2σ) core of short bursts is 4% (23%), and and there is no overlap of short bursts onto either the 1σ or 2σ core of long bursts. The central value for the long burst energy ratio distribution is $\sim$0.06 while the central value for the short burst distribution is $\sim$1.5.

Shown in Figure 6.2 is the distribution of 382 GRBs from the GBM spectral catalog [103]. Using the duration results from the GBM GRB Catalog from the first two years of operation [121], the figure strongly supports the original claim by [122] using BATSE GRBs and shows the distribution separated into long bursts and short bursts, and a correspondence has been found between the energy ratio and the observed duration estimate of the bursts. A fit was performed on the entire distribution and the χ^2 goodness-of-fit for the two lognormal functions is 12.2 for 14 degrees of freedom. Fitting a single lognormal function to the distribution results in a goodness-of-fit of 27.8 for 17 degrees of freedom. The change in χ^2 per degree of freedom results in a chance probability of 1×10^{-3} that the two log-normals are not preferred.

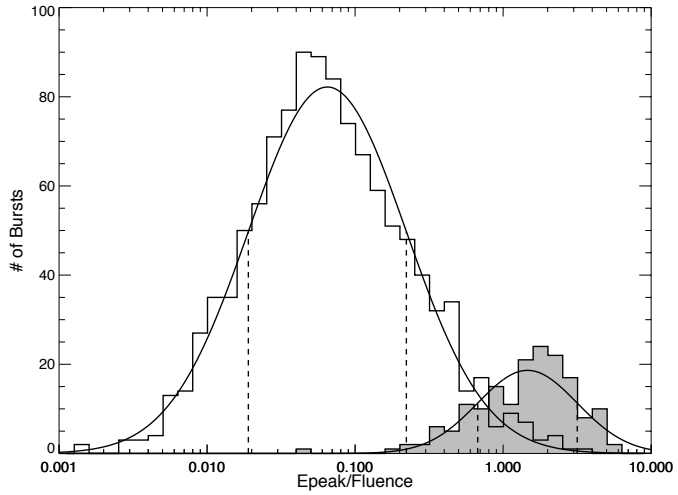

Figure 6.1: Histograms of the energy ratio distributions in the 20-2000 keV range for 1121 long bursts (white) and 168 short bursts (gray). There are clearly two distinct distributions, with long bursts centered around 0.6 and short bursts centered around 1.5. The solid curves are the best fit lognormal functions, and the dashed lines are the 1σ standard deviation of the distributions

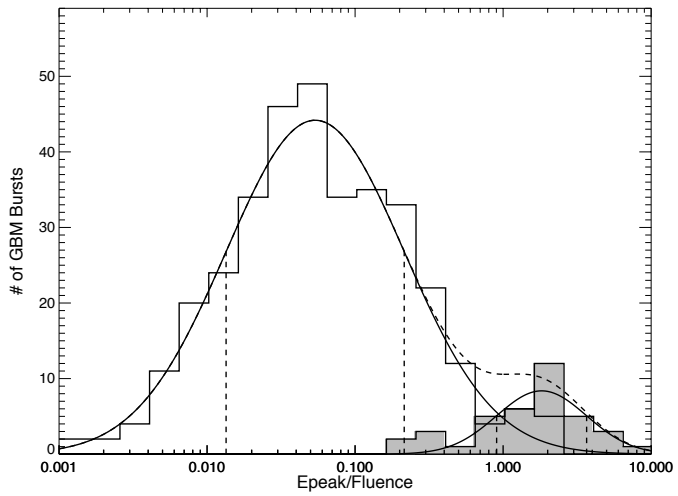

Figure 6.2: The E_p/Fluence energy ratio for 344 long GRBs (white) and 38 short GRBs (gray). The vertical dotted lines denote the 1σ standard deviation of each lognormal.

The energy ratio shows a clear distinction between two different types of GRBs. The fluence encodes the duration of the burst without deriving a subjective T_{90} estimate, and E_p/fluence physically represents a ratio of the energy at which most of the gamma-rays are emitted to the total energy emitted in gamma-rays. This quantity effectively serves as a spectral hardness ratio and shows an increased hardness for short bursts compared to long bursts, consistent with [25]. The low degree of correlation between the T_{90} distribution and the energy ratio distribution may be attributed to the fact that the former is an observed quantity in the observer's frame, while the latter is a quantity that contains spectral information from the rest frame of the GRB.

6.2 The Amati, Ghirlanda, and Yonetoku Correlations

Several authors have tried to establish a method for estimating the isotropic luminosity from the observed GRB properties. Using the lightcurves of the prompt gamma-ray emission, Fenimore & Ramirez-Ruiz [123] reported the variability–luminosity relation, indicating that more variable GRBs are brighter than less variable GRBs. Norris et al. [124] discovered the spectral lag–luminosity correlation, which relates the interval of peak arrival times between two energy bands with the luminosity. However, several authors note that correlations involving the time-series data might be due to the effect of the viewing angle from the GRB jet [125, 126]. An alternative to using the lightcurve properties as luminosity indicators is to use the spectral properties of GRBs. Originally, based on the spectral analysis with the cosmological K-correction, a correlation between E_p and the isotropic equivalent energy radiated, E_{iso} was found [117, 127]. The correlation between E_p and E_{iso}, known as the Amati

relation, was the first correlation that was considered to be a redshift indicator. As a number of afterglow jet breaks were identified and jet opening angles were determined, a beaming factor was added to E_{iso} to correct for the amount of collimation in the explosion. This lead to the E_p–E_γ correlation, known as the Ghirlanda relation, where E_γ is the collimation- corrected energy [118]. Instead of studying the spectrum integrated over the duration of the burst and corresponding gamma-ray fluence to estimate the energy, Yonetoku et al. [119] sought to use the peak flux of the GRB and the spectrum at the peak flux to determine another luminosity indicator, E_p–L_{iso}, where L_{iso} is the isotropic equivalent peak luminosity.

In an attempt to relate the rest-frame E_p with the total energy release in gamma-rays, Amati et al. [117] discovered a correlation between the rest-frame E_p and E_{iso}, the bolometric energy release in gamma-rays assuming isotropic emission. The correlation is highly susceptible to scatter and outliers, and may be a result of selection effects due to detector trigger and spectral criteria [128–132]. Ghirlanda et al. [118] found a similar correlation using E_γ, the collimation-corrected energy release. The Ghirlanda relation contains less scatter and fewer outliers, but requires an additional piece of information: the jet opening angle. Both of these correlations require the redshift of the GRB, yet previous papers [130, 131] have devised a way to test the correlations with GRBs that have no observed redshift. The equation used by Band & Preece [131], also adopted here is

$$\frac{E_{p,obs}^{1/\eta_i}}{S_\gamma} = \frac{4\pi d_L^2 C_i^{1/\eta_i}}{E_{n,i}\ (1+z)^{1+1/\eta_i}}\ f_b, \tag{6.1}$$

where $E_{p,obs}$ and S_γ are the observed E_p and gamma-ray fluence respectively, C_i are the best-fit normalizations and η_i are the reported best-fit power law indices from the respective Amati and Ghirlanda relations, $E_{n,i}$ is the normalization energy (10^{52} erg for the Amati Relation and 10^{51} erg for the Ghirlanda Relation), and f_b is the beaming fraction, which is related to the jet opening angle and always has a value of unity for the Amati Relation. This equation is composed of physically observable quantities on the left-hand side, and the right-hand side is a function of redshift. Band & Preece [131] referred to this equation as the energy ratio. Plotting the equality in Equation 6.1 as a function of redshift results in Figure 6.3, which shows that both relations have an upper limit value for the energy ratio as a maximum value over redshift. Focused on the Ghirlanda upper limit, it can be defined as

$$G_L = \frac{4\pi d_{L,lim}^2 C^{1/\eta}}{[10^{51}\ \mathrm{erg}]\ (1+z_{lim})^{1+1/\eta}}, \tag{6.2}$$

where $d_{L,lim}$ and z_{lim} are the limiting luminosity distance and redshift as found by the Ghirlanda relation respectively, such that the energy ratio equality becomes

$$\frac{E_{peak}^{1/\eta}}{S_\gamma} = G_L\ f_b. \tag{6.3}$$

The formulation of Equation 6.3 makes it trivial to transform the Ghirlanda upper limit over redshift into the observable E_p–fluence plane. This is shown in Figure 6.4, and note that the transformation causes the upper limit to become a lower limit as depicted, therefore any burst that exists below the lower limit is a violator of

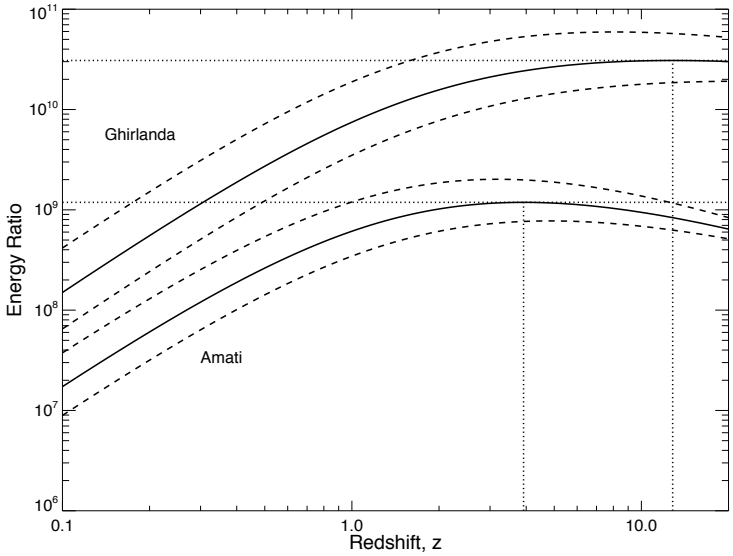

Figure 6.3: The Amati and Ghirlanda energy ratios as a function of redshift. The dashed lines are the 1σ uncertainties due to the propagation of the best-fit parameter errors, and the dotted lines show where the upper limit occur for each relation. The curve for the Ghirlanda Relation was produced using a beaming fraction $f_b = 1$.

the corresponding E_p–energy relation. This examination shows that very few bursts ($\sim$ 18%) fall above the Amati relation lower limit, though all GBM bursts exist above the Ghirlanda relation lower limit. More importantly, when the long and short bursts are plotted separately for GBM, the observation is that most long bursts are clustered between the Amati and Ghirlanda lower limits, while most of the short bursts are linearly dispersed along the Ghirlanda lower limit. Here the beaming factor is assumed to be of unity for the Ghirlanda relation in the Figure 6.4, indicating that the opening jet angle is 90°, which is consistent with previous findings from BATSE [122]. Interestingly, if the beaming factor is decreased (and therefore the jet opening angle), the Ghirlanda lower limit no longer represents an absolute lower limit

and shifts up along the fluence axis toward the bulk of long bursts, and eventually all short bursts will violate the new Ghirlanda limit. This gives support to the findings that long bursts have a dispersion of jet angles from small angles on the order of a degree up to 50 degrees [45,133,134], and short bursts have larger average jet opening angles of 40–90 degrees, as is supported theoretically by Livio & Waxman [135] and observationally by Watson et al. [136].

A similar correlation to the Amati and Ghirlanda relations is the Yonetoku relation [119]. This relation correlates the E_p at the peak flux of the GRB with the peak luminosity. The correlation is represented as

$$\frac{L_{iso}}{10^{52}\ \mathrm{erg\ s^{-1}}} = C_Y \left[\frac{E_p(1+z)}{1\ \mathrm{keV}}\right]^{\eta_Y}, \tag{6.4}$$

where C_Y and η_Y are the best fit power law amplitude and index, which was reported by Yonetoku et al. [119] as $C_Y = (2.72 \pm 0.15) \times 10^{-5}$ and $\eta_Y = 1.94 \pm 0.19$. It has been suggested that the E_p–L_{iso} is a more realistic luminosity indicator since the brightest portion of the GRB is going to be least susceptible to dimming by the inverse square law for more distant GRBs. In addition, the E_p of the spectrum over the duration may not accurately reflect the true physical spectrum since there exists much spectral evolution throughout the duration of the GRB. By using the relation between flux and luminosity,

$$L(F_\gamma; z) = 4\pi d_L^2 F_\gamma, \tag{6.5}$$

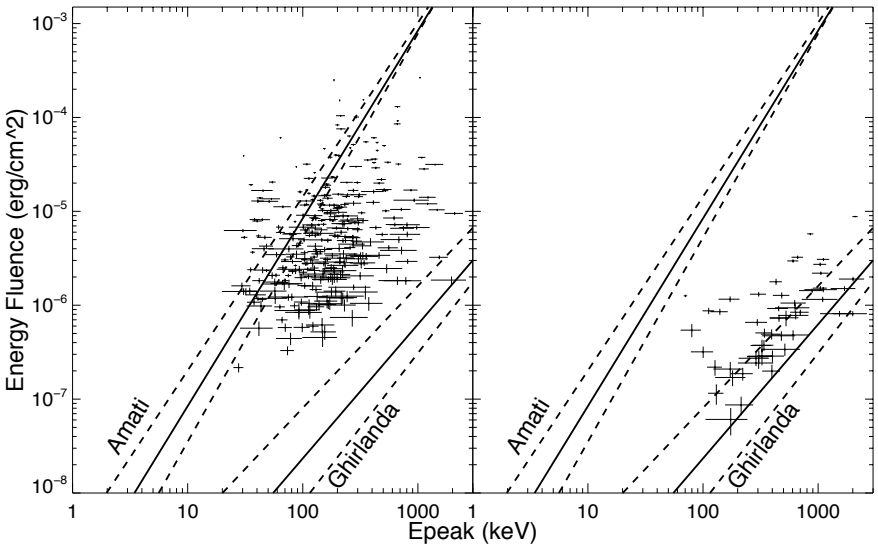

Figure 6.4: Plot of 382 GBM bursts in the E_p-fluence plane. The left side shows the 344 long GRBs and the right shows the 38 short. The solid lines are the Amati and Ghirlanda upper limits, which in this plane become lower limits, and the dashed lines are the corresponding 1σ errors.

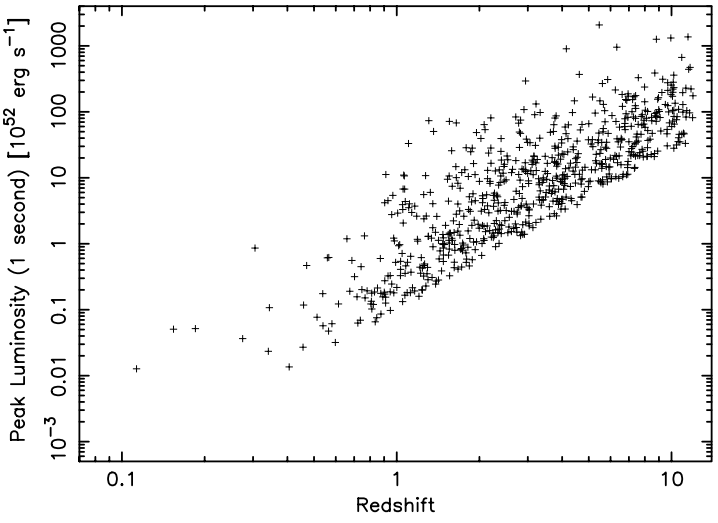

Figure 6.5: Plot of the luminosity and the redshift derived from the E_p–L_{iso} relation for a sample of BATSE GRBs. The truncation of the lower end of the luminosity is caused by the flux limit of BATSE.

the Yonetoku relation can the be inverted and the redshift can be expressed as a function of the observed E_p and F_γ,

$$\frac{d_L^2}{(1+z)^{\eta_Y}} = \frac{10^{52} C_Y}{4\pi F_p} E_p^{\eta_Y}. \tag{6.6}$$

Depending on the assumed cosmological model, d_L may not allow for an analytical solution for the redshift, therefore, in general the equation must be solved numerically for the redshift and corresponding d_L. Figure 6.5 shows the L_{iso} and derived redshift using the Yonetoku relation for a sample of BATSE GRBs [119].

6.3 Jet Opening Angle Limits from the Ghirlanda Limit

As indicated, the combination of the E_p–Fluence plane and the Ghirlanda lower limit admit a limit to the jet opening angles for GRBs, since the Ghirlanda lower limit appears to describe a true cutoff in the E_p–fluence plane that is consistent among multiple instruments. The lower limit can be solved from Ghirlanda's best fit equation [118], which was calibrated with GRBs that had well-constrained jet opening angles from afterglow studies, in terms of the beaming fraction, observed E_p, and fluence [122, 131]. Using the definition from Equation 6.3, the Ghirlanda lower limit equation can be rearranged to solve for the limiting beaming fraction in terms of the E_p and fluence:

$$f_{b,lim} = \frac{E_{peak}^{1/\eta}}{S_\gamma \, G_L}. \tag{6.7}$$

Then, using the definition of the beaming fraction,

$$f_b = 1 - \cos\theta_j, \tag{6.8}$$

Equation 6.7 results in an equation for the lower limit of the jet opening angle of a GRB using information from the E_p and fluence:

$$\theta_{j,lim} = \cos^{-1}\left(1 - \frac{E_{peak}^{1/\eta}}{S_\gamma\ G_L}\right), \tag{6.9}$$

where S_γ is the observed gamma-ray fluence, η is the best-fit Ghirlanda power law index, and G_L is the Ghirlanda limit line characterized as a normalization. This equation gives a lower bound to the jet opening angle as well as the collimation-corrected energy, E_γ. If a particular burst has a confirmed redshift measurement, then replacing the z_{lim} and $d_{L,lim}$ with the corresponding values for that burst in Equation 6.2 would result in the estimation of the jet opening angle itself. Shown in Figure 6.6 is a plot of the derived jet opening angle as a function of redshift for a number of example E_p and fluence values. There exists a clear lower limit for each burst at z_{lim} and due to the degeneracy of the relation as a function of redshift, there exists two redshifts that could produce a given jet opening angle. The relation flattens out between $z \sim$8–70, therefore, this relation is only expected to be reliable at $z \lesssim 8$. To calculate the uncertainty on the derived jet opening angle, let

$$\kappa = E_p^{1/\eta}; \quad \xi(z) = \frac{\kappa}{S_\gamma\ G_L(z)}, \tag{6.10}$$

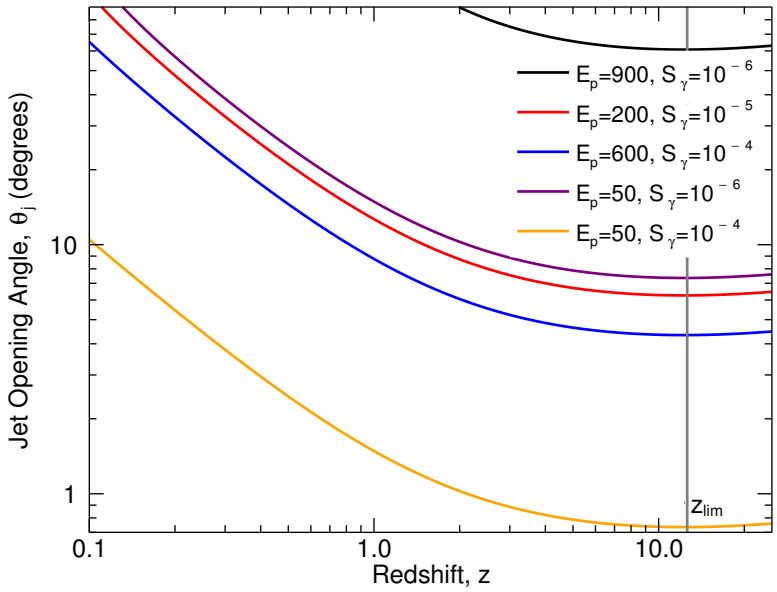

Figure 6.6: The jet opening angle as a function of redshift, for five example spectral scenarios. The vertical line marks z_{lim}, the limiting redshift that results in a lower bound on the opening angle.

and using the formal propagation of uncertainties from the E_p and fluence, the propagated uncertainties on the derived opening angles become:

$$\sigma_\kappa = \frac{\kappa}{\eta} \frac{\sigma_{E_p}}{E_p};$$

$$\sigma_\xi = \xi(z) \sqrt{\left(\frac{\sigma_\kappa}{\kappa}\right)^2 + \left(\frac{\sigma_{S_\gamma}}{S_\gamma}\right)^2}; \tag{6.11}$$

$$\sigma_{\theta_j} = \sigma_\xi \left[1 - (1 - \xi(z))^2\right]^{-1/2}.$$

Table 6.1: Comparison of Inferred Jet Opening Angles to Derived Jet Opening Angles

GRB	z	E_p (keV)	S_γ ($\times 10^{-5}$ erg cm^{-2})	Derived θ_j	Inferred θ_j
970508	0.84	884±343	0.36±0.03	74.3±24.4	18.3±1.0 [134]
980703	0.97	281±32	3.98±0.09	8.32±0.68	7.7±1.0 [140]
990123	1.60	617±7	27.4±0.09	4.19±0.04	2.1±0.9 [134]
990510	1.62	158±5	2.40±0.04	5.31±0.13	3.1±0.5 [134]
991216	1.02	382±6	17.4±0.05	4.80±0.05	2.7±1.0 [134]
090323	3.57	728±5	17.8±0.55	4.34±0.20	2.6±0.6 [137, 138]
090328	0.74	512±21	5.88±0.14	12.70±0.40	5.2±1.4 [137, 138]
090618	0.54	188±3	25.6±0.20	3.76±0.05	4.2±2.7 [141]
090902B	1.82	298±0.2	19.2±0.04	2.79±0.01	3.4±0.4 [137, 138]
090926A	2.11	337±6	24.5±0.72	2.53±0.05	7.0±3.0 [137, 139]
091127	0.49	35±2	2.62±0.07	3.85±0.13	4.0±0.9 [142, 143]

Table 6.1 shows the reported jet opening angles for bursts from afterglow studies in the redshift sample and compares them to the derived jet opening angles. It should be noted that Cenko et al. [137] used radio observations to constrain the physical parameters in their sample, while radio measurements were not used by McBreen et al. [138] or Rau et al. [139]. Using the eleven bursts with well-constrained reported jet angles, the Pearson's correlation coefficient for the reported angles and the derived angles is 0.93 with a probability of $\sim 2 \times 10^{-5}$ that the two quantities are not correlated given the null hypothesis. Figure 6.7 shows the lower limit to the jet opening angles for 382 GRBs from the GBM spectral catalog that have E_p and fluence errors less than 40% of the mean value, resulting in an error in the jet opening angle lower limit of no more than 40% for 85% of the calculated values.

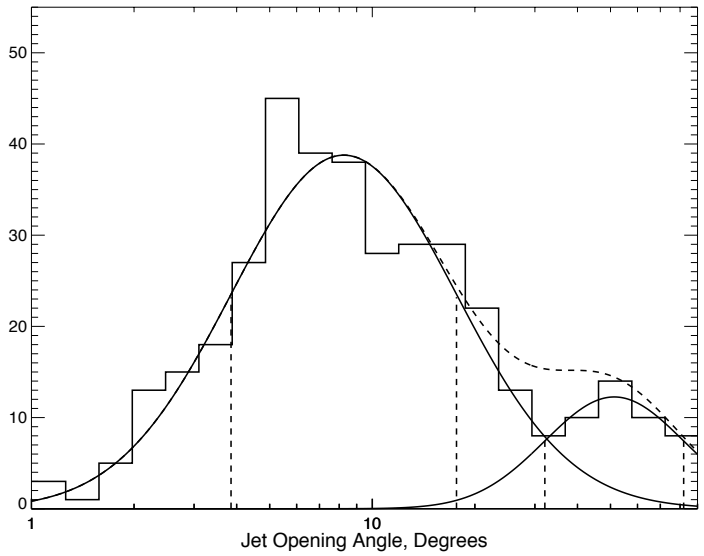

Figure 6.7: Distribution of jet opening angle lower limits for 382 GBM GRBs. The vertical dotted lines show the 1σ standard deviations of the respective distributions.

6.4 Current Problems with using GRBs as Standard Candles

Due to their vast range of comoving distances, GRBs have long been proposed to be used as standard candles for measuring distances far into the early universe. Several problems exist, however, that prevent GRBs from being cosmological probes in this way. Observationally, the spectral and temporal characteristics of GRBs are far-ranging and are distributed over large areas of parameter space. Perhaps these large distributions can be explained by a number of factors, such as the amount of collimation, the Lorentz factor, and even displacement angle of the observer from the center of the jet. I investigate a number of difficulties in using GRBs as standard candles by performing simulations of spectral, temporal, and redshift properties of GRBs.

The simulated spectral parameters were drawn from the distribution of spectral parameters corresponding to the GRB Band function contained in the BATSE [102] and GBM [103] Spectral catalogs. The temporal properties were drawn from the distribution of T_{90} found in the BATSE 4B GRB catalog [13], while the distribution of redshifts were drawn from the distribution of all known GRBs with spectroscopic redshifts [144]. In each case, 10^5 simulated spectra were created by generating a random Gaussian deviate based on the observed distribution of each Band function parameter. Similarly, the simulated durations were generated by random deviates based on the observed two-Gaussian, bimodal T_{90} distribution. These simulations aim at studying the systematic mathematical correlation between the observed Band function spectral parameters and the flux or fluence.

6.4.1 Problems with Luminosity Indicators

A number of proposed luminosity indicators attempt to use the spectral parameter E_p as a proxy for the rest-frame luminosity of the burst [117–119]. These methods, however, contain a key problem: the photon model–in this case the Band function [31]–is parametrized by E_p, and the flux and fluence, which is used to calculate the rest-frame luminosity or energy, is derived from integrating the photon model over energy. Therefore, there exists a purely mathematical correlation between the E_p and flux (or fluence), which can lead to an artificial correlation between the rest-frame E_p and the luminosity or energy. Even assuming a physical correlation between the luminosity or energy and E_p, one must be aware that there is a mixture of artificial correlation due to this complication. In order for such a physical correlation

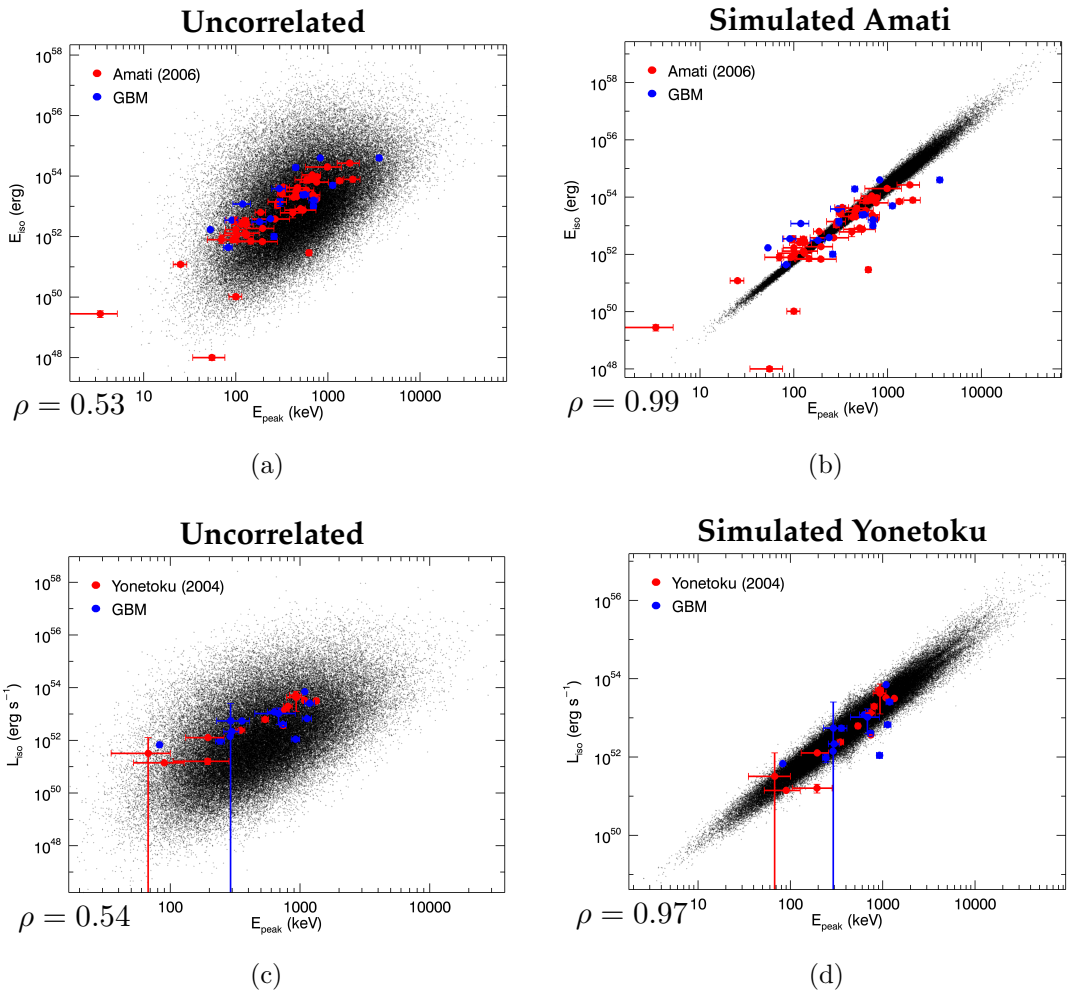

Figure 6.8: Simulations depicting the mathematically artificial correlation for Figure 6.8(a) E_p–E_{iso} and Figure 6.8(c) E_p–L_{iso}. The corresponding simulated Amati and Yonetoku relations are shown in Figure 6.8(b) and Figure 6.8(d). The simulated data are in black, and the observed data are over-plotted in red and blue.

to be ascertained and used, it must be determined the contribution of the artificially induced correlation.

Integrating each simulated Band spectrum over the simulated duration, and using the simulated fluence together with the simulated redshift, E_{iso} can be calculated for each synthesized Band spectrum. Additionally, E_{iso} can be simulated by assuming that the E_p is a luminosity indicator from the Amati relation. This is accomplished by assuming that the uncertainty of the best-fit Amati relation parameters are normally distributed and generating Gaussian deviates for both best-fit parameters based on the 3σ uncertainty. The simulated E_p and Amati relation parameters can be used to generate E_{iso} under the assumption of the Amati relation. Using the simulated spectra as well as the data from Amati et al. [117] and the GBM GRBs with known redshift, Figure 6.8(a) depicts a plot of the artificially introduced correlation between the rest- frame E_p and isotropic energy E_{iso} without the assumption that the Amati relation shows a true correlation. A K-S test can be performed between the observed and simulated E_{iso} values to determine if the observed values are more likely drawn from the distribution only resulting from a mathematical correlation between the observed E_p and fluence or from the distribution that assumes a true correlation between the rest-frame E_p and E_{iso}. Overplotting the data and performing a K-S test between the observed and simulated E_{iso}, it is found that the hypothesis that the observed E_{iso} is drawn from the same distribution as the simulated E_{iso} can only be rejected at 1σ confidence. The same test can be performed by simulating the Amati relation given the 3σ uncertainty in the relation, as in Figure 6.8(b). In the case of the pure Amati relation, the K-S test shows that the hypothesis that the observed E_{iso}

values are drawn from the same distribution produced by the simulated Amati relation can be rejected at 92% confidence. Although not largely conclusive, this indicates a greater chance that the distribution of E_{iso} values is attributable to the mathematical correlation between the E_p and fluence rather than the Amati relation by itself. Additionally, comparing the Pearson correlation coefficient between the rest-frame E_p and E_{iso} to the simulated values in each case will indicate if the observed correlation can arise purely from the mathematical correlation or if there exists an additional component to the correlation. Comparing the Pearson correlation coefficient of the observed E_p and E_{iso} to the simulated values finds $\sim$0% chance probability that the observed correlation is due to the Amati relation, and $\sim$20% chance probability that the observed correlation is due to the mathematical artifact alone. This indicates that the observed correlation between the rest-frame E_p and E_{iso} may contain a significant amount of artificial correlation and that the 3σ uncertainty in the correlation is not enough to account for the amount of dispersion observed.

Similarly, the same correlative analysis was performed using the Yonetoku relation [119], shown in Figure 6.8(c) and Figure 6.8(d). The connection between the rest-frame E_p and the isotropic luminosity, L_{iso}, has a stronger statistical foundation than what was found for the Amati relation. In this case, the K-S test shows that the null hypothesis that the observed L_{iso} values are drawn from the mathematical correlation between E_p and flux can be rejected at the 2σ level. Interestingly, the hypothesis that the observed L_{iso} values are drawn from a true Yonetoku relation cannot be rejected at more than the 16% level. The Pearson correlation coefficient of the data shows that the correlation between E_p and L_{iso} is supported by only

$\sim$5% chance probability that it is due to the mathematical correlation. Alternatively there is $\sim$0% chance probability that the data correlation is due to the Yonetoku correlation. This, in addition to the K-S test, indicates that the Yonetoku relation does have some statistical support, although the true correlation between E_p and L_{iso} slikely has a larger dispersion than the 3σ dispersion assumed in the simulations.

6.4.2 Problems with Estimating Pseudo-Redshifts

One particular use of GRBs as standard candles is the ability to take an observed quantity and to infer the redshift of the burst from that property. This pseudo-redshift estimation is not only important to study the GRB progenitor formation rate and density, but can serve as an important check on the luminosity relation in question. In particular, we can check how accurately we can recover the redshift of bursts that have spectroscopic estimations as well as examine the limitations of the luminosity relation with respect to the estimation of redshift.

In the case of the Amati relation, it inherently truncates pseudo-redshift estimates at $\sim$3 due to the behavior of the relation as a function of redshift [130, 131]. In addition, when comparing the pseudo-redshift estimates to the spectroscopic redshifts, there appears to exist a 0.4 dex dispersion about unity, shown in Figure 6.9(a). When the uncertainty in parameters is fully propagated to the pseudo-redshift estimation, it appears that redshifts greater than $z = 2$ typically result in uncertainties of approximately half an order of magnitude. This is shown in Figure 6.9(b). The combination of the poor performance in prediction accuracy and the relatively enormous uncertainties make the Amati relation of little use to producing pseudo-redshifts.

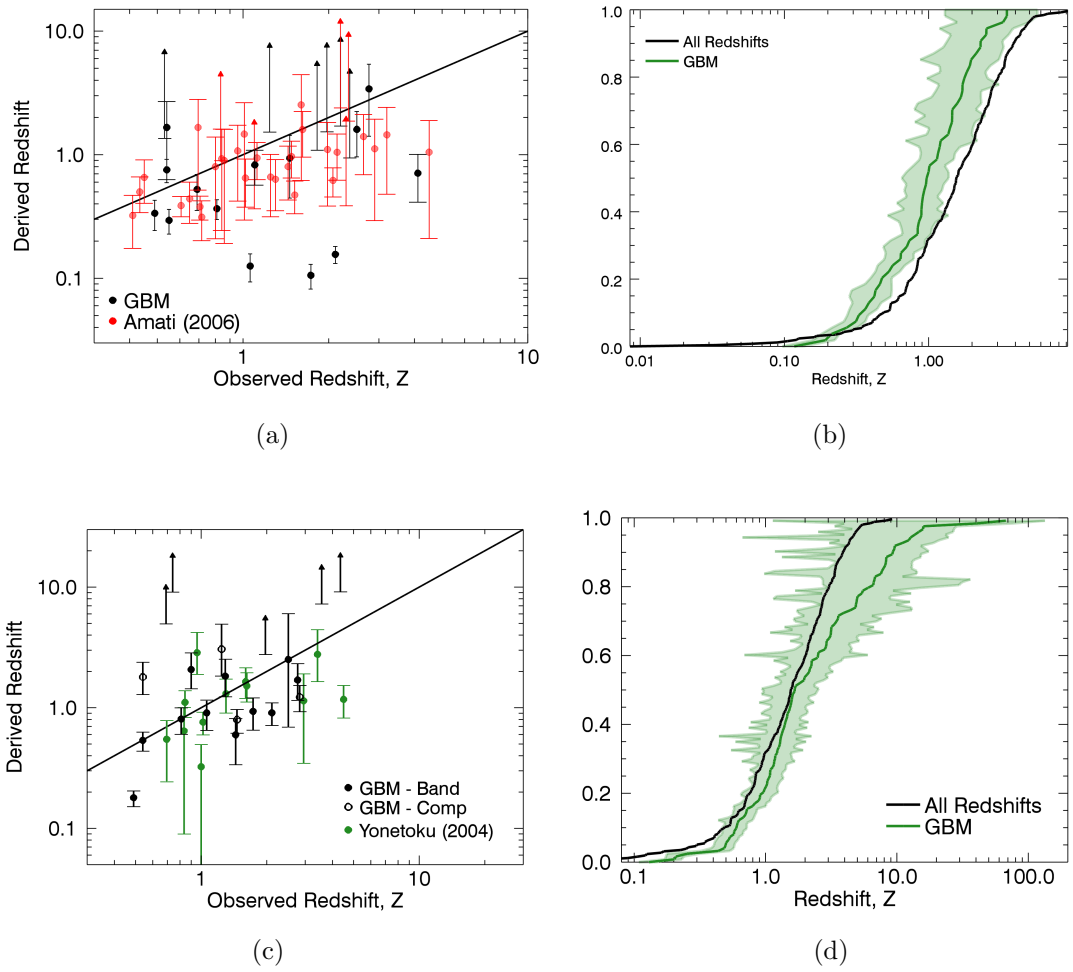

Figure 6.9: The pseudo-redshifts plotted against the corresponding spectroscopic redshifts for the Amati relation Figure 6.9(a) and the Yonetoku relation Figure 6.9(c). The black lines show a one-to-one correlation. The cumulative distribution of pseudo-redshifts for all GBM bursts best fit by a Band function derived using the Amati relation Figure 6.9(b) and the Yonetoku relation Figure 6.9(d). The 1σ errors are included in the cumulative distribution to show the relative error increases as a function of the redshift. The black distribution is the cumulative distribution of all GRBs with spectroscopic redshift.

Similarly, the Yonetoku relation can be used to produce pseudo-redshifts, found in Figure 6.9(c) and Figure 6.9(d). For typical values for the best fit index (~ -2), the pseudo-redshift estimates are not truncated, contrary to the results from the Amati relation. However, when attempting to recover known spectroscopic redshifts of bursts with pseudo-redshifts, there still exists a 0.3 dex dispersion about unity. In addition, full propagation of uncertainty leads to an increasing amount of uncertainty as the redshift estimate increases, similar to what was seen with the Amati relation. These results indicate that pseudo-redshifts produced from the Yonetoku relation alone are not always reliable and are of little use when the associated uncertainties are large.

6.5 Problems Introduced by Jet Collimation

Another problem with using GRBs as standard candles is caused by the collimation of the relativistic outflow. The true distribution of jet opening angles (and thus the amount of jet collimation) is unknown and the existing distribution of inferred collimation is almost certainly biased toward smaller jet opening angles. Even the method by which jet angles are inferred contains a large amount of uncertainty. This is in large part due to the fact that the estimation of the jet angle depends in largely on the jet break time and the E_{iso}. In fact, as shown in Equation 3.1, there is strictly a power law relation between the collimation-corrected energy and the jet opening angle, but taking into account the uncertainty in the spectral parameters, which affects the uncertainty in E_{iso}, as well as typical uncertainties in the jet break time and circumburst density, the power law relation becomes highly dispersed. This

results in over 2 decades of dispersion (1σ) in collimation-corrected energy for a typical jet angle with an uncertainty of $\sim 1^{\circ}$. In addition, jet opening angles are observed to distribute between $\sim$1-10°, but the corresponding collimation-corrected energies for those bursts distribute over 3 decades with no clear correlation with the amount of collimation in the burst. This signals a large difficulty in using GRBs as standard candles since correcting for collimation should naturally produce a clear trend in the burst energies.

6.6 Problems Introduced by the Bulk Lorentz Factor

A contributing factor to the dispersion of observed properties in GRBs is the bulk Lorentz factor of the outflow. For observational purposes, assume the simplest model where the evolution of the Lorentz factor during the prompt emission of the burst does not change significantly and the beam profile does not play a significant role in the calculation of the Lorentz factor. If GRBs are assumed to be standard candles in the rest-frame, a simple relation can be used: $F_{\gamma,obs} \approx L_{\gamma}\ \delta^4$, where $F_{\gamma,obs}$ is the observed energy flux in gamma-rays, L_{γ} is the luminosity in the rest-frame, which is assumed to be constant for all GRBs, and $\delta = (\Gamma - \sqrt{\Gamma^2 - 1}\cos\theta_v)^{-1}$ is the relativistic doppler factor. Rearranging, this becomes

$$\Gamma\left(1 - \sqrt{1 - \frac{1}{\Gamma^2}}\right) \approx \left(\frac{L_{\gamma}}{4\pi d_L^2 F_{\gamma,obs}}\right)^{1/4} \sec\theta_v, \tag{6.12}$$

which gives an equation for the Lorentz factor Γ in terms of the luminosity, observed energy flux, the luminosity distance, and the viewing angle. Taking the observed

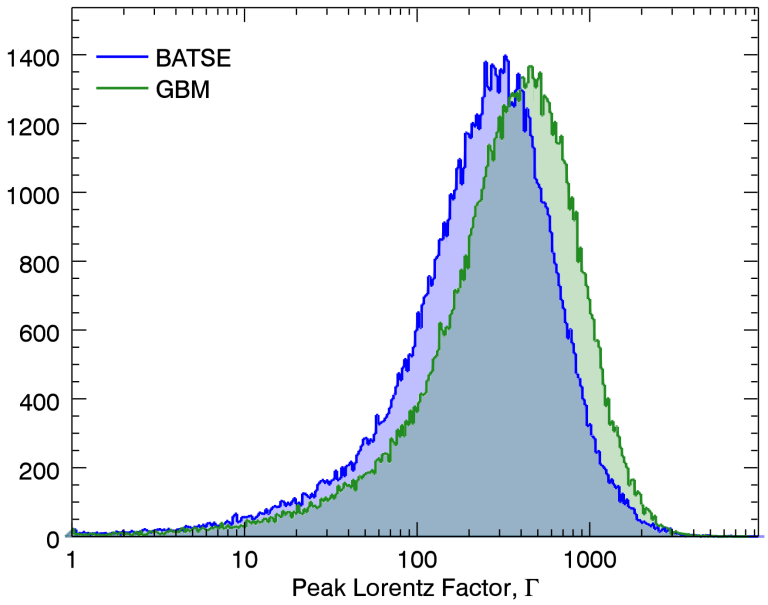

Figure 6.10: Lorentz factor distributions assuming that GRBs are standard candles in the rest-frame. The figure shows the difference between the distributions using the BATSE and GBM flux distributions.

energy flux distributions from the BATSE and GBM spectral catalogs, the luminosity distance calculated using the standard cosmology and the current spectroscopic redshift distribution [144], and a uniform viewing angle distribution, the bulk Lorentz factor distribution can be numerically calculated. Shown in Figure 6.10, the Lorentz factor distribution assuming GRBs are standard candles spans at least an order of magnitude. Note that this is a best case scenario that is detector-dependent due to the observed flux distribution as well as redshift-biased. Those factors alone could further broaden the Lorentz factor distributions. This key result indicates that even if GRBs are standard candles, as assumed here, the Lorentz factors can widely disperse observed spectral parameters.

6.7 Off-Axis Viewing Angle

GRB 980425 was associated with SN 1998bw and occurred a a redshift of $z = 0.0085$, which is more than order of magnitude closer than any other GRB with measured redshift. The observed properties of GRB 980425 are $E_p = 55.1 \pm 11.6$ keV and $L_{iso} = (4.37 \pm 0.47) \times 10^{46}$ erg s^{-1}, which is at least 10^{-4} times dimmer than most other GRB luminosities. Therefore GRB 980425 is widely discrepant for all of the previously described correlations.

It was shown that the low-luminosity of GRB 980425 could be explained as the effect of an off-axis viewing angle [145]. The gamma-ray emissions are concentrated in the forward direction by the relativistic beaming effect. Therefore the peak energy is blueshifted by the Lorentz factor of the emitting material as $E_p = \Gamma E_p(1 + z)$ and the observed flux becomes $F_\gamma \propto \Gamma^4 L_{iso}$. If the observer is viewing at an off-axis direction from the relativistic jet, the fractional component of Γ toward the observer becomes small. Then the observed E_p is proportional to the doppler factor, δ and the luminosity depends on δ as $L_{iso} \propto \delta^4$.

Assuming the on-axis property of GRBs with the spectral shape of $\alpha = -1$, $\beta = -2.1$, and $E_p = 2.6$ MeV, the spectral properties were simulated for an off-axis observing angle. When a jet opening angle of $\theta_j \sim 10 - 30^\circ$ is seen from an off-axis viewing angle of $\theta_v \sim \theta_j + 6^\circ$, the observed quantities of GRB 980425 can be explained [145]. If the observer exists at a few degrees outside the jet, the relativistic beaming effect rapidly decreases and the observed luminosity rapidly dims as δ^4.

CHAPTER 7

COSMOLOGY

In order to use GRBs to study cosmology, a thorough understanding of the geometry and dynamics of the universe is required. In this chapter, I discuss the derivation of the standard model of cosmology as well as observational methods to study cosmology. First, a brief introduction to the Einstein field equations and the Robertson-Walker solution in Section 7.1 and Section 7.2 respectively. From there, I discuss the Friedman equation in the context of the Robertson-Walker solution and resulting implications in Section 7.3 and Section 7.4. Useful cosmological distance measurements can be found in Section 7.6. Finally in Section 7.7 I will discuss a number of observational methods that have set constraints on the theoretical cosmological model.

7.1 Einstein's Field Equations

The spacetime geometry is determined by Einstein's field equations, which result from the presence of mass, energy, and momentum [146]. The metric tensor of a particular spacetime is determined by the amount and distribution of stress-energy present, and the relation between the the metric and energy-stress tensor is a set

of non-linear partial differential equations. The Einstein equations written in tensor form are

$$R^{\mu\nu} - \frac{1}{2}Rg^{\mu\nu} + \Lambda g^{\mu\nu} = -\frac{8\pi G}{c^4}T^{\mu\nu}, \tag{7.1}$$

where $R^{\mu\nu}$ is the Ricci tensor, R is the curvature, $g^{\mu\nu}$ is the metric tensor, Λ is the cosmological constant, G is the gravitational constant, and $T^{\mu\nu}$ is the stress-energy tensor. Einstein defined

$$G^{\mu\nu} = R^{\mu\nu} - \frac{1}{2}Rg^{\mu\nu}, \tag{7.2}$$

what is now referred to as the Einstein tensor, so that Equation 7.1 becomes

$$G^{\mu\nu} + \Lambda g^{\mu\nu} = -8\pi T^{\mu\nu} \tag{7.3}$$

by setting constants $c = G = 1$. The solutions to the Einstein equations define the metric tensor, and the movement of particles and energy can then be calculated using the geodesic equation

$$\frac{d^2x^\lambda}{dt^2} + \Gamma^\lambda_{\mu\nu}\frac{dx^\mu}{dt}\frac{dx^\nu}{dt} = 0, \tag{7.4}$$

where the $x(t)^\mu$ are spatial coordinates and $\Gamma^\lambda_{\mu\nu}$ are the Christoffel symbols for an affine space.

7.2 The Robertson-Walker Solution

A solution to the Einstein field equations is the Robertson-Walker (RW) Solution, which is a metric defining the distance between two points in a topological space. This solution is a result of assuming that the universe is isotropic and has a single

universal time coordinate [147]. In general, the distance components can be written as a time-dependent scale factor $R(t)$ and a time-independent comoving coordinate r and is

$$c^2 d\tau^2 = c^2 dt^2 - R^2(t)\big[f^2(r)dr^2 + g^2(r)d\varphi^2\big]. \tag{7.5}$$

Assuming a non-Euclidean space with curvature, the more specific form of the RW metric becomes

$$c^2 d\tau^2 = c^2 dt^2 - R^2(t)\left[\frac{dr^2}{1-kr^2} + r^2 d\varphi^2\right], \tag{7.6}$$

where k defines the curvature of the space. This form admits to extrema as a function of k: the metric possesses positive curvature when $k = +1$ and negative curvature if $k = -1$. A special case results when $k = 0$, causing the curvature $R = \infty$. This describes a spatially flat universe. Usually the scale factor is defined in terms of the current scale factor R_0, therefore the scale factor can be defined as $a(t) = R(t)/R_0$, such that presently $a(t) = 1$.

7.3 Dynamics of the Robertson-Walker Metric

For a dynamical system existing in a Euclidean space defined by the RW metric, the conservation of energy can be defined as

$$\dot{a}^2 - \frac{8\pi G}{3}\rho a^2 = -kc^2, \tag{7.7}$$

where ρ is the total density of the universe with contributions from matter, radiation, vacuum, etc. [148, 149]. Equation 7.7 is known as the Friedman equation. By

inspecting the spatially flat case ($k = 0$), the critical density, ρ_c, can be defined as

$$\rho_c = \frac{3\dot{a}^2}{8\pi G a^2}, \tag{7.8}$$

so that a universe with $\rho > \rho_c$ will be spatially closed, and a universe with $\rho < \rho_c$ will be spatially open. Since the separation of two points according to the RW metric is $a(t)dr$, we can define

$$H = \frac{\dot{a}}{a}, \tag{7.9}$$

according to Hubble's Law, where H is the Hubble parameter. It is important to note that both H and ρ are available to change as a function of time, therefore the current values are usually denoted H_0 and ρ_0 respectively. To determine the total amount of energy in the universe requires the inspection of each contribution to the density. The most common contributions are matter, radiation, and vacuum energy. Since the density of matter particles decreases in three dimensional Euclidean space, $\rho_m \propto R^{-3}$. Similarly the energy density of radiation decreases but by an additional factor due to redshift, therefore $\rho_r \propto R^{-4}$. The vacuum energy is usually assumed to be related to the cosmological constant from Equation 7.3. The equation of state of ρ_Λ is not generally known, but is assumed to be constant in time, therefore $\rho_\Lambda = \text{constant}$ (for details, see Section 7.5). It is usually advantageous to define a density parameter as the ratio of the density to the critical density, $\Omega = \rho/\rho_c$, therefore each density contribution can be written as its corresponding density parameter. The total density

can then be written as

$$\rho_0 = \frac{3H_0^2}{8\pi G}\left[\Omega_r a^{-4} + \Omega_m a^{-3} + \Omega_\Lambda\right], \tag{7.10}$$

where $a = R/R_0$. In addition, the density is related to the curvature by Equation 7.7 such that $k = 1 - \sum \Omega_i$. The evolution of the scale factor is dependent on both H and Ω, which are both redshift dependent. This fact allows for the relation between the comoving distance and the redshift as

$$R_0 dr = \frac{c}{H(z)}dr = \frac{c}{H_0}\left[\Omega_r(1+z)^4 + \Omega_m(1+z)^3 + (1-\Omega)(1+z)^2 + \Omega_\Lambda\right]^{-1/2}dz. \tag{7.11}$$

This equation is important since the redshift is an observational parameter and the comoving distance determines the apparent brightness of a distant object. Equation 7.11 then allows for the use of objects with observed brightness and known distance to determine the values of H and Ω_i.

Another important property of a non-static universe is its rate of expansion, which implies that the universe started from a singularity at $t = 0$, usually called the Big Bang. This expansion is usually defined by the deceleration parameter, q as

$$q = -\frac{\ddot{a}a}{\dot{a}^2} = -\left[\frac{\dot{H}}{H^2} + 1\right]. \tag{7.12}$$

This also results in $q = \Omega_m/2 + \Omega_r - \Omega_\Lambda$ if Ω_Λ is represented by the cosmological constant. Additionally, the current scale factor is of interest,

$$R_0 = \frac{c}{H_0}\left[\frac{\Omega_0 - 1}{k}\right]^{-1/2}. \tag{7.13}$$

Here, the Hubble constant sets the curvature length, which becomes infinitely large as Ω_0 approaches unity. When $\Omega_0 = 0$ then the curvature length equals the Hubble length, $D_H = c/H_0$.

7.4 Solutions to the Friedman Equation

Friedman found cosmological solutions to the Einstein equations in 1922 [148] for a matter-only universe, and later Lemaître discovered the linear distance-redshift relationship in 1927 [150] resulting from the Friedman model. Now, however, the more general solutions incorporate radiation and vacuum energy. In the case of the Friedman model, the Hubble parameter can change over time. Applied to a fluid with a given equation of state, the solutions yield the time evolution and geometry of the universe as a function of the fluid density. Typically the radiation contribution is neglected since the current density parameter for radiation is $\Omega_r \approx 6 \times 10^{-5}$, although the assumption fails at early times when $\rho_m/\rho_r \propto (1+z)^{-1}$. The defined matter-radiation equality epoch is given by $1 + z \approx 1100$. At redshifts higher than this, the universal dynamics were dominated by the relativistic particle content.

7.4.1 Static Universe (Einstein Model)

The static solution to the Friedman equation results in a universe which neither contracts nor expands. The stationary constraint implies that the $\dot{a}$ (velocity) and $\ddot{a}$ (acceleration) terms in Equation 7.7 are zero and results in

$$\rho = \frac{3kc^2}{8\pi G a^2}. \tag{7.14}$$

This implies that $\rho = 3\rho_\Lambda$ which means that ρ_m is twice that of ρ_Λ and $k = +1$, thereby describing a spatially closed universe. This also implies that if the universe is to be stationary, ρ_Λ must counteract the attraction of matter, therefore inducing a negative pressure. If the balance between the densities is slightly perturbed, the universe will contract with a slightly larger ρ_m or expand with a slightly larger ρ_Λ.

7.4.2 de Sitter Universe

If the universe is dominated by vacuum energy, it will expand due to the negative pressure presented by a positive cosmological constant. The expansion is not affected by any other compensating factor, therefore the scale factor will exponentially increase, $R(t) \propto e^{Ht}$. It becomes clear from this model that the cause of the expansion is exactly Λ and the negative pressure that it represents.

7.4.3 Bouncing and Loitering Universes

Although most cosmological models resulting from a big bang will either eventually contract or keep expanding depending on the total density, there are some cases

when a universe may slow before completely collapsing and rebound in expansion or the expansion slows such that the scale factor is approximately a constant. The former case is known as a bouncing universe, and since the universe has a predetermined maximum size before contracting and minimum size before expanding, the maximum redshift possible is represented by

$$1 + z \leq 2f\left(\frac{1}{3}f^{-1}(\Omega_m^{-1} - 1)\right), \tag{7.15}$$

where $f = \cosh(r)$ if $\Omega_m < 0.5$ and $f = \cos(r)$ otherwise. For example, assuming $\Omega_m \approx 0.3$ then the maximum redshift possible would be $z \approx 1.25$. Since there are obviously objects with redshifts greater than the maximum possible, the bouncing universe model can easily be ruled out.

7.4.4 Flat Universe (Einstein–de Sitter Model)

The case where only matter and radiation are considered and $\Omega = 1$ implying $k = 0$ results in a flat universe and is known as the Einstein-de Sitter model. The Friedman equation in Equation 7.7 in this model becomes $\dot{a}^2 = H_0^2(\Omega_m a^{-1} + \Omega_r a^{-2})$ which can be integrated to show time as a function of the scale factor

$$H_0 t = \frac{2}{3\Omega_m^2}\left[(a\Omega_m - 2\Omega_r)\sqrt{\Omega_r + a\Omega_m} + 2\Omega_r^{3/2}\right]. \tag{7.16}$$

For a matter-only universe $H_0 t = 2/3a^{3/2}$ and $H_0 t = 1/2a^2$ for a radiation-only universe, which implies two different epochs in time [147]. This serves as an example

that a model containing multiple source densities can evolve to enter epochs where a particular source density is more dominant than the rest.

7.5 The Equation of State of Dark Energy

In general, a perfect fluid can be characterized by its equation of state, which is the ratio of the pressure of the fluid to its energy density. Already, I have suggested that the expansion of the universe is similar to the movement of a fluid by such terms as "Hubble flow." Indeed matter, radiation, and vacuum energy can be thought of as fluids, and therefore are each described by an equation of state. For any cosmological fluid, the energy density can be represented as

$$\rho \propto R^{-3(1+w)}, \tag{7.17}$$

where R is the scale factor, and $w = p/\rho$ is the power law index characterizing the equation of state. Ordinary, non-relativistic matter exerts no pressure (no kinetic energy) compared to its energy density, indicating that $w_m = 0$. The energy density then is purely diluted by the expansion of a volume, $\rho_m \propto R^{-3}$. The equation of state for radiation is $w_r = 1/3$, indicating that the radiation pressure is one third the radiation energy density. Pure radiation is then diluted by expansion as $\rho_r \propto R^{-4}$. The additional factor of R^{-1} results from the fact that radiation has momentum and wavelength that is redshifted by the expansion. The equation of state of vacuum energy, or what is commonly known as dark energy, likely describes the accelerated expansion of the universe. If dark energy is required to cause an accelerated expansion

then the pressure exerted needs to counteract matter and radiation pressure, therefore the equation of state needs to be negative. Usually the dark energy equation of state is assumed to be $w_\Lambda = -1$, which causes the energy density to be expressed as $\rho_\Lambda \propto e^{Ht}$. The standard model of cosmology is then usually referred to as Λ + Cold Dark Matter (ΛCDM) as the dark energy component is assumed to be attributed to the cosmological constant and non-baryonic matter is theorized to be slow moving and weakly interacting with baryonic matter and radiation [151, 152]. There is no theoretical reason why the dark energy equation of state should be a constant other than it is the simplest representation. It may be the case that Ω_Λ or w_Λ evolve over redshift, although there is no theoretical preference for the functional form of the evolution either. The simplest evolution for dark energy is perhaps a constant $w_\Lambda \neq -1$, representing a scalar field and usually known as quintessence. A time-dependent parameterization of the evolution of w_Λ may be $w_\Lambda(z) = w_0 + w'z$, which observationally is known as the Riess parametrization since observations using Type Ia Supernovae indicate that this model may be a good explanation at $z < 1.5$ [153, 154]. This, however, causes the Ω_Λ term to increase exponentially as the redshift increases and creates the unfortunate circumstance that dark energy is the dominant form of energy in the radiation-dominated epoch. Therefore an alternative has been proposed by Chevalier & Polarski [155] as well as Linder [156] such that the expansion about w_0 becomes $w(z) = w_0 + w_a z(1+z)^{-1}$. The Chevallier-Polarski-Linder (CPL) parametrization is stable at increasing redshift and does not suffer from the same problem as the Riess parametrization.

7.6 Distance and Time Measurements in Cosmology

Because a non-static universe implies that the distances between comoving objects are constantly changing, and the observation of distant objects covers time as well as space, there are a number of ways to describe the distance between two points. It is important to describe a set of distance measures to calculate the separation between objects on null geodesics which connect the observer to the object. Before distance measurements can be formulated, an inspection of the fundamental parameters is needed. The Hubble parameter H_0, as noted before, is the constant of proportionality between recession speed and the distance in the expanding Universe. The inverse of the Hubble parameter is the Hubble time, t_H, and the Hubble distance can be calculated by $D_H = c/H_0$. Both t_H and D_H set the fundamental scale of the universe.

The redshift for objects at small distances d may be approximated by $z \approx d/D_H$. This approximation fails, however, when the distance of the object is large enough that the cosmological redshift due to the Hubble flow dominates the peculiar velocity of the distant object. The redshift then will be proportional to the ratio of the current scale factor to the scale factor at the time the observed photons from the object were emitted,

$$1 + z = \frac{a(t_0)}{a(t_e)}. \tag{7.18}$$

If we let

$$f(z) = \left[\Omega_r(1+z)^4 + \Omega_m(1+z)^3 + (1-\Omega)(1+z)^2 + \Omega_\Lambda(1+z)^{w(z)}\right]^{1/2}, \tag{7.19}$$

then the distance of an object from which photons are observed today is known as the proper motion distance or comoving distance, D_c, and is found by integrating $f^{-1}(z)$ from Equation 7.19 over redshift and multiplying by the Hubble distance:

$$D_C = D_H \int_0^z \frac{dz'}{f(z')}. \tag{7.20}$$

Here, $f(z)$ is proportional to the time derivative of the logarithm of the scale factor, and since $dz = da$, $dz/f(z)$ is proportional to the the time-of-flight of a photon traveling across the redshift interval dz, divided by the scale factor at that time. For a flat universe, D_C in Equation 7.20 represents the exact comoving distance, however if the universe contains curvature $\Omega_k = 1 - \Omega$, then Equation 7.20 becomes

$$D_C = \begin{cases} \frac{D_H}{\sqrt{\Omega_k}} \sinh\left(\sqrt{\Omega_k}\frac{D_C}{D_H}\right) & \text{for } \Omega_k > 0 \\ D_C & \text{for } \Omega_k = 0 \\ \frac{D_H}{\sqrt{|\Omega_k|}} \sin\left(\sqrt{|\Omega_k|}\frac{D_C}{D_H}\right) & \text{for } \Omega_k < 0 \end{cases} \tag{7.21}$$

which accounts for the curvature through the trigonometric functions. The comoving distance is then the distance that would be measured today if a nearby object were locked into the Hubble flow. Figure 7.1 shows the comoving distance as a function of redshift for different world models.

The luminosity distance describes the relationship between the observed bolometric flux, F_{bol} and the bolometric luminosity of the object, L_{bol}, and is written

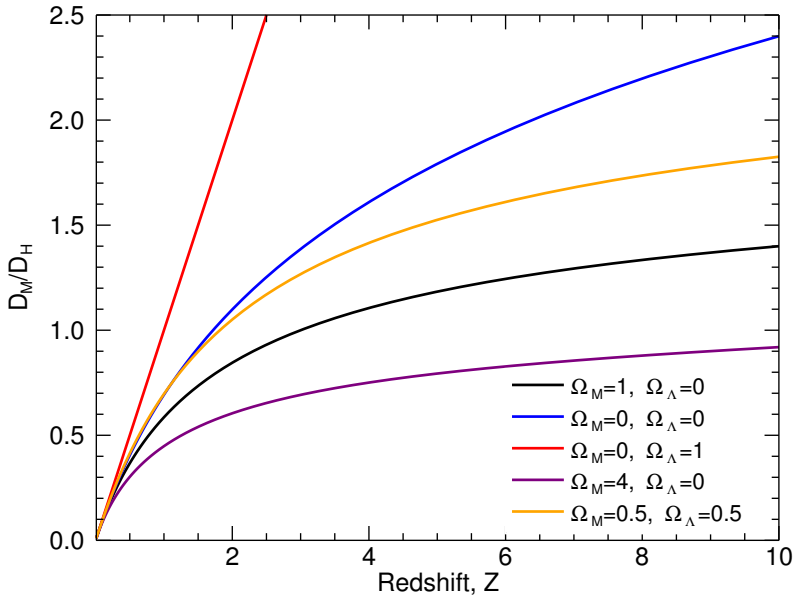

Figure 7.1: Dimensionless comoving distance as a function of redshift for different values of Ω_M and Ω_Λ and $w(z) = -1$.

as

$$d_L = \sqrt{\frac{L}{4\pi F_{bol}}}. \tag{7.22}$$

The luminosity distance is related to the comoving distance in Equation 7.21 by $d_L = (1+z)D_C$, and Figure 7.2 shows the luminosity distance as a function of redshift for different world models. In most cases the bolometric flux is not observable, but instead the differential flux over at a particular frequency, F_ν. The flux must be corrected by a factor known as the "K-correction" since the flux emitted by the object is redshifted into a different band when observed compared to when the flux was emitted. The flux is an integration over the observed frequency band of the frequency (or energy) spectrum of the object that is being observed. Therefore, the

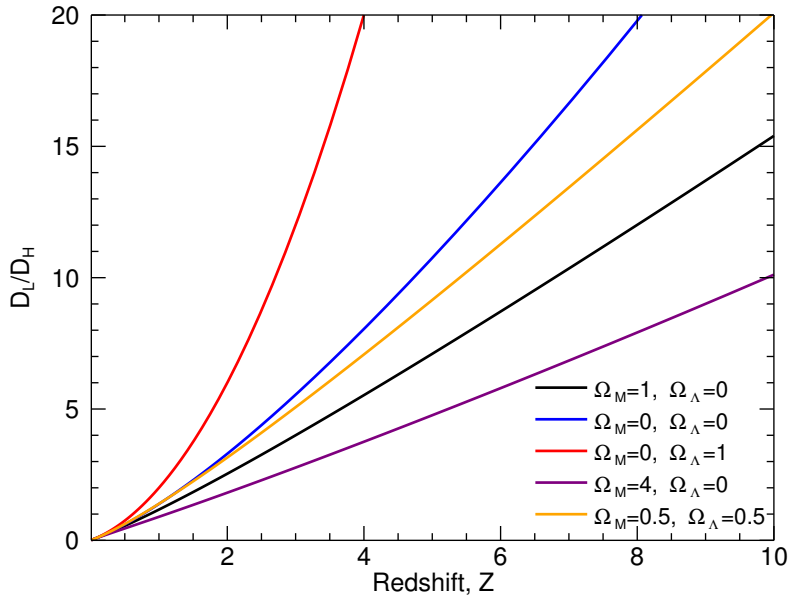

Figure 7.2: Dimensionless luminosity distance as a function of redshift for different values of Ω_M and Ω_Λ and $w(z) = -1$.

K-correction is dependent on the shape of the spectrum and F_ν is related to L_ν by

$$F_\nu = (1+z)\mathrm{K}\frac{L_\nu}{4\pi d_L^2}, \tag{7.23}$$

where

$$\mathrm{K} = \frac{L_{(1+z)\nu}}{L_\nu} \tag{7.24}$$

is the K-correction, represented by the ratio of the luminosity in the redshifted band to the luminosity in the observed band. The $(1+z)$ factor in Equation 7.23 is due to the redshifting of the bandwidth.

Generally, distances can be related to the luminosity of the observed object, and in many cases we want to describe this distance in terms of the observed luminosity. The distance modulus, μ, represents the magnitude between the object's observed bolometric flux and what the observed flux would be at a distance of 10 pc,

$$\mu = 5 \log_{10} \left(\frac{d_L}{10 \text{ pc}} \right). \tag{7.25}$$

The distance modulus is traditionally related to the apparent and absolute optical magnitude of nearby stars as $\mu = m - M$, where m is the apparent magnitude and M is the absolute magnitude. It is this relationship between the optical brightness and distance of nearby objects that allows μ to be used for objects, such as GRBs, that are observed at other wavelengths (energies). Once d_L is known for nearby stars from the magnitude–distance relation, then objects that have approximately the same d_L will have the same μ regardless in which energy band they are observed. In this way, μ can be thought of as simply the logarithmic luminosity distance normalized to some fiducial value. The distance modulus is often used when constructing Hubble diagrams and studying cosmology and will be an important parameter used throughout this dissertation.

When discussing the number densities of objects in the Hubble flow, a useful measure is the comoving volume, V_c. The comoving volume is the proper volume multiplied by three scale factors

$$dV_C = 4\pi [R_0 S_k(z)]^2 R_0 dr, \tag{7.26}$$

or as a function of redshift, is multiplied by $(1+z)^3$. Two factors of $(1+z)$ convert a proper area into a comoving area, the comoving volume element is typically expressed in solid angle $d\Omega$ and redshift dz as

$$dV_C = \frac{D_H(1+z)^2 D_A^2}{f(z)} d\Omega dz, \tag{7.27}$$

where $D_A = D_C/(1+z)$ is the angular diameter distance. For a flat universe, integrating over solid angle and redshift gives $dV_c = 4\pi D_C^3$. The comoving volume can then be used to predict luminosity densities and produce a luminosity function for a classes of objects.

When a distant object is observed, the observer is not only peering over distance, but also time. The amount of time from the present that the observer is looking is called the lookback time, t_L and is the difference between the age of the universe at observation and the age of the universe at the time the photons were emitted by the object. The product of $(1+z)f(z)$ is proportional to the derivative of z with respect to the lookback time, so

$$t_L = t_H \int_0^z \frac{dz'}{(1+z')f(z')}. \tag{7.28}$$

Alternatively, the age of the universe at a particular z can be determined by changing the limits of integration so that the integration is performed from $z' = z$ to $z' = \infty$. The lookback time and age of the universe for different world models is shown in Figure 7.3.

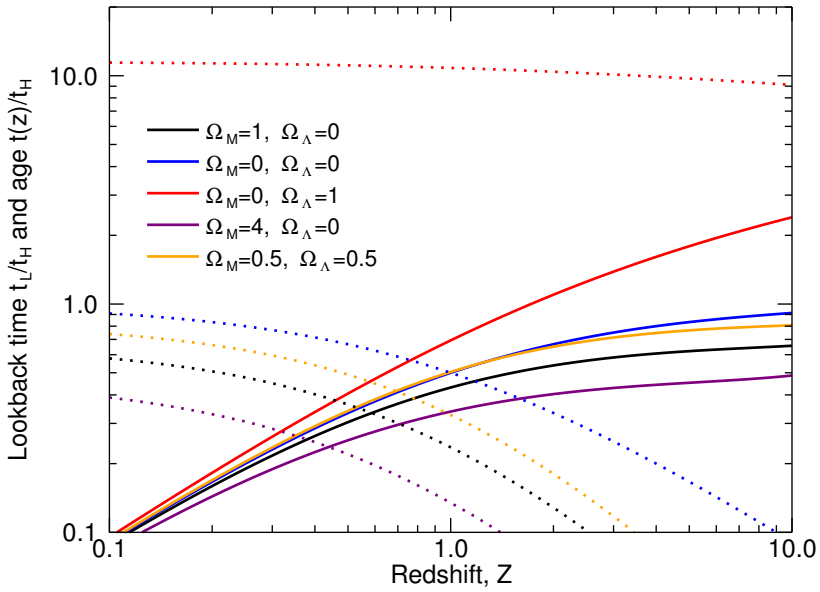

Figure 7.3: The dimensionless lookback time (solid lines) and age of the universe (dotted lines) as a function of redshift for different values of Ω_M and Ω_Λ and $w(z) = -1$. The point at which each set of lines cross is the redshift at which the universe is half of its present age.

7.7 Observational Cosmology

One of the main goals in observational astronomy is the ability to accurately measure distances in the universe. Different techniques have been developed to estimate distances in different regimes, and the culmination of all the techniques is known as the cosmic distance ladder. The first rung of the ladder, stellar parallax, is used to measure the distance to nearby stars by using the orbital position of the Earth to measure the change in position of closer stars relative to more distant stars. Currently this method is only accurate up to ∼500 pc, which is approximately 1% the

diameter of the Milky Way. At larger distances, the infinitesimal changes in apparent position are undetectable and another method is required.

In 1908, Henrietta Swan Leavitt discovered that a certain type of star, called a Cepheid variable, pulses with a particular period that is correlated to its luminosity [157]. It was later discovered that there are two classes of Cepheid variables following different correlations between the pulse period and luminosity, and the Type II Cepheid variables are lower mass and metal-poor compared to the Type I variety. The two classes of Cepheid variables were then used as the first set of "standard candles" to estimate distances from ∼100 pc to ∼100 kpc. It was by using Cepheid variables as standard candles and the observed redshift of their parent galaxies that Hubble and Humason discovered a correlation between the distance and redshift [158]. The redshifts, results of the recessional velocity of the galaxies, increased with increasing distance, indicating that the universe was expanding. The slope of the correlation is the well-known Hubble constant, and its discovery marked the beginning of the modern era of cosmology, albeit establishing the value of the Hubble constant at ~ 550 km s^{-1} Mpc^{-1}, which is ∼8 times the currently accepted value.

Following Hubble's discovery of an expanding universe, the hot Big Bang model of the universe was formulated, and the cosmic microwave background (CMB) was predicted as an observation of the model by Gamow and Alpher in 1948. In 1965, Penzias and Wilson detected the first confirmed temperature excess at 3.5 K attributed to the CMB. Two notable missions, the Cosmic Background Explorer (COBE) and the Wilkinson Microwave Anisotropy Probe (WMAP), have detected and mapped large scale anisotropies in the microwave background at 7 degree and

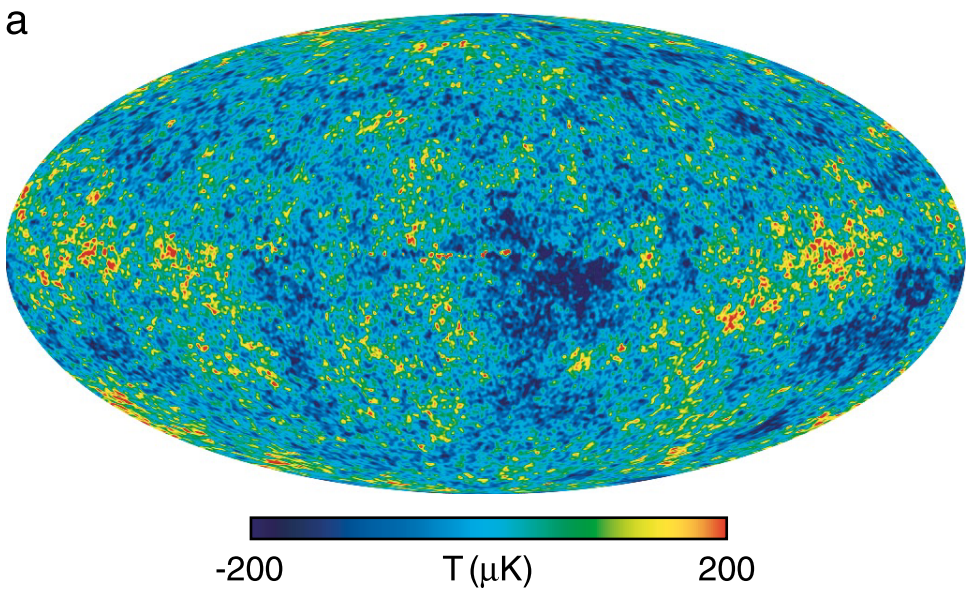

Figure 7.4: WMAP full-sky map of the Cosmic Microwave Background

13 arc-minute resolutions respectively, remnants from the expansion of the universe. A full-sky map of the CMB [159] from WMAP is shown in Figure 7.4. In 2009, the Planck spacecraft was launched by the European Space Agency to yield finer resolution measurements of the microwave anisotropies.

Exploring baryon acoustic oscillations (BAO) is another way to study cosmology. The BAO result from density fluctuations in baryonic matter, which create oscillations. In the early universe, pressure waves containing baryons and photons are created by the gravitational attraction of the matter and radiation pressure from Thomson scattering and move at an outward velocity of $\approx c/\sqrt{3}$ [160]. After the photons decouple from the baryonic matter, they diffuse away, attenuating the radiation pressure and creating a shell of baryonic matter at a particular radius, which is usually called the sound horizon. Since non-baryonic matter (dark matter) does not interact

with the photons, it experiences no radiation pressure to counteract the gravitational pressure and will stay at the center of the expanding shell of baryonic matter and photons. The configuration of dark matter and baryonic matter then gravitationally attract more matter, creating density anisotropies that eventually form galaxies [161]. Because the sound horizon dictates the scale for the separation between galaxies, and the numerous instances of pressure waves in the early universe would create overlap an interference in the oscillations observed today, the BAO provide on observational method to study the distribution of a large number of galaxies and determine the expansion rate of the universe [162]. The CMB provides an accurate estimate of the size of the sound horizon at recombination, and by comparing the sound horizon at recombination and the sound horizon observed today, the amount of expansion can be estimated. Currently, missions such as the Sloan Digital Sky Survey (SDSS) and the DEEP2 Survey have yielded spectroscopic and photometric redshifts for millions of galaxies in the sky out to redshifts of $z \approx 0.7$ [163]. Such large scale clustering analyses enable BAO to be used as standard candles and result in constraints on the cosmological expansion and current density [164, 165].

Another important standard candle are Type Ia Supernovae (SNe Ia). SNe Ia occur when a binary system comprised of a white dwarf and companion star undergoes mass transfer. Matter is transferred from the companion and is accreted onto the white dwarf, and the white dwarf gains mass until it reaches the Chandrasekhar mass limit and undergoes nuclear fusion. Since the white dwarfs explode at the same mass limit, the comoving luminosity for each SN Ia is the same. By determining the peak luminosity of the supernova, the distance can then be calculated for the supernova.

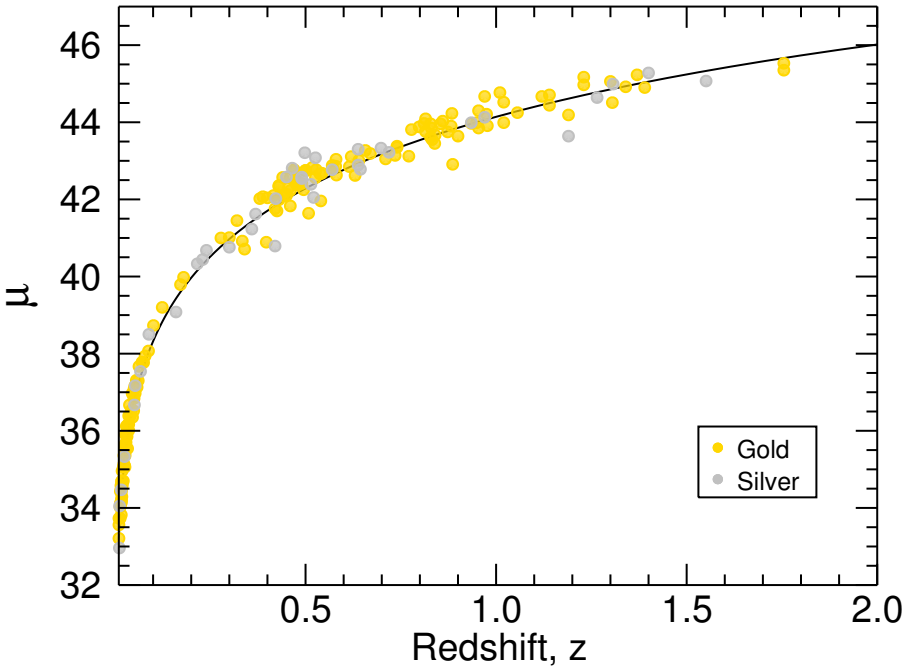

Figure 7.5: Hubble diagram of Type Ia Supernovae distance moduli and redshift. The slope yields a Hubble constant of $H_0 \approx 67$ km s^{-1} Mpc^{-1}.

Using SNe Ia extends the cosmological distance ladder out to $\sim$50 Mpc ($z \approx 1.5$), since their peak luminosities are on the order of the parent galaxy and can be observed over greater distances. SNe Ia have also been used to create a Hubble diagram to estimate the Hubble constant as shown in Figure 7.5. The Hubble constant is estimated from these observations as $H_0 \approx 67$ km s^{-1} Mpc^{-1} [153, 154].

CHAPTER 8

THE GRB HUBBLE DIAGRAM

Extending the Hubble diagram and therefore measuring the properties of the universe is at the forefront of modern cosmology. Very few observable objects exist at the redshifts from which GRBs emanate, and so they present a unique chance at extending the Hubble diagram into the early universe. Several studies have been performed to build the GRB Hubble diagram, but the lack of GRBs with known redshift has slowed the progress. This fact, coupled with the problem that there is a paucity of very low-z GRBs with characteristics similar to the higher-z majority, results in the fact that the distance modulus for GRBs at any redshift is largely unknown. A number of investigations have sought to circumvent this problem by constructing luminosity relations that are cosmologically-dependent, and attempt to constrain cosmological models without the direct use of distance moduli, thereby creating a circularity problem. In this chapter, I discuss some of the efforts to use GRBs as standard candles and the inherent problems in the methods. I then offer an alternative method that is independent of a cosmological model to estimate the redshift, distance modulus, and jet opening angle of GRBs.

8.1 Calculating the K-correction

Since we cannot measure the true bolometric flux or fluence of a GRB, we must correct for the change in bandpass and bandwidth by the redshifting of the spectrum. In addition, if we are studying GRBs that were observed with different instruments, it is likely that the GRBs were observed in different bandpasses, therefore the fluxes need to be expressed in the same energy range. To correct for these effects, we require the use of the K-correction. As shown in Equation 7.24, the K-correction is a ratio of the flux in the redshifted band to the flux in the observed band. More specifically for GRBs, we can calculate the K-correction for GRBs by integrating the energy spectrum. The flux of a GRB can be calculated as

$$F_{[e_1,e_2]} = \int_{e_1}^{e_2} \phi(E) E dE, \tag{8.1}$$

where $[e_1, e_2]$ is the observed bandpass, $E = h\nu$ is energy, and $\phi(E)$ is the photon model used to describe the GRB spectrum. To calculate the K-correction for a co-moving energy band, $[\bar{e}_1, \bar{e}_2]$, from an observed flux in band $[e_1, e_2]$, the ratio of the fluxes is required:

$$K[e_1, e_2, \bar{e}_1, \bar{e}_2, z, \phi(E)] = \frac{\bar{F}_{[\bar{e}_1/(1+z), \bar{e}_2/(1+z)]}}{F_{[e_1,e_2]}}. \tag{8.2}$$

For accurate propagation, the uncertainty needs to be calculated for the K-correction. The relative uncertainty of the redshift is orders of magnitude smaller

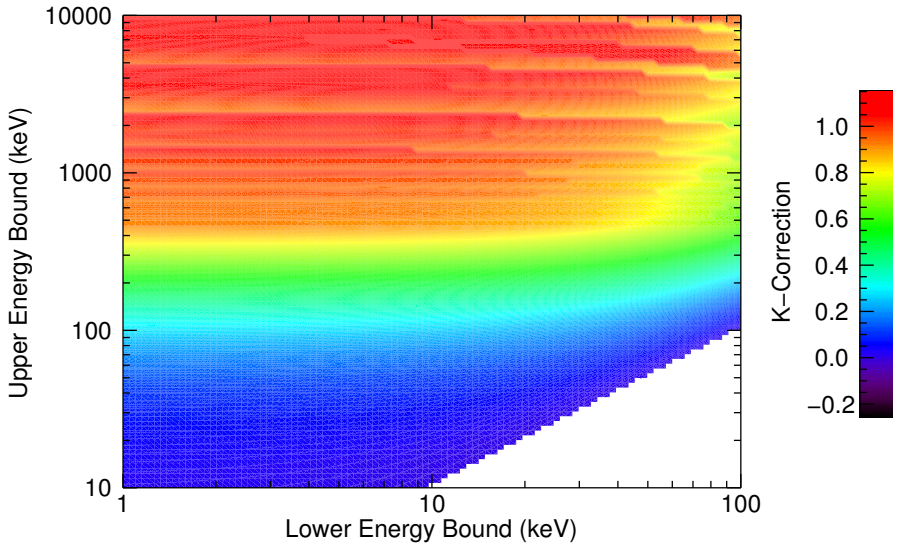

Figure 8.1: Contour map of the K-correction for GRB 090926A, which is best fit by a Band function in the 8 keV–1 MeV energy band. The axes display the lower and upper bound defined by the comoving bandpass.

than the typical uncertainties associated in calculating the observed flux, therefore the redshift contribution to the K-correction is ignored. The main uncertainty imparted upon the K-correction is from the uncertainty in the parametrized photon model. Therefore, the uncertainty in both flux terms must be calculated by integrating the derivative of the photon model with respect to each parameter,

$$\sigma_F^2 = \sum_i \left| \frac{\partial \phi(E;\Theta)}{\partial \Theta_i} \right|^2 \sigma_{\Theta_i}^2, \tag{8.3}$$

where the Θ_i are the photon model parameters. Since the K-correction is dependent on the integration of the of the best fit photon model, it usually exhibits complex behavior as a function of the comoving bandpass and is not easy to predict without the

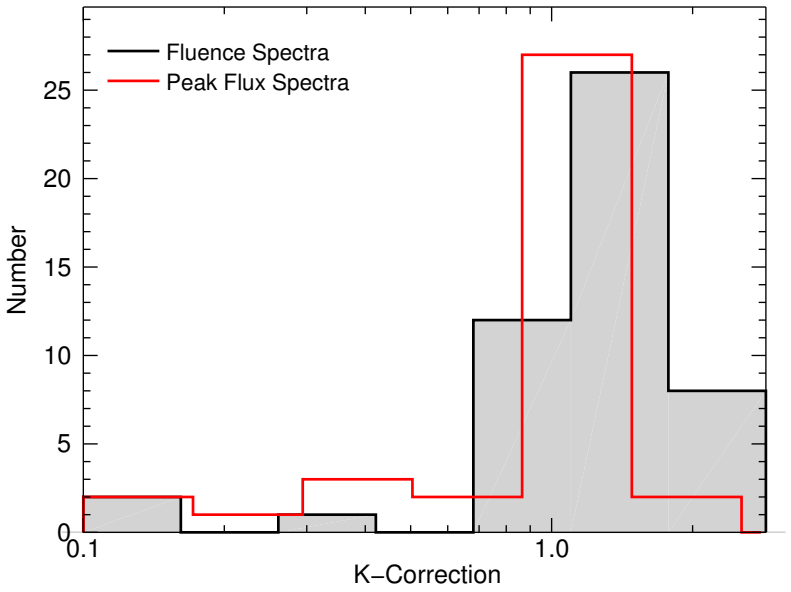

Figure 8.2: Histograms of the K-correction for 50 GRBs with fluence spectra and 37 GRBs with peak flux spectra. The first bin in each histogram contains values less than 0.1.

full calculation. Figure 8.1 displays this behavior in a contour map of the K-correction as a function of the comoving energy band for GRB 090926A ($z \approx 2.11$), best fit by a Band function. For the purposes of this dissertation, I will assume an approximation to the bolometric comoving bandpass as 1 keV–10 MeV, and distributions of K-correction values calculated for this energy band are shown in Figure 8.2 for 50 GRBs with fluence spectra and 37 GRBs with peak flux spectra. The corresponding K-correction values and the observed bandpasses are shown in Table A.1.

8.2 Using GRBs for Cosmology

An important point to note is that many of the previous calibrations of the GRB luminosity relations are dependent on cosmology. Alternatively, when studying cosmology with SNe Ia, this problem is circumvented by calibrating the relations using a sample of SNe Ia at low redshift, where the cosmological dependence of the luminosity is negligible, as can be seen in Figure 7.2. It is difficult to carry out a similar procedure with long GRBs since the observed rate drops off rapidly at low redshifts, and there are a number of cases of nearby GRBs with largely different properties compared to more distant GRBs, indicating that nearby GRBs may be intrinsically different (e.g. GRB 980425, GRB 031203 [125, 166–168]). The GRB relations presented in the previous section are each calibrated assuming a particular model, usually the ΛCDM model. For GRBs to be useful to investigate cosmology, the GRB relations need to be calibrated in a model-independent way, or else a circularity problem develops in that the cosmological investigation is contaminated by the cosmological model that is assumed by the correlations. There are a number of different approaches that have been attempted. The central requirement is that a simultaneous fit of the calibration parameters as well as the cosmology must be made. Usually the scatter of the data about the best-fit relation line and Hubble diagram is considered as a figure of merit. There have been efforts to use Markov Chain Monte Carlo to perform the simultaneous fitting [169] and other Bayesian methods to circumvent the circularity problem [170]. An extensive investigation by Schaefer [120] compared the Hubble diagram that was calibrated with 37 bursts at $z < 2$ to the

Hubble diagram with data from 69 GRBs at mixed redshift to show that the results from fits to the GRB Hubble diagram calibrated with the hybrid sample are robust. The circularity problem cannot be completely solved by means of a statistical approach, since a particular cosmological model is required as a prior. The parameters of the calibrations are still dependent and coupled to the cosmological parameters. The circularity problem can only be avoided in two cases [171]: through a physical interpretation of the calibration relations that would dictate the slope of the relation independent of cosmology or through the use of several low-redshift GRBs that are observably typical of GRBs at larger redshift. Instead of using extremely low-redshift GRBs for calibration, it has been proposed that using GRBs with redshifts at a small dispersion about a fiducial redshift would provide a similar solution [172, 173].

Because of the lack of low-redshift GRBs, the Hubble diagram method used in SN Ia cosmology is different from the methods used in GRB luminosity relations. In SN Ia cosmology the distance of nearby SNe Ia can be obtained by measuring Cepheid variables in the same galaxy as well as other galactic distance relations. In this case, Cepheid variables are used as the first rung of the cosmological distance ladder, and the SNe Ia are the next rung, as they depend on Cepheid variables to "anchor" the distance relation. Because of the tight correlation of the SN Ia Hubble diagram, distances to any SN Ia can be inferred by interpolating from the SN Ia data. Additionally, the distance moduli of SNe Ia are cosmologically model-independent and are obtained from observation. Type Ia Supernovae can then behave as the anchor for GRB calibrations, such that the GRB relations are calibrated in a model-independent way [174]. Furthermore, if the calibrated GRB relations do not evolve

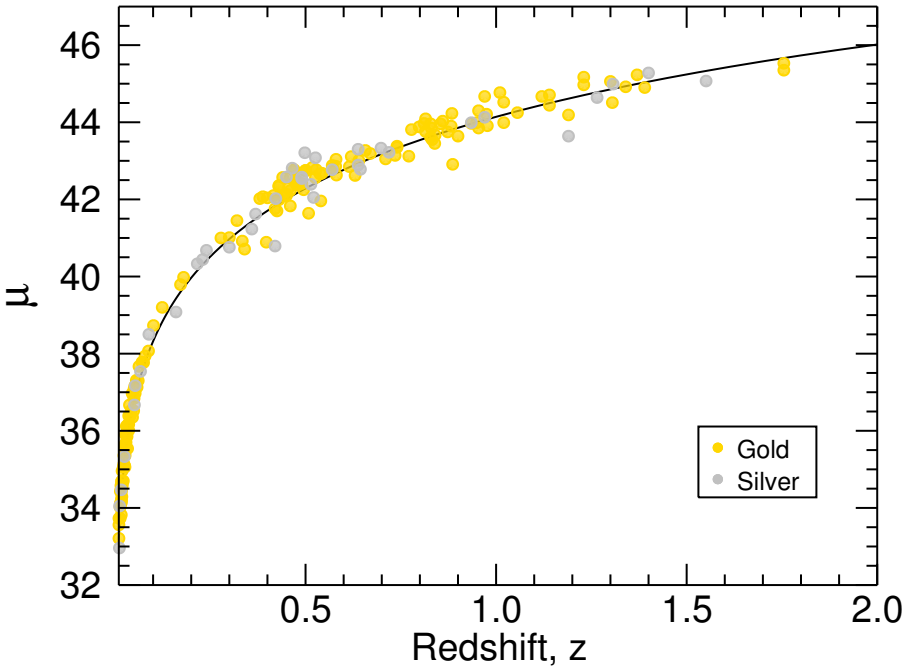

Figure 8.3: Hubble diagram of 206 SN Ia with measured redshift and distance modulus, μ. The best fit line is concordant cosmology.

over redshift, then the standard Hubble diagram method can be used to constrain cosmological parameters at high redshift. There exists a comprehensive list of of SN Ia redshifts and corresponding distance moduli that can be used to create a SN Ia Hubble diagram [153, 154]. The list constitutes 206 SNe Ia and is separated into two quality classes, gold and silver, based on the the quality of the observations. Figure 8.3 shows the Hubble diagram of the 168 SNe Ia in the gold sample and 38 SNe Ia in the silver sample. The SNe Ia in the combined samples range from $z = 0.0104$ to $z = 1.755$. The distance modulus for each SN was obtained by lightcurve template fitting as is usual for SN to produce a cosmologically independent estimate. Since there is significant overlap into the natural GRB redshift range $z > 0.5$, the SN Ia Hubble diagram can

be used to anchor the distance moduli of GRBs. The distance modulus for GRBs is a function of the luminosity distance, which from Equation 7.22 is dependent on the bolometric flux and luminosity, and is represented by Equation 7.25. This allows the luminosity distance to be represented as a distance modulus on the same scale as optical magnitudes of nearby sources such as galaxies and SNe. Significant coverage of the SN Ia Hubble diagram up to $z = 1.5$ indicates that the distance modulus for GRBs with $z < 1.5$ can be determined. Instead of using the best fit line to the data to predict the distance modulus of a GRB with a given redshift, a linear interpolation method is used such that the distance modulus for each GRB, $\mu(z'_i)$, can be determined by

$$\mu(z'_i) = \mu(z_{i-1}) + (z'_i - z_{i-1})\frac{\mu(z_{i+1}) - \mu(z_{i-1})}{z_{i+1} - z_{i-1}}, \tag{8.4}$$

where each GRB redshift, z'_i, is bracketed by the closest SN redshifts, z_{i-1} and z_{i+1}. The case where $z'_i = z_{i-1} = z_{i+1}$, results in exactly $\mu(z'_i) = \mu(z)$. This method produces accurate model-independent estimates of the distance moduli for GRBs in the SN Ia range. Since linear interpolation is approximate, it is important to include the uncertainty from the interpolation method in the uncertainty of the GRB distance modulus. The uncertainty, σ_μ can be calculated by

$$\sigma^2_{\mu'_i} = \left(\frac{z_{i+1} - z'_i}{z_{i+1} - z_{i-1}}\right)^2 \sigma^2_{\mu_{i-1}} + \left(\frac{z'_i - z_{i-1}}{z_{i+1} - z_{i-1}}\right)^2 \sigma^2_{\mu_{i+1}}, \tag{8.5}$$

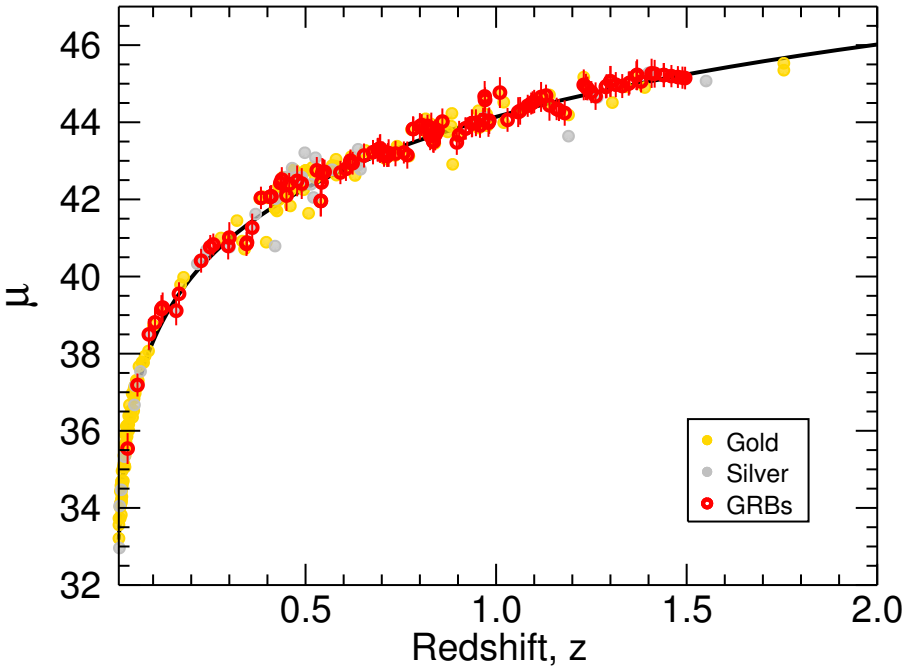

Figure 8.4: Hubble diagram of 119 GRBs at $z < 1.5$ by interpolating the SN Ia Hubble diagram.

where $\sigma^2_{\mu_{i-1}}$ and $\sigma^2_{\mu_{i+1}}$ are the uncertainty of the distance moduli of the corresponding nearest bracketing SN redshifts. By Equation 8.4 and Equation 8.5 the distance moduli of GRBs with $z < 1.5$ can be determined. Figure 8.4 shows the distance moduli of 119 GRBs with redshifts in the optimal range compared to the SNe sample. Although there exists two SNe Ia that surpass $z = 1.5$, the paucity of SNe Ia with redshifts above the set limit will cause the uncertainty in the interpolation to increase.

Using only GRBs in the $z < 1.5$ range, the interpolated distance moduli can be used to calibrate the various correlations. The additional assumption that is required to apply GRBs with $z > 1.5$ is that the correlations do not change with redshift. In

the case of the Ghirlanda relation, 9 GRBs satisfy the redshift requirement as well as the requirement that the time-integrated spectrum is well-modeled and the afterglow jet break time is inferred. For each GRB, the jet opening angle is determined by the jet break time and the estimated circumburst density. The efficiency of the process in converting the kinetic energy of the blast wave into radiation is assumed by 20% for all GRBs, which is consistent with previous estimates. Note that from Equation 3.1 the efficiency and circumburst density are only minor terms in the calculate of the jet angle, as the jet angle calculation is dominated primarily by the determination of the jet break time and the redshift. Instead of assuming a concordant cosmological model as is customary, the interpolated GRB distance modulus is converted to a luminosity distance for use in the calculation of both the jet angle and the collimation-corrected energy. Table 8.1 displays the characteristics needed to calculate the jet opening angle. Note that only the 9 GRBs with $z < 1.5$ are used. Figure 8.5 shows the E_p–E_γ correlation for the 9 GRBs used and includes the best fit line. It is important to note that the best fit line is no longer dependent on choosing a cosmological model, since the distance moduli are now considered absolute distance measurements. The best fit equation is

$$E_p(1+z) = 415.8 \pm 22.1 \left(\frac{E_\gamma}{10^{51}\ \mathrm{erg}} \right)^{0.54 \pm 0.02} \ \mathrm{keV} \tag{8.6}$$

with a χ^2 of 19.8 for 7 degrees of freedom. The relation can be inverted such that the jet angle can be found for a given redshift, E_p, and fluence. Note that this will only

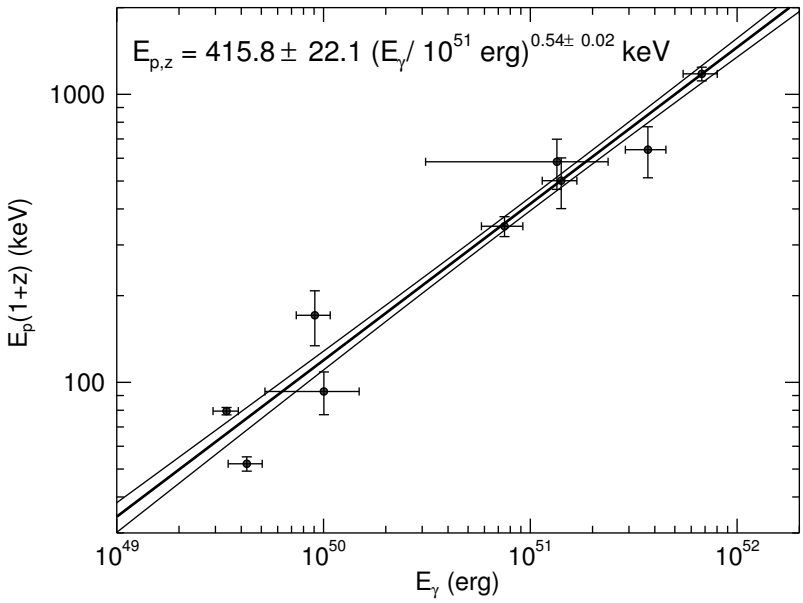

Figure 8.5: The rest-frame E_p–E_γ correlation for 9 GRBs with $z < 1.5$ and known distance modulus. The best fit line and 1σ contours are shown, and the χ^2 is 19.8 for 7 degrees of freedom.

Table 8.1: GRB parameters for the calculation of jet opening angles

GRB	z	t_j (days)	n_p (cm^{-3})	S_γ ($\times 10^{-6}$ erg cm^{-2})	k
970508	0.84 [86]	25.0 [45]	0.75 [134]	3.61±0.30	1.48±0.07
970828	0.96 [175]	2.20 [175]	0.01 [45]	96.0±9.00	1.16±0.87
980703	0.97 [176]	7.50 [177]	1.0 [45]	39.8±0.89	1.95±0.02
990123	1.60 [178]	2.04 [178]	0.002 [134]	274±0.92	0.93±0.02
990510	1.62 [179]	1.20 [180]	0.29 [134]	24.0±0.40	1.54±0.03
990705	0.84 [181]	1.00 [182]	3.00 [182]	75.0±8.00	1.81±0.22
990712	0.43 [179]	1.60 [42]	3.00 [42]	6.5±3.0	2.92±0.09
991216	1.02 [183]	1.20 [184]	4.7 [134]	174±0.53	1.60±0.001
030329	0.17 [185]	0.55 [186]	1.00 [186]	110±1.0	2.64±0.07
090323	3.57 [187]	17.6 [137]	3.30 [137]	178±5.49	1.33±0.01
090328	0.74 [188]	6.40 [137]	2460 [137]	58.8±1.37	1.15±0.00
090618	0.54 [189]	0.60 [141]	1.0 [141]	256±1.98	1.26±0.00
090902B	1.82 [190]	6.20 [137]	5.6×10^{-4} [137]	192±0.39	0.97±0.00
090926A	2.11 [191]	9.00 [137]	75.0 [137]	245±7.23	0.99±0.03
091127	0.49 [192]	0.38 [142]	1.0 [143]	26.2±0.70	1.63±0.05

be useful for GRBs at $z < 1.5$, otherwise the jet angle with also be a function of the assumed cosmology.

For the few GRBs with inferred jet breaks and jet angles, only 5 GRBs have sufficient time-resolved modeling at the peak flux of the burst. Therefore, a sample of 16 GRBs–3 detected by BATSE and 13 detected by GBM–with known redshift $z < 1.5$, was compiled (shown in Table 8.2) and the jet opening angle was estimated for each GRB by the aforementioned method. The collimation-corrected peak luminosity, L_γ was then calculated using the interpolated distance moduli and the peak flux. Figure 8.6 shows the E_p–L_γ correlation for the 16 GRBs. The best fit line is found to be

$$E_p(1+z) = 1101.4 \pm 64.0 \left(\frac{L_\gamma}{10^{51} \text{ erg s}^{-1}} \right)^{0.62 \pm +0.03} \text{ keV} \tag{8.7}$$

with a χ^2 of 176 for 14 degrees of freedom. The scatter is more apparent than in the E_p–E_γ relation, although it may be due to the increase in the number of GRBs in the E_p–L_γ correlation.

The correlation between the E_p at the peak flux and the peak L_{iso}, known as the Yonetoku relation, was discovered as an improvement to the Amati relation and a more direct luminosity relation. The E_p value at the peak flux of the burst, usually defined as the observed peak count rate or the model-dependent peak photon flux, is shown to correlate with the peak luminosity of the GRB. Figure 8.7 shows the E_p–L_{iso} correlation for 16 GRBs with $z < 1.5$. The best fit line is found to be

$$E_p(1+z) = 222.4 \pm 12.3 \left(\frac{L_{iso}}{10^{52} \text{ erg s}^{-1}} \right)^{0.73 \pm 0.04} \text{ keV} \tag{8.8}$$

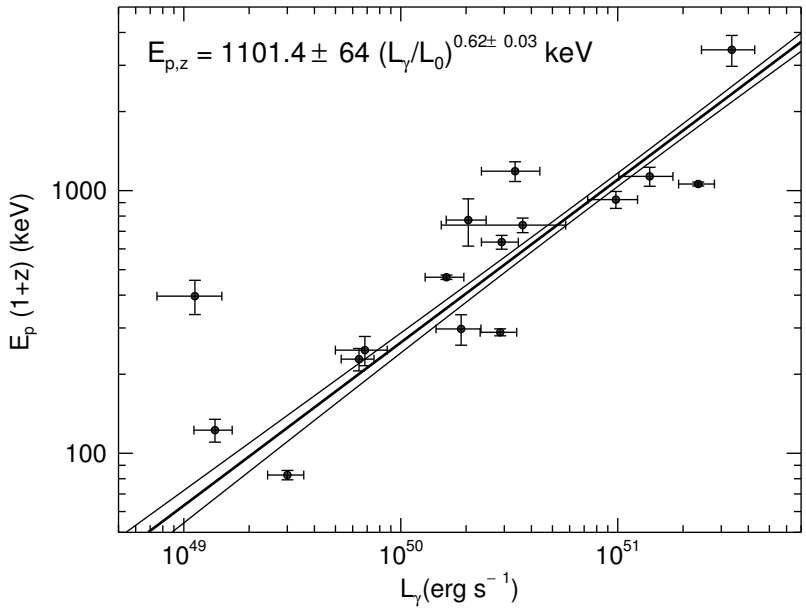

Figure 8.6: The rest-frame E_p–L_γ correlation for 16 GRBs with $z < 1.5$ and known distance modulus. The beaming fraction for each GRB was determined by inverting the E_p–E_γ correlation and solving for f_b. The best fit line and 1σ contours are shown, and the χ^2 is 176 for 14 degrees of freedom.

with a χ^2 of 300 for 21 degrees of freedom.

Perhaps the first complete correlation to be discovered to result in a proposed luminosity relation was the E_p–E_{iso} Amati relation. This was primarily due to the early exploration of the time-integrated spectrum, since time-resolved spectra can be more difficult to constrain. The Amati relation, however, is more susceptible to intrinsic artifacts than the other luminosity relations discussed and generally suffers from a larger dispersion in both rest-frame E_p and E_{iso}. Shown in Figure 8.8 is the E_p–E_{iso} correlation for 23 GRBs, 3 detected by BATSE and 20 detected by GBM,

Table 8.2: Parameters of GRBs used in E_p–L_γ

GRB	z	Fluence E_p (keV)	Peak E_p (keV)	S_γ ($\times 10^{-6}$ erg cm^{-2})	F_γ ($\times 10^{-6}$ erg s^{-1} cm^{-2})
980703	0.97	902.4±22.3	392.1±80.1	39.84±0.89	1.41±0.06
990506	1.30	288.7±11.1	203.5±3.9	168.53±1.02	5.54±0.25
991216	1.02	162.8±31.9	524.5±9.1	174.71±0.53	51.39±1.68
080916A	0.69	167.8±19.2	234.6±35.0	40.94±5.26	0.83±0.10
090328	0.74	349.5±9.5	531.1±39.4	54.21±0.66	4.17±0.12
090424	0.54	110.2±14.0	187.5±5.7	52.89±2.15	11.06±0.14
090618	0.54	144.4±19.2	413.5±25.0	24.96±0.82	13.28±0.25
090926B	1.24	119.4±26.1	110.2±14.0	8.70±0.40	0.39±0.09
091003	0.90	133.8±10.7	388.9±24.8	63.35±6.55	8.40±0.16
091127	0.49	92.8±9.1	55.5±2.3	26.16±0.70	5.70±0.09
091208B	1.06	158.8±14.7	144.4±19.2	8.16±0.29	2.75±0.11
100414A	1.37	281.4±33.0	478.0±39.7	124.92±5.67	5.30±0.14
100724A	1.29	1425.5±191.8	517.7±44.7	613.80±15.40	17.80±1.57
100814A	1.44	180.9±21.5	119.4±26.1	24.32±3.89	3.50±1.05
100816A	0.81	180.9±21.5	133.8±10.7	5.54±0.87	2.77±0.45
101219B	0.55	180.9±21.5	85.2±20.6	4.06±0.32	0.23±0.06
110213A	1.46	180.9±21.5	92.8±9.1	14.12±0.43	1.31±0.13
111228A	0.48	180.9±21.5	82.7±8.3	14.11±0.28	1.56±0.08
120711A	1.41	180.9±21.5	1425.5±191.8	203.69±1.04	7.81±0.17

with $z < 1.5$. The best-fit line is found to be

$$E_p(1+z) = 63.2 \pm 3.0 \left(\frac{E_{iso}}{10^{52}\ \mathrm{erg}} \right)^{0.65\pm0.02} \ \mathrm{keV} \tag{8.9}$$

with a χ^2 of 849 for 21 degrees of freedom. The reduced χ^2 is much larger than what was found for the other relations, indicating a significant amount of scatter. Because of its aforementioned susceptibility to mathematical artifacts and the large intrinsic scatter, the Amati relation is not a reliable luminosity relation, and cannot be adequately used to investigate the GRB in the rest frame nor is it adequate to be used to study cosmology.

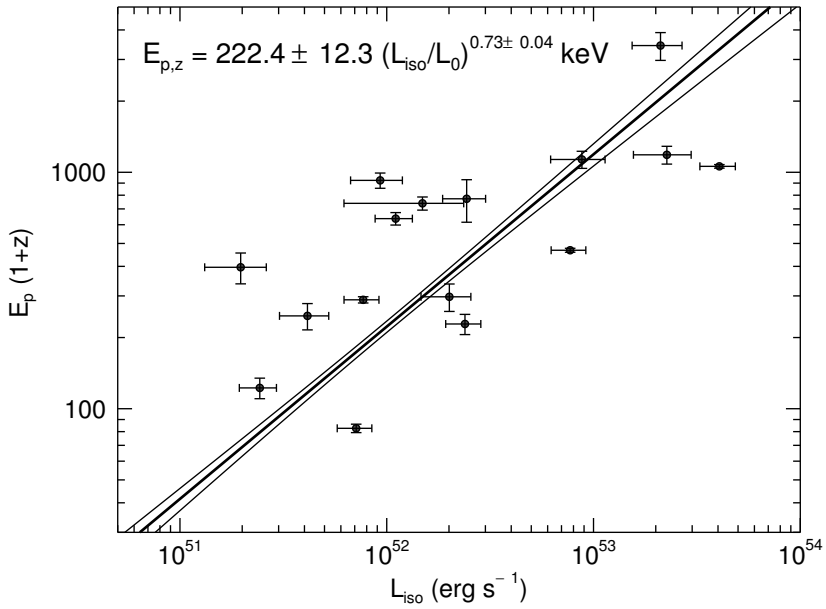

Figure 8.7: The rest-frame E_p–L_{iso} correlation for 16 GRBs with $z < 1.5$ and known distance modulus. The best fit line and 1σ contours are shown, and the χ^2 is 300 for 21 degrees of freedom.

Each of the four relations discussed attempt to use E_p as a luminosity indicator. The Amati relation contains the most scatter and is the least usable as a luminosity relation, therefore I will not be considering it for the following methods. The E_p–E_γ and E_p–L_γ relations have considerably less scatter than their isotropic counterparts, indicating that the jet opening angle is an important property of each GRB that is different from burst to burst. Therefore, to have a complete picture of GRBs and their use to study cosmology, a measurement of the jet opening angle is a requirement. The difficulty with this requirement is that, although there are thousands of known GRBs with observed spectra, the number of GRBs with known redshift is a small subset of all detected GRBs. And due to the difficulties in observing a jet break in

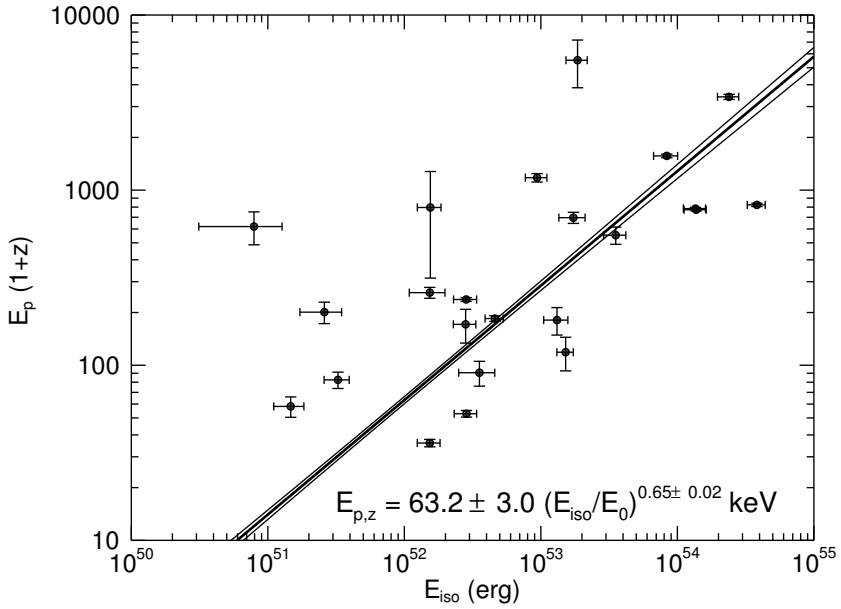

Figure 8.8: The rest-frame E_p–E_{iso} correlation for 23 GRBs with $z < 1.5$ and known distance modulus. The best fit line and 1σ contours are shown, and the χ^2 is 849 for 21 degrees of freedom.

the optical afterglow and the requirement of a redshift, the number of GRBs with inferred jet opening angles are a small subset of the GRBs with known redshift. This results in approximately two orders of magnitude difference between the number of observed GRBs and the number of GRBs with inferred jet opening angle. This is one main reason why the GRB community has been slow to determine both the emission mechanism and the use of GRBs to cosmology.

I have already discussed using the Ghirlanda relation to estimate the jet opening angle for GRBs with known redshift, however between BATSE and GBM this results in ∼50 GRBs with consistently measured spectra. Solid cosmological results with SNe Ia required ∼100-200 SNe with known redshift, and the method used to

convert SNe Ia into standard candles is more accurate than any corresponding method for GRBs. In addition, GRBs cover a much larger range of redshift than SNe, therefore a large number of GRBs are required to provide comparable results to that from SNe Ia at larger redshift. It has been indicated that the E_p–L_{iso} relation can be used to estimate the redshift for GRBs without known redshift. Indeed, I have shown that pseudo-redshift estimated from the Yonetoku relation are within 0.3 orders of magnitude of the true value for the sample of 23 GRBs from BATSE and GBM as well as the GRBs from Yonetoku et al. [119], and the pseudo-redshifts do not appear to suffer from a truncation effect. Therefore, the Yonetoku relation can be used to produce redshift estimates for a large number of GRBs up to $z \sim 10$, albeit with increasing uncertainty at larger redshifts.

Using the Yonetoku relation to estimate the redshift and then using the estimated redshift and the Ghirlanda relation to estimate the jet opening angle solves two unknown parameters for the burst. The final unknown quantity for GRBs at $z > 1.5$ is the distance modulus. Ideally, the final relation discussed, the E_p–L_γ relation, could be used to estimate the distance modulus given the estimated redshift and jet opening angle. However, in the estimation of the redshift and jet angle using the Yonetoku and Ghirlanda relations respectively, a cosmological model must be assumed. In fact, during the estimation of the redshift, the luminosity distance and the redshift must be numerically separated so that a particular redshift estimate can only exist with a particular luminosity distance defined by the cosmological model. This simultaneous determination of redshift and luminosity can be considered a theoretical estimate based on the theoretical cosmological model in use. The application of the E_p–L_γ

relation can solve for the luminosity distance given a particular GRB peak spectrum, estimated redshift, and estimated jet opening angle. This luminosity distance (and the resulting distance modulus) can then be considered an observed distance modulus based of the E_p–L_γ correlation. For each set of cosmological parameters the observed distance moduli for the GRBs can be compared to the theoretical distance moduli for the given cosmology, and a goodness of fit can be determined. Since the luminosity relations were calibrated by GRBs at $z < 1.5$, the relation parameters are all independent of cosmology, and the remaining required assumption is that the relations hold over a large redshift range at least up to $z \sim 10$.

The expectation is that the luminosity relations are in general constant over redshift since they are based on the amount of relativistic beaming, energy conservation of the shocked outflow, and the light travel time [120]. While factors like the metallicity of the progenitor and the density of the circumburst medium may be orders of magnitude different from burst to burst, the light travel time and amount of relativistic beaming is unaffected by these differences. The physical beaming angle for GRBs may change drastically as well from burst to burst, but there is no reason to expect that bursts at different redshift will tend to have different physical beaming angles. A change in metallicity might affect the intrinsic luminosity, but the intrinsic spectrum and corresponding E_p would be affected as well. Therefore, there exists few physical mechanisms that would cause the luminosity relations to significantly change over redshift. Then, if the assumption that the luminosity relations are

constant holds true, the cosmological model that provides the best agreement between the theoretical and observed distance moduli is the best fitting cosmological model to GRBs.

8.3 Determination of Redshift, Distance Modulus and Jet Opening Angle

The method developed by Schaefer [120] to produce a GRB Hubble diagram was to take several different luminosity relations and solve the luminosity distance for each one. The weighted average of the distance modulus from each each relation would then be computed to produce the final distance modulus for each GRB. This method allowed the estimation of the distance modulus given that the redshift was already known as well as certain observational properties. A significant problem in constructing a usable GRB Hubble diagram is that currently only a small fraction of GRBs have known redshifts. An even smaller fraction of GRBs with known redshift have a complete set of observed properties that are required to compute the distance modulus. For example, the redshifts for GRBs detected by *Swift* are far more likely to be determined that the redshifts of GRBs detected by GBM alone. Consequentially, it is unlikely that the required E_p for a GRB will ever be known if it is observed only by *Swift* due to its low-energy bandpass. Alternatively, two of the largest and most comprehensive samples of observed GRB properties are contained in the BATSE and GBM Catalogs. As far as studying detailed cosmology, though, the catalogs are regarded as irrelevant since only $\sim$50 out of the combined $\sim$3700 observed GRBs have known redshift. Certainly if the redshift were known for a significant fraction of these events, the catalogs of observed properties would be powerful as cosmological tools.

For many GRBs the redshift, distance modulus, and jet opening angle represent three unknown quantities that are required for studying their physical nature as well as using them as cosmological tools. I have previously discussed three luminosity relations that can each be used to convert the E_p into a luminosity indicator. Each of the luminosity relations were calibrated with GRBs of known redshift and distance moduli and the resulting power law parameters are cosmologically model-independent. If the correlations are assumed to be constant with redshift, then the correlations should should be applicable for GRBs of any redshift. Making this assumption, we now have three unknown variables, and the three relations can be viewed as three equations for which a particular set of redshift, distance modulus, and jet opening angle satisfy. Although each relation is a power law and is nonlinear, transforming to logarithmic space simplifies the problem significantly. If the K-correction for each relation is ignored ($K \approx 1.0$), then the problem can be posed as a system of linear equations in logarithmic space. The equations can be readily solved by rearranging the relations so that the unknowns are on one side and the coefficients of each unknown fill the coefficient matrix $\mathbf{A}$, while the constant terms (no dependence on z, μ, or θ) fill the constant vector $\mathbf{b}$. The linear set of equations is then represented as $\mathbf{Ax}=\mathbf{b}$, where $\mathbf{x}$ is the solution vector. An efficient algorithm to solve this matrix equation is Lower-Upper (LU) decomposition, which is a modified form of Gaussian elimination. The resulting solution vector will be the logarithmic solutions to the equations, which can then be transformed back into linear space, and the solutions recovered (details shown in Appendix D). If, however, the K-correction is included in the calculation, the system will be nonlinear even in logarithmic space. In this

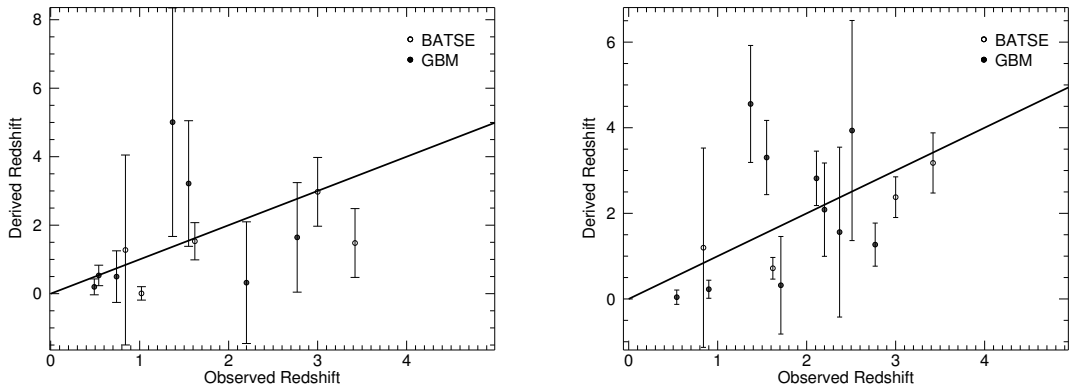

(a) Without K-correction

(b) With K-correction

Figure 8.9: Derived redshift compared to the true observed redshift

case, the solutions to the equations can be attained by linearizing them as much as possible by transforming them into logarithmic space and grouping the unknowns together, similar to the linear case. Then an algorithm such as Newton-Raphson can be generalized to find the root of all three equations simultaneously by calculating a new set of K-corrections for each step of the algorithm. Obviously including the K-correction makes the process of finding a solution less efficient, however, it increases the accuracy of the solution since the relations were each calibrated with K-corrected energies and luminosities. The uncertainties for z, μ, and θ are then a combination of the uncertainties resulting from each relation. As a check, a comparison of the estimated redshift and the observed true redshift is shown in Figure 8.9.

Only those GRBs that lie sufficiently close to each best-fit luminosity relation line will produce acceptable estimates. Various effects can cause significant dispersion around the best fit relations. For example, the line-of-sight viewing angle with respect

to the center of the GRB jet will certainly be different. If the viewing angle is large, then the flux and fluence will decrease, and so will the observed luminosity [145]. Similarly, the bulk Lorentz factor will vary for different bursts which will also change the observed E_p and luminosity. The real distribution of Γ is unknown, but if the distribution is broad ($1\sigma \gtrsim$ an order of magnitude) then the correlations could be significantly affected since the comoving E_p, $E'_p \propto E_p(1+z)/\Gamma$, and the comoving luminosity, $L'_{iso} \propto L_{iso}/\Gamma^2$ [193,194]. Figure 8.10 shows the derived redshift, distance modulus, and jet opening angle. For a number of GRBs, the redshift, distance modulus, and opening angle cannot be accurately estimated due to the fact that they likely exist far away from the best fit correlations.

The Schaefer method is efficient at estimating the distance modulus for GRBs when the redshift is already known. The method I have described is more predictive, although not dissimilar from the Schaefer method. Instead of using multiple luminosity relations to determine a single unknown parameters in a small sample, we can use multiple relations to determine several unknown parameters for a much larger sample. The method I have presented uses only three relations to solve for three unknown parameters, however, the method can be generalized for use with other luminosity relations. For example, the parameters could be estimated as described using the E_p–E_γ, E_p–L_{iso}, and E_p–L_γ relations, and another estimate could be produced by another set of luminosity indicators. In the spirit of the Schaefer method, the resulting parameters could then be averaged to produce a final set of parameters for each GRB. In the following analysis, I choose to use only the three luminosity relations mentioned and leave the improvements in the method for future study.

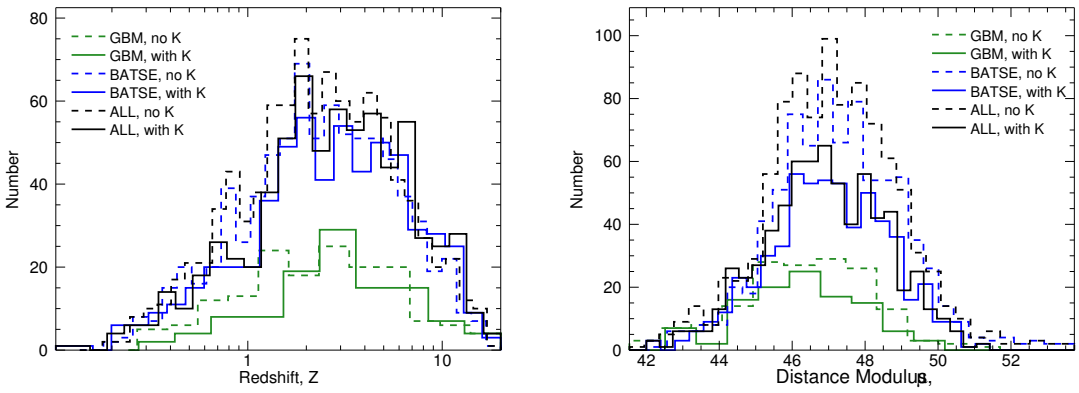

(a) (b)

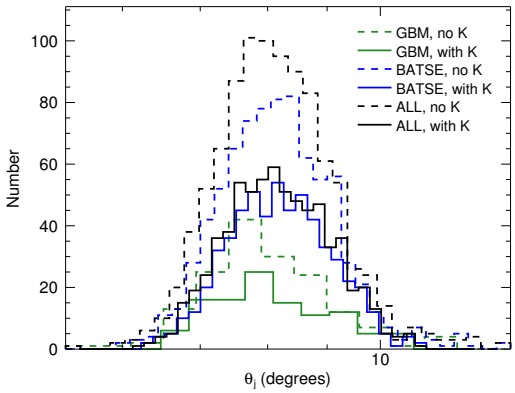

(c)

Figure 8.10: Derived redshift, distance modulus and jet opening angle for 161 (112) GBM GRBs without (with) K-correction and 797 (579) BATSE GRBs without (with) K-correction.

8.4 Methodology for Fitting the Hubble Diagram

Using the SN Ia sample as an anchor to the GRB Hubble diagram as well as the $z < 1.5$ GRBs, the redshift and distance modulus estimated for GBM and BATSE GRBs can be added to the Hubble diagram. This results in a total of 7 samples: the calibration sample of SNe Ia and $z < 1.5$ GRBs, the GBM sample calculated with and without the K-correction (hereafter GBM silver and GBM gold respectively), the BATSE sample calculated with and without the K-correction (hereafter BATSE silver and BATSE gold respectively), and the GBM + BATSE sample calculated with and without the K-correction (hereafter ALL silver and ALL gold respectively). The inclusion of the K-correction in some of the samples is intended to investigate if the K-correction provides a noticeable improvement or change in results, since the nonlinear solution presented in Section 8.3 requires a more costly algorithm to calculate. For the derived redshifts and distance moduli, I make a quality cut such that the relative uncertainty on either quantity is no larger than unity. This removes most GRBs at $z < 1$, however, since the Hubble diagram is known out to $z \approx 1.5$, this is not a problem. The calibration sample contains 168 SNe Ia from the Riess gold sample [153, 154] and 119 GRBs at $z < 1.5$ with μ determined by linear interpolation from the SNe. The GBM silver sample contains 124 GRBs with $z < 20$ and the GBM gold sample contains 45 GRBs $z < 20$. The difference in size between the two samples is due in large part to the quality of the measurements of all spectral parameters. If the high-energy spectral index β is unconstrained, for example, the uncertainty in the K-correction will be large and contributes to the uncertainty in the

redshift and distance modulus. The BATSE silver sample numbers 618 GRBs, while the BATSE gold sample yields 344 GRBs at $z < 20$. The exact derived values and corresponding uncertainties for each GRB in each sample is shown in Appendix E. Each sample will be fully investigated to determine self-consistency and the ideal sample to constrain cosmological parameters. Figure 8.11 shows the GRB Hubble diagrams for GBM and BATSE. Note that the calibration sample at $z < 1.5$ have small relative uncertainties and the derived samples have larger uncertainties and dispersion. The samples including the K-correction have a larger average uncertainty due to the propagation of the uncertainty from the calculation of the K-correction. First, I investigate the joint probability distributions of cosmological parameters with typical concordant assumptions about the universe. Only two parameters will be investigated at a time, while all other parameters will be fixed to concordant values. Taking the parameters Ω_M and Ω_Λ as an example, I set up an evenly spaced grid in parameter space such that the parameter space can be sufficiently sampled. At each grid point the theoretical distance modulus, μ_{th} is calculated for each GRB and is compared to the observed distance modulus μ_{obs}. To determine the goodness-of-fit at each grid point, as well as to determine the most preferred set of parameters and corresponding confidence interval, the χ^2 statistic is computed at each grid point. Because the GRBs with both derived redshift and distance modulus have associated uncertainties, I factor this into the calculation of χ^2 as

$$\chi^2 = \sum_i^N \frac{(\mu_{th,i} - \mu_{obs,i})^2}{\sigma^2_{z_{obs},i} + \sigma^2_{\mu_{obs},i}}, \tag{8.10}$$

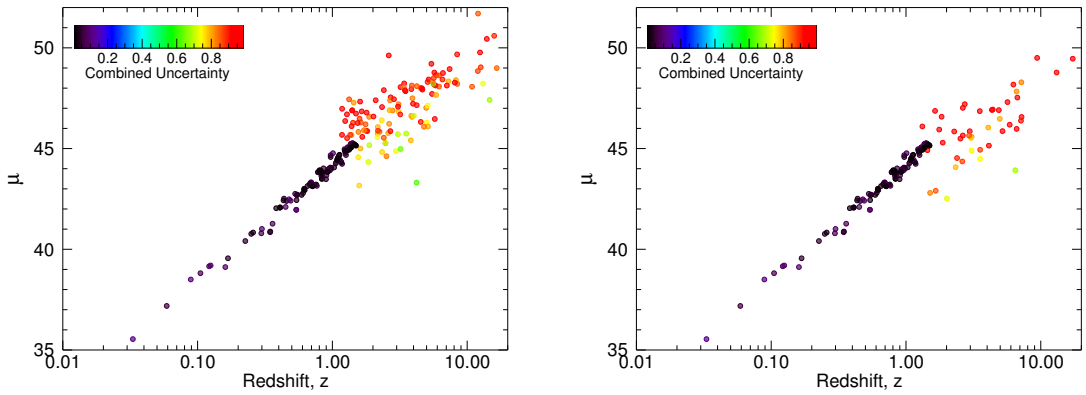

(a) GBM silver

(b) GBM gold

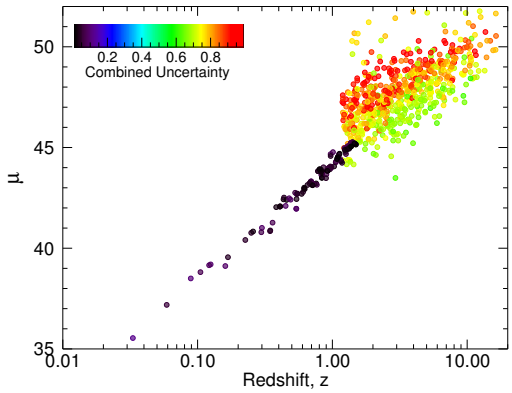

(c) BATSE silver

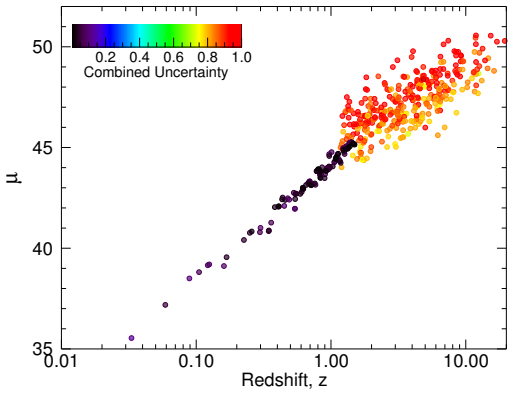

(d) BATSE gold

Figure 8.11: Hubble diagrams for GRBs based on the different samples. The color represents the combined total relative uncertainty.

where the sum is over N GRBs in the sample. The most preferred set of parameters is then indicated by the grid point which produces the minimum χ^2 value, χ^2_{min}, and the confidence interval is determined by $\Delta\chi^2_i = \chi^2_i - \chi^2_{min}$, which is a χ^2 distribution of m degrees of freedom, where m is the number of free parameters. In this case, $m = 2$ and $\Delta\chi^2 = \chi^2(2)$. The 1σ confidence interval, for example, can then simply be computed by determining at which grid points the $\Delta\chi^2$ values exist within

$P \leq 0.68$. A contour map of $\Delta\chi^2$ can then be created to display the joint confidence interval of the parameter space. For display purposes, the contour algorithm uses linear interpolation to determine the values of the $\Delta\chi^2$ map between grid points. In each sample except the calibration sample, the large uncertainty in μ_{obs} and z_{obs} at high redshift will cause $\chi^2/\text{dof} < 1$ indicating that the data are being overfit. To compensate for this effect, each sample is also binned to minimize statistical fluctuations in the data and uncertainties. The binning of the data reduces the resolution of the Hubble diagram, but since the Hubble diagram does not have discernible small scale features and what we want to find is the overall structure and shape, the binning should not oversimplify the Hubble diagram. The number of bins for each sample is calculated as $N_{bins} = \lfloor\sqrt{N}\rfloor$ where N is the total number of bursts in the sample. While allowing a single bin to contain no less than 5 measurements, the binning is performed over the redshifts of the sample and the corresponding distance moduli are assigned to the correct bins. The average of all measurements within each bin is computed and the uncertainty within a bin is $\sigma_{bin} = \sqrt{\sum(\sigma_i^2)/n}$, where n is the number of measurements in the bin. The binned Hubble diagrams are shown in Figure 8.4. There exists a feature at $1 < z < 2$ which is near the threshold set such that the relative uncertainty in the redshift and distance modulus is less than unity. Redshifts near this threshold still have relative uncertainties $\sim$1 which also affects the derived distance modulus. The silver samples appear to consistently track above the Hubble diagrams for the gold sample, which could affect the best fit cosmological parameters.

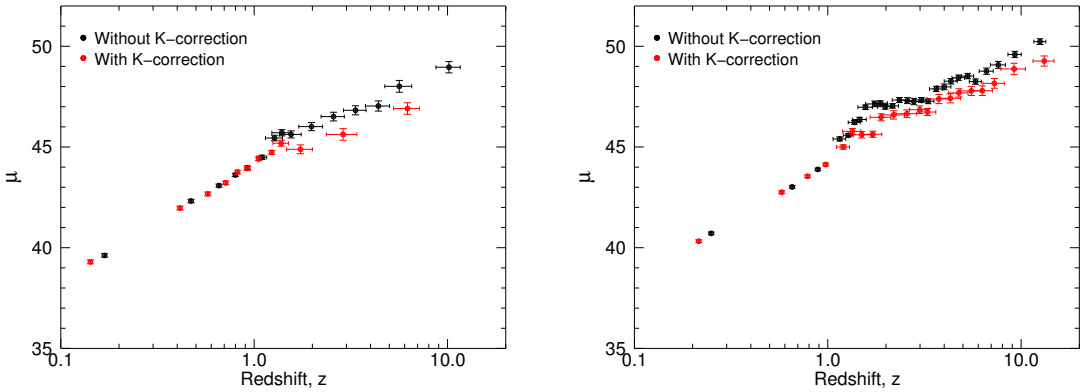

(a) GBM

(b) BATSE

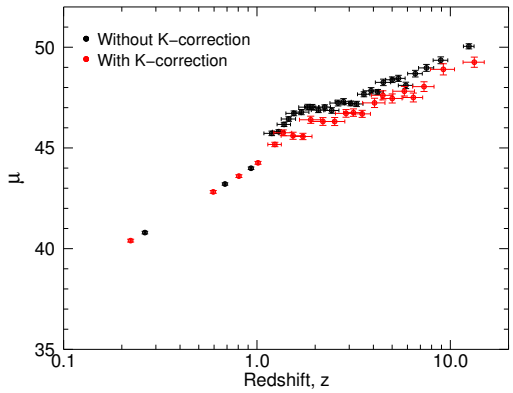

(c) ALL

Figure 8.12: Hubble diagrams for GRBs based on the different samples, binned.

Although the two dimensional χ^2 maps of the parameter space can be useful, several assumptions have been made. Primarily, all parameters except the two being investigated are fixed at particular values. While low-z observations have indicated concordant values for many of these parameters, the GRB Hubble diagram extends to much higher redshift where the values of the parameters may be different from the values found by nearer observations. Therefore, it is important to determine not just the joint probability distribution for only two parameters at a time, but to determine the joint probability distribution of as many parameters as possible simultaneously. With the large sample of GRBs with $z \lesssim 20$ it may be possible to determine the best set of parameters with adequate confidence, thereby ruling out particular cosmological models and determining the evolution of dark energy. To estimate the joint probability distribution of more than two parameters, the $\Delta\chi^2$ map method is no longer an efficient method due to the large parameter space, therefore I investigate the use of a Monte Carlo Markov Chain (MCMC). While the $\Delta\chi^2$ method relies on frequentist statistics, the MCMC is dependent on Bayesian statistics and the likelihood. In general, Bayes' rule states

$$P(M|D) = \frac{P(D|M)\ P(M)}{P(D)} \tag{8.11}$$

where $P(D|M)$ is the probability of the data given the model, known as the likelihood function, $P(M)$ is the probability of the model, known as the prior probability, $P(D)$ is the probability of the data, and the $P(M|D)$ is the probability of the model given the data, known as the posterior probability. In Bayesian statistics, the posterior

probability is the quantity of interest. The prior probability, $P(M)$ is an important quantity to the estimation of $P(M|D)$ since it reflects any prior evidence or preference towards a particular model or set of parameters. The likelihood function estimates the likelihood that the data observed could have been produced by the given model, and it is the core of Bayesian statistics. If the measurement uncertainties are Gaussian distributed, then the general likelihood function is

$$\mathcal{L} = \prod_{i}^{N} \frac{1}{\sqrt{2\pi}\sigma_{D,i}} \exp\left[\frac{-(D_i - M_i)^2}{2\sigma_{D_i}^2}\right]. \tag{8.12}$$

Since the likelihood is usually a product of small individual likelihoods, it is usually preferred to use the log-likelihood:

$$\ln(\mathcal{L}) = -\sum_{i}^{N}\left[\ln(\sqrt{2\pi}) + \ln(\sigma_{D,i}) + \frac{(D_i - M_i)^2}{2\sigma_{D_i}^2}\right]. \tag{8.13}$$

The MCMC is initialized at a starting set of parameters Θ_0. The model is calculated for the Θ_0 and the likelihood $\mathcal{L}_0$ is determined. A new set of parameters are selected Θ_1 randomly based on the values Θ_0 (e.g. a uniform distribution or Gaussian centered on Θ_0), the new model is calculated, and the new likelihood $\mathcal{L}_1$ is determined. The likelihood ratio test is performed to determine the probability that Θ_1 is preferred over Θ_0:

$$\mathcal{R} = \frac{\mathcal{L}_1}{\mathcal{L}_0} = \exp\big(\ln(\mathcal{L}_1) - \ln(\mathcal{L}_0)\big). \tag{8.14}$$

If $\mathcal{R} \geq 1$ then $\mathcal{L}_1$ is preferred over $\mathcal{L}_0$ and Θ_1 is accepted as the next link in the parameter chain. If $\mathcal{R} < 1$ then Θ_1 will only be accepted as the next link in the

chain if a random uniform deviate $0 < u < 1$ satisfies $\mathcal{R} \geq u$. This rule allows the chain to explore the parameter space and prevents the chain from becoming trapped in a local minimum. If Θ_1 is not accepted as the next link of the chain, Θ_0 becomes the next link in the chain, and the process is repeated. Once the MCMC sufficiently explores the parameter space, the resulting Θ_i represent the joint posterior probability distributions, with one artifact. The initialization of the parameters at the beginning of the MCMC leave an artifact in the distributions that is known as "burn-in" that needs to be removed. Once the burn-in is removed, the final normalized histograms of Θ approximate the posterior probability distribution.

Using the described MCMC method on each sample, I produce joint probability density functions for the cosmological parameters. Each MCMC contains 10^5 links, of which the first 10^4 are removed for burn-in. Since I have no preference towards any set of parameters for the cosmological model, the next set of parameters will be chosen based on a uniform deviate centered at the previous set of parameters. The entire parameter space is left unbounded, thereby not biasing the region in which the maximum likelihood could exist. Similar to the $\Delta\chi^2$ map method, the uncertainty from both z_{obs} and μ_{obs} are factored into the calculation of the likelihood. During the MCMC, the chain may encounter parameter states for which the distance modulus of high redshifts cannot be calculated (i.e. bounce or loitering universes). These states are removed from the chain since the data cannot exist in these particular states.

CHAPTER 9

TESTING COSMOLOGY WITH GRBS

Now that the GRB Hubble diagram has been constructed, GRBs together with SNe Ia can be used to study the universe. The distance equations in Section 7.6 allow easy testing of cosmological models with measurements of redshift and distance. Using methods described in Section 8.4, I test several possible cosmological models and attempt to provide adequate constraints on the cosmological parameters. A general inspection of the joint probability distributions for a number of two-parameter configurations will be discussed in Section 9.1, and a more detailed inspection of the ability of the data to constrain particular models using Bayesian statistics will be discussed in Section 9.2.

9.1 Results from χ^2 Mapping

The χ^2 mapping method is widely used to investigate the joint probability distributions of two-parameter configurations. For models with more than two parameters, assumptions must be made to fix the value of the parameters not being investigated. In this section, unless otherwise noted, I assume $H_0 = 70$, which is in good agreement with the current best constrained results. In addition, unless the

otherwise noted, if Ω_M and/or Ω_Λ are not being investigated, then they are fixed to values of $\Omega_M = 0.27$ and $\Omega_\Lambda = 0.73$ respectively, which is in excellent agreement with the current best constrained results.

9.1.1 Ω_M–Ω_Λ

One of the primary goals of cosmology is to accurately determine the mass density Ω_M and dark energy density Ω_Λ of the universe. The two quantities define the curvature of the universe, and therefore determine the origin and destination of the universe. Starting with the calibration sample of SN Ia + GRBs and using the χ^2 map method, the joint confidence intervals were computed for a $w = -1$ cosmological constant, and the map is shown in Figure 9.1. The corresponding 1σ, 2σ, and 3σ contours are shown for both the unbinned and binned data. The $\Omega_k = 1 - \Omega_M + \Omega_\Lambda = 0$ line shows the curvature of the universe and the calibration sample shows $\sim 2\sigma$ agreement with a flat universe. The area above the line defining a loitering or bounce universe is invalid due to the fact that objects with $z > 1.5$ could not exist in such a universe. The gray region around the loitering line defines the area where the theoretical luminosity distance could not be calculated for some of the high-z GRBs due to the fact that a universe defined by those particular Ω_M and Ω_Λ values could not extend to such high redshift. Lines denoting the deceleration parameter show the regions in which the universe is decelerating or accelerating in expansion. The best fitting values at $\Omega_M = 0.34^{+0.08}_{-0.10}$, $\Omega_\Lambda = 1.15^{+0.16}_{-0.20}$ for the individual data points and $\Omega_M = 0.37^{+0.09}_{-0.11}$, $\Omega_\Lambda = 1.13^{+0.18}_{-0.24}$ for the binned data, results in $q_0 \approx -1$. Although the Ω_Λ values are larger than the standard model, they are in good agreement with

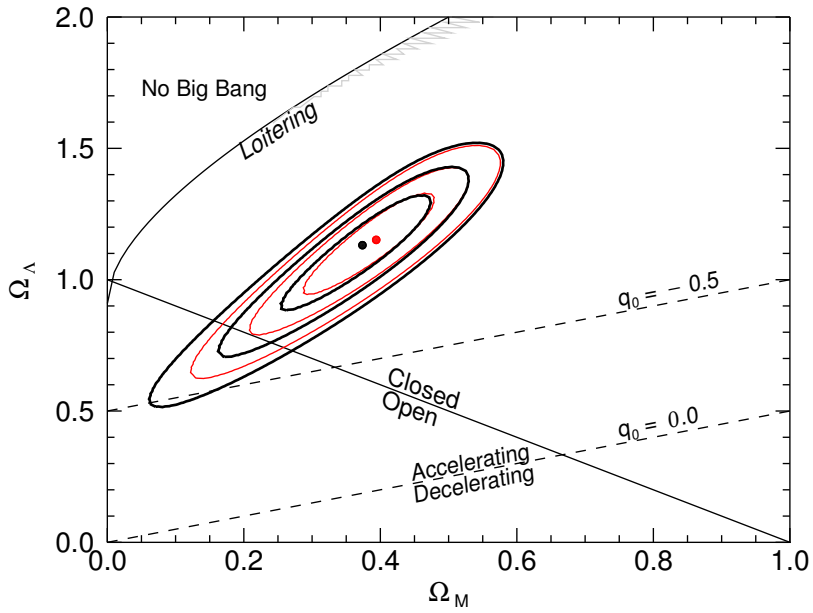

Figure 9.1: The joint probability distributions of Ω_M–Ω_Λ from the calibration sample. The corresponding 1σ, 2σ, and 3σ contours are shown. The best-fit parameters are $\Omega_M = 0.34^{+0.08}_{-0.10}$, $\Omega_\Lambda = 1.15^{+0.16}_{-0.20}$ with $\chi^2/\mathrm{dof} = 113/286$ for the raw data (red) and $\Omega_M = 0.37^{+0.09}_{-0.11}$, $\Omega_\Lambda = 1.13^{+0.18}_{-0.24}$ with $\chi^2/\mathrm{dof} = 18/14$ for the binned data (black).

Riess et al. [153, 154] and SN Ia results in general. The same method was performed on each of the six samples to investigate the ability of the high redshift GRB data to constrain cosmology. The results for the six samples are shown in Figure 9.2. Each sample shows a clear preference to $\Omega_\Lambda > 1$, and the difference between the binned and unbinned data are immediately noticeable. The large uncertainties associated with the unbinned data is prone to over-fitting, where statistical fluctuations likely dominate the results. The binned data mitigate this problem by averaging over z and μ and decreasing the average uncertainty. Because the binning causes a decrease in resolution of the Hubble diagram, the confidence contours for the binned data will

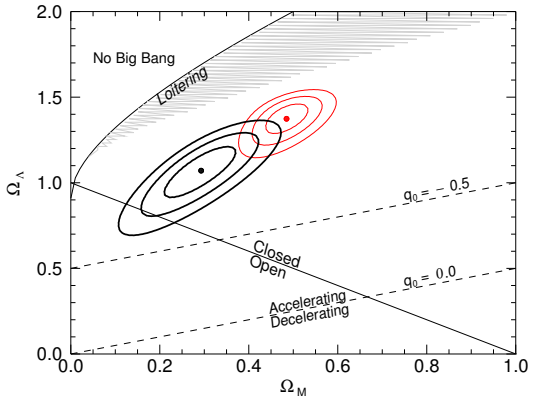

(a) GBM silver

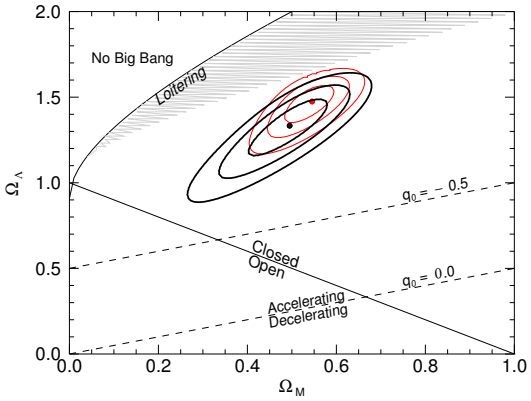

(b) GBM gold

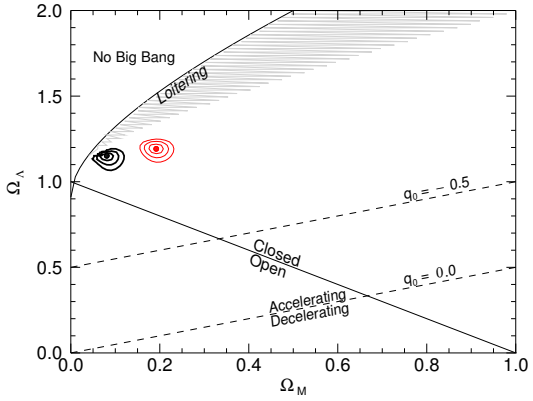

(c) BATSE silver

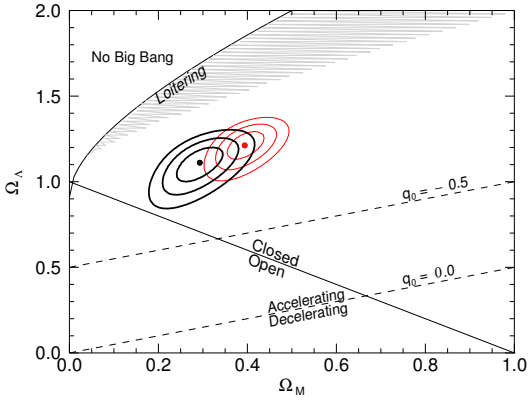

(d) BATSE gold

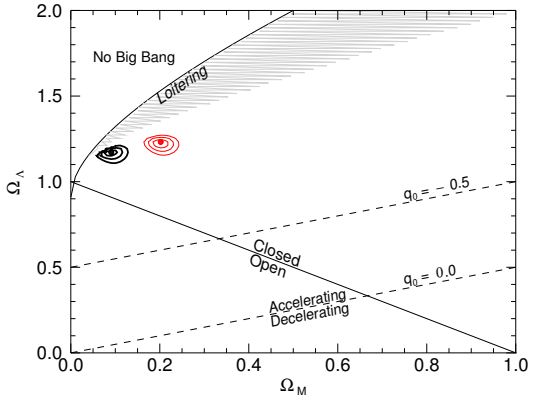

(e) All silver

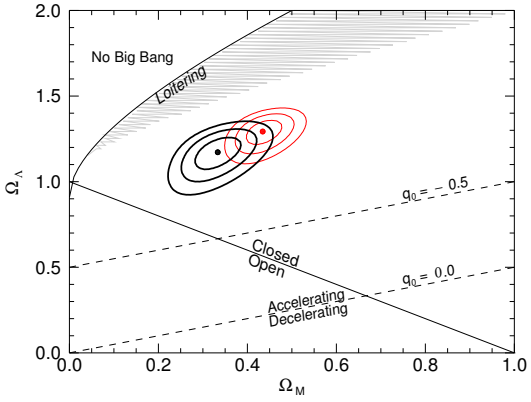

(f) All gold

Figure 9.2: The joint probability distributions for the raw (red) and binned (black) data in the Ω_M–Ω_Λ plane.

Table 9.1: Best fit parameters for Ω_M–Ω_Λ

	Unbinned			Binned		
Sample	Ω_M	Ω_Λ	χ^2/dof	Ω_M	Ω_Λ	χ^2/dof
Calibration	$0.34^{+0.08}_{-0.10}$	$1.15^{+0.16}_{-0.20}$	113/285	$0.37^{+0.09}_{-0.11}$	$1.13^{+0.18}_{-0.24}$	18/14
GBM silver	$0.48^{+0.03}_{-0.03}$	$1.37^{+0.08}_{-0.06}$	225/409	$0.29^{+0.06}_{-0.08}$	$1.07^{+0.14}_{-0.14}$	31/20
GBM gold	$0.55^{+0.05}_{-0.04}$	$1.47^{+0.09}_{-0.10}$	173/330	$0.49^{+0.06}_{-0.04}$	$1.33^{+0.14}_{-0.14}$	23/16
BATSE silver	$0.18^{+0.01}_{-0.01}$	$1.19^{+0.01}_{-0.01}$	1564/903	$0.08^{+0.01}_{-0.01}$	$1.15^{+0.01}_{-0.01}$	230/28
BATSE gold	$0.39^{+0.02}_{-0.03}$	$1.21^{+0.08}_{-0.04}$	230/629	$0.29^{+0.02}_{-0.02}$	$1.11^{+0.06}_{-0.08}$	36/23
All silver	$0.20^{+0.01}_{-0.01}$	$1.23^{+0.01}_{-0.01}$	1713/1027	$0.09^{+0.01}_{-0.01}$	$1.17^{+0.01}_{-0.01}$	191/30
All gold	$0.43^{+0.03}_{-0.03}$	$1.29^{+0.06}_{-0.06}$	298/674	$0.33^{+0.04}_{-0.04}$	$1.17^{+0.08}_{-0.06}$	37/24

generally be larger than the unbinned data. One particular point to note is that in Figure 9.2(c) & (e) the confidence contours are unusually small and are close to the loitering line. The size of the contours is related to the fact that the K-correction was not factored in to the calculation of the redshift and distance modulus, and therefore the uncertainties for each will be smaller. The locations of the contours are likely due to the inaccuracy introduced by neglecting the K-correction. A similar result would be found with the GBM data in Figure 9.2(a) if the number of GBM GRBs dominated the number from the calibration sample. The results from the gold samples are consistent with the calibration sample, although the joint probability distributions are smaller. The best-fit values and 1σ uncertainties are shown in Table 9.1.

9.1.2 Ω_M–w_0 for a Flat Universe

Although the concordant cosmology is the ΛCDM model where $w_\Lambda = -1$, there is no physical reason to expect that dark energy behaves like a cosmological

constant. In fact, several studies have shown that there might exist at least a small deviation from $w_\Lambda = -1$ for samples $z > 0.5$ [153, 154, 195]. Allowing $w_0 = w_\Lambda$ to vary and assuming a flat universe, the calibration sample was used to investigate the Ω_M–w_0 plane. The best fit Ω_M and w_0 and confidence bounds are shown in Figure 9.3. Ω_M is constrained adequately by the data, but the lower bound of w_0

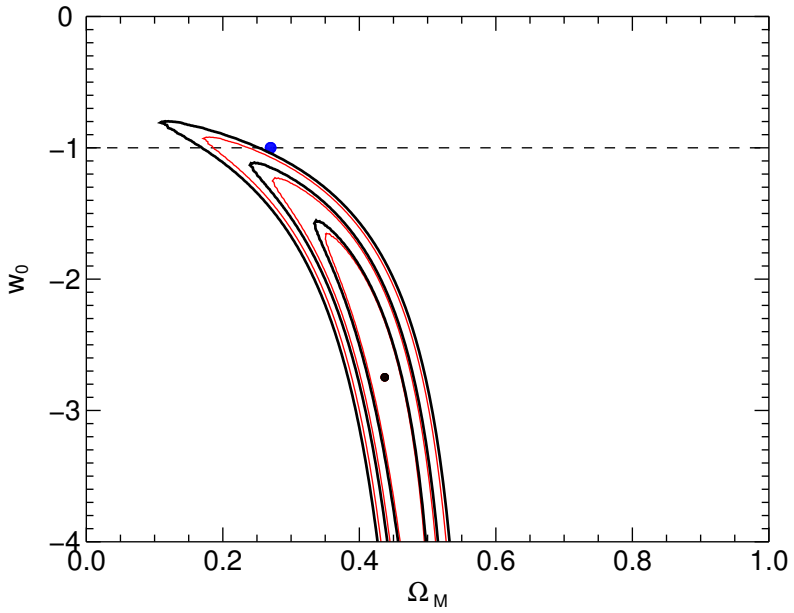

Figure 9.3: The joint probability distributions of Ω_M–w_0 from the calibration sample. The corresponding 1σ, 2σ, and 3σ contours are shown. The best-fit parameters are $\Omega_M = 0.44^{+0.06}_{-0.09}$, $w_0 = -2.75^{+1.17}_{-1.17\downarrow}$ with $\chi^2/\mathrm{dof} = 109/285$ for the raw data (red) and $\Omega_M = 0.44^{+0.06}_{-0.10}$, $w_0 = -2.75^{+1.13}_{-1.13\downarrow}$ with $\chi^2/\mathrm{dof} = 15/14$ for the binned data (black).

is unconstrained. The best fit point is at $\Omega_M = 0.44^{+0.06}_{-0.09}$, $w_0 = 2.75^{+1.17}_{-1.17\downarrow}$ for the unbinned data and $\Omega_M = 0.44^{+0.06}_{-0.10}$, $w_0 = 2.75^{+1.13}_{-1.13\downarrow}$ for the binned data, which are $\sim 3\sigma$ from the $w_0 = -1$ line that indicates a cosmological constant. It is clear that there is a preference to decreasing Ω_M with increasing w_0. The six GRB samples

Table 9.2: Best fit parameters for Ω_M–w_0

	Unbinned			Binned		
Sample	Ω_M	w_0	χ^2/dof	Ω_M	w_0	χ^2/dof
Calibration	$0.44^{+0.06}_{-0.09}$	$-2.75^{+1.17}_{-1.17\downarrow}$	109/285	$0.44^{+0.06}_{-0.10}$	$-2.75^{+1.13}_{-1.13\downarrow}$	15/14
GBM silver	$0.49^{+0.02}_{-0.04}$	$-4.00^{+0.20}_{-0.20\downarrow}$	251/409	$0.33^{+0.11}_{-0.13}$	$-1.70^{+1.45}_{-0.57}$	33/20
GBM gold	$0.49^{+0.02}_{-0.05}$	$-4.00^{+1.21}_{-1.21\downarrow}$	191/330	$0.47^{+0.04}_{-0.09}$	$-3.43^{+0.57}_{-0.57\downarrow}$	26/16
BATSE silver	$0.26^{+0.03}_{-0.02}$	$-1.66^{+0.24}_{-0.16}$	1646/903	$0.11^{+0.03}_{-0.02}$	$-1.17^{+0.12}_{-0.04}$	222/28
BATSE gold	$0.47^{+0.02}_{-0.05}$	$-3.80^{+1.29}_{-1.29\downarrow}$	246/629	$0.37^{+0.09}_{-0.09}$	$-1.78^{+1.05}_{-0.44}$	44/23
All silver	$0.30^{+0.03}_{-0.03}$	$-1.86^{+0.36}_{-0.24}$	1817/1027	$0.13^{+0.03}_{-0.03}$	$-1.25^{+0.12}_{-0.08}$	241/30
All gold	$0.49^{+0.02}_{-0.03}$	$-4.00^{+0.28}_{-0.28\downarrow}$	327/674	$0.41^{+0.07}_{-0.08}$	$-2.55^{+0.80}_{-0.80\downarrow}$	47/24

were also investigated in the Ω_M–w_0 plane and are shown in Figure 9.4. Each sample shows a preference to $w_0 < -1$. Figure 9.4(c) & (e) again show a strong deviation from the other samples in both location and constraint. The only gold sample that has a fully constrained 1σ contour is shown in Figure 9.4(d). The best-fit values and 1σ uncertainties for each sample are shown in Table 9.2. The most preferred values from the ALL gold sample are consistent with the calibration sample. An important point to note is that in the case of the binned data as well as the unbinned data, the gold samples are statistically preferred over the corresponding silver samples.

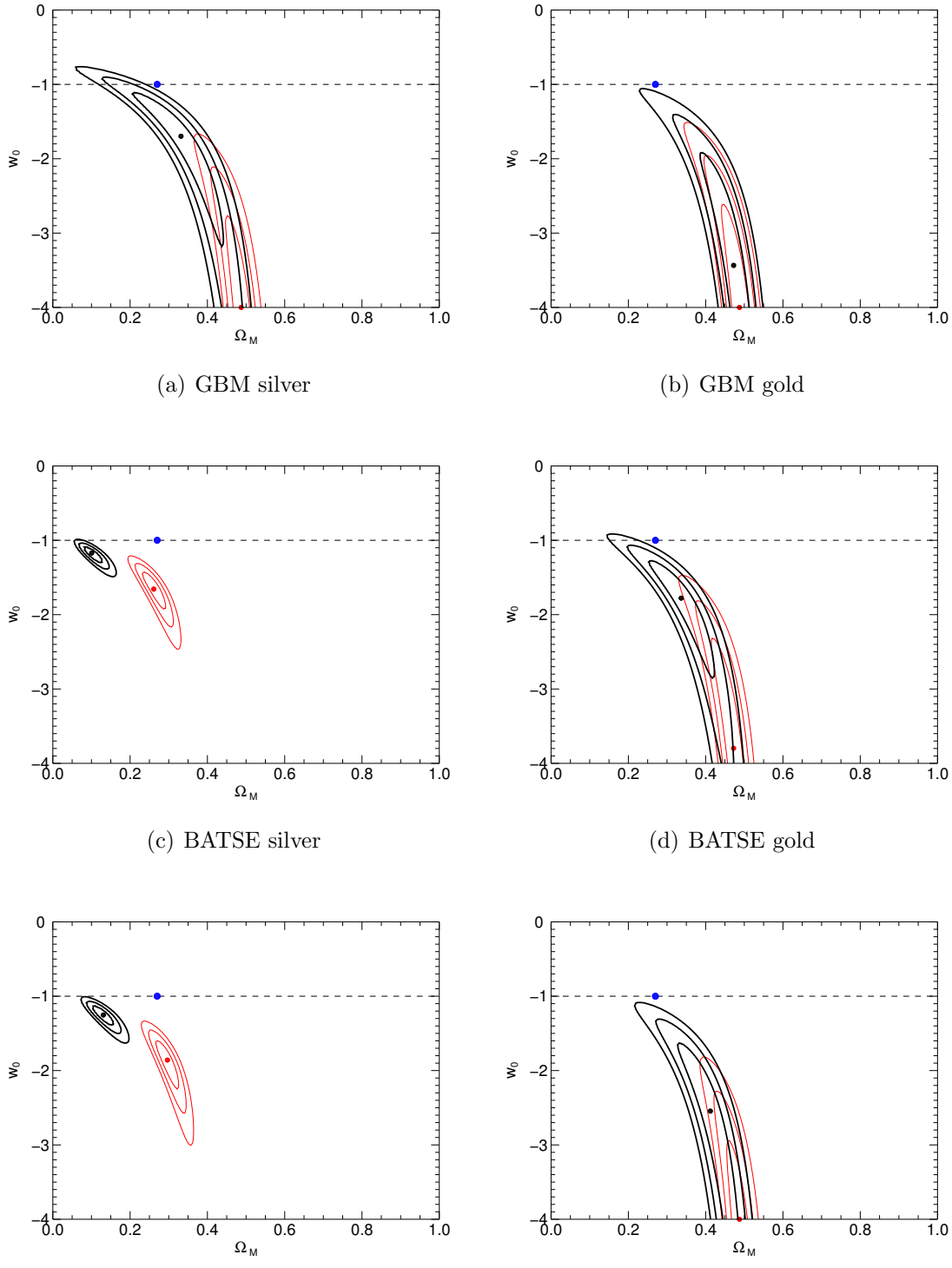

(a) GBM silver

(b) GBM gold

(c) BATSE silver

(d) BATSE gold

(e) All silver

(f) All gold

Figure 9.4: The joint probability distributions for the raw (red) and binned (black) data in the Ω_M–w_0 plane assuming a flat universe.

9.1.3 Ω_M–w_0 for $\Omega_\Lambda = 0.73$

It is clear that assuming a flat universe causes w_0 to be unconstrained in most cases. If, instead, the value for Ω_Λ is fixed to its nominally assumed value and the curvature is allowed the freedom to float, it may be possible to better constrain w_0. Shown in Figure 9.5 is the best fit Ω_M–w_0 for the calibration sample assuming $\Omega_\Lambda = 0.73$. Immediately it is shown that w_0 is much more constrained than if the

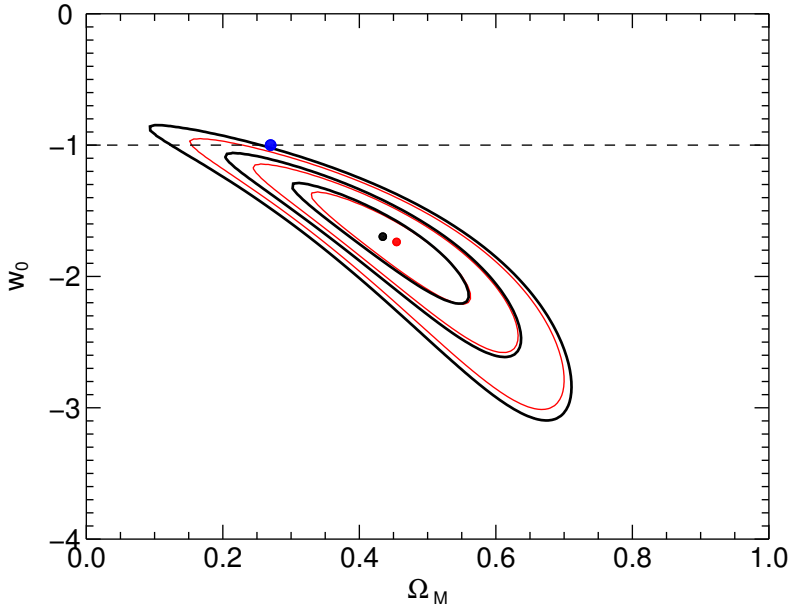

Figure 9.5: The joint probability distributions of Ω_M–w_0 from the calibration sample for $\Omega_\Lambda = 0.73$. The corresponding 1σ, 2σ, and 3σ contours are shown. The best-fit parameters are $\Omega_M = 0.45^{+0.10}_{-0.12}$, $w_0 = -1.74^{+0.36}_{-0.44}$ with $\chi^2/\mathrm{dof} = 110/285$ for the raw data (red) and $\Omega_M = 0.43^{+0.12}_{-0.12}$, $w_0 = -1.70^{+0.36}_{-0.48}$ with $\chi^2/\mathrm{dof} = 16/14$ for the binned data (black).

universe is assumed to be flat. This result is likely due to the fact that the SNe Ia alone typically show preference to a $\Omega_k > 0$ closed universe. The best fit values are $\Omega_M = 0.45^{+0.10}_{-0.12}$, $w_0 = -1.74^{+0.36}_{-0.44}$ for the unbinned data and $\Omega_M = 0.43^{+0.12}_{-0.12}$,

Table 9.3: Best fit parameters for Ω_M–w_0 for $\Omega_\Lambda = 0.73$

	Unbinned			Binned		
Sample	Ω_M	w_0	χ^2/dof	Ω_M	w_0	χ^2/dof
Calibration	$0.45^{+0.10}_{-0.12}$	$-1.74^{+0.36}_{-0.44}$	110/285	$0.43^{+0.12}_{-0.12}$	$-1.70^{+0.36}_{-0.48}$	16/14
GBM silver	$0.61^{+0.07}_{-0.08}$	$-2.34^{+0.40}_{-0.48}$	242/409	$0.34^{+0.10}_{-0.11}$	$-1.54^{+0.28}_{-0.36}$	33/18
GBM gold	$0.61^{+0.08}_{-0.09}$	$-2.26^{+0.40}_{-0.57}$	186/330	$0.55^{+0.11}_{-0.12}$	$-2.02^{+0.44}_{-0.56}$	24/16
BATSE silver	$0.29^{+0.02}_{-0.02}$	$-1.82^{+0.16}_{-0.20}$	1645/903	$0.12^{+0.02}_{-0.01}$	$-1.54^{+0.08}_{-0.16}$	241/28
BATSE gold	$0.52^{+0.07}_{-0.06}$	$-2.02^{+0.28}_{-0.40}$	240/629	$0.36^{+0.08}_{-0.08}$	$-1.62^{+0.24}_{-0.32}$	42/23
All silver	$0.33^{+0.02}_{-0.03}$	$-1.98^{+0.20}_{-0.20}$	1808/1027	$0.15^{+0.02}_{-0.02}$	$-1.56^{+0.12}_{-0.20}$	257/30
All gold	$0.60^{+0.06}_{-0.07}$	$-2.34^{+0.40}_{-0.44}$	315/674	$0.43^{+0.08}_{-0.08}$	$-1.82^{+0.28}_{-0.40}$	44/24

$w_0 = -1.70^{+0.36}_{-0.48}$ for the unbinned data. The results show that the optimal solution from the SN Ia + calibrated GRBs is $\sim 3\sigma$ from the $w_0 = -1$ cosmological constant. The six GRB samples were then investigated under the assumption that $\Omega_\Lambda = 0.73$ and are shown in Figure 9.6. Allowing the shape of the universe to vary, the dark energy equation of state can be constrained. The GRB Hubble diagram appears to prefer a $w_0 < -1$ equation of state to such a degree that the cosmological constant is ruled out at $> 3\sigma$. The best-fit values and 1σ uncertainties are listed in Table 9.3. When allowing the curvature to vary, the goodness-of-fit for every case of the gold samples are improved when compared to fixing $\Omega_k = 0$. This indicates that the SNe Ia + GRB data prefer a closed universe over a flat universe given a scalar value for $w(z)$.

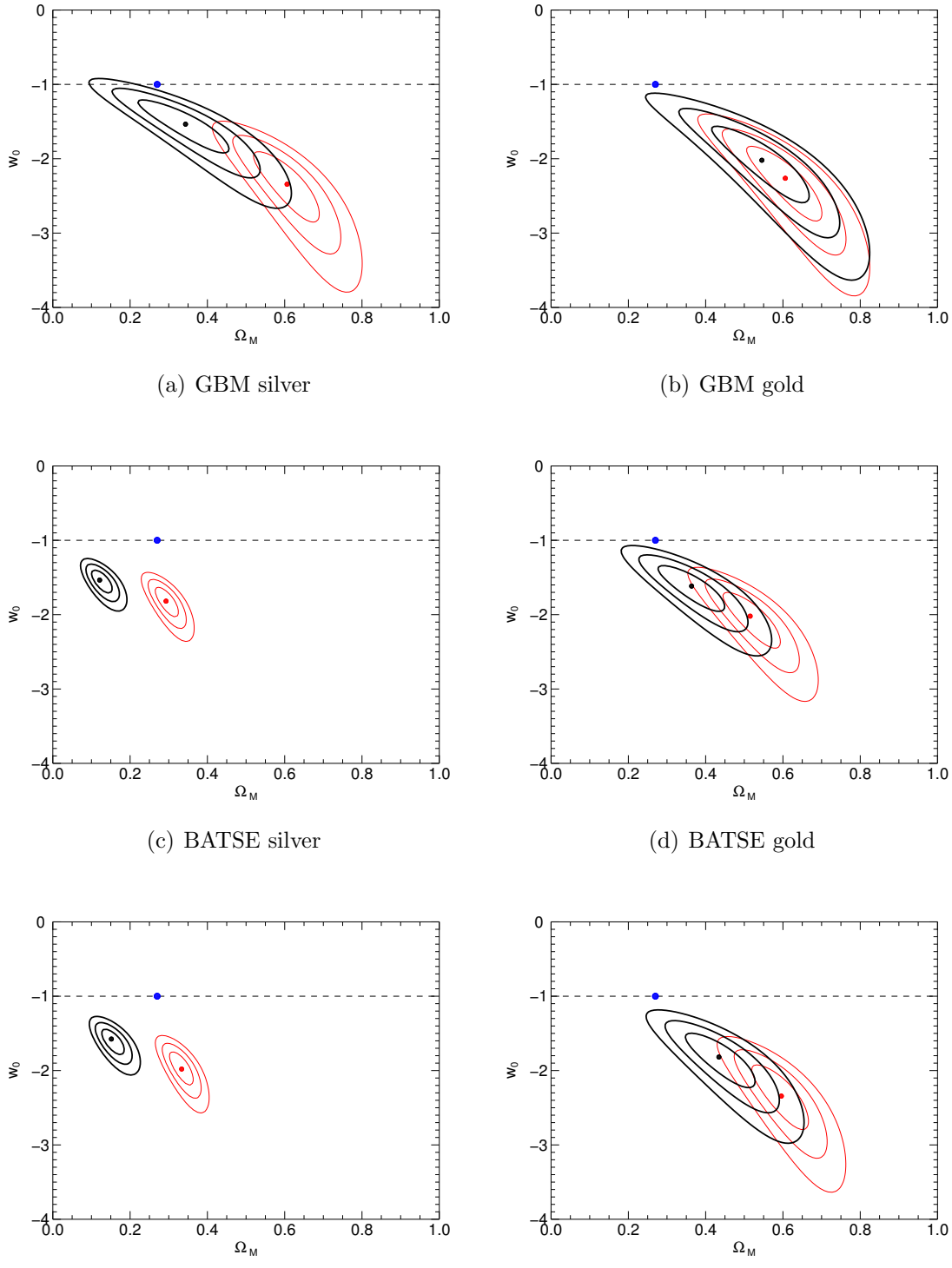

(a) GBM silver

(b) GBM gold

(c) BATSE silver

(d) BATSE gold

(e) All silver

(f) All gold

Figure 9.6: The joint probability distributions for the raw (red) and binned (black) data in the Ω_M–w_0 plane assuming $\Omega_\Lambda = 0.73$.

9.1.4 Ω_Λ–Ω_k, $w_0 = -1$

Perhaps another way to view the impact that Ω_Λ has on the curvature of the universe is the relationship Ω_Λ–Ω_k. Assuming $w_0 = -1$, Figure 9.7 shows the relationship for the calibration sample. The gray area indicates that values of Ω_Λ and Ω_k for which the calculation of high-z distance moduli fails. As has been shown previously, the SN Ia data strongly prefers $\Omega_\Lambda \approx 1$. The line indicating a flat universe

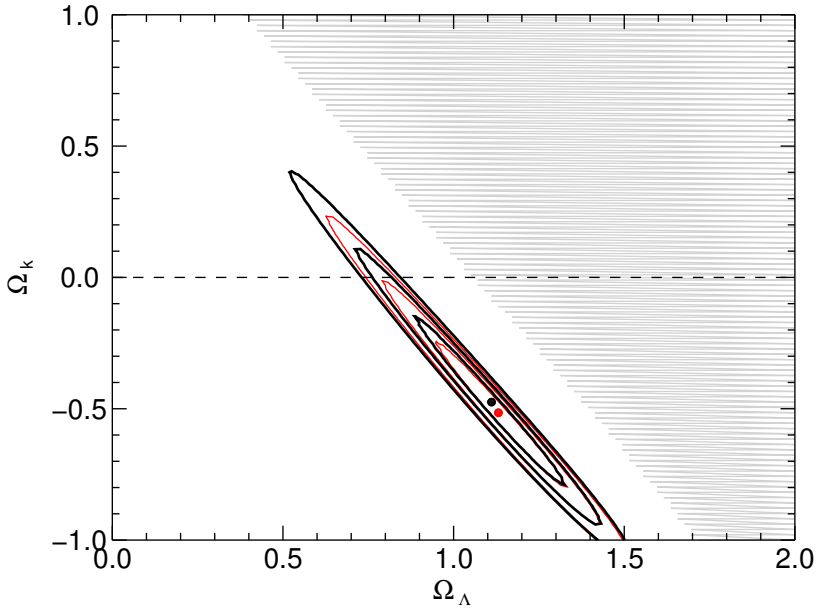

Figure 9.7: The joint probability distributions of Ω_Λ–Ω_k from the calibration sample. The corresponding 1σ, 2σ, and 3σ contours are shown. The gray area indicates the parameter space where objects at redshift $z > 1.5$ cannot exist. The best-fit parameters are $\Omega_\Lambda = 1.13^{+0.18}_{-0.18}$, $\Omega_k = -0.52^{+0.26}_{-0.26}$ with $\chi^2/\mathrm{dof} = 113/285$ for the raw data and $\Omega_\Lambda = 1.11^{+0.22}_{-0.20}$, $\Omega_k = -0.47^{+0.30}_{-0.32}$ with $\chi^2/\mathrm{dof} = 18/14$ for the binned data.

is within $\sim 2\sigma$. The best fit values are $\Omega_\Lambda = 1.13^{+0.18}_{-0.18}$, $\Omega_k = -0.52^{+0.26}_{-0.26}$ for the unbinned data and $\Omega_\Lambda = 1.11^{+0.22}_{-0.20}$, $\Omega_k = -0.47^{+0.30}_{-0.32}$ for the binned data. The results from the GRB samples are shown in Figure 9.8. All samples strongly prefer $\Omega_\Lambda > 1$

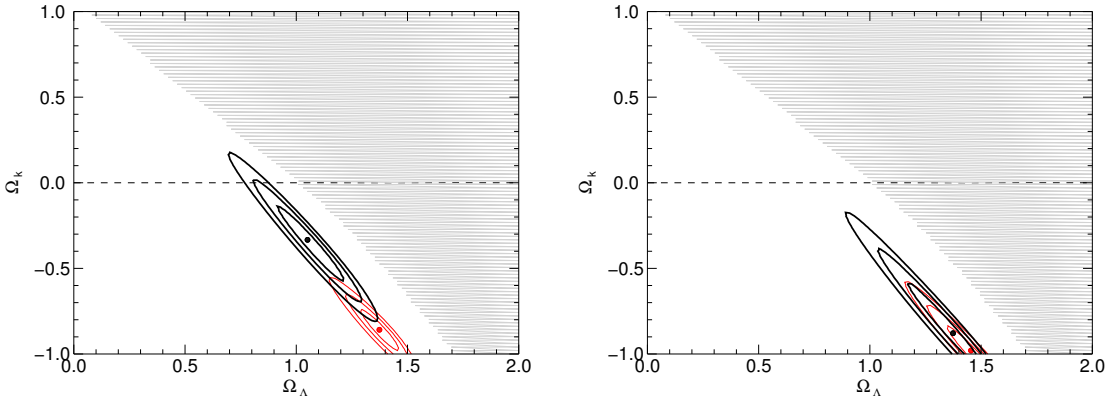

(a) GBM silver

(b) GBM gold

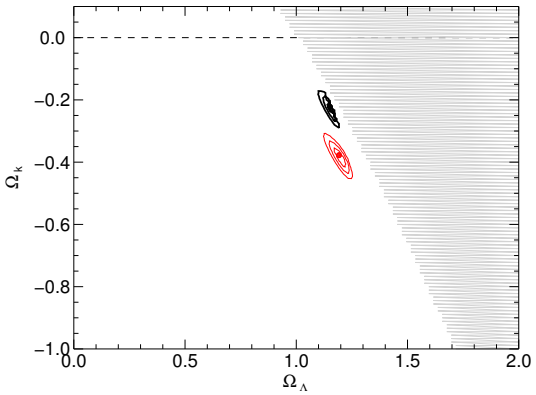

(c) BATSE silver

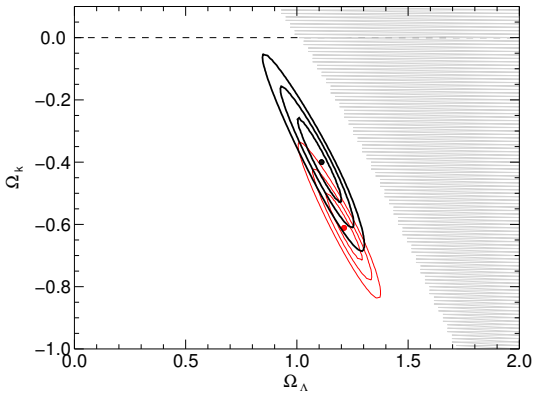

(d) BATSE gold

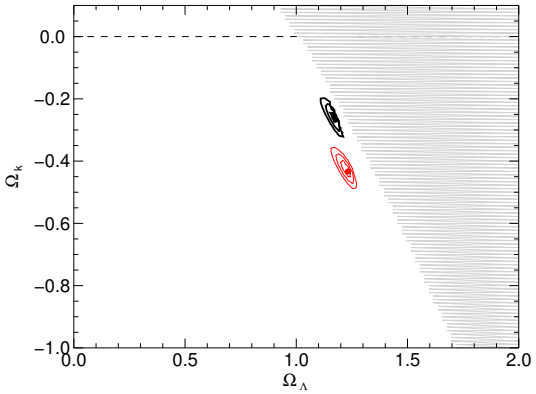

(e) All silver

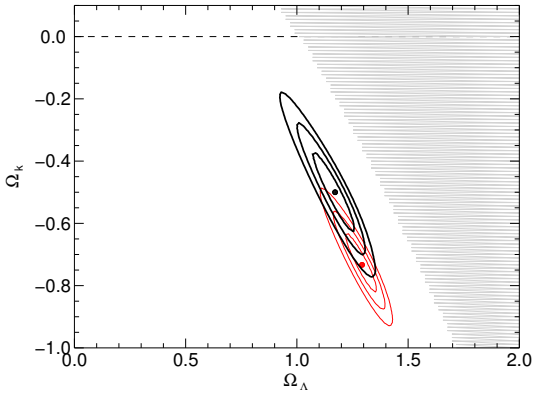

(f) All gold

Figure 9.8: The joint probability distributions for the raw (red) and binned (black) data in the Ω_Λ–Ω_k plane.

Table 9.4: Best fit parameters for Ω_Λ–Ω_k

	Unbinned			**Binned**		
Sample	Ω_Λ	Ω_k	χ^2/dof	Ω_Λ	Ω_k	χ^2/dof
Calibration	$1.13^{+0.18}_{-0.18}$	$-2.75^{+0.26}_{-0.26}$	113/285	$1.11^{+0.22}_{-0.20}$	$-0.47^{+0.30}_{-0.32}$	18/14
GBM silver	$1.37^{+0.08}_{-0.08}$	$-0.86^{+0.12}_{-0.10}$	225/409	$1.05^{+0.12}_{-0.16}$	$-0.33^{+0.22}_{-0.18}$	31/18
GBM gold	$1.45^{+0.10}_{-0.04}$	$-0.98^{+0.02}_{-0.14}$	173/330	$1.37^{+0.20}_{-0.10}$	$-0.88^{+0.12}_{-0.28}$	22/16
BATSE silver	$1.19^{+0.02}_{-0.02}$	$-0.38^{+0.03}_{-0.02}$	1564/903	$1.15^{+0.01}_{-0.01}$	$-0.22^{+0.03}_{-0.01}$	174/28
BATSE gold	$1.21^{+0.08}_{-0.08}$	$-0.61^{+0.10}_{-0.11}$	230/629	$1.11^{+0.10}_{-0.08}$	$-0.40^{+0.12}_{-0.13}$	36/23
All silver	$1.23^{+0.01}_{-0.01}$	$-0.43^{+0.01}_{-0.02}$	1713/1027	$1.17^{+0.01}_{-0.01}$	$-0.26^{+0.01}_{-0.01}$	191/30
All gold	$1.29^{+0.06}_{-0.06}$	$-0.73^{+0.08}_{-0.09}$	298/674	$1.17^{+0.08}_{-0.08}$	$-0.50^{+0.12}_{-0.12}$	37/24

and a closed universe. All samples except for the GBM silver samples exclude a flat universe at the 3σ level. As was shown in the previous section, however, this does not necessarily indicate that $\Omega_k < 0$ is the overall preferred curvature since the dark energy equation of state can affect the curvature of the Hubble diagram. Therefore, the preference of the data to a closed universe may be a result of an incorrect assumption, namely $w_0 = -1$. The best fit results from each sample and their corresponding 1σ uncertainties are shown in Table 9.4.

9.1.5 Ω_M–Ω_k, $w_0 = -1$

Similar to the previous section, the relationship between Ω_M and Ω_k can be explored as an alternative to Ω_M–Ω_Λ. Assuming $w_0 = -1$, Figure 9.9 shows the relationship for the calibration sample. The gray area indicates that values of Ω_M and Ω_k for which the calculation of high-z distance moduli fails. The calibration sample shows a preference towards the concordant Ω_M value and $\Omega_k < 0$. The line indicating a flat universe is still within $\sim 2\sigma$. The best fit values are $\Omega_\Lambda = 0.39^{+0.10}_{-0.08}$, $\Omega_k = -0.56^{+0.30}_{-0.20}$ for the unbinned data and $\Omega_M = 0.37^{+0.11}_{-0.09}$, $\Omega_k = -0.49^{+0.34}_{-0.22}$ for the binned data. The results from the GRB samples are shown in Figure 9.10. All samples prefer the concordant Ω_M and a closed universe, except for Figure 9.10(c) & (e), which show significant deviation from the other samples. All samples except for the GBM silver sample exclude a flat universe at the 3σ level. As was shown in the previous section, however, this does not necessarily indicate that $\Omega_k < 0$ is the overall preferred curvature since the dark energy equation of state can affect the curvature of the Hubble diagram. Therefore, the preference of the data to a closed universe may be a result of an incorrect assumption, namely $w_0 = -1$. The best fit results from each sample and their corresponding 1σ uncertainties are shown in Table 9.5.

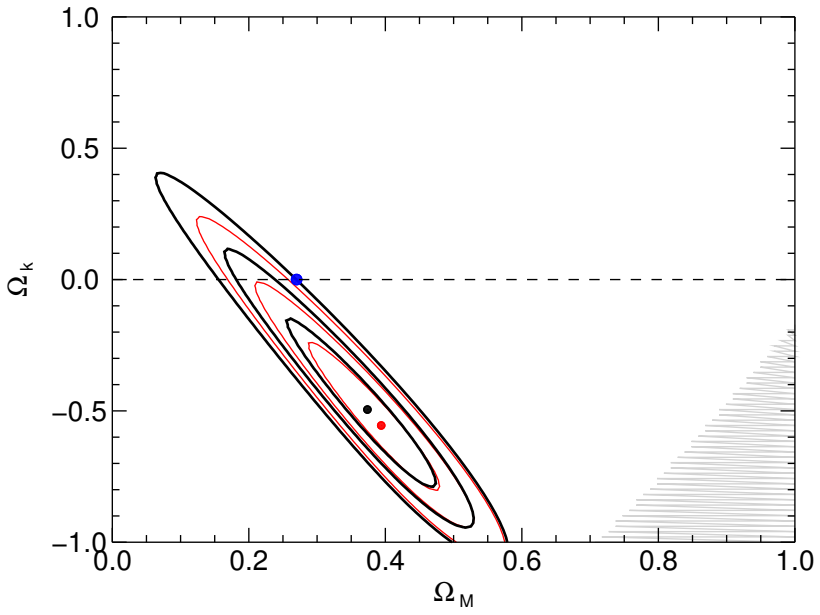

Figure 9.9: The joint probability distributions of Ω_M–Ω_k from the calibration sample. The corresponding 1σ, 2σ, and 3σ contours are shown and the blue point marks the value for a flat ΛCDM universe. The gray area indicates the parameter space where objects with at redshift $z > 1.5$ cannot exist. The best-fit parameters are $\Omega_M = 0.39^{+0.10}_{-0.08}$, $\Omega_k = -0.56^{+0.30}_{-0.20}$ with $\chi^2/\mathrm{dof} = 113/285$ for the raw data and $\Omega_\Lambda = 0.37^{+0.11}_{-0.09}$, $\Omega_k = -0.49^{+0.34}_{-0.22}$ with $\chi^2/\mathrm{dof} = 18/14$ for the binned data.

Table 9.5: Best fit parameters for Ω_M–Ω_k

	Unbinned			**Binned**		
Sample	Ω_M	Ω_k	χ^2/dof	Ω_M	Ω_k	χ^2/dof
Calibration	$0.39^{+0.10}_{-0.08}$	$-0.56^{+0.30}_{-0.20}$	113/285	$0.37^{+0.11}_{-0.09}$	$-0.49^{+0.34}_{-0.22}$	18/14
GBM silver	$0.48^{+0.04}_{-0.04}$	$-0.86^{+0.10}_{-0.06}$	225/409	$0.29^{+0.08}_{-0.07}$	$-0.37^{+0.22}_{-0.14}$	31/18
GBM gold	$0.54^{+0.05}_{-0.02}$	$-1.00^{+0.14}_{-0.14\downarrow}$	173/330	$0.49^{+0.09}_{-0.08}$	$-0.84^{+0.16}_{-0.24}$	22/16
BATSE silver	$1.19^{+0.01}_{-0.01}$	$-0.39^{+0.02}_{-0.01}$	1564/903	$0.07^{+0.01}_{-0.01}$	$-0.22^{+0.01}_{-0.01}$	174/28
BATSE gold	$0.39^{+0.03}_{-0.04}$	$-0.61^{+0.11}_{-0.10}$	230/629	$0.29^{+0.05}_{-0.04}$	$-0.40^{+0.12}_{-0.13}$	36/23
All silver	$0.20^{+0.01}_{-0.01}$	$-0.42^{+0.01}_{-0.01}$	1713/1027	$0.09^{+0.01}_{-0.01}$	$-0.27^{+0.03}_{-0.01}$	191/30
All gold	$0.43^{+0.03}_{-0.04}$	$-0.72^{+0.09}_{-0.09}$	298/674	$0.33^{+0.04}_{-0.04}$	$-0.51^{+0.11}_{-0.11}$	37/24

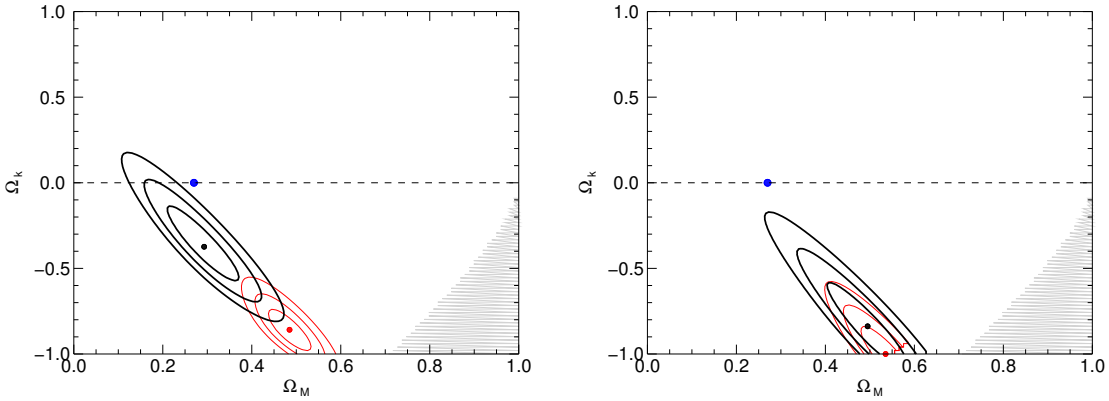

(a) GBM silver

(b) GBM gold

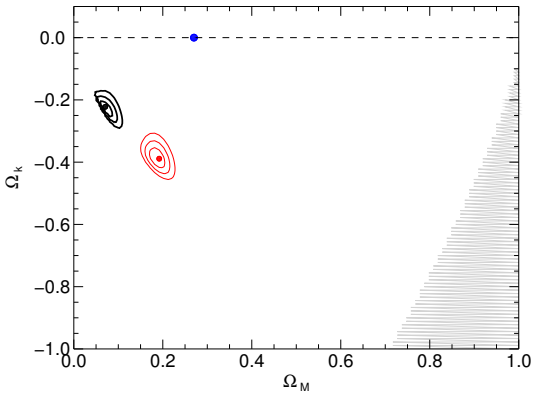

(c) BATSE silver

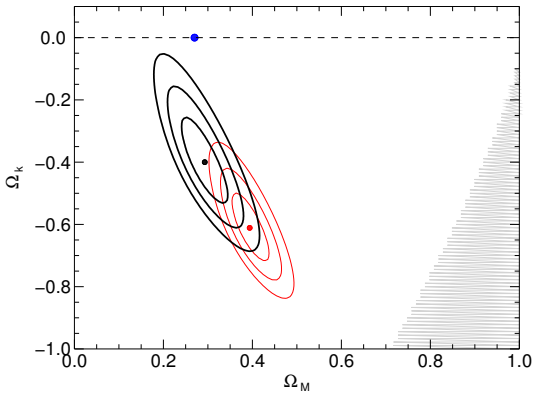

(d) BATSE gold

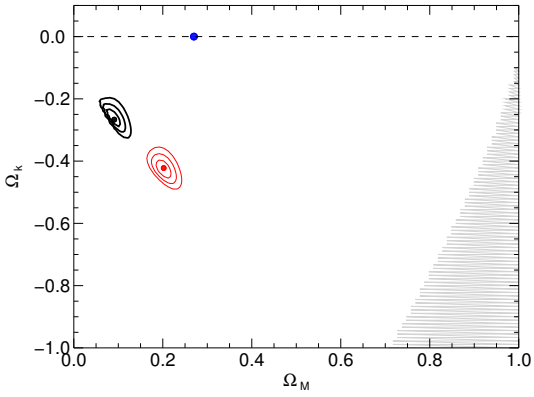

(e) All silver

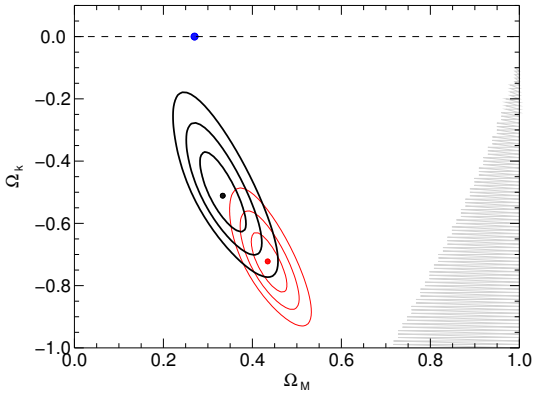

(f) All gold

Figure 9.10: The joint probability distributions for the raw (red) and binned (black) data in the Ω_M–Ω_k plane. The blue point marks the value for a flat ΛCDM universe.

9.1.6 Ω_k–w_0, $\Omega_M = 0.73$

Since the previous sections appear to indicate that assuming $w_0 = -1$ resulting in a cosmological constant causes the fitted curvature to deviate significantly from a flat cosmology, it is of interest to investigate the Ω_k–w_0 plane to determine if allowing for a dynamical dark energy equation of state can eliminate the deviation from $\Omega_k = 0$. The result from the calibration sample is shown in Figure 9.11. The

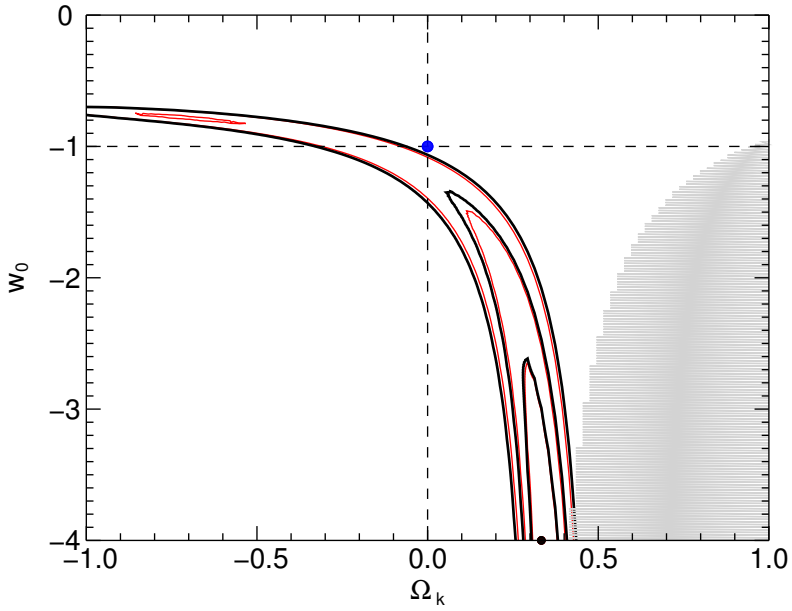

Figure 9.11: The joint probability distributions of Ω_k–w_0 from the calibration sample. The corresponding 1σ, 2σ, and 3σ contours are shown and the blue point marks the value for a flat universe with a cosmological constant. The gray area indicates the parameter space where objects with at redshift $z > 1.5$ cannot exist. The best-fit parameters are $\Omega_k = 0.33^{+0.04}_{-0.04}$, $w_0 = -4.00^{+1.23}_{-1.23\downarrow}$ with $\chi^2/\mathrm{dof} = 108/285$ for the raw data and $\Omega_k = 0.33^{+0.04}_{-0.04}$, $w_0 = -4.00^{+1.25}_{-1.25}$ with $\chi^2/\mathrm{dof} = 13/14$ for the binned data.

gray area indicates that values of Ω_k and w_0 for which the calculation of high-z distance moduli fails. The best fit values are $\Omega_k = 0.33^{+0.04}_{-0.04}$, $w_0 = -4.00^{+1.23}_{-1.23\downarrow}$ for the

Table 9.6: Best fit parameters for Ω_k–w_0, $\Omega_M = 0.27$

	Unbinned			Binned		
Sample	Ω_k	w_0	χ^2/dof	Ω_k	w_0	χ^2/dof
Calibration	$+0.33^{+0.04}_{-0.04}$	$-4.00^{+1.23}_{-1.23\downarrow}$	108/285	$+0.33^{+0.04}_{-0.04}$	$-4.00^{+1.25}_{-1.25\downarrow}$	13/14
GBM silver	$-0.80^{+0.04}_{-0.06}$	$-0.76^{+0.02}_{-0.02}$	224/409	$-0.47^{+0.38}_{-0.18}$	$-0.90^{+0.03}_{-0.30}$	31/18
GBM gold	$-0.86^{+0.02}_{-0.04}$	$-0.74^{+0.02}_{-0.01}$	170/330	$-0.88^{+0.08}_{-0.16}$	$-0.74^{+0.03}_{-0.02}$	21/16
BATSE silver	$-0.39^{+0.04}_{-0.04}$	$-1.13^{+0.04}_{-0.01}$	1592/903	$-0.19^{+0.06}_{-0.08}$	$-1.54^{+0.14}_{-0.15}$	278/28
BATSE gold	$-0.64^{+0.06}_{-0.06}$	$-0.81^{+0.03}_{-0.01}$	228/629	$-0.47^{+0.10}_{-0.16}$	$-0.91^{+0.06}_{-0.08}$	35/23
All silver	$-0.45^{+0.02}_{-0.04}$	$-1.08^{+0.05}_{-0.03}$	1734/1027	$-0.23^{+0.06}_{-0.08}$	$-1.45^{+0.19}_{-0.13}$	271/30
All gold	$-0.70^{+0.04}_{-0.04}$	$-0.79^{+0.03}_{-0.01}$	297/674	$-0.56^{+0.08}_{-0.10}$	$-0.87^{+0.05}_{-0.02}$	35/24

unbinned data and $\Omega_k = 0.33^{+0.04}_{-0.04},\ w_0 = -4.00^{+1.25}_{-1.25\downarrow}$ for the binned data. The ΛCDM cosmology is at $\sim 3\sigma$ from the best fit value, which is unconstrained on the lower bound of w_0. The calibration sample prefers an open universe, although there exists a separate small 2σ contour indicating a closed universe. The 3σ contours are extremely large, as the SN Ia data cannot accurately constrain both the curvature and the dark energy equation of state. The results from the GRB samples are shown in Figure 9.12. The contours for all samples except the BATSE and ALL silver samples appear to prefer a closed universe and $w_0 > -1$. For the gold sample, the cosmological constant is within 3σ, particularly for Figure 9.12(d) & (f) where the cosmological constant is with 2σ. Only Figure 9.12 (d) for the BATSE gold sample includes the flat universe line within 3σ. The best fit values for each sample along with their corresponding 1σ uncertainties are in Table 9.6.

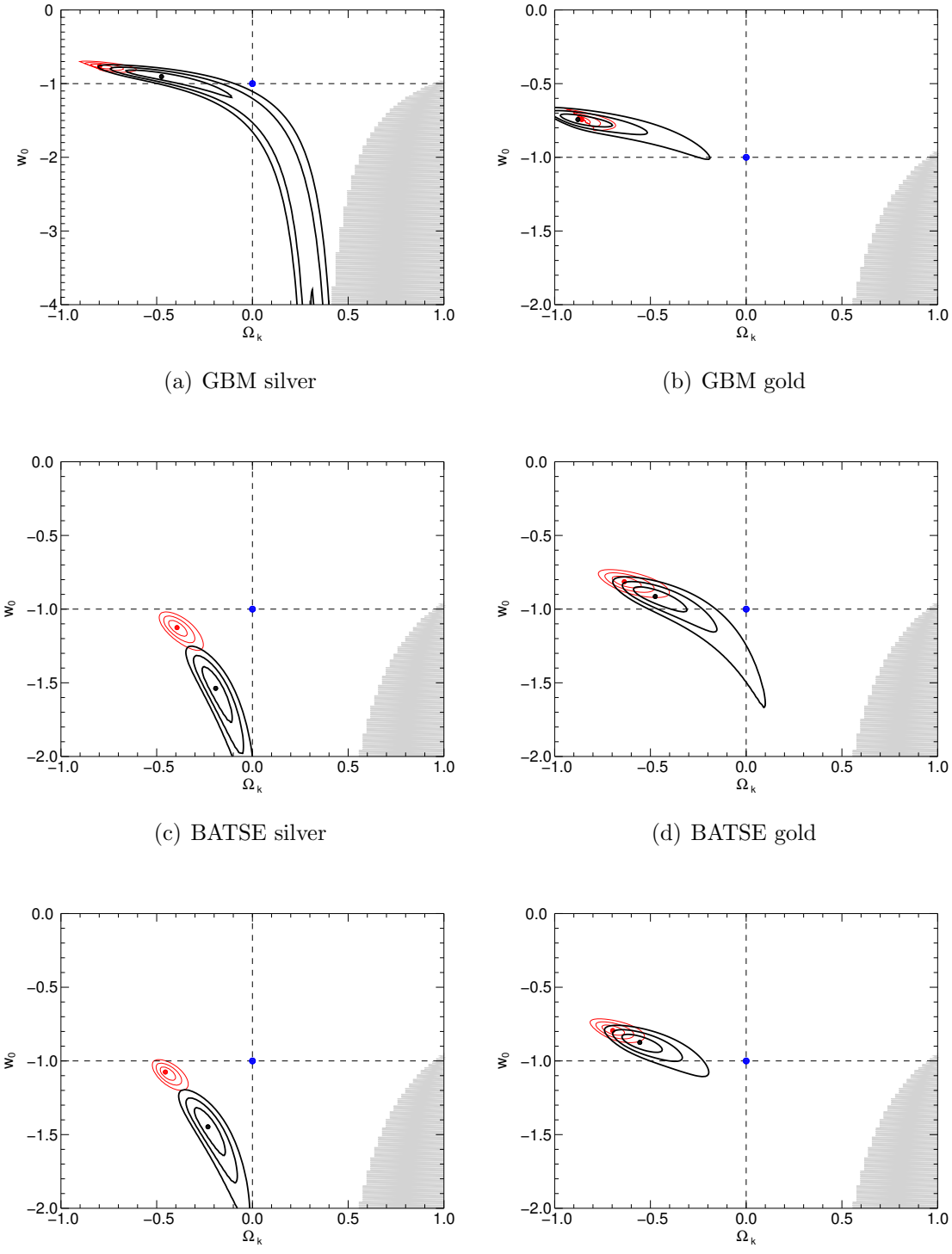

(a) GBM silver

(b) GBM gold

(c) BATSE silver

(d) BATSE gold

(e) All silver

(f) All gold

Figure 9.12: The joint probability distributions for the raw (red) and binned (black) data in the Ω_k–w_0 plane. The blue point marks the value for a flat universe with a cosmological constant.

9.1.7 $w(z)$ for a Flat Universe

Instead of assuming a constant equation of state, but rather an equation of state that evolves over time or redshift. As discussed previously, there are several theoretical possibilities for the representation of the equation of state, though there is no particular theoretical preference. I choose to investigate the Riess representation where $w(z) = w_0 + w'$ and the CPL representation where $w(z) = w_0 + w_a z(1+z)^{-1}$. The following χ^2 maps aim to show the relationship w_0–w' and w_0–w_a for a flat universe.

9.1.7.1 Riess Cosmology

The Riess cosmological model indicates that $w_0 = -1.31$ and $w' = 1.48$ from SN Ia data alone. Therefore an estimate of the relationship is desirable for SN Ia + GRB data. The results of the calibration data are shown in Figure 9.13. The gray region shows the 1σ region found by Riess et al. [154] for SNe Ia. The lines and blue marker denote the value for a cosmological constant. The value for a cosmological constant is just outside of 3σ from the best fit from the calibration data. The most likely values are $w_0 = -1.70^{+0.30}_{-0.30},\ w' = 2.06^{+1.09}_{-1.27}$ for the unbinned data and $w_0 = -1.66^{+0.34}_{-0.34},\ w' = 1.88^{+1.27}_{-1.39}$ for the binned data. Evidence for $w' = 0$ exists within 2σ and evidence for $w_0 = -1$ exists within 3σ. The results from the remaining GRB samples are shown in Figure 9.14. Each sample shows a $> 3\sigma$ deviation from the cosmological constant. Figure 9.14 (d), the BATSE sample, is the only gold sample that supports a scalar $w(z)$ within 3σ. All samples show a similar relationship and

similar values to those found in the calibration sample. The best fit values for each sample along with their corresponding 1σ uncertainties are shown in Table 9.7.

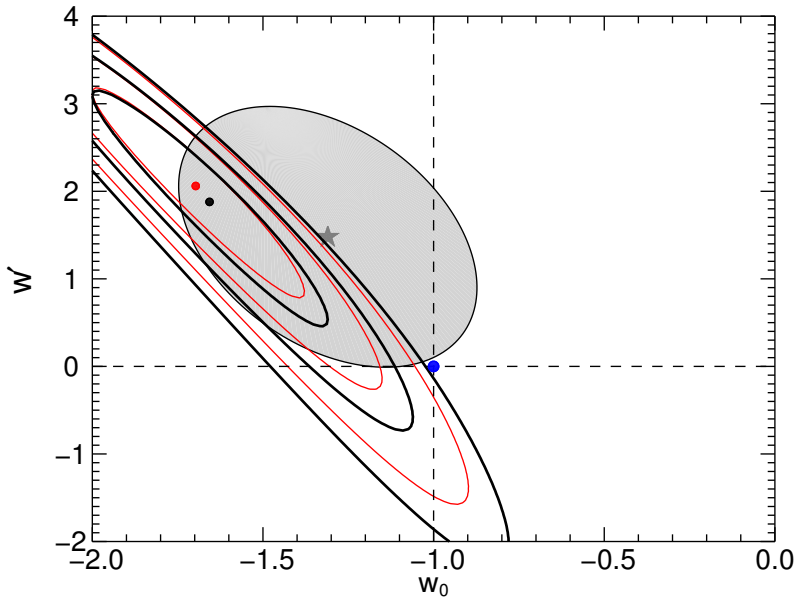

Figure 9.13: The joint probability distributions of w_0–$w\prime$ for $\Omega_M = 0.27$ and a flat universe from the calibration sample. The corresponding 1σ, 2σ, and 3σ contours are shown, and the blue point marks the value for a cosmological constant. The shaded oval represents the 1σ contour for SN Ia Hubble Diagram from Riess et al. [153, 154]. The best-fit parameters are $w_0 = -1.70^{+0.30}_{-0.30}$, $w' = 2.06^{+1.09}_{-1.27}$ with $\chi^2/\mathrm{dof} = 110/285$ for the raw data and $w_0 = -1.66^{+0.34}_{-0.34}$, $w' = 1.88^{+1.27}_{-1.39}$ with $\chi^2/\mathrm{dof} = 16/14$ for the binned data.

Table 9.7: Best fit parameters for Riess $w(z)$, assuming $\Omega_M = 0.27$, a flat universe

	Unbinned			**Binned**		
Sample	w_0	$w\prime$	χ^2/dof	w_0	$w\prime$	χ^2/dof
Calibration	$-1.70^{+0.30}_{-0.30}$	$2.06^{+1.09}_{-1.27}$	110/285	$-1.66^{+0.34}_{-0.34}$	$1.88^{+1.27}_{-1.39}$	16/14
GBM silver	$-2.00^{+0.21}_{-0.21}$	$3.27^{+0.73}_{-0.61}$	222/409	$-1.70^{+0.21}_{-0.21}$	$1.64^{+0.79}_{-0.91}$	30/18
GBM gold	$-2.06^{+0.24}_{-0.24}$	$3.67^{+0.78}_{-0.85}$	172/330	$-1.94^{+0.27}_{-0.30}$	$3.17^{+1.13}_{-1.06}$	20/16
BATSE silver	$-2.33^{+0.15}_{-0.18}$	$2.22^{+0.33}_{-0.22}$	1608/903	$-1.33^{+0.48}_{-0.55}$	$-4.78^{+3.22}_{-3.22\downarrow}$	282/28
BATSE gold	$-1.79^{+0.18}_{-0.18}$	$2.23^{+0.49}_{-0.42}$	227/629	$-1.72^{+0.18}_{-0.21}$	$1.67^{+0.49}_{-0.49}$	35/23
All silver	$-2.42^{+0.18}_{-0.15}$	$2.56^{+0.22}_{-0.33}$	1751/1027	$-1.30^{+0.48}_{-0.52}$	$-4.56^{+3.11}_{-3.11\downarrow}$	279/30
All gold	$-1.88^{+0.18}_{-0.21}$	$2.73^{+0.61}_{-0.48}$	295/674	$-1.79^{+0.18}_{-0.21}$	$2.00^{+0.55}_{-0.48}$	35/24

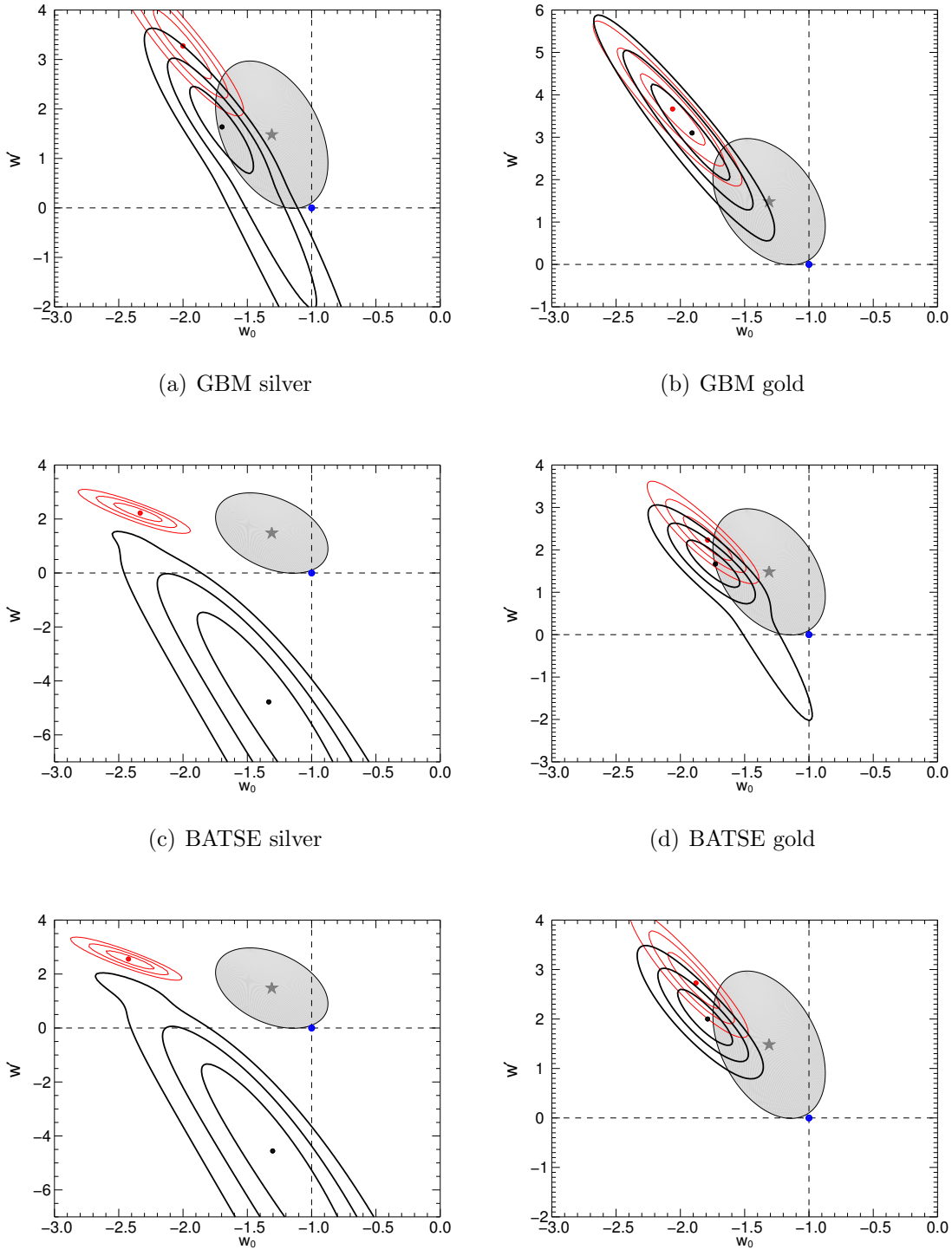

(a) GBM silver

(b) GBM gold

(c) BATSE silver

(d) BATSE gold

(e) All silver

(f) All gold

Figure 9.14: The joint probability distributions for the raw (red) and binned (black) data in the w_0–w' plane. The blue point marks the value for a cosmological constant.

9.1.7.2 CPL Cosmology

The Riess representation has been criticized for being unstable at large redshifts, therefore another possible expansion about w_0 is the CPL representation where $w(z) = w_0 + w_a z(1+z)^{-1}$. Assuming $\Omega_M = 0.27$ and a flat universe, the calibration results are shown in Figure 9.15. The lines and blue marker denote the value for a cosmological constant. The value for a cosmological constant is just outside of 3σ

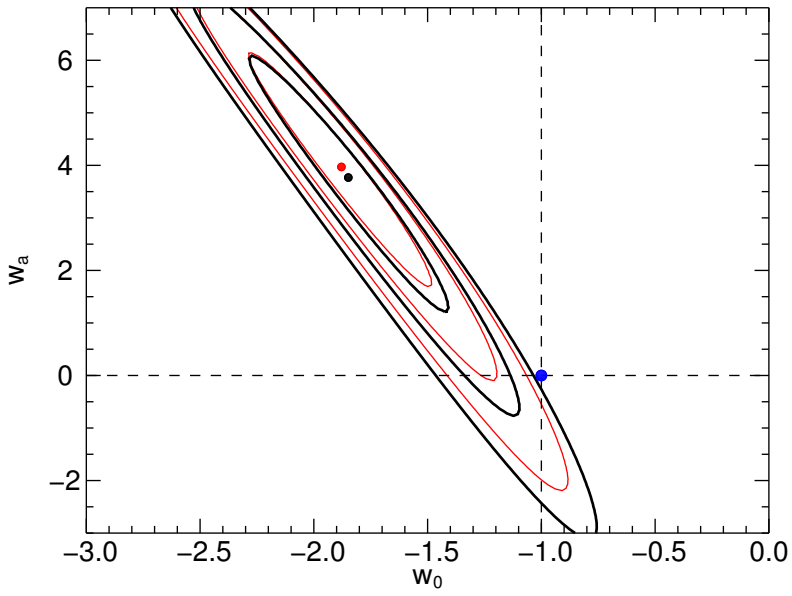

Figure 9.15: The joint probability distributions of w_0–w_a for $\Omega_M = 0.27$ and a flat universe from the calibration sample. The corresponding 1σ, 2σ, and 3σ contours are shown, and the blue point marks the value for a cosmological constant. The best-fit parameters are $w_0 = -1.88^{+0.39}_{-0.39}$, $w_a = 3/97^{+2.12}_{-2.22}$ with $\chi^2/\mathrm{dof} = 109/285$ for the raw data and $w_0 = -1.85^{+0.42}_{-0.42}$, $w_a = 3.77^{+2.22}_{-2.53}$ with $\chi^2/\mathrm{dof} = 15/14$ for the binned data.

from the best fit from the calibration data. The most likely values are

$w_0 = -1.88^{+0.39}_{-0.39}$, $w_a = 3.97^{+2.12}_{-2.22}$ for the unbinned data and $w_0 = -1.85^{+0.42}_{-0.42}$,

$w_a = 3.77^{+2.22}_{-2.53}$ for the binned data. Evidence for $w_a = 0$ exists within 2σ and evi-

Table 9.8: Best fit parameters for the CPL cosmology, $\Omega_M = 0.27$ flat universe

	Unbinned			**Binned**		
Sample	w_0	$w\prime$	χ^2/dof	w_0	$w\prime$	χ^2/dof
Calibration	$-1.88^{+0.39}_{-0.39}$	$3.97^{+1.09}_{-2.12}$	109/285	$-1.85^{+0.42}_{-0.42}$	$3.77^{+2.22}_{-2.53}$	15/14
GBM silver	$-2.39^{+0.21}_{-0.09}$	$6.90^{+0.10}_{-1.01}$	228/409	$-1.94^{+0.70}_{-0.33}$	$3.77^{+1.72}_{-4.34}$	32/18
GBM gold	$-2.36^{+0.21}_{-0.09}$	$7.00^{+1.11\uparrow}_{-1.11}$	176/330	$-2.21^{+0.33}_{-0.24}$	$6.09^{+0.90}_{-1.82}$	21/16
BATSE silver K	$-1.12^{+0.27}_{-0.45}$	$-3.95^{+3.15}_{-1.05}$	1643/903	$-1.45^{+0.21}_{-0.21}$	$-5.00^{+3.15}_{-3.15\downarrow}$	283/28
BATSE gold	$-2.18^{+0.21}_{-0.24}$	$5.45^{+1.09}_{-0.91}$	230/629	$-2.06^{+0.27}_{-0.27}$	$4.27^{+1.18}_{-1.27}$	39/23
All silver	$-1.15^{+0.33}_{-1.00}$	$-3.38^{+6.38}_{-1.62}$	1816/1027	$-1.39^{+0.18}_{-0.42}$	$-5.00^{+3.23}_{-3.23\downarrow}$	280/30
All gold	$-2.33^{+0.24}_{-0.18}$	$6.45^{+0.54}_{-1.00}$	300/674	$-2.15^{+0.24}_{-0.27}$	$5.00^{+1.18}_{-1.09}$	39/24

dence for $w_0 = -1$ exists within 3σ. The results from the remaining GRB samples are shown in Figure 9.16. Each sample shows a $> 3\sigma$ deviation from the cosmological constant. Figure 9.16 (d), the BATSE sample, is the only gold sample that supports a scalar $w(z)$ within 3σ. All samples show a similar relationship and similar values to those found in the calibration sample. The best fit values for each sample along with their corresponding 1σ uncertainties are shown in Table 9.8.

!

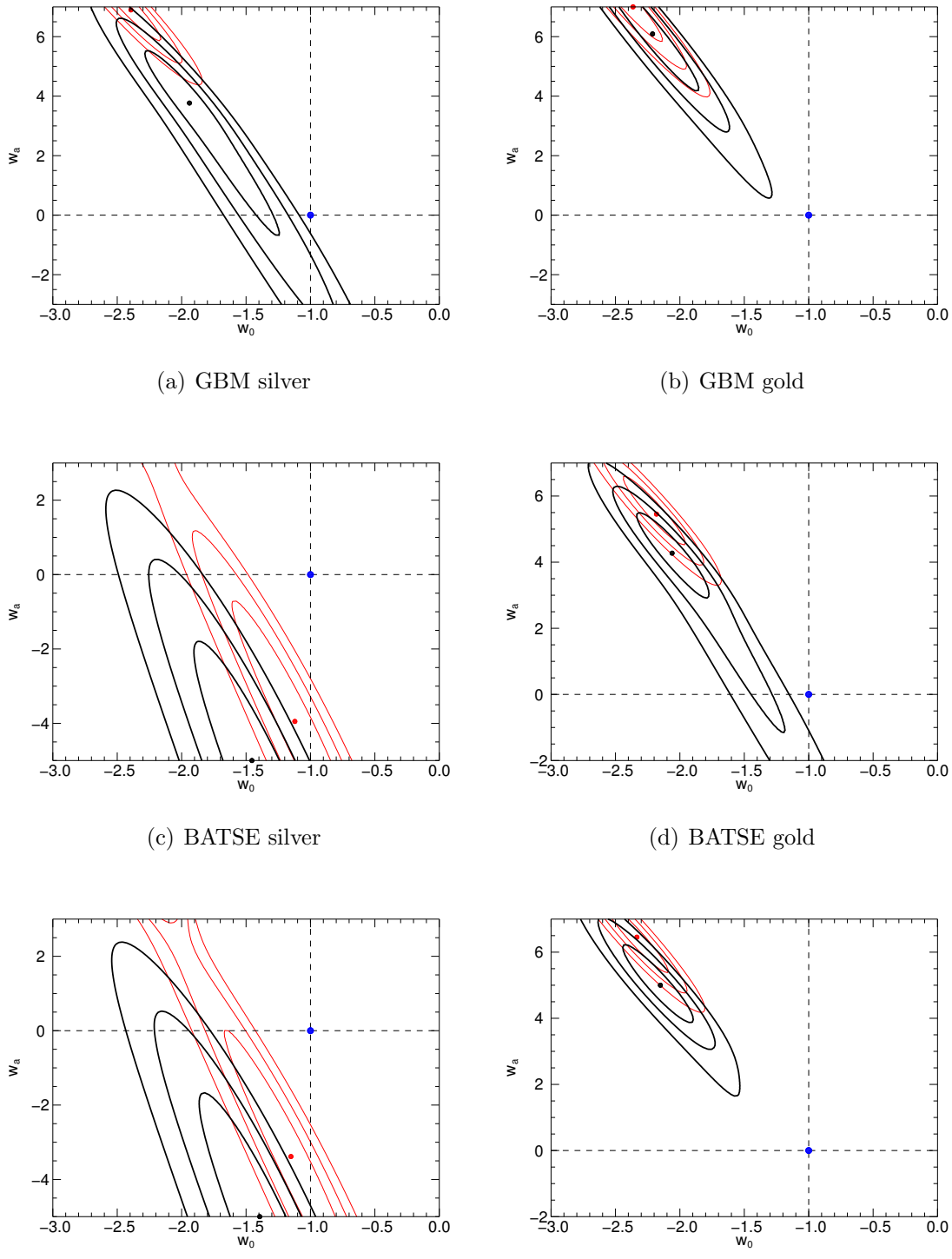

(a) GBM silver

(b) GBM gold

(c) BATSE silver

(d) BATSE gold

(e) All silver

(f) All gold

Figure 9.16: The joint probability distributions for the raw (red) and binned (black) data in the w_0–$w\prime$ plane. The blue point marks the value for a cosmological constant.

9.1.8 Ω_M–H_0 for a Flat Universe

The current recessional velocity of the objects in the universe, H_0 is an important quantity to determine as it sets a baseline for observation of $H(z)$. Although the estimation of H_0 has been well estimated to be 73.8 ± 2.4 [195], it is important to investigate the impact that observations from the matter-dominated era has on constraining H_0. The results from the calibration sample are shown in Figure 9.17. The best known value of H_0 is shown as well as the corresponding 1σ uncertainty. The calibration sample shows $> 3\sigma$ deviation from the current best known value for H_0, indicating that the SNe Ia alone predict a lower value for H_0. The best known values are $\Omega_M = 0.35^{+0.07}_{-0.07}$, $H_0 = 64.6^{+2.02}_{-2.02}$ for the unbinned data and $\Omega_M = 0.34^{+0.08}_{-0.06}$, $H_0 = 64.8^{+1.82}_{-2.02}$ for the binned data. It is apparent that decreasing the matter density causes an observed increase in H_0. The results from the GRB samples are shown in Figure 9.18. All samples show $> 3\sigma$ deviation from the currently best accepted values. The samples result in similar confidence regions as resulted from the calibration sample. This indicates that GRBs, like SNe Ia, tend to prefer a $60 < H_0 < 70$. The tabulated best fit values are show in Table 9.9.

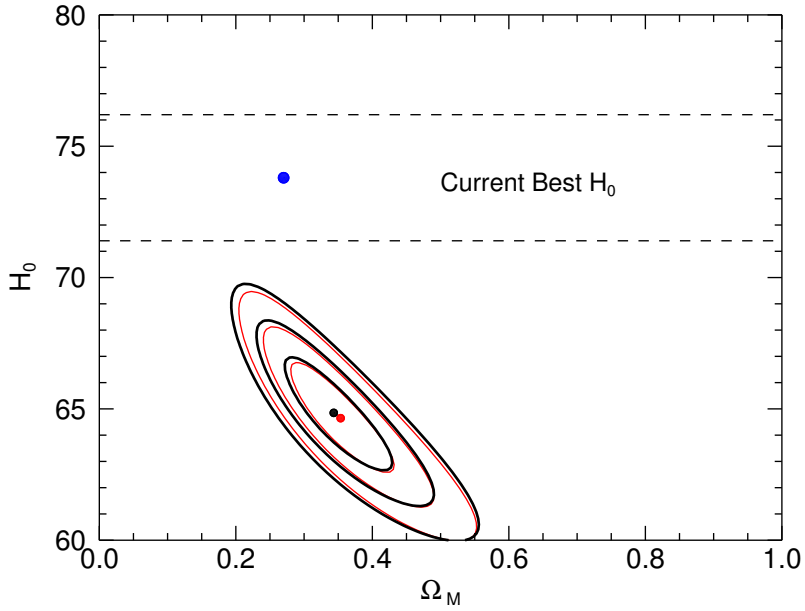

Figure 9.17: The joint probability distributions of Ω_M–H_0 for a flat universe from the calibration sample. The corresponding 1σ, 2σ, and 3σ contours are shown, and the blue point marks the concordant matter density. The best-fit parameters are $\Omega_M = 0.35^{+0.07}_{-0.07}$, $H_0 = 64.6^{+2.02}_{-2.02}$ with $\chi^2/\mathrm{dof} = 104/285$ for the raw data and $\Omega_M = 0.34^{+0.08}_{-0.06}$, $H_0 = 64.8^{+1.82}_{-2.02}$ with $\chi^2/\mathrm{dof} = 10/14$ for the binned data.

Table 9.9: Best fit parameters for Ω_M–H_0 for a flat universe

	Unbinned			**Binned**		
Sample	Ω_M	H_0	χ^2/dof	Ω_M	H_0	χ^2/dof
Calibration	$0.35^{+0.07}_{-0.07}$	$64.6^{+2.0}_{-2.0}$	104/285	$0.34^{+0.08}_{-0.06}$	$64.8^{+1.8}_{-2.0}$	10/14
GBM silver	$0.44^{+0.08}_{-0.07}$	$63.0^{+1.8}_{-1.8}$	257/409	$0.29^{+0.07}_{-0.06}$	$65.3^{+2.0}_{-2.0}$	26/18
GBM gold	$0.42^{+0.08}_{-0.07}$	$63.4^{+2.0}_{-1.8}$	195/330	$0.37^{+0.09}_{-0.07}$	$64.4^{+2.0}_{-2.0}$	24/16
BATSE silver	$0.24^{+0.04}_{-0.03}$	$64.4^{+1.4}_{-1.6}$	1655/903	$0.09^{+0.02}_{-0.02}$	$67.3^{+1.6}_{-1.2}$	226/28
BATSE gold	$0.41^{+0.07}_{-0.06}$	$63.4^{+1.8}_{-2.0}$	249/629	$0.30^{+0.06}_{-0.06}$	$65.1^{+2.0}_{-2.0}$	39/23
All silver	$0.28^{+0.04}_{-0.03}$	$63.6^{+1.4}_{-1.8}$	1830/1027	$0.11^{+0.02}_{-0.02}$	$66.9^{+1.4}_{-1.6}$	245/30
All gold	$0.46^{+0.08}_{-0.06}$	$62.6^{+1.8}_{-1.8}$	337/674	$0.34^{+0.08}_{-0.06}$	$64.2^{+2.0}_{-1.8}$	44/24

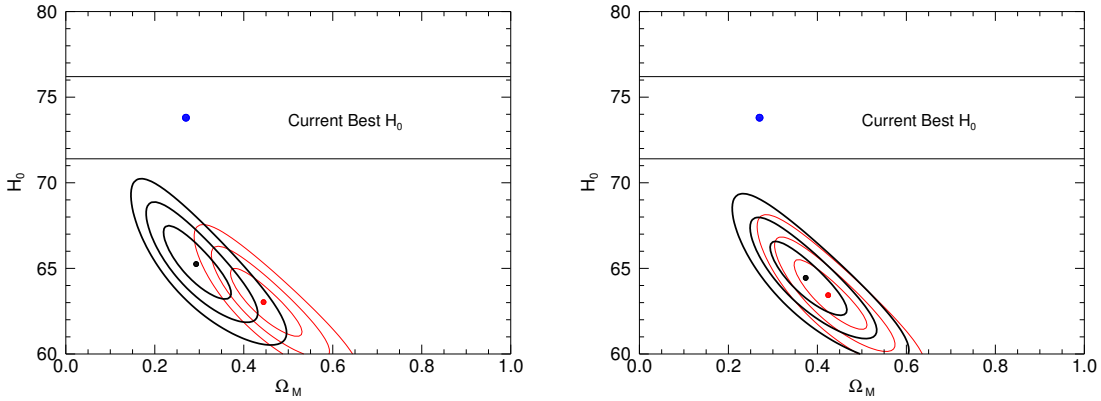

(a) GBM silver

(b) GBM gold

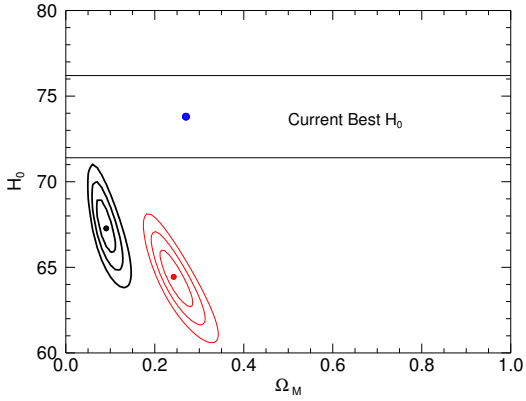

(c) BATSE silver

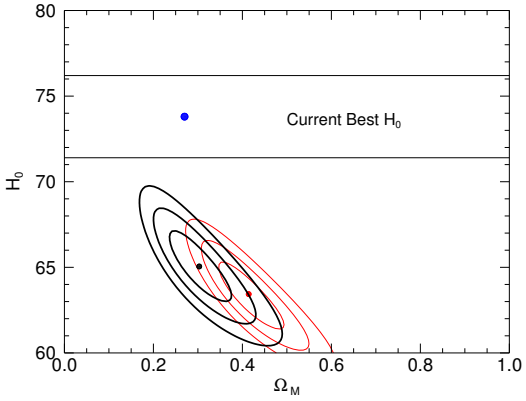

(d) BATSE gold

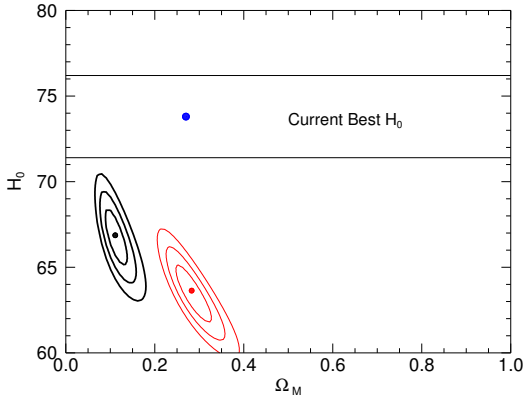

(e) All silver

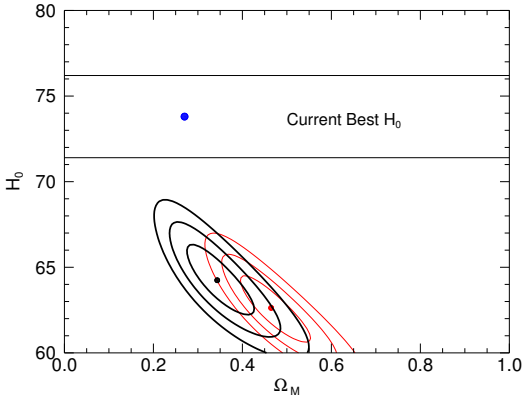

(f) All gold

Figure 9.18: The joint probability distributions for the raw (red) and binned (black) data in the Ω_M–H_0 plane. The blue point marks the concordance value for Ω_M.

9.1.9 H_0–w_0 for a Flat Universe

It is also of interest to investigate the connection between H_0 and the constant equation of state w_0. Assuming $\Omega_M = 0.27$ and a flat universe, the χ^2 map for the calibration sample was completed and is shown in Figure 9.19. The best known value for H_0 and the 1σ uncertainty is shown as well as the line denoting a cosmological constant and the point representing a ΛCDM universe. The best fit values are

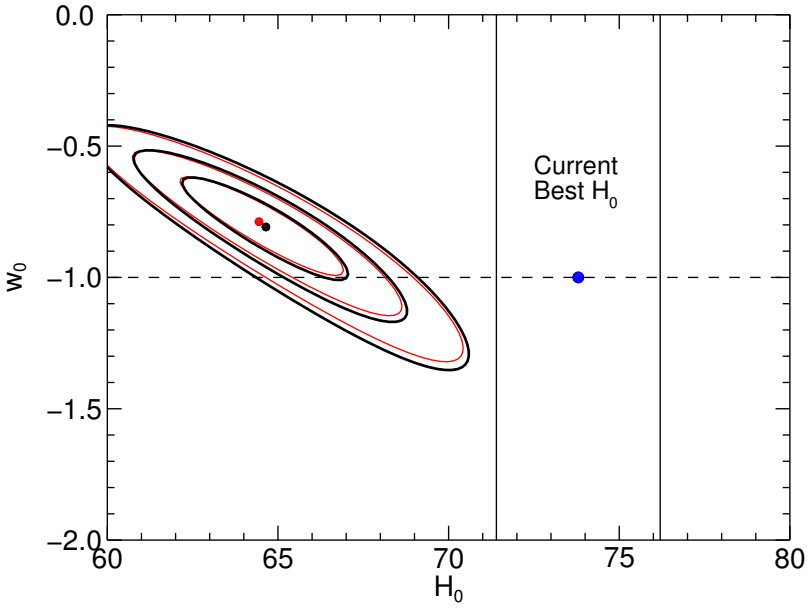

Figure 9.19: The joint probability distributions of H_0–w_0 for a flat universe from the calibration sample. The corresponding 1σ, 2σ, and 3σ contours are shown, and the blue point marks the value for a cosmological constant. The best-fit parameters are $H_0 = 64.4^{+2.2}_{-2.2}$, $w_0 = -0.79^{+0.20}_{-0.16}$ with $\chi^2/\mathrm{dof} = 105/285$ for the raw data and $H_0 = 64.6^{+2.2}_{-2.2}$, $w_0 = -0.81^{+0.18}_{-0.16}$ with $\chi^2/\mathrm{dof} = 10/14$ for the binned data.

$H_0 = 64.4^{+2.2}_{-2.2}$, $w_0 = -0.79^{+0.20}_{-0.16}$ for the unbinned data and $H_0 = 64.6^{+2.2}_{-2.2}$, $w_0 = -0.81^{+0.18}_{-0.16}$ for the binned data. The best known value for H_0 is $> 3\sigma$ from value found from the calibration sample. It was already noted in the previous section that

Table 9.10: Best fit parameters for H_0–w_0 for a flat universe

	Unbinned			**Binned**		
Sample	H_0	w_0	χ^2/dof	H_0	w_0	χ^2/dof
Calibration	$64.4^{+2.2}_{-2.2}$	$-0.79^{+0.20}_{-0.16}$	105/285	$64.6^{+2.2}_{-2.2}$	$-0.81^{+0.18}_{-0.16}$	10/14
GBM silver	$63.2^{+2.4}_{-2.6}$	$-0.65^{+0.22}_{-0.16}$	267/409	$65.3^{+2.2}_{-2.4}$	$-0.65^{+0.22}_{-0.20}$	26/18
GBM gold	$63.6^{+2.4}_{-2.2}$	$-0.69^{+0.16}_{-0.20}$	200/330	$64.6^{+2.2}_{-2.4}$	$-0.79^{+0.18}_{-0.22}$	26/16
BATSE silver	$67.9^{+2.2}_{-2.0}$	$-1.47^{+0.22}_{-0.26}$	1644/903	$64.6^{+1.8}_{-1.6}$	$-1.52^{+0.26}_{-0.22}$	272/28
BATSE gold	$64.0^{+2.8}_{-2.4}$	$-0.73^{+0.18}_{-0.22}$	259/629	$65.7^{+2.4}_{-2.4}$	$-0.99^{+0.20}_{-0.24}$	66/23
All silver	$69.1^{+2.2}_{-2.2}$	$-1.56^{+0.26}_{-0.39}$	1818/1027	$65.3^{+1.8}_{-1.8}$	$-1.52^{+0.26}_{-0.24}$	272/30
All gold	$62.6^{+2.8}_{-2.6}$	$-0.59^{+0.18}_{-0.20}$	352/674	$65.5^{+2.4}_{-2.6}$	$-0.93^{+0.22}_{-0.24}$	47/24

the SNe Ia prefer $H_0 < 70$, therefore it is not surprising that the calibration sample still under-predicts H_0. It is, interesting to note, however, that decreasing w_0 tends to shift H_0 closer to the nominal value. The cosmological constant is $\sim 1\sigma$ from the best value found from the calibration sample. The results from the remaining samples are shown in Figure 9.20. The $w_0 = -1$ line exists within 3σ of the best fit values for each sample and exists with 1σ for each of the gold sample. The best fit value of w_0 is found to be less than that from the calibration sample, resulting in a shift closer to the nominal H_0 value. As a result, the range of the current best H_0 is within 3σ of the values found in Figure 9.20(d) & (f). The best fit values for each sample along with the corresponding 1σ uncertainties are shown in Table 9.10.

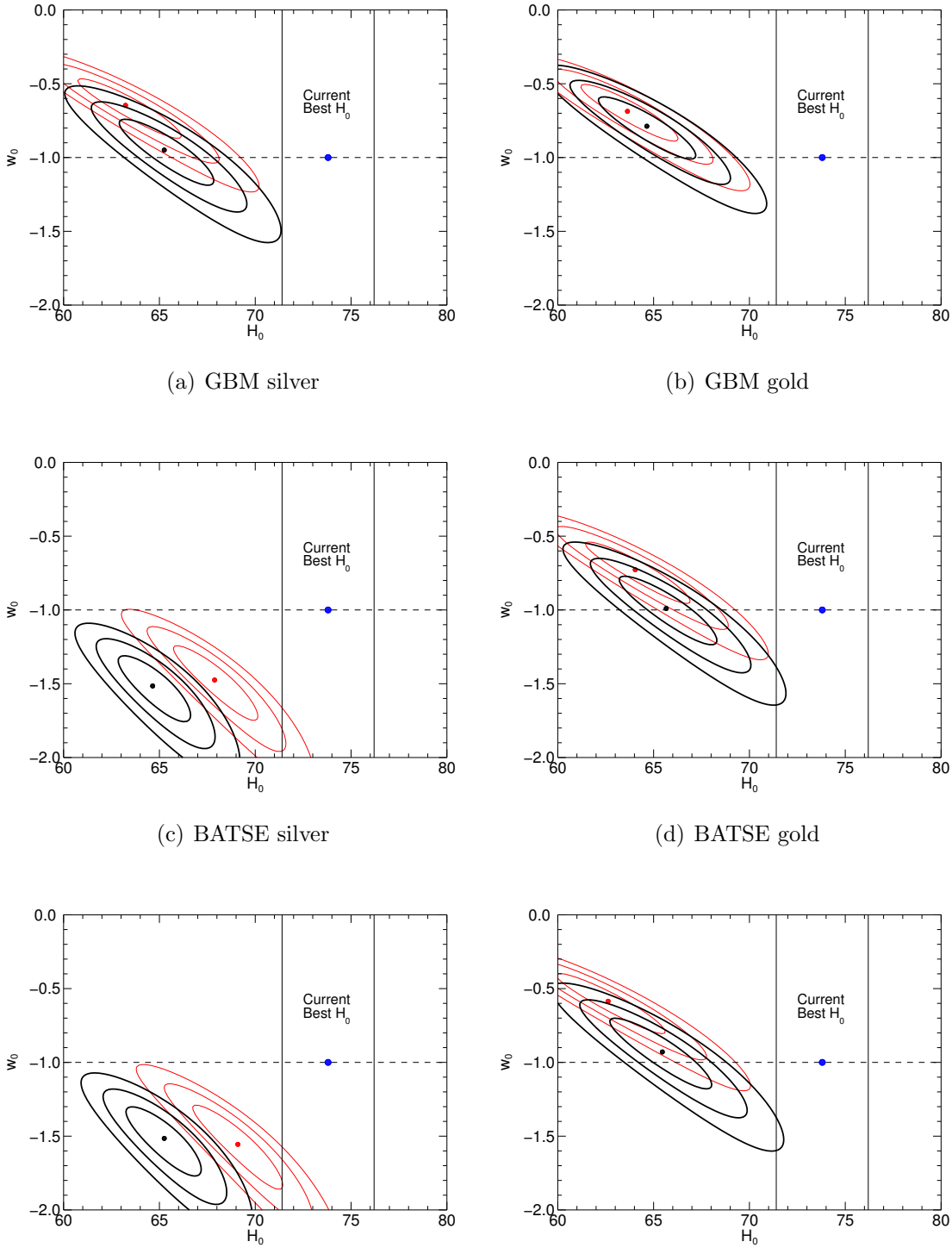

(a) GBM silver

(b) GBM gold

(c) BATSE silver

(d) BATSE gold

(e) All silver

(f) All gold

Figure 9.20: The joint probability distributions for the raw (red) and binned (black) data in the H_0–w_0 plane. The blue point marks the value for a cosmological constant.

9.2 Results from MCMC

Although much can be learned from the two-dimensional χ^2 maps of the previous section, certain constraining assumptions have to be made. In this section, I use Markov Chain Monte Carlo to estimate the probability density function (PDF) for each parameter simultaneously with two different priors. Since SNe Ia have shown a strong degeneracy between Ω_Λ and $w(z)$, each sample was examined using the prior that $\Omega_\Lambda = 0.73$, known hereafter as the weak prior. Additionally, since much of the $z > 1.5$ data have large uncertainties, to attempt to constrain H_0 and $w(z)$ as much as possible, each sample was also examined with the prior that $\Omega_M = 0.27$ and $\Omega_\Lambda = 0.73$, known hereafter as the strong prior. These priors are based on the current excellent constraint from WMAP + BAO + SNe Ia [196, 197]. Each MCMC was run for 10^5 links and the first 10^4 links were removed to allow for burn-in. The resulting chains were then binned into histograms to produce a close approximation to the true probability density distribution for each parameter. The location of the peak probability density, corresponding to the best fit parameter, of a Gaussian distribution is the mean of the distribution. However, the probability distributions are not always similar to Gaussians, and may be heavily skewed. For this reason, to find the peak probability density, each distribution was smoothed with a boxcar average and the bin corresponding to the largest density of the smoothed distribution was selected. The corresponding 1σ confidence intervals were then selected by integrating the probability density distribution each direction starting from the peak probability density. This process was performed for each sample including the calibration sam-

ple and for a universe with a constant w_0, one with $w(z)$ following the Riess model, and finally $w(z)$ following the CPL model. Each set of probability distributions are presented with the unbinned data in red and shaded and the binned data in black and unshaded. The peak for each distribution is marked as well as the 1σ confidence interval.

9.2.1 Constant $w(z) = w_0$

Assuming that w_0 is a constant, separate of redshift, the MCMC was run for each sample. The tabulated preferred values and their corresponding 1σ uncertainties for all samples are contained in Table 9.11. The calibration sample is shown in Figure 9.21. The weak prior results in $\Omega_M \approx 0.4$ and $H_0 \approx 65$. The equation of state parameter is already well constrained at $w_0 \approx -1$, the fiducial value indicating that Ω_Λ is represented by a cosmological constant. The strong prior results in $H_0 \approx 65$ and finds $w_0 \approx -0.8$, which rejects the cosmological constant at just over 1σ.

The results from the GBM samples are shown in Figure 9.22 and Figure 9.23. The GBM silver sample with the weak prior finds $\Omega_M \approx 0.4$ for the binned data and $\Omega_M \approx 0.6$ for the unbinned data. The Hubble constant appears to prefer ≈ 66, which is typical for what is found with SNe Ia alone. The PDFs for w_0 show that the binned data prefer the $w_0 \approx -1$ region, while the unbinned data find $w_0 < -1.5$ and excludes the cosmological constant from the 1σ region. The GBM silver sample with the strong prior shifts H_0 slightly to ≈ 65 and both PDFs for w_0 are shifted to slightly larger values where $w_0 = -1$ is still contained within 1σ. The GBM gold sample with the weak prior finds $\Omega_M > 0.4$ for both unbinned and binned data and

the $H_0 \approx 66$. The PDF for w_0 shows that $w = -1$ is within 1σ for the binned data, but outside the 1σ confidence region for the unbinned data. The strong prior finds $H_0 \approx 65$ and $w_0 \approx -1$ with $w_0 = -1$ within 1σ for the binned data only.

The results from the BATSE samples are shown in Figure 9.24 and Figure 9.25. The BATSE silver sample with the weak prior finds $\Omega_M \approx 0.15$ for the binned data and $\Omega_M \approx 0.35$ for the unbinned data. H_0 appears to be shifted slightly to ≈ 67, which is typical for what is found with SNe Ia alone. The PDFs for w_0 show that the binned data prefer the $w_0 \approx -1.2$ region, while the unbinned data find $w_0 \approx -1.4$ and both exclude the cosmological constant from the 1σ region. The BATSE silver sample with the strong prior shifts H_0 slightly to a lower value, and the PDF of w_0 for the unbinned data is shifted to > -1 values, while the binned data is shifted to < -1.2, and both reject the cosmological constant at 1σ. The BATSE gold sample with the weak prior finds $\Omega_M \approx 0.4$ for the binned data and $\Omega_M > 0.5$ for the unbinned data. The Hubble constant is largely unchanged at ≈ 66, and the PDF for w_0 shows that $w = -1$ is within 1σ for the both datasets, which prefer the $w_0 < -1$ region. The strong prior finds $H_0 \approx 65$ and $w_0 \approx -1$ for the binned data, while $w_0 \approx -0.8$ with $w_0 = -1$ just outside 1σ for the unbinned data.

The results from the ALL samples are shown in Figure 9.26 and Figure 9.27. The ALL silver sample with the weak prior finds $\Omega_M \approx 0.15$ for the binned data and $\Omega_M \approx 0.6$ for the unbinned data. The Hubble constant appears to be shifted slightly to ≈ 67 for the binned data, while the unbinned data finds ≈ 66. The PDFs for w_0 show that the binned data prefer the $w_0 \approx -1.2$ region, while the unbinned data find $w_0 \approx -1.7$ and both exclude the cosmological constant from the 1σ region. The

ALL silver sample with the strong prior shifts H_0 slightly to a lower value for both datasets, and the PDF of w_0 for the unbinned data is shifted to > -1 values, while the binned data is shifted to ≈ -1.2, and both reject the cosmological constant at 1σ. The ALL gold sample with the weak prior finds $\Omega_M \approx 0.5$ for the binned data and $\Omega_M < 0.4$ for the unbinned data. The Hubble constant is largely unchanged at ≈ 66, and the PDF for w_0 shows that $w = -1$ is within 1σ for the binned dataset only, which prefers the $w_0 < -1$ region. The strong prior finds $H_0 \approx 65$ and $w_0 \approx -0.8$ for both datasets and the cosmological constant is within the 1σ region of the binned data only.

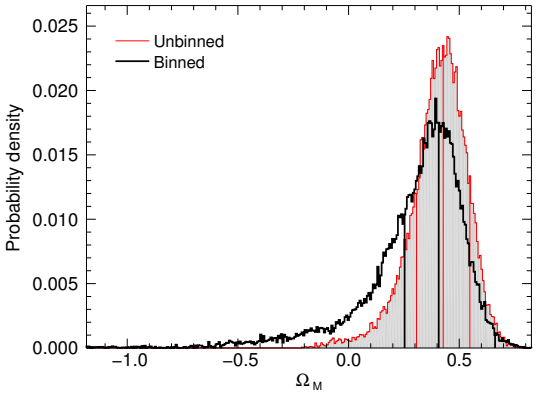

(a) Ω_M, Weak Prior

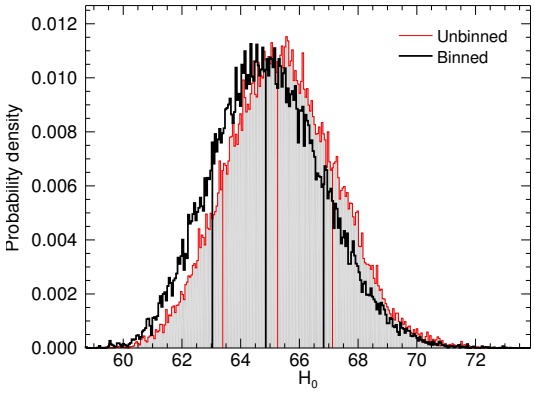

(b) H_0, Weak Prior

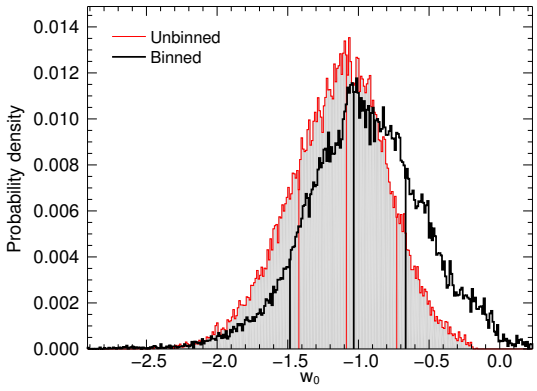

(c) w_0, Weak Prior

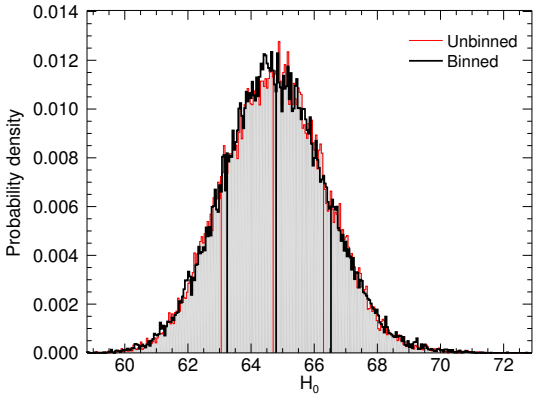

(d) H_0, Strong Prior

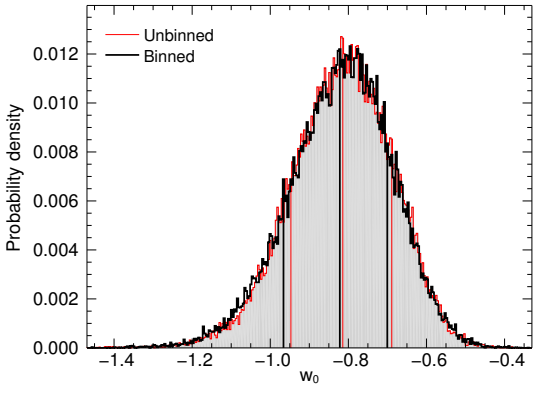

(e) w_0, Strong Prior

Figure 9.21: The probability distributions for the raw (red) and binned (black) data from the MCMC with a constant w_0 for the calibration sample.

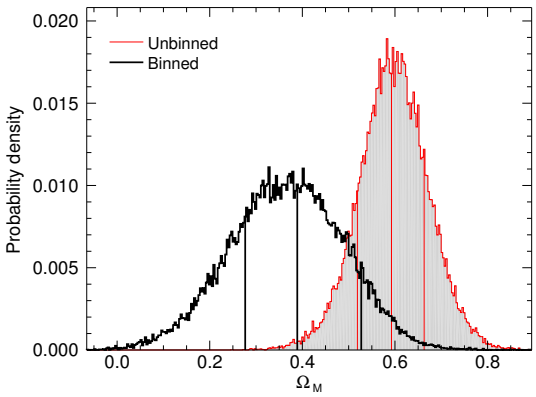

(a) Ω_M, Weak Prior

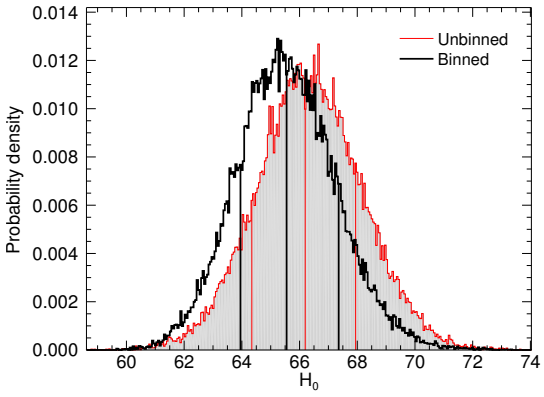

(b) H_0, Weak Prior

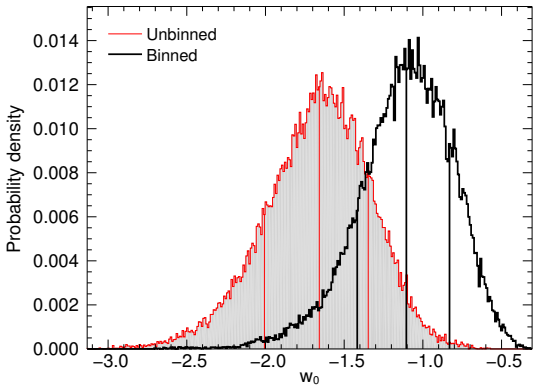

(c) w_0, Weak Prior

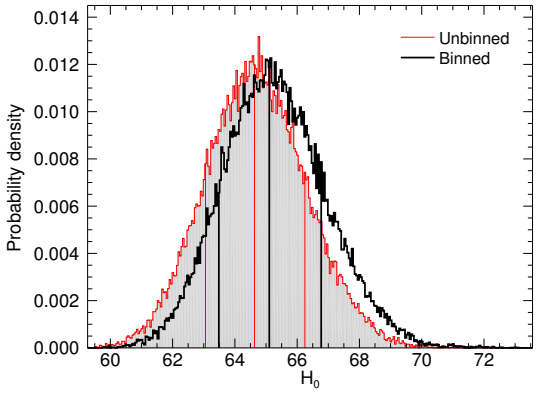

(d) H_0, Strong Prior

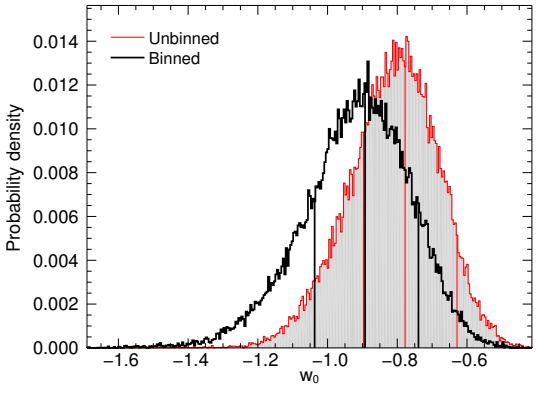

(e) w_0, Strong Prior

Figure 9.22: The probability distributions for the raw (red) and binned (black) data from the MCMC with a constant w_0 for the GBM silver sample.

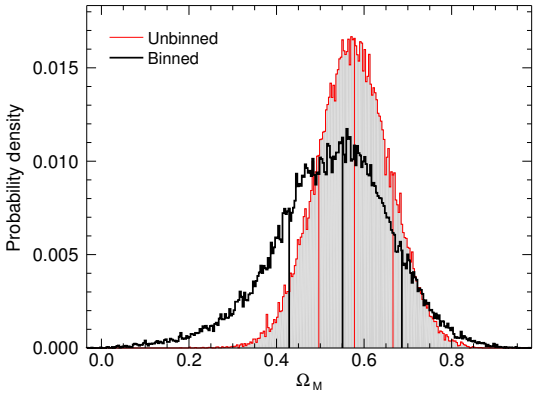

(a) Ω_M, Weak Prior

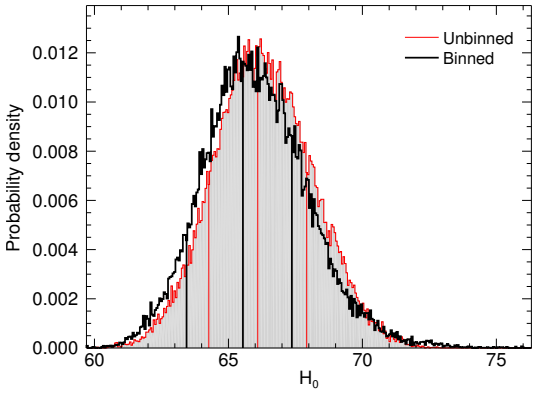

(b) H_0, Weak Prior

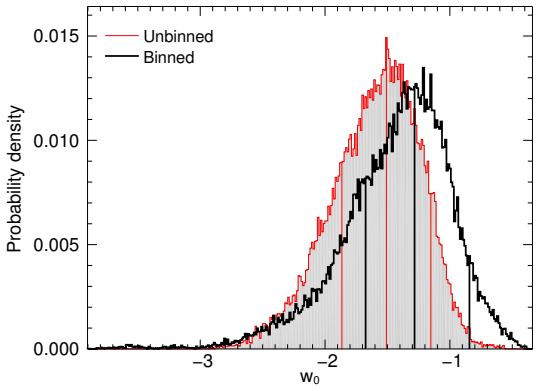

(c) w_0, Weak Prior

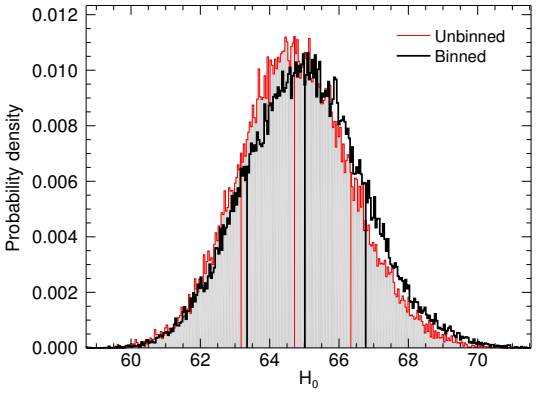

(d) H_0, Strong Prior

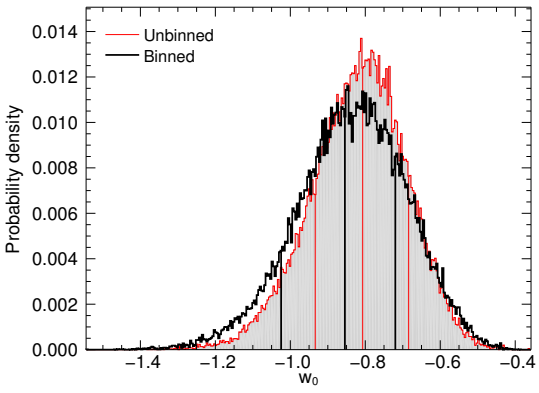

(e) w_0, Strong Prior

Figure 9.23: The probability distributions for the raw (red) and binned (black) data from the MCMC with a constant w_0 for the GBM gold sample.

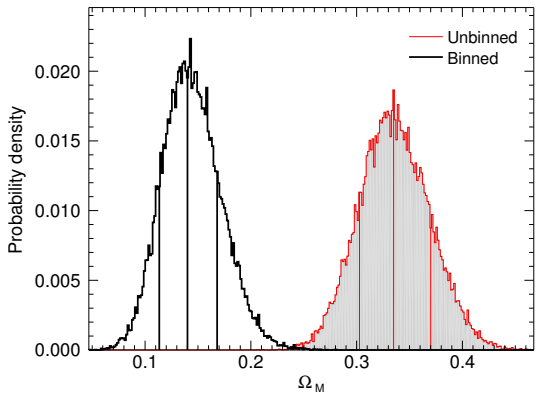

(a) Ω_M, Weak Prior

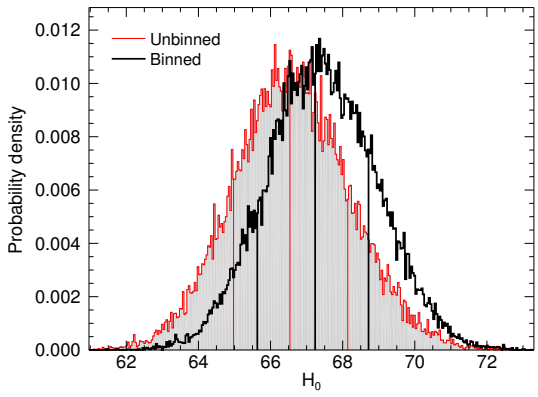

(b) H_0, Weak Prior

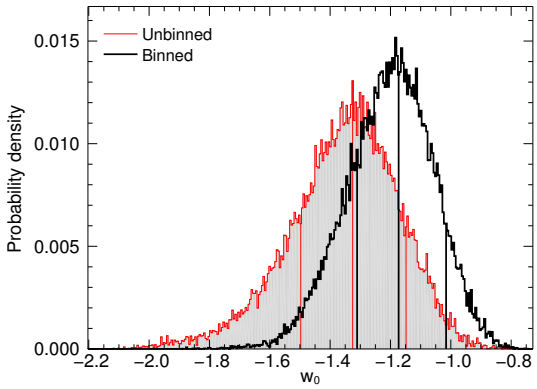

(c) w_0, Weak Prior

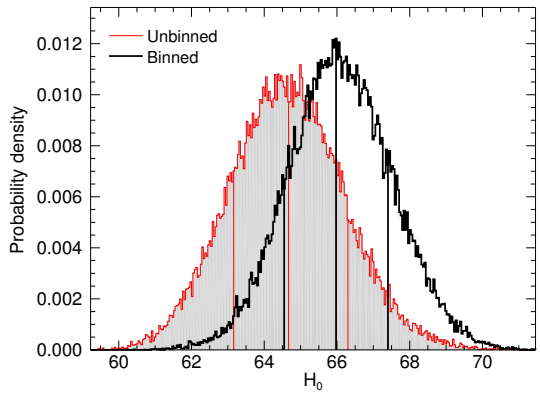

(d) H_0, Strong Prior

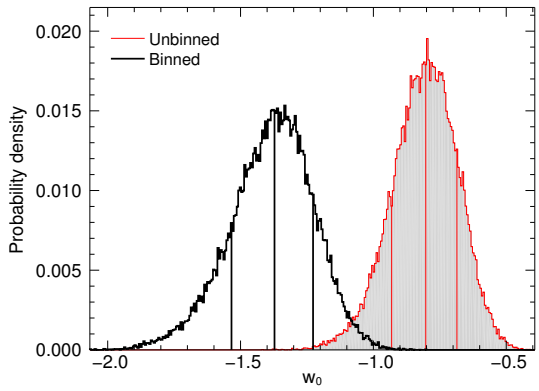

(e) w_0, Strong Prior

Figure 9.24: The probability distributions for the raw (red) and binned (black) data from the MCMC with a constant w_0 for the BATSE silver sample.

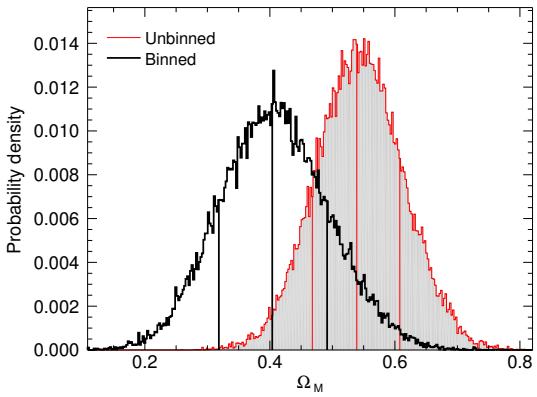

(a) Ω_M, Weak Prior

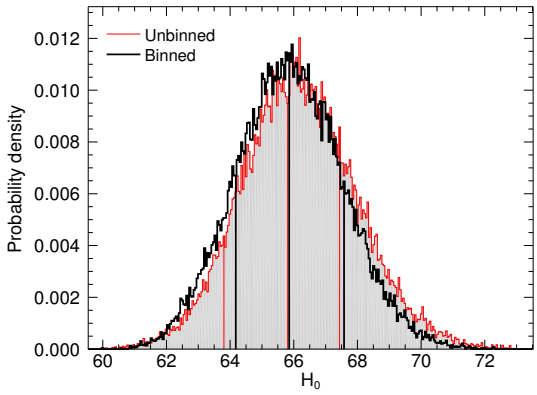

(b) H_0, Weak Prior

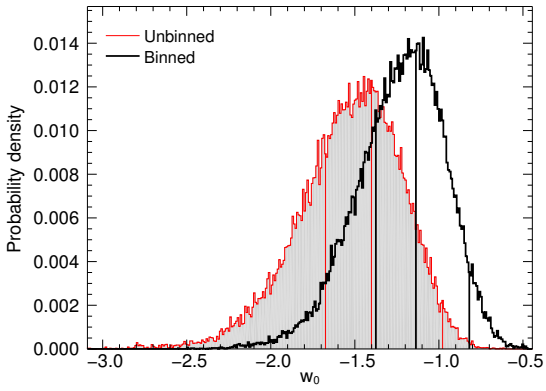

(c) w_0, Weak Prior

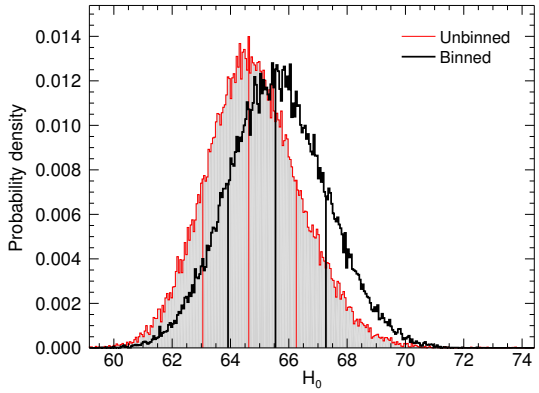

(d) H_0, Strong Prior

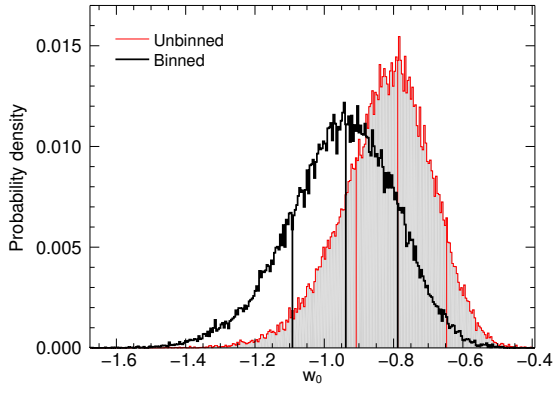

(e) w_0, Strong Prior

Figure 9.25: The probability distributions for the raw (red) and binned (black) data from the MCMC with a constant w_0 for the BATSE gold sample.

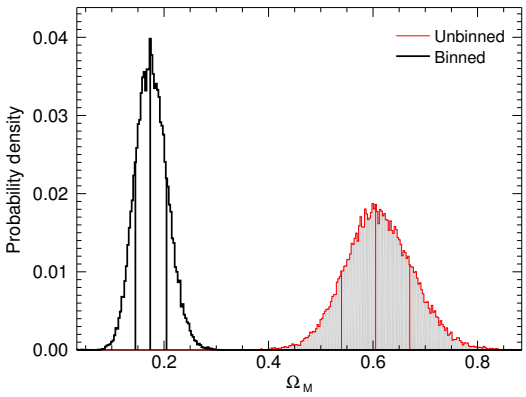

(a) Ω_M, Weak Prior

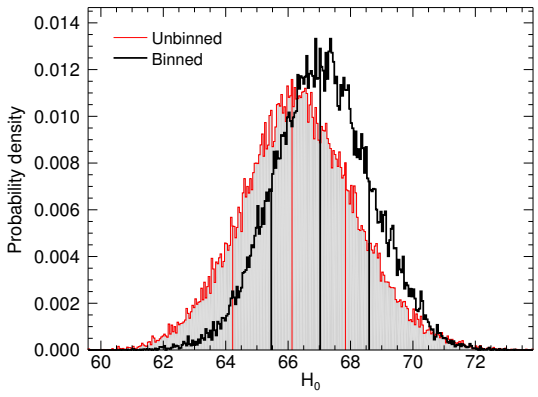

(b) H_0, Weak Prior

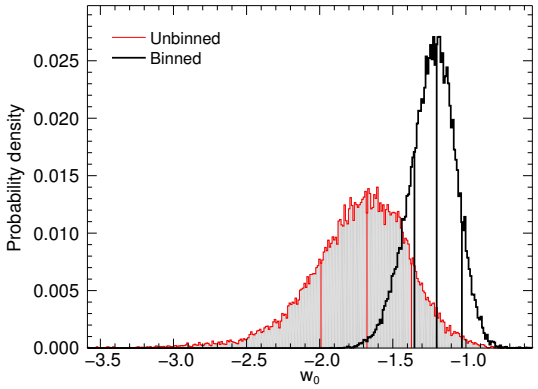

(c) w_0, Weak Prior

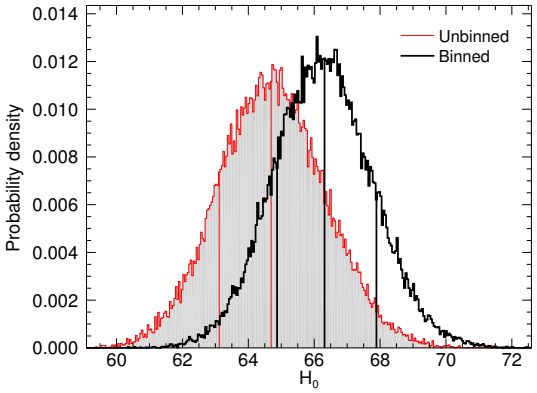

(d) H_0, Strong Prior

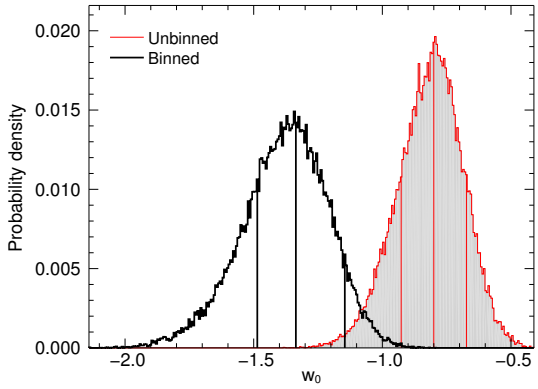

(e) w_0, Strong Prior

Figure 9.26: The probability distributions for the raw (red) and binned (black) data from the MCMC with a constant w_0 for the ALL silver sample.

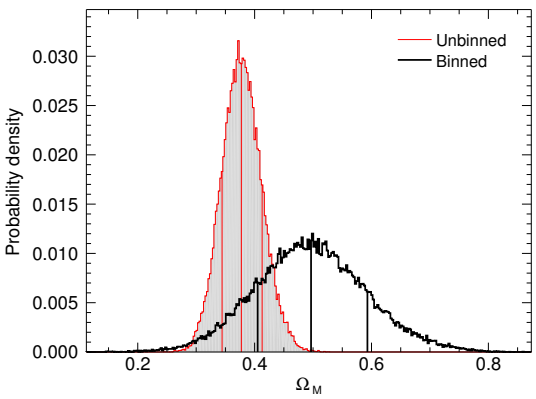

(a) Ω_M, Weak Prior

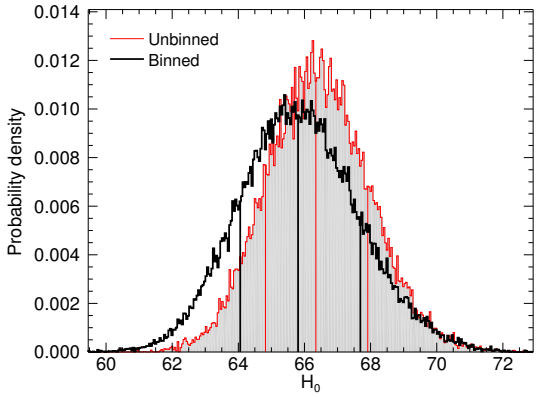

(b) H_0, Weak Prior

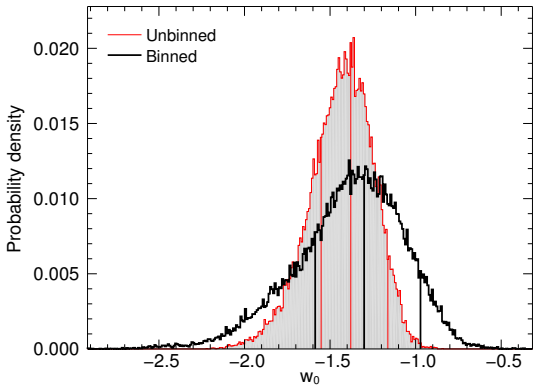

(c) w_0, Weak Prior

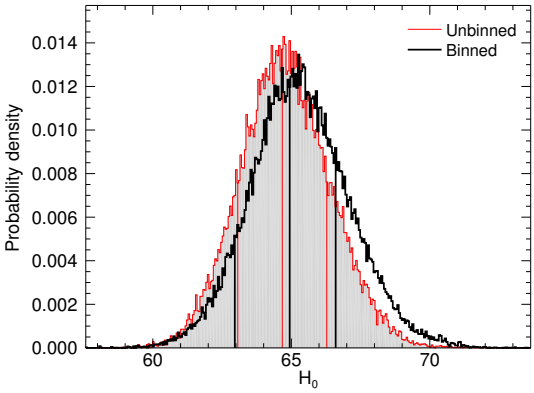

(d) H_0, Strong Prior

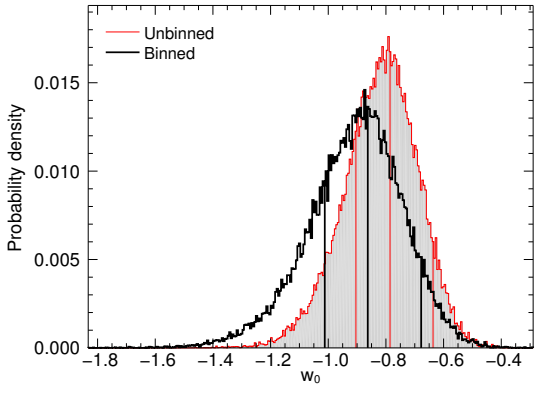

(e) w_0, Strong Prior

Figure 9.27: The probability distributions for the raw (red) and binned (black) data from the MCMC with a constant w_0 for the ALL gold sample.

Table 9.11: Best fit cosmological parameters for constant $w(z) = w_0$

		Weak Prior		**Strong Prior**	
Sample	Ω_M	H_0	w_0	H_0	w_0
Unbinned					
Calibration	$0.43^{+0.12}_{-0.12}$	$65.3^{+1.9}_{-1.9}$	$-1.09^{+0.36}_{-0.34}$	$64.7^{+1.6}_{-1.6}$	$-0.81^{+0.12}_{-0.13}$
GBM Silver	$0.59^{+0.07}_{-0.07}$	$66.2^{+1.7}_{-1.9}$	$-1.66^{+0.31}_{-0.35}$	$64.6^{+1.6}_{-1.6}$	$-0.78^{+0.15}_{-0.12}$
GBM Gold	$0.58^{+0.09}_{-0.08}$	$66.1^{+1.8}_{-1.8}$	$-1.51^{+0.36}_{-0.36}$	$64.7^{+1.6}_{-1.5}$	$-0.81^{+0.12}_{-0.13}$
BATSE Silver	$0.33^{+0.04}_{-0.03}$	$66.5^{+1.6}_{-1.6}$	$-1.33^{+0.18}_{-0.17}$	$64.7^{+1.6}_{-1.5}$	$-0.80^{+0.12}_{-0.13}$
BATSE Gold	$0.54^{+0.07}_{-0.07}$	$65.8^{+1.6}_{-2.0}$	$-1.40^{+0.42}_{-0.27}$	$64.6^{+1.6}_{-1.6}$	$-0.79^{+0.14}_{-0.12}$
ALL Silver	$0.61^{+0.07}_{-0.07}$	$66.1^{+1.7}_{-1.9}$	$-1.68^{+0.30}_{-0.31}$	$64.7^{+1.6}_{-1.6}$	$-0.80^{+0.13}_{-0.13}$
ALL Gold	$0.38^{+0.04}_{-0.03}$	$66.3^{+1.6}_{-1.5}$	$-1.38^{+0.22}_{-0.17}$	$64.7^{+1.6}_{-1.6}$	$-0.79^{+0.15}_{-0.11}$
Binned					
Calibration	$0.41^{+0.25}_{-0.15}$	$64.9^{+2.0}_{-1.8}$	$-1.03^{+0.37}_{-0.45}$	$64.8^{+1.7}_{-1.6}$	$-0.82^{+0.12}_{-0.14}$
GBM Silver	$0.39^{+0.14}_{-0.11}$	$65.6^{+1.8}_{-1.6}$	$-1.10^{+0.27}_{-0.31}$	$65.1^{+1.7}_{-1.6}$	$-0.89^{+0.15}_{-0.14}$
GBM Gold	$0.55^{+0.14}_{-0.12}$	$65.5^{+1.8}_{-2.1}$	$-1.28^{+0.44}_{-0.39}$	$65.0^{+1.8}_{-1.7}$	$-0.85^{+0.13}_{-0.17}$
BATSE Silver	$0.14^{+0.03}_{-0.03}$	$67.2^{+1.5}_{-1.6}$	$-1.17^{+0.16}_{-0.14}$	$66.0^{+1.4}_{-1.4}$	$-1.37^{+0.15}_{-0.16}$
BATSE Gold	$0.40^{+0.09}_{-0.09}$	$65.9^{+1.7}_{-1.7}$	$-1.14^{+0.32}_{-0.24}$	$65.5^{+1.7}_{-1.6}$	$-0.94^{+0.15}_{-0.15}$
ALL Silver	$0.17^{+0.03}_{-0.03}$	$67.0^{+1.6}_{-1.6}$	$-1.20^{+0.17}_{-0.15}$	$66.3^{+1.6}_{-1.4}$	$-1.34^{+0.19}_{-0.14}$
ALL Gold	$0.50^{+0.10}_{-0.09}$	$66.3^{+1.6}_{-1.5}$	$-1.30^{+0.33}_{-0.29}$	$64.9^{+1.7}_{-2.0}$	$-0.86^{+0.19}_{-0.15}$

9.2.2 Riess Cosmology

Assuming the Riess representation of $w(z)$, the MCMC was run for each sample. The tabulated preferred values and their corresponding 1σ uncertainties for all samples are contained in Table 9.12. The calibration sample is shown in Figure 9.28. The weak prior results in $\Omega_M \approx 0.6$ and $H_0 \approx 65$. The equation of state parameters are generally poorly constrained. While w_0 for the binned date is close to the cosmological constant value, the unbinned data exhibit two possible preferred values at $w_0 < -1$ and $w_0 > 0$. The w' parameter is completely unconstrained by the calibration data and its PDF indicates that the calibration data together with the weak prior is unable to determine w'. The strong prior results in $H_0 \approx 66$ and is able to constrain w_0 and w' much more adequately. w_0 is found to be < -1 although it easily contains $w_0 = -1$ with 1σ. The w' parameter is found to locate at > 0 and includes $w' = 0$ within 1σ.

The results from the GBM samples are shown in Figure 9.29 and Figure 9.30. The GBM silver sample with the weak prior finds a slightly lower Ω_M compared to the calibration sample, but with a long tail extending to negative matter densities. The PDFs for the $w(z)$ parameters are broad and the 1σ confidence region for w_0 spans from ~ -1.2 to > 0 for the unbinned data, while the confidence region for the binned data spans from $\sim= 0.8$ to ~ 0.4, which excludes $w_0 = -1$ at the 1σ level. The unbinned data constrain $w' > 0$ at the 1σ level and the binned data result in uncertainty down to $w' \approx -2$. The GBM silver sample with the strong prior forces $w_0 < -1$ such that the cosmological constant value is at $\sim 3\sigma$ level, while

the binned data still easily contain $w_0 = -1$ within 1σ. The w' parameter for the unbinned data is also forced far away from the $w' = 0$ cosmological constant value, although the binned data provides much less constraint and the possibility of $w' = 0$ is still valid within 1σ. The GBM gold sample with the weak prior finds Ω_M near its nominal value, however there exists a long tail in the PDF extending to negative matter densities. The PDF for w_0 shows that $w = -1$ is well within 1σ for the binned data, although the unbinned data exhibit two preferences that overlap at $w \approx -1$. The weak prior is not able to easily constrain w' and the PDF displays multiple peaks, indicating that a stable distribution could not be found. The strong prior constrains both w_0 and w' much more sufficiently than the weak prior, although the PDFs for w_0 are shifted to $w_0 < -1$ such that $w_0 = -1$ is outside of the 1σ confidence region for both unbinned and binned data. Similarly, the PDFs for w' are forced to $w' > 0$ such that w' is excluded at the 1σ level.

The BATSE samples are shown in Figure 9.31 and Figure 9.32. The BATSE silver sample with the weak prior finds Ω_M close to the nominal value for the unbinned data, yet the binned data have a PDF that is almost entirely concentrated in the negative matter density region. The corresponding w_0 and w' are well-constrained for the binned data, with w_0 showing preference toward > -1 values, although $w_0 = -1$ is within 1σ of the unbinned data preference. The w' PDF for the binned data is well-constrained at $w' > 0$, excluding the $w' = 0$ point, while the unbinned data are unconstrained, distributing about $-12 < w' < -1$. The strong prior for the BATSE silver sample adequately constrains $w_0 \approx -1.5$ for the unbinned data and $w_0 \approx 0.5$ for the binned data, excluding the cosmological constant value at over 1σ. The w'

parameter is constrained to ≈ 1.5 for the unbinned data and is not well-constrained for the binned data, with the 1σ region extending from ≈ -9.5 to ≈ -5.5. The BATSE gold sample with the weak prior prefers values for Ω_M near the nominal value, however, a significant tail extends into the negative matter density region. The w_0 parameter in this case prefers the region $-1 < w_0 < 0$, with $w_0 = -1$ within 1σ. The unbinned data primarily show preference to $w' > 0$, while the binned data show likely regions at $w' \approx 0.5$ and $w' \approx -2$, with the latter region largely unconstrained. The strong prior results in a strong preference of $w_0 \approx -1.25$ with $w_0 = -1$ at the border of the 1σ region for the binned data. The w' parameter shows a strong preference to > 0 values , with $w' = 0$ rejected at the 1σ level for both binned and unbinned data and a long tail to $w' < 0$ for the binned data.

The ALL samples are shown in Figure 9.33 and Figure 9.34. The ALL silver sample with the weak prior finds Ω_M near the nominal value for the unbinned data, but the binned data PDF is completely concentrated in the negative matter density region. The PDFs for w_0 are well-constrained with the unbinned data showing preference toward $w_0 \approx -0.2$ and containing $w_0 = -1$ within the 1σ region and the binned data showing preference toward $w_0 \approx -0.5$ and excluding the cosmological constant value. The w' value is constrained to > 0 for the binned data, and unconstrained for the unbinned data, spanning negative values to $w' < -10$. The strong prior combined with the ALL silver sample sufficiently constrain w_0 for the unbinned data at ≈ -2 and at ≈ 0.2 for the binned data. Both datasets reject the $w_0 = -1$ point at $\sim 3\sigma$ level. The unbinned data strongly prefer a $w' > 0$ value, rejecting the fiducial value at the 3σ level. The binned data, however, prefer $w' < 0$ and the 1σ region covers a

large area of parameter space $-8 < w' < -4$, but still reject the fiducial value at the 3σ level. The ALL gold sample with the strong prior finds a largely unconstrained PDF for Ω_M which peaks near the nominal value but possesses a significant tail to the negative matter density region. The PDF for w_0 is concentrated near the cosmological constant value, and the sample shows a strong preference to $w' > 0$, with $w' = 0$ excluded from the 1σ region. The strong prior results in good constraint of w_0 and w'. The sample prefers $w_0 \approx -1.5$ and rejects the cosmological constant value $w_0 = -1$ at the 1σ level. The sample also strongly prefers $w' > 1.5$ with the fiducial $w' = 0$ value rejected at the 3σ level.

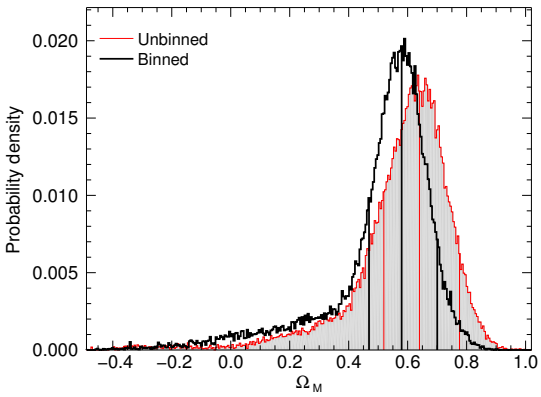

(a) Ω_M, Weak Prior

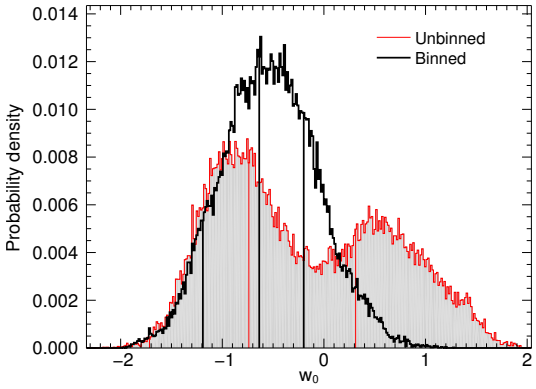

(b) w_0, Weak Prior

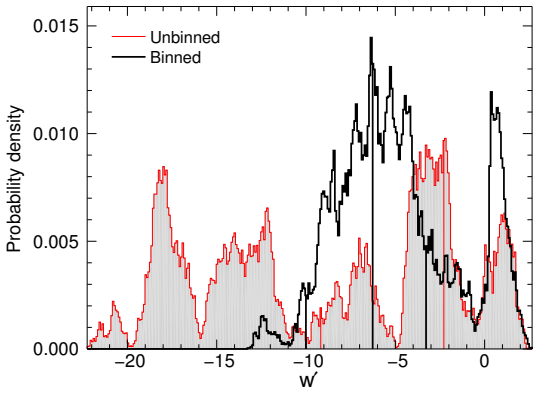

(c) w', Weak Prior

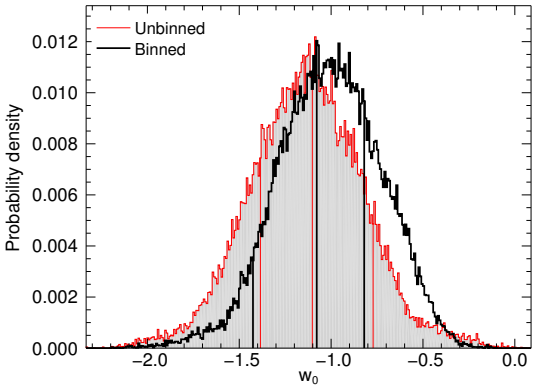

(d) w_0, Strong Prior

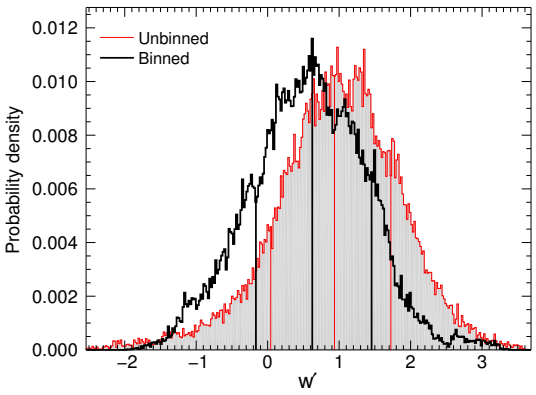

(e) w', Strong Prior

Figure 9.28: The probability distributions for the raw (red) and binned (black) data from the MCMC with a Riess $w(z)$ for the calibration sample.

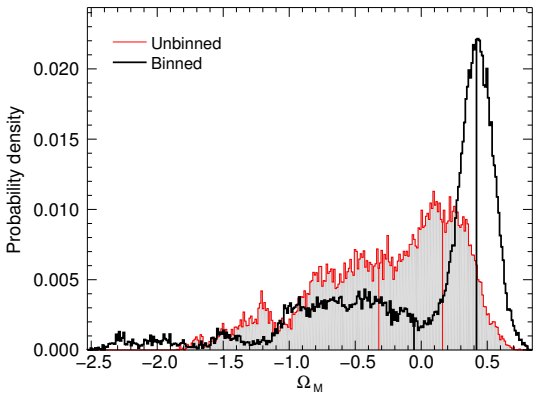

(a) Ω_M, Weak Prior

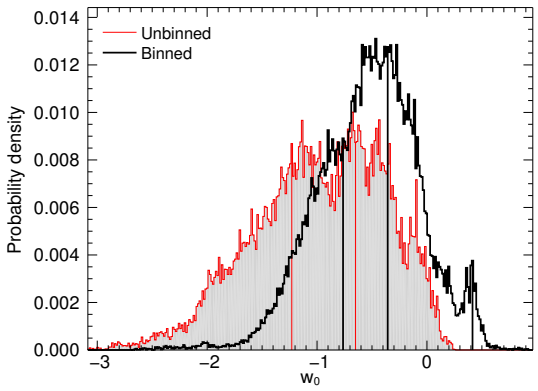

(b) w_0, Weak Prior

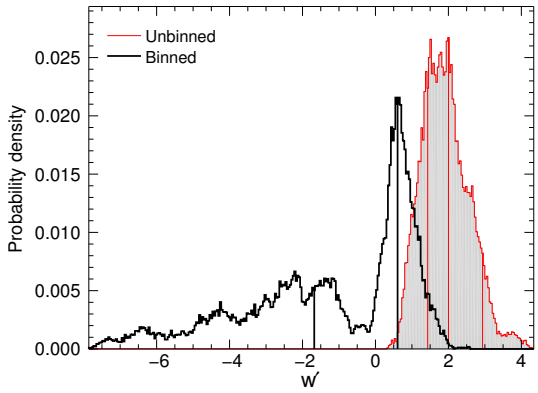

(c) w', Weak Prior

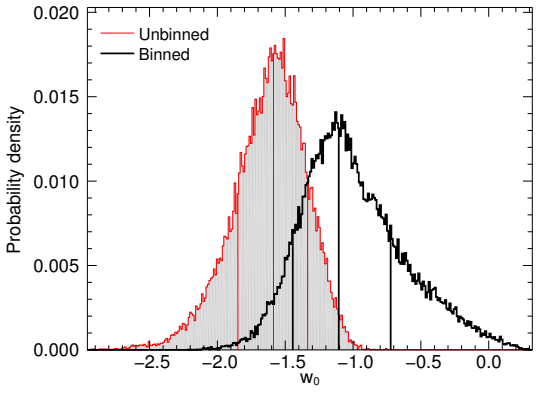

(d) w_0, Strong Prior

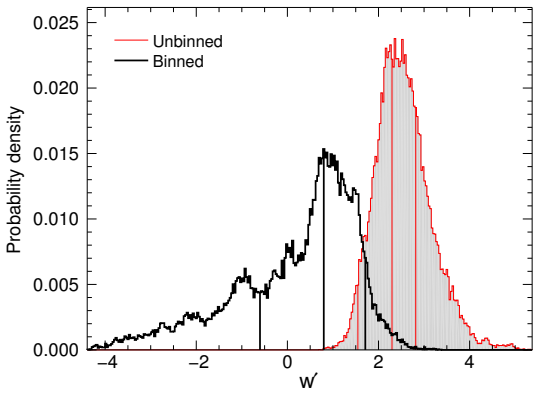

(e) w', Strong Prior

Figure 9.29: The probability distributions for the raw (red) and binned (black) data from the MCMC with a Riess $w(z)$ for the GBM silver sample.

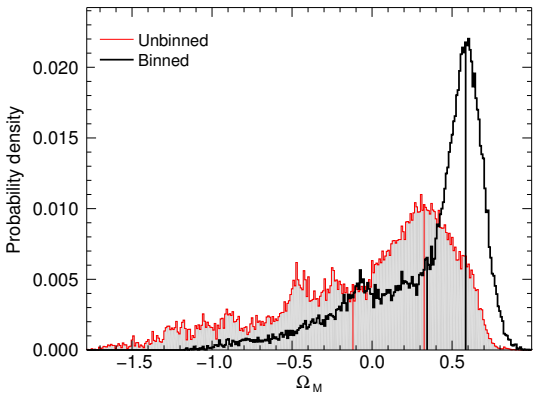

(a) Ω_M, Weak Prior

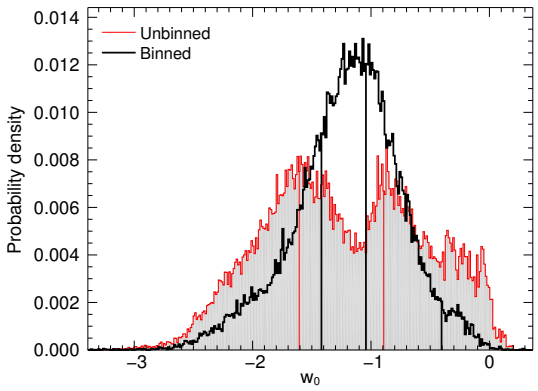

(b) w_0, Weak Prior

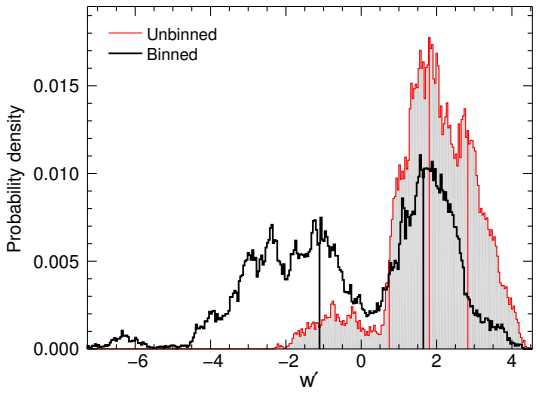

(c) w', Weak Prior

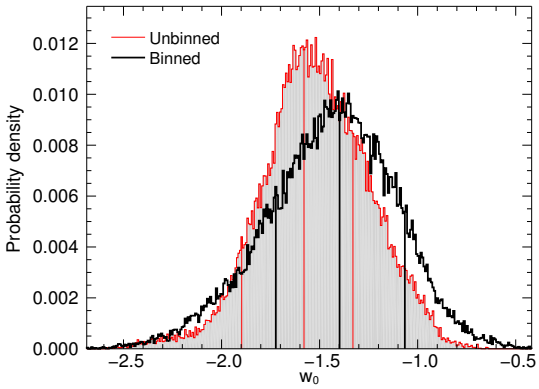

(d) w_0, Strong Prior

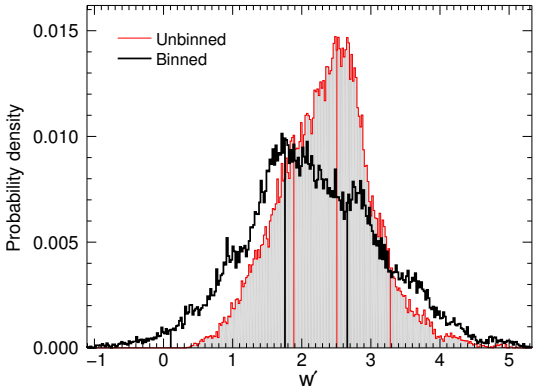

(e) w', Strong Prior

Figure 9.30: The probability distributions for the raw (red) and binned (black) data from the MCMC with a Riess $w(z)$ for the GBM gold sample.

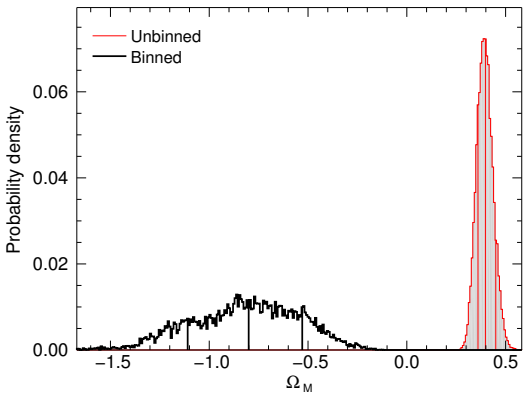

(a) Ω_M, Weak Prior

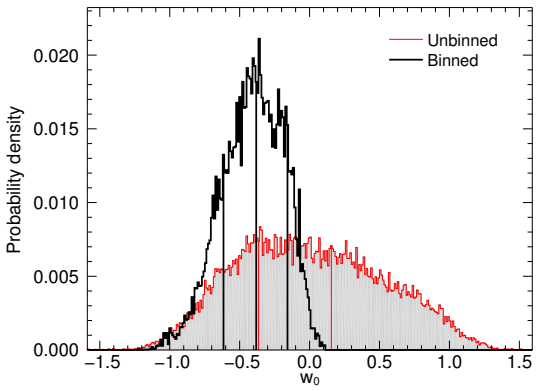

(b) w_0, Weak Prior

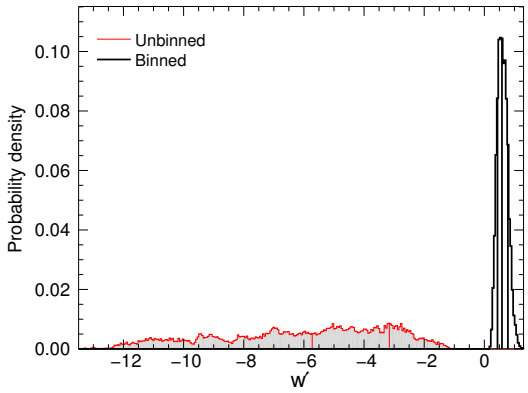

(c) w', Weak Prior

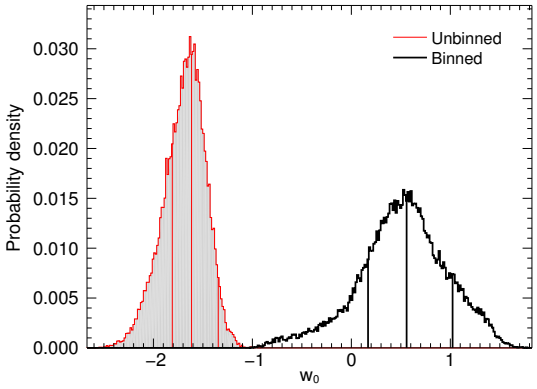

(d) w_0, Strong Prior

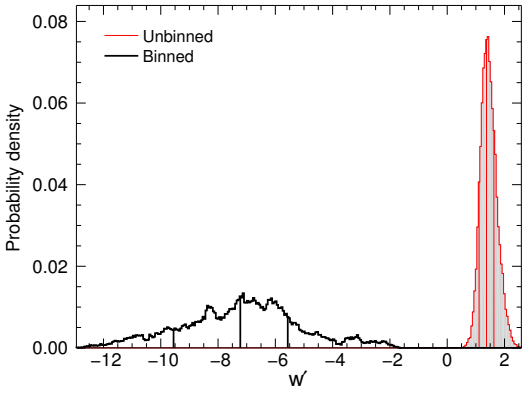

(e) w', Strong Prior

Figure 9.31: The probability distributions for the raw (red) and binned (black) data from the MCMC with a Riess $w(z)$ for the BATSE silver sample.

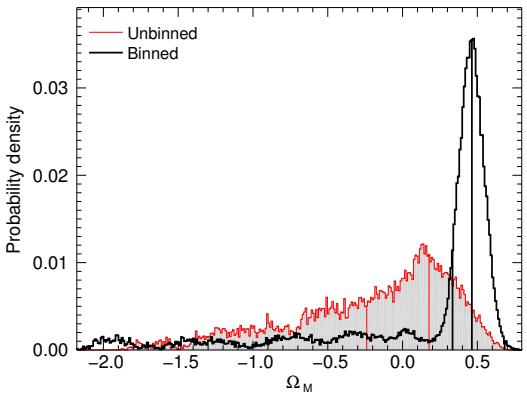

(a) Ω_M, Weak Prior

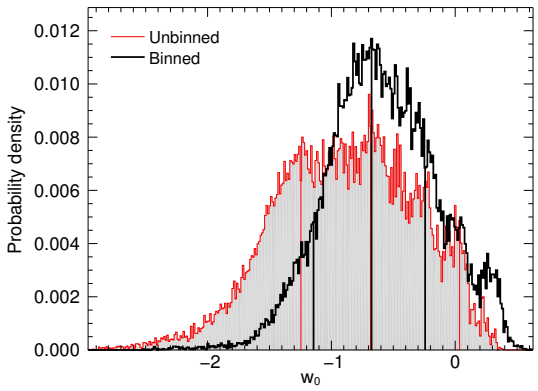

(b) w_0, Weak Prior

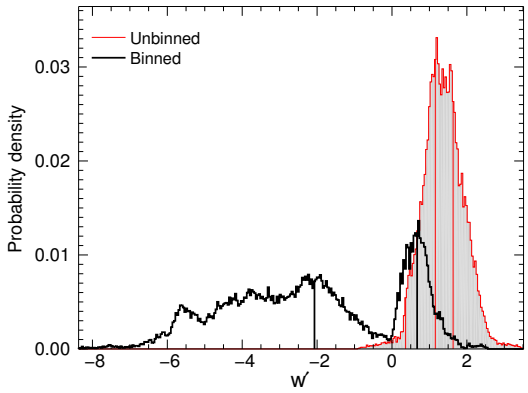

(c) w', Weak Prior

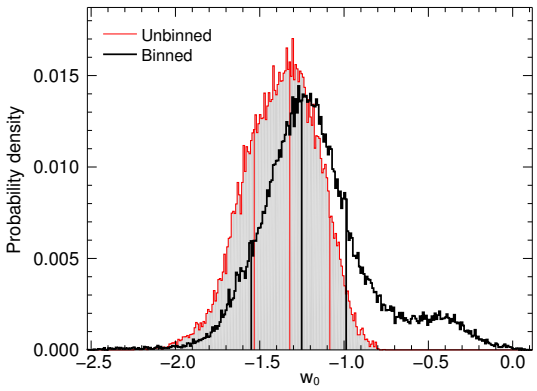

(d) w_0, Strong Prior

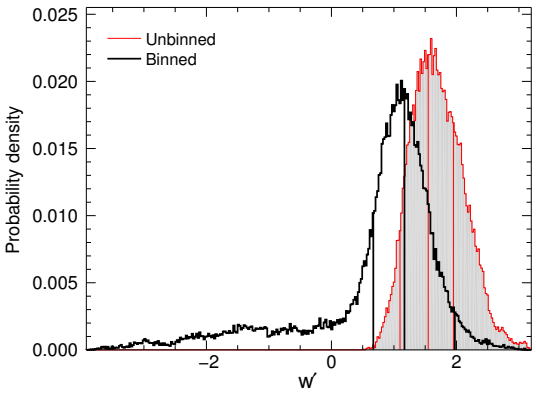

(e) w', Strong Prior

Figure 9.32: The probability distributions for the raw (red) and binned (black) data from the MCMC with a Riess $w(z)$ for the BATSE gold sample.

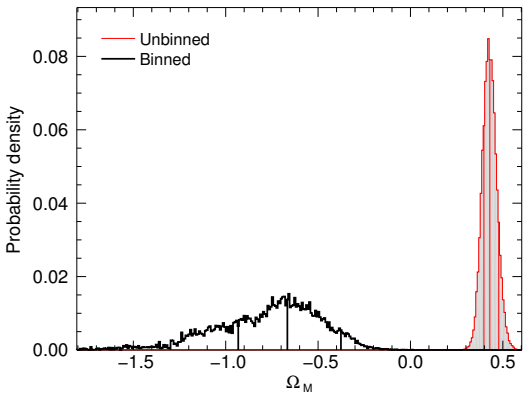

(a) Ω_M, Weak Prior

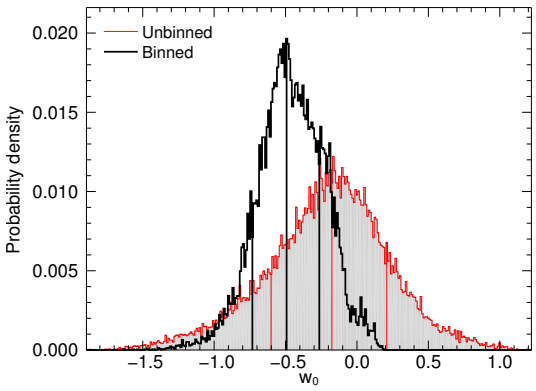

(b) w_0, Weak Prior

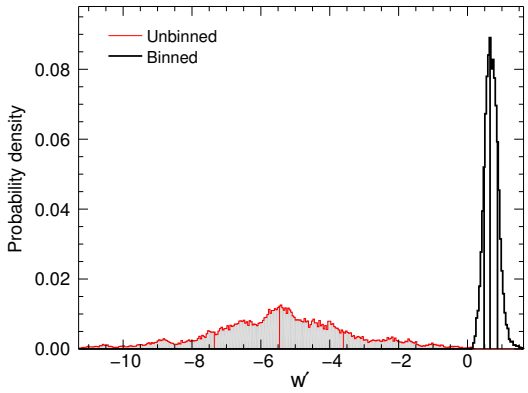

(c) w', Weak Prior

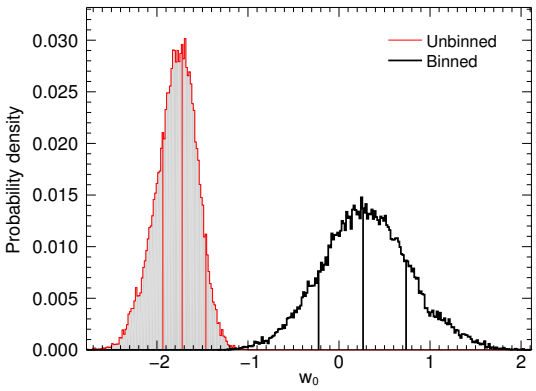

(d) w_0, Strong Prior

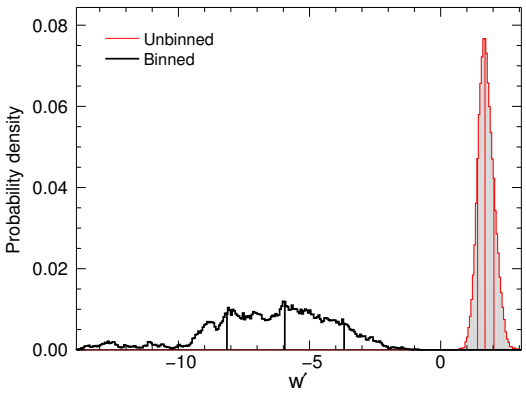

(e) w', Strong Prior

Figure 9.33: The probability distributions for the raw (red) and binned (black) data from the MCMC with a Riess $w(z)$ for the ALL silver sample.

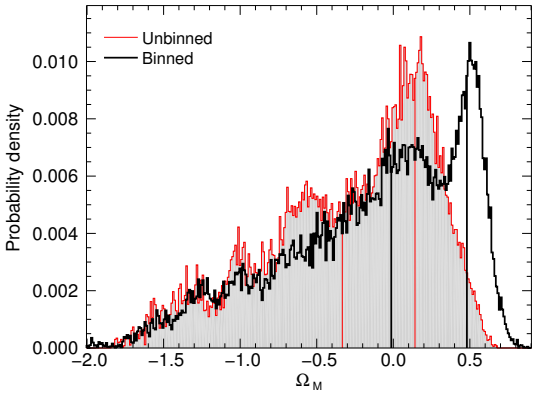

(a) Ω_M, Weak Prior

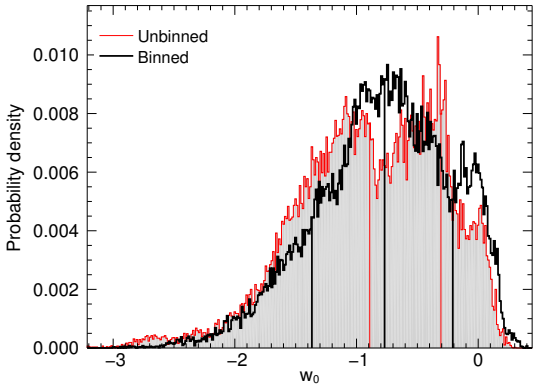

(b) w_0, Weak Prior

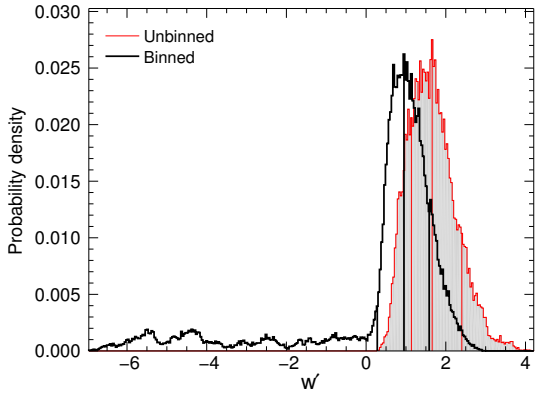

(c) w', Weak Prior

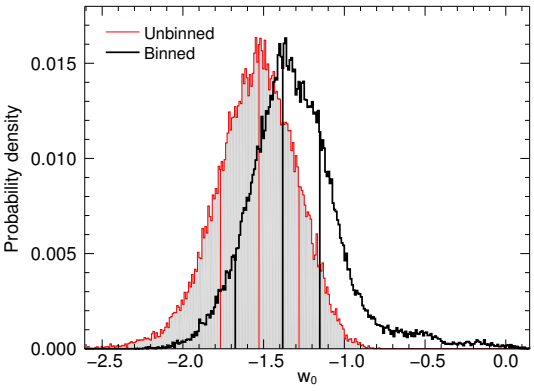

(d) w_0, Strong Prior

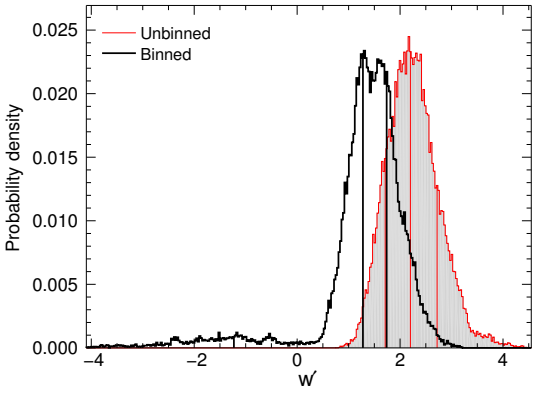

(e) w', Strong Prior

Figure 9.34: The probability distributions for the raw (red) and binned (black) data from the MCMC with a Riess $w(z)$ for the ALL gold sample.

Table 9.12: Best fit cosmological parameters for $w(z) = w_0 + w'z$

		Weak Prior			Strong Prior		
Sample	Ω_M	H_0	w_0	w'	H_0	w_0	w'
Unbinned							
Calibration	$0.64^{+0.14}_{-0.12}$	$64.7^{+2.3}_{-2.0}$	$-0.74^{+1.05}_{-0.98}$	$-2.28^{+4.65}_{-6.89}$	$65.7^{+1.9}_{-1.9}$	$-1.10^{+0.33}_{-0.29}$	$0.94^{+0.79}_{-0.89}$
GBM Silver	$0.16^{+0.63}_{-0.48}$	$66.0^{+1.6}_{-1.7}$	$-0.65^{+0.90}_{-0.58}$	$2.00^{+0.94}_{-0.57}$	$67.0^{+1.8}_{-1.9}$	$-1.59^{+0.25}_{-0.26}$	$2.30^{+0.52}_{-0.75}$
GBM Gold	$0.33^{+0.58}_{-0.44}$	$66.4^{+2.0}_{-2.0}$	$-1.61^{+0.71}_{-1.78}$	$1.81^{+1.02}_{-1.06}$	$66.8^{+1.8}_{-1.8}$	$-1.58^{+0.25}_{-0.32}$	$2.51^{+0.77}_{-0.62}$
BATSE Silver	$0.40^{+0.03}_{-0.04}$	$62.9^{+1.8}_{-1.9}$	$-0.36^{+0.52}_{-1.22}$	$-3.16^{+2.27}_{-2.56}$	$67.6^{+1.6}_{-1.7}$	$-1.61^{+0.27}_{-0.19}$	$1.37^{+0.26}_{-0.26}$
BATSE Gold	$0.18^{+0.55}_{-0.42}$	$65.9^{+1.9}_{-1.7}$	$-0.68^{+0.43}_{-0.47}$	$1.16^{+0.48}_{-0.79}$	$66.3^{+1.7}_{-1.8}$	$-1.32^{+0.24}_{-0.21}$	$1.55^{+0.40}_{-0.45}$
ALL Silver	$0.43^{+0.05}_{-0.03}$	$63.1^{+1.8}_{-1.8}$	$-0.18^{+0.38}_{-0.43}$	$-5.46^{+1.85}_{-1.89}$	$68.2^{+1.8}_{-1.6}$	$-1.72^{+0.26}_{-0.20}$	$1.69^{+0.34}_{-0.28}$
ALL Gold	$0.14^{+0.53}_{-0.47}$	$66.0^{+1.9}_{-1.7}$	$-0.31^{+0.61}_{-0.59}$	$1.66^{+0.74}_{-0.52}$	$67.2^{+1.9}_{-1.8}$	$-1.53^{+0.25}_{-0.24}$	$2.20^{+0.52}_{-0.49}$
Binned							
Calibration	$0.58^{+0.12}_{-0.11}$	$64.6^{+1.8}_{-1.8}$	$-0.64^{+0.44}_{-0.55}$	$-6.27^{+2.99}_{-3.74}$	$65.4^{+1.9}_{-1.7}$	$-1.09^{+0.26}_{-0.55}$	$0.62^{+0.83}_{-0.79}$
GBM Silver	$0.42^{+0.41}_{-0.47}$	$64.6^{+1.7}_{-1.8}$	$-0.36^{+0.77}_{-0.41}$	$0.61^{+2.00}_{-2.28}$	$65.6^{+1.9}_{-1.9}$	$-1.11^{+0.38}_{-0.33}$	$0.80^{+0.91}_{-1.40}$
GBM Gold	$0.58^{+0.41}_{-0.24}$	$65.8^{+1.9}_{-1.8}$	$-1.04^{+0.64}_{-0.38}$	$1.65^{+2.68}_{-2.76}$	$66.6^{+1.9}_{-1.9}$	$-1.40^{+0.33}_{-0.32}$	$1.76^{+0.90}_{-1.65}$
BATSE Silver	$0.80^{+0.27}_{-0.31}$	$68.5^{+1.5}_{-1.3}$	$-0.38^{+0.22}_{-0.23}$	$-3.16^{+0.20}_{-0.15}$	$60.9^{+1.8}_{-1.7}$	$0.56^{+0.46}_{-0.39}$	$-7.32^{+1.66}_{-2.33}$
BATSE Gold	$0.46^{+0.22}_{-0.13}$	$65.0^{+1.9}_{-1.7}$	$-0.49^{+0.23}_{-0.24}$	$0.67^{+1.87}_{-2.74}$	$66.3^{+1.7}_{-1.8}$	$-1.25^{+0.26}_{-0.30}$	$1.17^{+0.81}_{-0.50}$
ALL Silver	$0.67^{+0.29}_{-0.27}$	$68.2^{+1.5}_{-1.3}$	$-0.49^{+0.23}_{-0.24}$	$0.66^{+0.22}_{-0.17}$	$61.8^{+1.8}_{-1.7}$	$0.26^{+0.47}_{-0.49}$	$-5.94^{+2.26}_{-2.21}$
ALL Gold	$0.48^{+0.40}_{-0.49}$	$65.4^{+1.8}_{-1.7}$	$-0.77^{+0.56}_{-0.60}$	$0.95^{+0.63}_{-0.67}$	$66.5^{+1.8}_{-1.7}$	$-1.38^{+0.23}_{-0.29}$	$1.28^{+0.46}_{-2.51}$

9.2.3 CPL Cosmology

Assuming the CPL representation of $w(z)$, the MCMC was run for each sample. The tabulated preferred values and their corresponding 1σ uncertainties for all samples are contained in Table 9.13. The calibration sample is shown in Figure 9.35. The weak prior results in an unconstrained Ω_M for the unbinned data and $\Omega_M \approx 0.4$ for the binned data with a long tail in the PDF extending into the negative matter density region. The equation of state parameters are generally poorly constrained. While w_0 for the binned date is close to the cosmological constant value, the unbinned data exhibit two possible preferred values at $w_0 < -1$ and $w_0 \approx 0$. The w_a parameter is completely unconstrained by the binned calibration data and its PDF indicates that the calibration data together with the weak prior is unable to determine w_a. The unbinned calibration data finds $w_a > 0$ with a broad PDF. The strong prior is able to constrain w_0, which includes the cosmological constant value within the 1σ confidence level for both unbinned and binned data. The value for w_a is still unconstrained, as the MCMC is unable to reach a stable distribution. The region of $-9 < w_a < 6$ is contained within 3σ.

The results from the GBM samples are shown in Figure 9.36 and Figure 9.37. The GBM silver sample with the weak prior finds $\Omega_M \approx 0.2$, but the unbinned data show long tails that extend into the $\Omega_M < 0$ and $\Omega_M > 1$, while the binned data PDF has a long tail extending to negative matter densities. The PDFs for the $w(z)$ parameters are broad and the 1σ confidence region for w_0 spans from ~ -5.0 to ~ -1.5 for the unbinned data, while the confidence region for the binned data spans

from ~ -2.0 to ~ -0.4, which includes $w_0 = -1$ at the 1σ level. The unbinned data cannot adequately constrain w_a with spikes in the PDF at > 4 but with a long tail and another preference at ≈ 0. The binned data finds $w_a \approx 2$ and excludes $w_a = 0$ at the 1σ level. The GBM silver sample constrains w_0 and w_a much more sufficiently. w_0 for the unbinned data is found to prefer $w_0 = -1$ but includes the cosmological constant value within 1σ. The binned data finds $w_0 \approx -0.5$ and excludes $w_0 = -1$ at the 1σ level. The w_a parameter for the unbinned data is forced far away from the $w_a = 0$ cosmological constant value, although the binned data provides much less constraint and the possibility of $w_a = 0$ is still valid within 1σ. The GBM gold sample with the weak prior finds Ω_M larger than its nominal value, and there exists a long tail in the PDF of the binned data extending to negative matter densities. The PDF for w_0 shows that $w = -1$ is well within 1σ for the binned data, although the unbinned data rejects the cosmological constant at 1σ. The weak prior is not able to easily constrain w_a and the PDFs displays multiple peaks, indicating that a stable distribution could not be found. The strong prior constrains $w_0 < 1$ for the binned data and rejects $w_0 = -1$ at the 1σ level. The unbinned data is much broader and includes the cosmological constant at the 1σ level. Similarly, the PDFs for w_a are broad but exclude $w_a = 0$ at the 3σ level.

The BATSE samples are shown in Figure 9.38 and Figure 9.39. The BATSE silver sample with the weak prior finds Ω_M close to the nominal value for the binned data, yet the unbinned data have a PDF that is almost entirely concentrated in the negative matter density region. The corresponding w_0 and w_a are well-constrained with w_0 showing preference toward < -1 values, although $w_0 = -1$ is within 1σ of

both the binned and unbinned data PDF. The w_a PDF for the binned data is well-constrained at $w_a \approx 0$, while the unbinned data prefer $w_a \approx -0.5$ and includes $w_a = 0$ at the 1σ level. The strong prior for the BATSE silver sample adequately constrains $w_0 \approx -1.5$ for the unbinned data and $w_0 \approx 0.5$ for the binned data, excluding the cosmological constant value at over 1σ. The w_a parameter is constrained to ≈ -2 for the unbinned data and includes $w_a = 0$ at the 1σ level. The binned data show preference to an extreme value at $w_a \approx -10$. The BATSE gold sample with the weak prior prefers values for Ω_M near the nominal value, however, a significant tail extends into the negative matter density region. The w_0 parameter in this case prefers the region $-2 < w_0 < 0$, with $w_0 = -1$ within 1σ region. The unbinned data primarily show preference to $w_a < 0$, while the binned data are unable to adequately constrain w_a. The strong prior results in a preference of $w_0 \approx -0.5$ with $w_0 = -1$ well within the border of the 1σ region for the binned data. The unbinned data shows a strong preference toward $w_0 < -1.5$ and rejects the cosmological constant value at the 1σ level. The w_a parameter shows a strong preference to > 0 values for the unbinned data, with $w_a = 0$ rejected at the 3σ level. The PDF from the binned data is much broader and provides less constraint, including the $w_a = 0$ value within 1σ.

The ALL samples are shown in Figure 9.40 and Figure 9.41. The ALL silver sample with the weak prior finds Ω_M near the nominal value for the binned data, and the unbinned data PDF is shifted to larger values. The PDFs for w_0 are well-constrained with the unbinned data showing preference toward $w_0 \approx 0$ and excluding the $w_0 = -1$ from the 1σ region and the binned data showing preference toward $w_0 \approx 0.5$ and excluding the cosmological constant value. The w_a value is constrained

to ~ -8 for the binned data, and unconstrained for the unbinned data, spanning negative values to $w_a < -14$. The strong prior for the ALL silver sample sufficiently constrains w_0 for the unbinned data at ≈ -2 and at ≈ 0.5 for the binned data. Both datasets reject the $w_0 = -1$ point at $\sim 3\sigma$ level. The unbinned data strongly prefer a $w_a > 0$ value, rejecting the fiducial value at the 3σ level. The binned data, however, prefer $w_a < -5$ and the 1σ region covers a large area of parameter space $-16 < w_a < -5$, and rejects the fiducial value at the 3σ level. The ALL gold sample with the strong prior finds a largely unconstrained PDF for Ω_M which peaks at values larger than the nominal value but possesses a significant tail to the negative matter density region. The PDF for w_0 is concentrated near the cosmological constant value, and the sample cannot constrain w_a as the PDFs do not appear to have reached the stable distribution. The strong prior results in good constraint of w_0 and w_a. The sample prefers $w_0 < -1$ and rejects the cosmological constant value $w_0 = -1$ at the 1σ level. The sample also strongly prefers $w_a > 1.5$ with the fiducial $w_a = 0$ value rejected at the 3σ level.

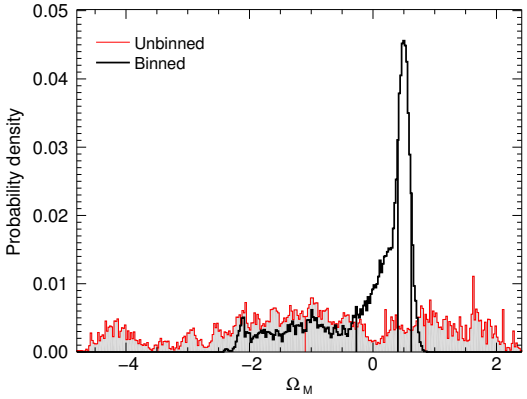

(a) Ω_M, Weak Prior

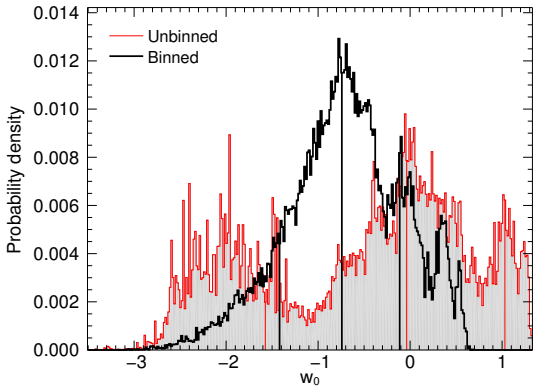

(b) w_0, Weak Prior

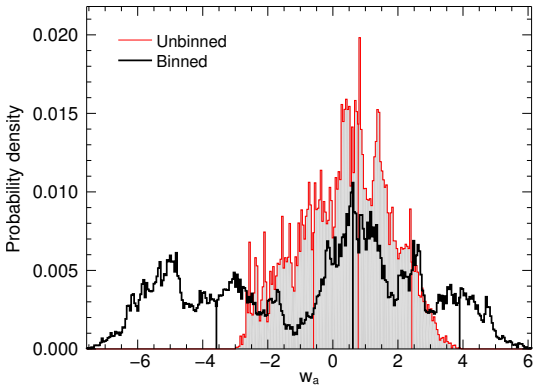

(c) w_a, Weak Prior

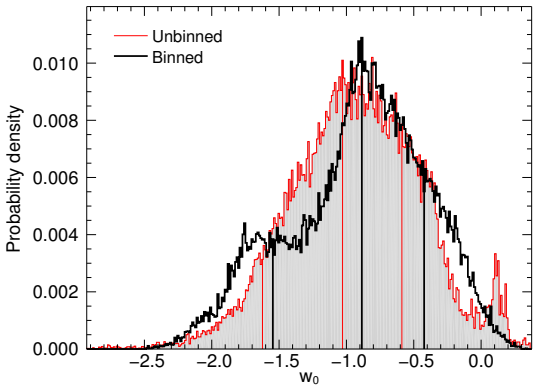

(d) w_0, Strong Prior

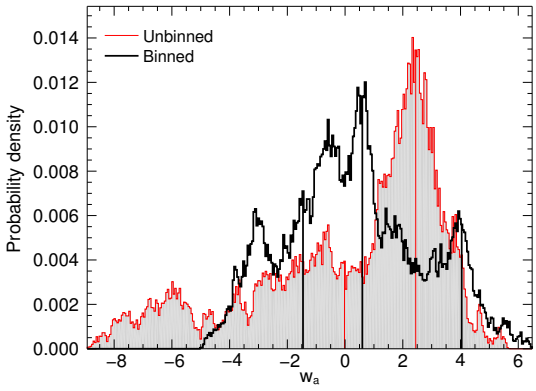

(e) w_a, Strong Prior

Figure 9.35: The probability distributions for the raw (red) and binned (black) data from the MCMC with a CPL $w(z)$ for the calibration sample.

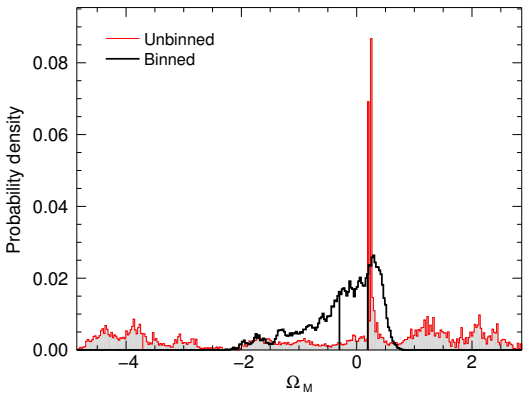

(a) Ω_M, Weak Prior

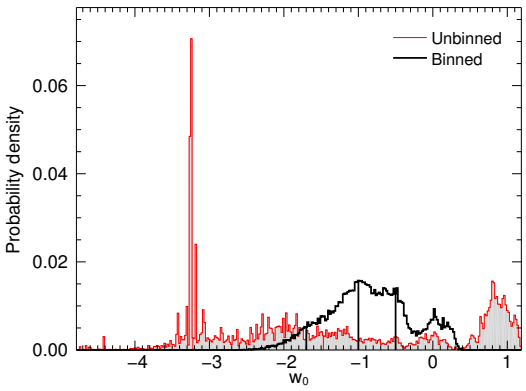

(b) w_0, Weak Prior

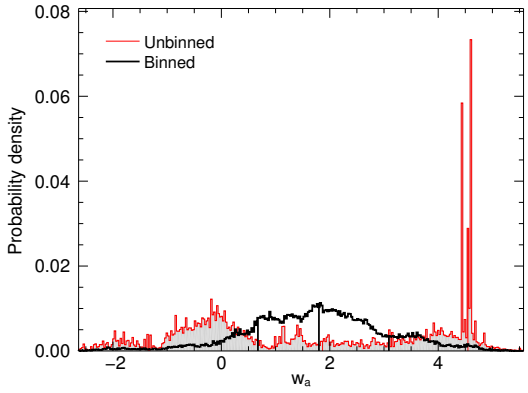

(c) w_a, Weak Prior

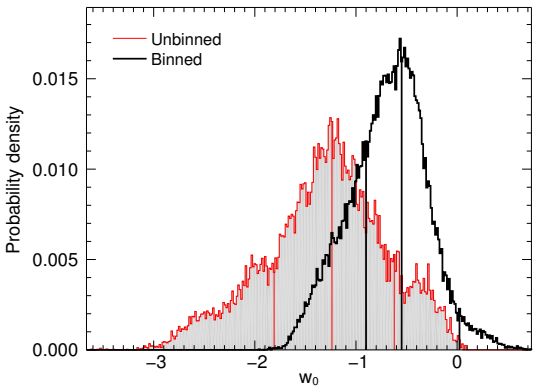

(d) w_0, Strong Prior

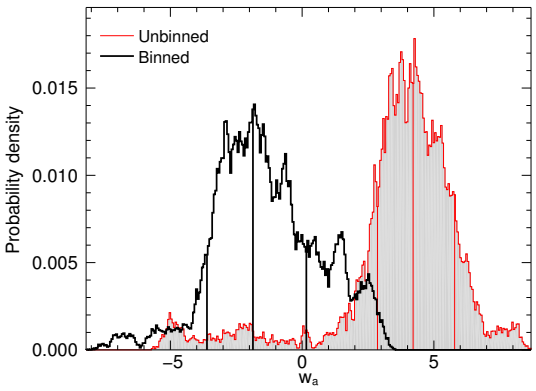

(e) w_a, Strong Prior

Figure 9.36: The probability distributions for the raw (red) and binned (black) data from the MCMC with a CPL $w(z)$ for the GBM silver sample.

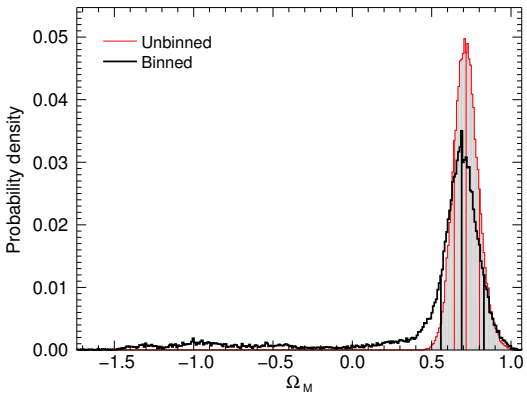

(a) Ω_M, Weak Prior

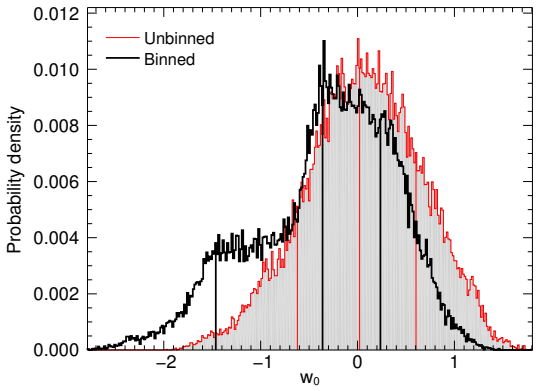

(b) w_0, Weak Prior

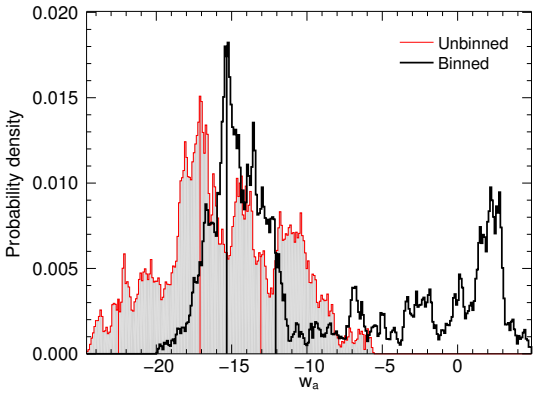

(c) w_a, Weak Prior

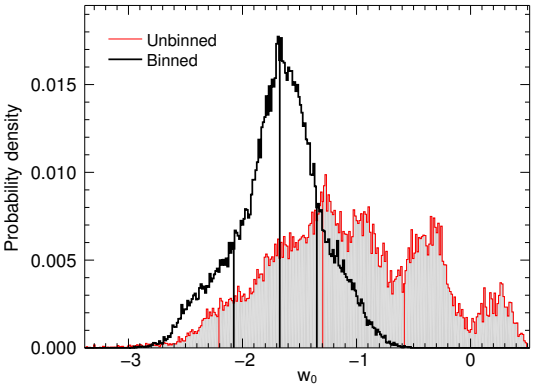

(d) w_0, Strong Prior

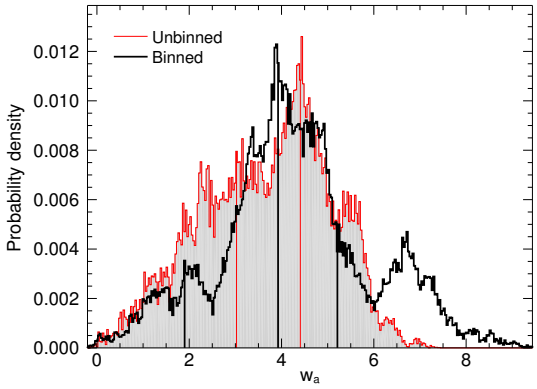

(e) w_a, Strong Prior

Figure 9.37: The probability distributions for the raw (red) and binned (black) data from the MCMC with a CPL $w(z)$ for the GBM gold sample.

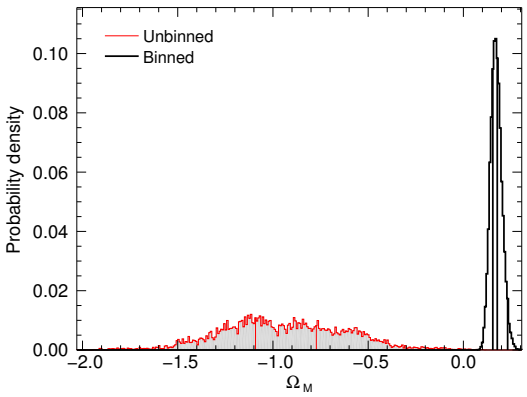

(a) Ω_M, Weak Prior

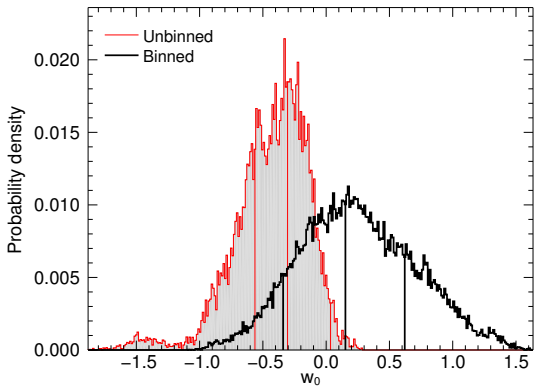

(b) w_0, Weak Prior

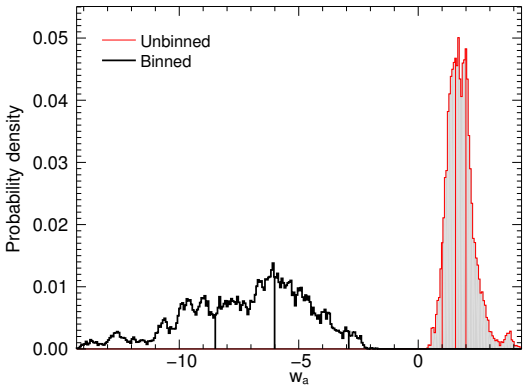

(c) w_a, Weak Prior

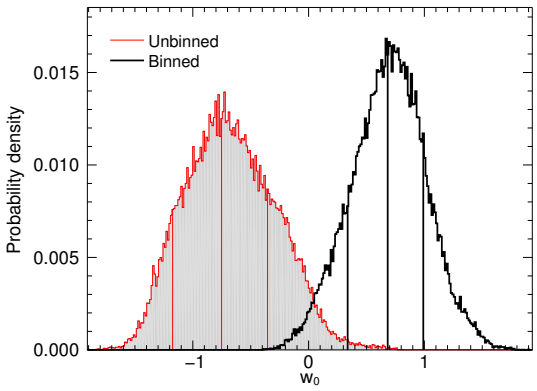

(d) w_0, Strong Prior

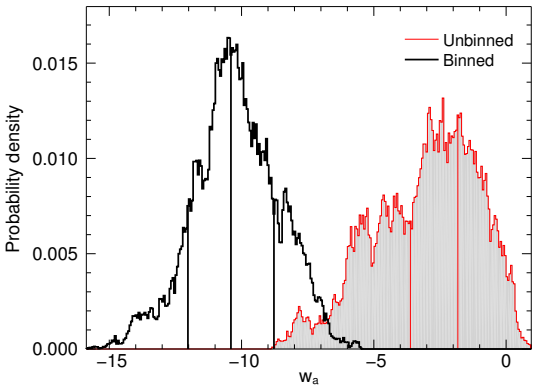

(e) w_a, Strong Prior

Figure 9.38: The probability distributions for the raw (red) and binned (black) data from the MCMC with a CPL $w(z)$ for the BATSE silver sample.

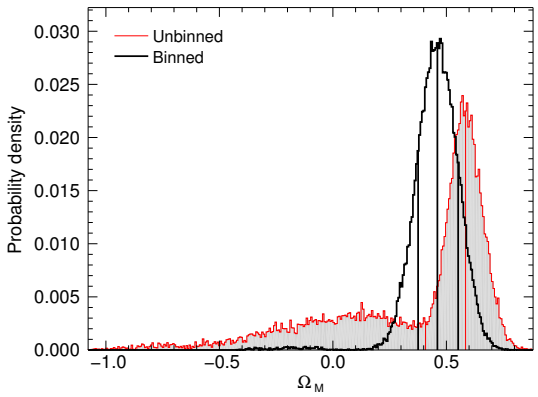

(a) Ω_M, Weak Prior

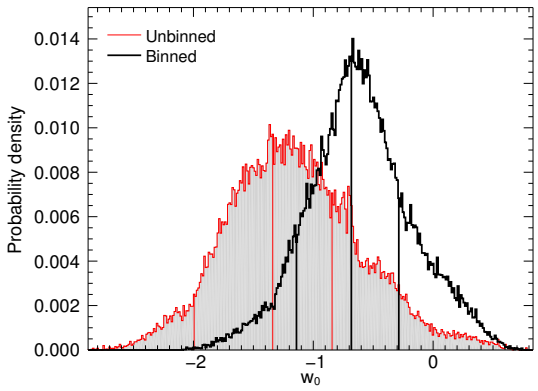

(b) w_0, Weak Prior

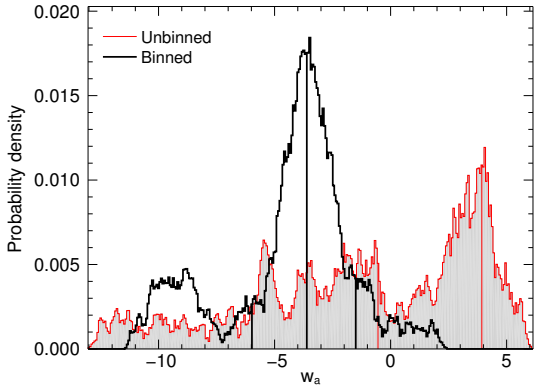

(c) w_a, Weak Prior

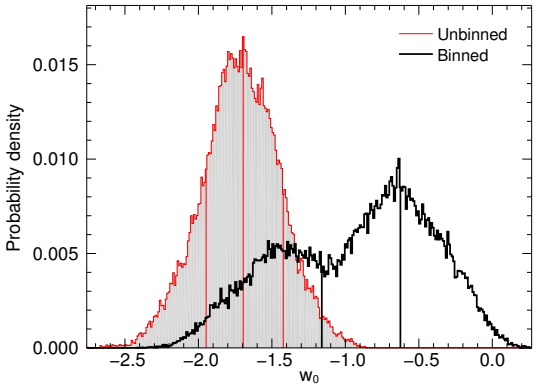

(d) w_0, Strong Prior

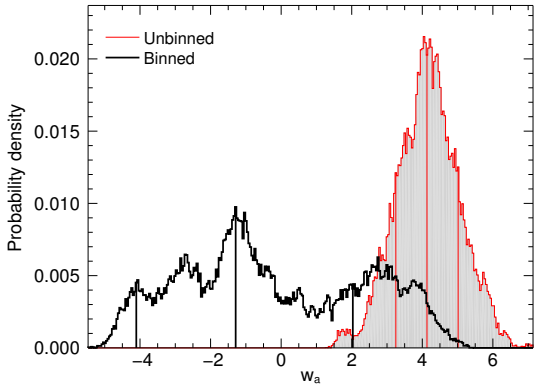

(e) w_a, Strong Prior

Figure 9.39: The probability distributions for the raw (red) and binned (black) data from the MCMC with a CPL $w(z)$ for the BATSE gold sample.

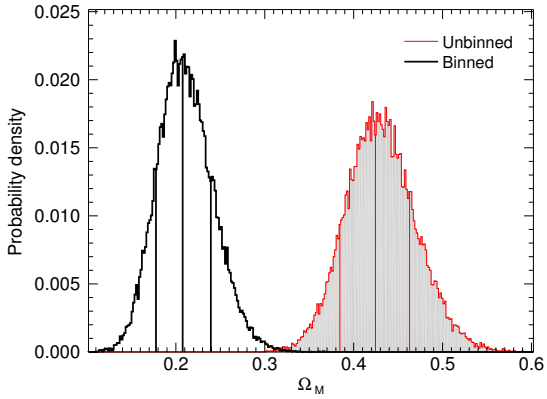

(a) Ω_M, Weak Prior

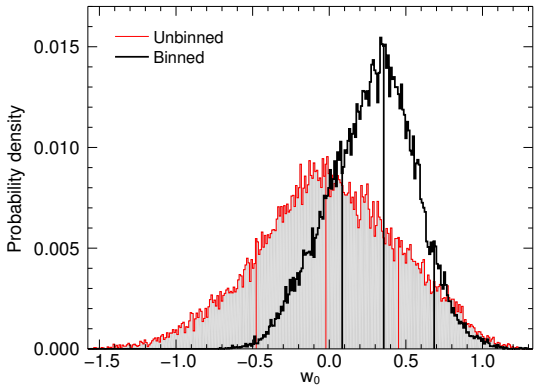

(b) w_0, Weak Prior

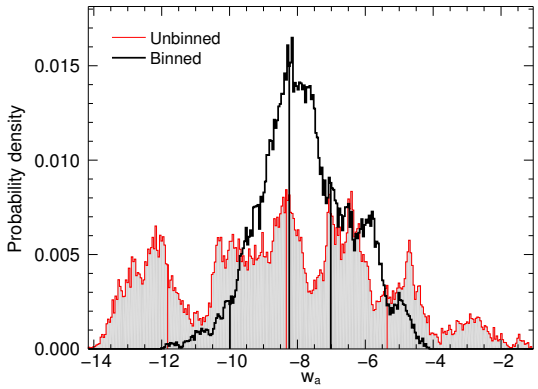

(c) w_a, Weak Prior

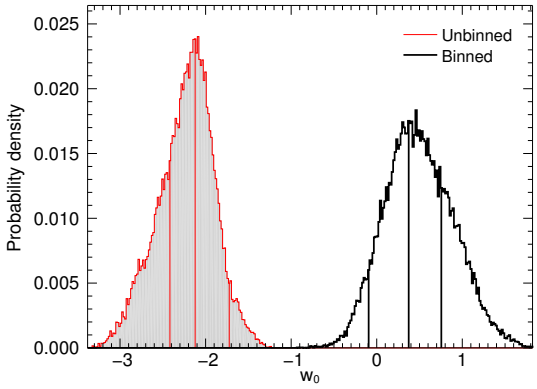

(d) w_0, Strong Prior

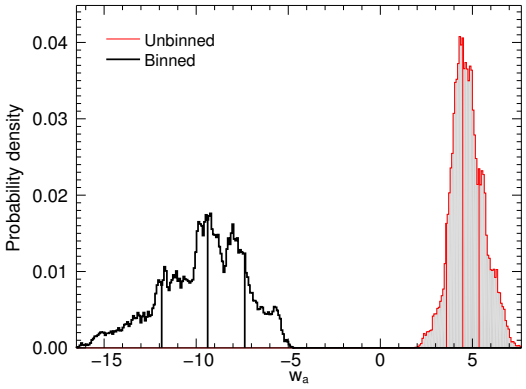

(e) w_a, Strong Prior

Figure 9.40: The probability distributions for the raw (red) and binned (black) data from the MCMC with a CPL $w(z)$ for the ALL silver sample.

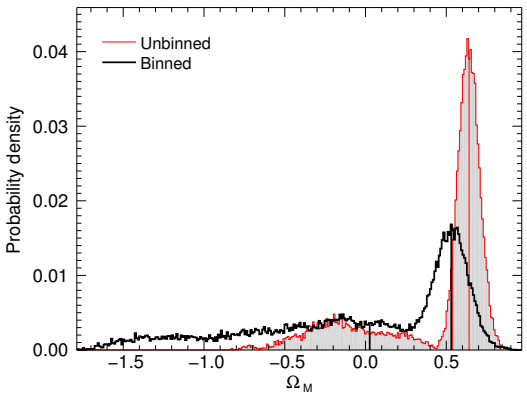

(a) Ω_M, Weak Prior

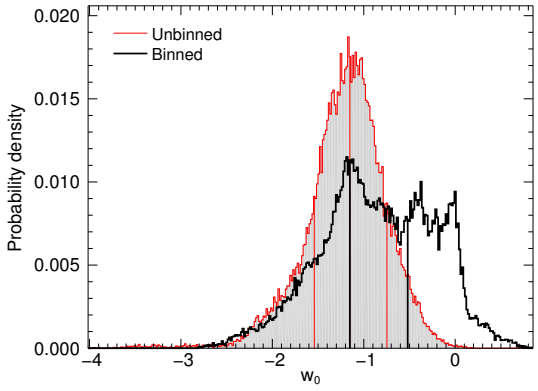

(b) w_0, Weak Prior

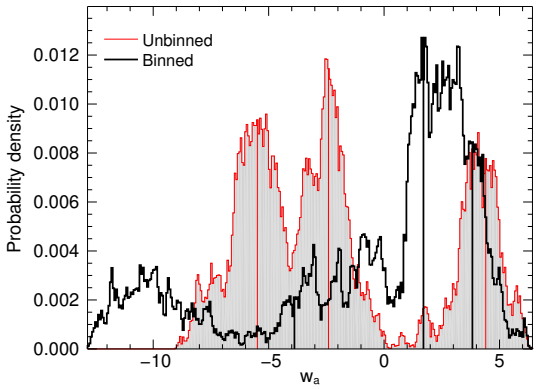

(c) w_a, Weak Prior

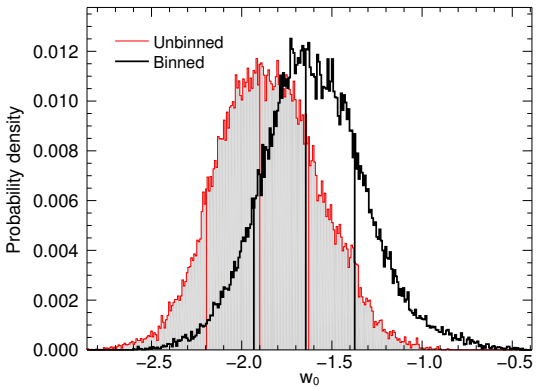

(d) w_0, Strong Prior

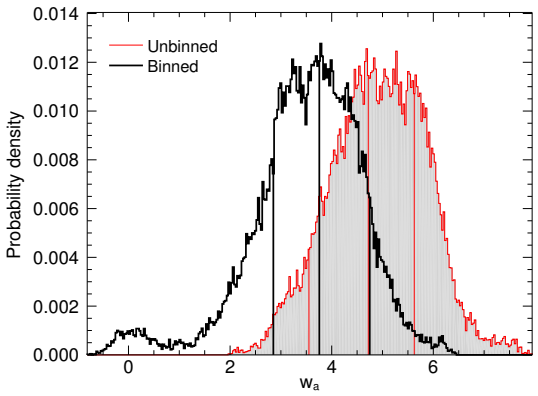

(e) w_a, Strong Prior

Figure 9.41: The probability distributions for the raw (red) and binned (black) data from the MCMC with a CPL $w(z)$ for the ALL gold sample.

Table 9.13: Best fit cosmological parameters for CPL $w(z)$

	Weak Prior				Strong Prior		
Sample	Ω_M	H_0	w_0	w_a	H_0	w_0	w_a
Unbinned							
Calibration	$-1.10^{+1.95}_{-2.39}$	$65.1^{+4.0}_{-2.1}$	$-0.04^{+1.07}_{-1.54}$	$0.78^{+1.65}_{-1.37}$	$65.6^{+1.9}_{-1.8}$	$-1.03^{+0.44}_{-0.59}$	$2.45^{+3.24}_{-2.47}$
GBM Silver	$0.20^{+1.57}_{-3.91}$	$66.3^{+11.7}_{-6.1}$	$-3.22^{+1.75}_{-1.55}$	$4.55^{+1.01}_{-2.68}$	$66.9^{+1.7}_{-1.7}$	$-1.24^{+0.62}_{-0.57}$	$4.21^{+1.58}_{-1.35}$
GBM Gold	$0.72^{+0.08}_{-0.07}$	$63.8^{+1.9}_{-2.1}$	$0.02^{+0.58}_{-0.64}$	$-17.10^{+4.04}_{-5.41}$	$67.0^{+2.1}_{-1.6}$	$-1.30^{+0.72}_{-0.91}$	$4.41^{+3.02}_{-1.38}$
BATSE Silver	$-1.09^{+0.32}_{-0.61}$	$67.4^{+1.6}_{-1.4}$	$-0.30^{+0.34}_{-0.26}$	$1.56^{+0.43}_{-0.56}$	$66.3^{+1.7}_{-1.7}$	$-1.67^{+0.33}_{-0.40}$	$3.93^{+1.29}_{-2.02}$
BATSE Gold	$0.58^{+0.29}_{-0.18}$	$66.0^{+2.0}_{-2.0}$	$-1.34^{+0.50}_{-0.66}$	$3.93^{+2.17}_{-4.47}$	$67.0^{+1.8}_{-1.7}$	$-1.70^{+0.27}_{-0.25}$	$4.13^{+0.88}_{-0.88}$
ALL Silver	$0.42^{+0.04}_{-0.04}$	$63.1^{+1.7}_{-1.8}$	$-0.02^{+0.50}_{-0.50}$	$-8.33^{+2.97}_{-3.50}$	$68.3^{+1.8}_{-2.2}$	$-2.12^{+0.40}_{-0.29}$	$4.48^{+0.89}_{-0.89}$
ALL Gold	$0.64^{+0.19}_{-0.10}$	$65.6^{+2.0}_{-2.0}$	$-1.15^{+0.41}_{-0.39}$	$-2.41^{+6.81}_{-3.508}$	$67.2^{+1.8}_{-1.8}$	$-1.90^{+0.27}_{-0.30}$	$4.72^{+0.90}_{-1.17}$
Binned							
Calibration	$0.40^{+0.22}_{-0.67}$	$64.8^{+2.0}_{-1.9}$	$-0.74^{+0.63}_{-0.68}$	$0.61^{+3.28}_{-4.19}$	$64.9^{+2.1}_{-2.1}$	$-0.89^{+0.46}_{-0.66}$	$0.60^{+3.44}_{-2.06}$
GBM Silver	$0.19^{+0.62}_{-0.49}$	$65.6^{+1.8}_{-1.7}$	$-1.00^{+0.50}_{-0.70}$	$1.80^{+1.29}_{-1.13}$	$64.9^{+1.8}_{-1.7}$	$-0.55^{+0.57}_{-0.35}$	$-1.87^{+2.03}_{-1.74}$
GBM Gold	$0.70^{+0.14}_{-0.13}$	$64.7^{+2.1}_{-1.9}$	$-0.36^{+0.60}_{-1.10}$	$-15.33^{+3.25}_{-9.25}$	$66.6^{+1.8}_{-1.9}$	$-1.67^{+0.33}_{-0.40}$	$3.93^{+1.29}_{-2.02}$
BATSE Silver	$0.18^{+0.05}_{-0.02}$	$63.0^{+2.0}_{-1.9}$	$0.15^{+0.47}_{-0.49}$	$-6.01^{+3.10}_{-2.48}$	$60.5^{+1.6}_{-1.6}$	$0.68^{+0.31}_{-0.35}$	$-10.40^{+1.63}_{-1.63}$
BATSE Gold	$0.46^{+0.09}_{-0.08}$	$64.5^{+1.9}_{-1.9}$	$-0.68^{+0.40}_{-0.46}$	$-3.61^{+2.11}_{-2.36}$	$65.5^{+2.0}_{-2.0}$	$-0.63^{+0.88}_{-0.53}$	$-1.29^{+3.32}_{-2.82}$
ALL Silver	$0.21^{+0.03}_{-0.03}$	$62.5^{+1.7}_{-1.8}$	$0.36^{+0.33}_{-0.27}$	$-8.24^{+1.22}_{-1.75}$	$61.5^{+1.7}_{-1.8}$	$0.37^{+0.38}_{-0.47}$	$-9.38^{+2.01}_{-2.50}$
ALL Gold	$0.53^{+0.42}_{-0.50}$	$65.9^{+2.2}_{-1.9}$	$-1.15^{+0.63}_{-2.86}$	$1.71^{+2.12}_{-5.59}$	$66.6^{+1.7}_{-1.8}$	$-1.64^{+0.27}_{-0.29}$	$3.76^{+0.99}_{-0.90}$

CHAPTER 10

DISCUSSION

The calibrated GRB Hubble diagram can potentially provide useful constraints on cosmological models, particularly on the evolution of dark energy and the expansion of the universe. In this chapter, I discuss the motivation and possible physical explanation for the chosen luminosity relations. The luminosity relations are certainly affected by a considerable amount of scatter, and the physical sources of this scatter will be enumerated. In addition, I shall mention some of the limitations and systematics involved with the method used to determine the redshift and distance modulus as well as offer ideas to improve the accuracy and uncertainty of the estimates. Seven different samples were used to not only probe cosmology, but to also investigate the similarities between the samples, and I will compare and contrast the samples and emphasize which samples are of the highest statistical and scientific quality. Last but not least, I investigate the results from the SN Ia + GRB Hubble diagram, compare to previous results from other efforts, and discuss the overall cosmological implications.

10.1 Physical Motivation for the Luminosity Relations

Most of the luminosity relations discussed were originally discovered as a result of a search for empirical correlations between observed parameters. It is only more recently that efforts have attempted to link the empirical correlations to a physical justification. Unfortunately, a clear connection between the E_p and the luminosity or total energy has evaded explanation. Perhaps, in the context of the internal shock model, the E_p is related to the synchrotron frequency, which is then boosted by the bulk Lorentz factor.

Consider two shells of magnetized outflow with an initial separation of R_0 and with different Lorentz factors Γ and $a\Gamma$ ($a > 1$). The two shells will interact at a distance R_i from the central engine, where

$$R_i = \frac{2a^2}{a^2 - 1} R_0 \Gamma^2. \tag{10.1}$$

Previous simulations show that often $a \approx 2$ [198], which result in $R_i = (8/3)R_0\Gamma^2$. If each shell carries the same amount of energy, namely $E_{sh} = 10^{50} E_{sh,50}$ erg in bulk motion, then $R_i = 6 \times 10^{12} (E_{sh,50}/\Gamma^2)^{1/2}$ cm. Typically, $R_i > R_t$, where R_t is the radius at which the expanding shell becomes optically thin to Thomson scattering and characterizes the evolution of the fireball [199]. This is required for the fireball to become transparent and the radiation to escape. The electrons from the outflow are accelerated in a collision-less shock, and each attain a random Lorentz factor corresponding to equipartition with other forms of energy, $\gamma_{eq} = (\Gamma' - 1) n_p m_p / (n_e m_e)$,

where Γ' is the Lorentz factor of the faster shell in the rest frame of the slower shell [60, 62, 64, 200]. A dimensionless coefficient, $\epsilon_e = \gamma/\gamma_{eq}$, parametrizes any deviations from the equipartition value [201]. The observed luminosity in the equipartition regime is equivalent to $L = \epsilon_e P_{sh}$, where $P_{sh} = 4\pi R^2 \Gamma^2 n'_p m_p c^3$ is the kinetic power carried by a single shell [202]. The outflowing plasma is highly magnetized, and a typical value for the field is estimated by assuming that the field energy in the emitting region constitutes some fraction, ϵ_B, of the randomized energy. In that case, at the distance where the shells interact, the Poynting flux carries a power of $L_B = R^2\Gamma^2 B'^2 c/2 = \epsilon_B L_s$ [95]. This corresponds to

$$B' = (8\pi\epsilon_B n'_p m_p c^2)^{1/2} = \left(\frac{2\epsilon_B L}{c\epsilon_e}\right)^{1/2} \frac{1}{\Gamma R}. \tag{10.2}$$

The typical synchrotron frequency can be written as $\nu_{peak} = 2c\gamma^2 B'\Gamma/3\pi m_e c(1+z)$ [203, 204], which at R_i results in

$$h\nu_{peak} = E_p = 450 \frac{\epsilon_e^{3/2}(\Gamma'-1)^2 \epsilon_B^{1/2} L_{52}^{1/2}}{R_{i,14}(1+z)} \text{ keV}. \tag{10.3}$$

The above equation can be rearranged such that

$$L_{52} = 4.94 \times 10^{-6} R_{i,14}^2 \epsilon_e^{-3} (\Gamma'-1)^{-4} \epsilon_B^{-1} \left[\frac{E_p(1+z)}{1 \text{ keV}}\right]^2. \tag{10.4}$$

Equation 10.4 sets up the theoretical framework for the correlation between the luminosity and E_p *within* a particular GRB, based on the Lorentz factor and collision radius. Indeed, there have been several discoveries [205–209] of correlations between

the rest frame time-resolved E_p and the luminosity or cumulative luminosity. In the context of the internal luminosity correlations, if a decay in luminosity is observed, then a cooling of E_p will also be observed. This indicates that if the behavior is true for all GRBs, then each GRB will exhibit a particular correlation between E_p and luminosity at the peak luminosity. The correlation between E_p and luminosity will only be observed over different GRB spectra if each E_p and luminosity are observed from the same reference point in time (e.g. at the peak luminosity). In this manner, the E_p–L_γ relation can be explained. The E_p–E_γ relation, instead, averages the E_p over the entire burst and compares it to the burst fluence. This effectively compares the time-integrated E_p to the time-integrated flux, which will show a similar relationship to E_p–L_γ. The corresponding isotropic energy and luminosity correlations can be explained in the same way, however the energy and luminosity are uncorrected for jet collimation, and therefore will introduce dispersion into the correlations.

Sources for additional dispersion can be found in Equation 10.4. The Lorentz factor, Γ, decays throughout the burst, but the initial bulk Lorentz factor may differ from burst to burst. Also, the shell collision radius can vary based on the kinetic energy of each shell, the environment density, and the magnetic field. These factors can cause significant scatter in the observed correlations. Furthermore, even if the amount of jet collimation is accounted for in the calculation of the luminosity or energy, the viewing angle of the observer to the jet axis will vary and the observed E_p and flux will change [210, 211]. The viewing angle currently is not able to be directly inferred (with the exception of GRB 980425 [145]), and only limits can imposed on the Lorentz factor for very few bursts [212–215]. The estimation of the magnetic field

is also limited to constraints from late-time X-ray observations of the afterglow [216,217], which typically result in a lower limit of the magnetic field. All of these factors conspire to create the observed scatter in the correlations and complicate attempts at using the correlations as luminosity indicators.

10.2 Improving the Estimation of z, μ, and θ_j

As was discussed in the previous section, the luminosity relations exhibit significant intrinsic scatter, which disrupts the accuracy and precision to which the luminosity relations can be used. The estimation of z, μ, and θ_j by the discussed method accounts for the uncertainty in the GRB spectral parameters as well as the uncertainty in the calibrated luminosity relations. The amount of scatter, however, was not factored in to the propagation of uncertainty, and could potentially be the dominant source of uncertainty in the estimates. This problem was mitigated by making a strict quality cut based on the uncertainty of the estimated parameters, as well as truncating the range of estimated values. For example, a particular GRB that exists several σ from the best fit correlation lines will produce produce $z < 0$ or $z >> 20$ (or $\theta_j > 90°$). By excluding nonphysical solutions to the relations, I was able to filter out most deviant GRBs. However, a more desirable solution is to include the scatter in the estimation of the uncertainty, but to ensure that it does not dominate the spectral uncertainties. A possible method to accomplish this task is akin to the method used to average the distance modulus produced from multiple luminosity relations for GRBs with known redshift (Schaefer method) [218]. The Schaefer method uses six different correlations as luminosity relations to determine the

distance modulus: the lag-luminosity relation (τ_{lag}–L_{iso}), the variability–luminosity relation (V–L_{iso}), E_p–L_{iso}, E_p–E_γ, the rise time–luminosity relation (τ_{RT}– L_{iso}), and the pulse number-luminosity relation (N_{pulse}–L_{iso}). Although all but one correlation used the isotropic luminosity or energy, the additional scatter involved in using the uncorrected luminosity and energy is mitigated by averaging the distance modulus resulting from each relation. Similarly, groups of two or three luminosity relations could be used to determine z, μ, and θ_j, and then the results from each group could be averaged together to provide a more constrained and accurate estimate than any single group of relations.

10.3 Consistency of the GRB samples

In addition to using GRBs to study cosmology, I investigate the similarities and differences between the different GRB samples. Primarily, in the context of estimating z and μ, I wanted to determine if neglecting the K-correction resulted in a large difference in results. As discussed previously, including the K-correction is obviously the most accurate procedure, however, the procedure is much more computationally expensive. Several studies have shown that the average value for the K-correction is $\sim$1, and is therefore neglected. An important point, though, is that because I am using data from two different instruments with different bandpasses, the observed flux is only over the observed band, and the calibration of the relations required the inclusion of the K-correction.

There are some distinct differences between the samples including the K-correction and neglecting the K-correction. The Hubble diagrams of the binned data

in Figure 8.4 show that the samples neglecting the K-correction consistently over-predict the Hubble diagrams of the data including the K-correction. This inconsistency is drastic enough to cause significant differences in the best-fit cosmological parameters. The silver samples, particularly the BATSE sample and the ALL sample, show a strong preference to a low $\Omega_M < 0.2$. While all samples prefer $\Omega_\Lambda > 1$, the BATSE and ALL silver samples have tight error contours due to the large number of data points. In addition, the silver samples are unable to constrain the both w_0 and w' for either of the investigated dynamical dark energy equations of state. These deviations indicate that the samples neglecting the K-correction produce significantly different results, particularly when large numbers of GRBs are used. Therefore, it is not advisable to use the silver samples due to these problems.

The raw extended GRB data have, on average, much larger uncertainties than the GRBs calibrated using SNe Ia. The large uncertainties, by themselves, will cause the fit at high redshift to be poor. However, to counteract this effect, we can use a large number of estimates at high redshift. A difficulty arises because of the large uncertainties, specifically the data will tend to be over-fit by the model and the preferred model will reflect the statistical fluctuations in the sample. Because of this problem and the fact that there are a large number of data points, the data can be binned so that each bin reflects the average value of z and μ and the error from each datapoint is propagated into the bin. Binning the data in this way allows us to find a clear trend in the data and to fit a model to it without worrying about statistical fluctuations dominating the fitting process. One key point is to ensure that the binned data can reproduce the results from the true raw data points. Comparing the

unbinned data to the binned data in the calibration sample shows good agreement between the results and confidence intervals. This should be expected since the calibration sample has much smaller uncertainties compared to the high-redshift data and statistical fluctuations are not prevalent. When comparing the unbinned samples to the binned samples in the χ^2 maps, it is immediately obvious that in most cases the uncertainties are smaller in the unbinned case, and the two samples usually find two different minima. The fact that the uncertainties are smaller in the unbinned case is expected, since the number of points in the unbinned case is N and the number of points in the binned case is $\approx \sqrt{N}$. The two different minima suggest that the model tends to fit the statistical fluctuations in the unbinned data. Indeed, an inspection of the χ^2_{min} for each sample shows that for the most of the cases, the unbinned $\chi^2 << \text{dof}$. For these reasons, the binned samples are statistically preferred over the unbinned samples, at least until the uncertainties in the high-redshift GRBs can be tightened.

10.4 Implications from the GRB Hubble Diagram

The GRB Hubble diagram, along with the SNe Ia used for calibration, span over three orders of magnitude in redshift and distance, representing the widest ranging Hubble diagram to date. With such a wide coverage of distance, the shape of the universe can be probed, as well the properties of dark energy. The leading concordant theory is that the dark energy equation of state $w_\Lambda = -1$ which results in a constant Ω_Λ for all redshift. This implies that in the early universe, after recombination and the universe became transparent to radiation, matter was the dominant form energy

in the universe, leading to the so-called "matter-dominated" era. The current era is then dominated by dark energy and has led to an accelerated expansion of the universe instead of a deceleration that is theorized in the matter-dominated era. If the concordant model is true, then GRBs can primarily be used to explore the matter-dominated era and the behavior of dark energy at early times. The current best measurements of the current matter and dark energy density show that $\Omega_M = 0.27$ and $\Omega_\Lambda = 0.73$ which imply that the universe has very nearly flat curvature. These measurements have primarily come from the observation of the CMB from WMAP [196] and baryon acoustic oscillations (BAO) from the deep sky galactic surveys such as the SDSS [197]. It has also been shown that results from SNe Ia agree with these observations, although SNe Ia tend to prefer a slightly larger value for Ω_Λ [153, 154]. Measurements from these samples indicate that $w_\Lambda \approx -1$ is preferred, although large uncertainties prevail, especially when investigating a time-dependent equation of state $w(z)$. This is the main problem that the GRB Hubble diagram aims at resolving.

Type Ia Supernovae show agreement with the standard cosmological model, although the data could also support a dynamical Ω_Λ and $w(z)$. Observations of SNe Ia exist out to only $z \sim 1.5$, a distance at which many cosmological models with dynamical Ω_Λ are virtually indistinguishable. GRBs exhibit significant overlap in redshift with high-z SNe Ia but are also observed at redshifts up to ~ 8. I have developed a method to estimate the redshift and distance modulus of GRBs and extend the redshift range of GRBs up to ~ 20. Therefore, GRBs can be used mainly to extend the Hubble diagram of SNe Ia to high redshift where different models of dynamical Ω_Λ are distinguishable. As shown in Figure 10.1, the Hubble diagram of

SNe Ia + GRBs can be explained by the standard model up to $z \approx 2.5$, but then diverges at larger redshift. Indeed SN Ia data alone leave open the possibility that the concordant model is not the only likely model for dark energy.

The results from the SN Ia + GRB Hubble diagram indicate several interesting points. If a static Ω_Λ is assumed, Ω_M can be easily recovered, but the GRB data at $z > 3$ force $\Omega_\Lambda > 1$ such that Ω_Λ dominates at earlier epochs and forces the universe into a closed geometry. If, instead, the curvature is assumed flat (and $H_0 = 70$), then Ω_M can nearly be recovered at its nominal value while a constant Ω_Λ is ruled out at the 3σ level. This result is shown in Figure 9.4. Note that the MCMC have shown a strong preference toward $H_0 < 70$ which results in an amplitude shift of the Hubble diagram. While the MCMC have shown that H_0 is not sensitive to the value of the $w(z)$ parameters, the $w(z)$ parameters are sensitive to H_0. Therefore, when the MCMC simultaneously fits H_0 and $w(z)$, there is an agreement with a cosmological constant at $\sim 1\sigma$ as shown in Figure 9.27.

Similarly, fixing Ω_Λ to its nominal value and allowing the curvature to vary results in a slightly closed universe and the cosmological constant is ruled out at the 3σ level. In fact, if a cosmological constant is assumed, it becomes increasingly difficult for Ω_Λ to find a flat universe if the curvature is allowed to vary, with the preferred best fit value at $\Omega_k = -0.5$ instead of $\Omega_k = 0$ for a flat universe. It is clear that assuming a cosmological constant affects the curvature of the best fit model, however assuming the nominal value for Ω_Λ and allowing the Ω_k and w_0 to vary does not alleviate the curvature problem as the flat geometry is still far outside 3σ, while the cosmological constant is within 2σ.

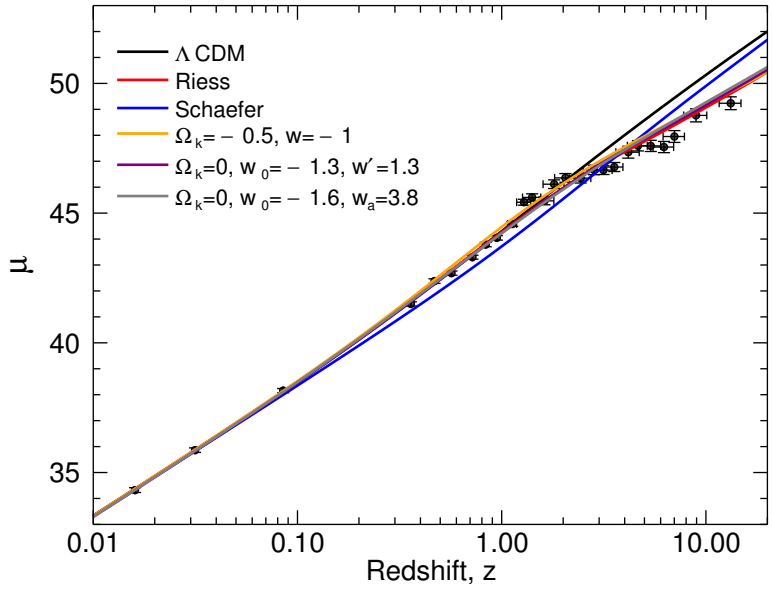

(a) SN Ia + GRB Hubble diagram

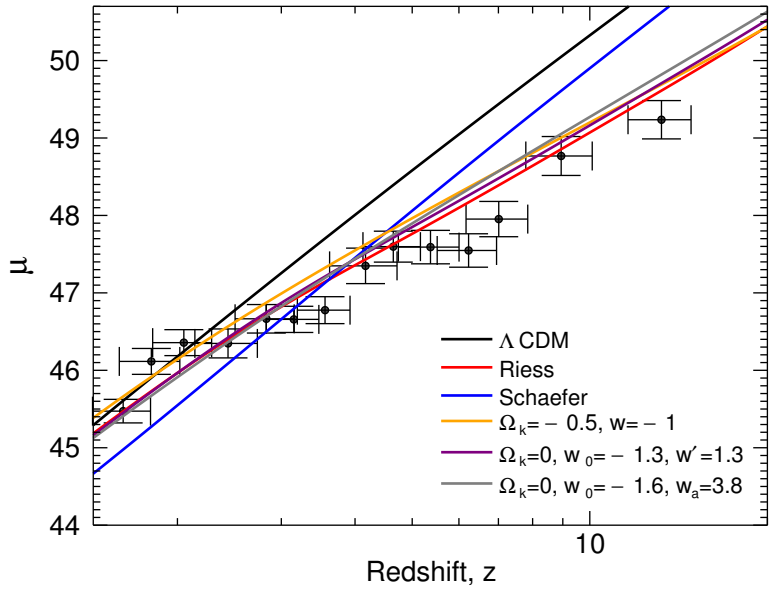

(b) SN Ia + GRB Hubble diagram, zoomed

Figure 10.1: [*Top*] The combined SN Ia + GRB data, binned. [*Bottom*] Zoomed in on $1.5 < z < 20$.

Even with only SNe Ia it was recognized that the $w_\Lambda = w(z)$ could be dependent on redshift, as the Riess parametrization found that w_0 recovered the value for the cosmological constant at $\sim 1\sigma$, but preferred $w_0 < -1$ and $w' > 0$. If Ω_M and Ω_Λ are fixed at their concordant values then the values found for the Riess representation are in agreement with the SNe Ia data at the 1σ level, however rejects the cosmological constant at the 3σ level. Even allowing H_0 to vary in the MCMC rejects the cosmological constant for the Riess representation at the $\approx 3\sigma$ level. In fact, the best fit model using the Riess $w(z)$ for a flat geometry very closes matches the result of the $w_0 = -1$, $\Omega_\Lambda > 1$ closed universe and is in fact preferred since $\chi^2/\text{dof} = 32/24$ for the Riess $w(z)$ and $\chi^2/\text{dof} = 37/24$ for the $w_0 = -1$ closed universe.

As mentioned previously, the Riess $w(z)$ has the unfortunate property of dominating the radiation density during the radiation- dominated era, therefore, the CPL $w(z)$ was investigated. Results using the Schaefer method [218] indicated that the best fit parameters for the CPL representation are $w_0 \approx 0.2$ and $w_a \approx -1.4$, however the results contain one important problem. The luminosity relations that were used were never calibrated, and therefore any estimation of the distance modulus from the luminosity relations were cosmological model-dependent. The inaccuracy introduced can be seen in the SN Ia + GRB Hubble diagram in Figure 10.1 where the best fit parameters create an enormous deviation from the SNe Ia at $z > 0.1$. The calibrated SN Ia + GRB Hubble diagram, however, exclude the cosmological constant at the 3σ level. This model very closely matches the Riess $w(z)$, although the χ^2 is slightly larger at $\chi^2/\text{dof} = 36/24$. These results, combined with the strict restraints on the curvature imposed by the CMB and BAO suggest that dark energy may not be repre-

Table 10.1: Comparison of Cosmological Models, Binned (Unbinned)

Model	Ω_M	Ω_Λ	H_0	w_0	w' or w_a	χ^2
ΛCDM	0.27	0.73	70	-1	0	70 (369)
Riess [153]	0.27	0.73	65	-1.32	1.48	32 (306)
Schaefer CPL	0.27	0.73	65	0.20	-1.40	296 (652)
$w(z) = w_0$, weak prior	0.50 (0.38)	0.73	66.3 (66.3)	-1.30 (-1.38)	0	43 (348)
$w(z) = w_0$, strong prior	0.27	0.73	64.9 (64.7)	-0.86 (-0.79)	0	47 (355)
Riess, weak prior	0.48 (0.14)	0.73	65.4 (66.0)	-0.77 (-0.31)	0.95 (1.00)	146 (947)
Riess, strong prior	0.27	0.73	66.5 (67.2)	-1.28 (-1.53)	1.28 (2.20)	32 (292)
CPL, weak prior	0.53 (0.64)	0.73	65.9 (65.6)	-1.15 (-1.15)	1.71 (-2.41)	87 (313)
CPL, strong prior	0.27	0.73	66.6 (67.2)	-1.64 (-1.90)	3.76 (4.72)	36 (305)

sented by a cosmological constant, but instead is dynamical and changes with redshift. In fact, when comparing similar $w(z)$, the best fit CPL representation from the SN Ia + GRB Hubble diagram can be found within 1σ of the values Riess et al. [154] found with SNe in addition to priors from WMAP and BAO that $w \approx -1$ at $z \approx 1089$, the surface of last scattering.

Figure 10.1 shows the final binned SN Ia + GRB Hubble diagram from the ALL gold sample, as well as a number of possible models, the parameters of which are shown in Table 10.1. The ΛCDM model shows a significant deviation at $z \gtrsim 2.5$, where it over-predicts the distance modulus of high-z GRBs. The Schaefer best fit CPL $w(z)$ is shown to deviate significantly from the SN Ia data at $z > 0.1$, signifying the importance of calibrating the GRB luminosity relations. The Riess $w(z)$ is already a very close match to the GRB Hubble diagram, and the best fit $w(z)$ only deviates sightly and is within the uncertainty of the Riess model. Additionally, there is little difference between the best fit Riess $w(z)$ and the best fit CPL parametrization of $w(z)$. The best fit $w = -1$ cosmology is shown as well, depicting how the assumption

that Ω_Λ is a cosmological constant forces the geometry into a $\Omega_k = -0.5$ closed universe. The residuals are shown in Figure 10.2 for the models shown in Figure 10.1.

By calculating the deceleration parameter of both the Riess $w(z)$ and the CPL $w(z)$, the redshift at which the universe entered the current Ω_Λ-dominated era can be determined. The transition redshift for the Riess representation is

$$\Omega_M - \Omega_\Lambda(-1 - 3w_0 - 3w' z_T)(1 + z_T)^{w_0 - w'} e^{3w' z_T}. \tag{10.5}$$

Using the results from the ALL gold sample and the strong prior, the transition redshift is found to be $z_T \approx 0.71$. Similarly, the transition redshift for the CPL is found by

$$\Omega_M - \Omega_\Lambda\left(-1 - 3w_0 + 3\frac{w_a z_T}{1 + z_T}\right)(1 + z_T)^{w_0 + w_a} e^{-3\frac{w_a z_T}{1 + z_T}}. \tag{10.6}$$

The results from the ALL gold sample with the strong prior in this case results in $z_T \approx 0.55$. These values indicate that the transition from deceleration to acceleration was made ~ 6.5 Gyr or ~ 5.6 Gyr ago respectively.

10.5 Conclusions

In this dissertation I endeavoured to use the bulk spectral properties of GRB prompt emission to study cosmology. Using spectroscopy information from the GBM and BATSE GRB spectral catalogs, as well as correlations in the observed spectra, I have shown a number of methods to estimate quantities important to understanding GRBs. Particularly, I developed a method to accurately estimate the jet opening angle

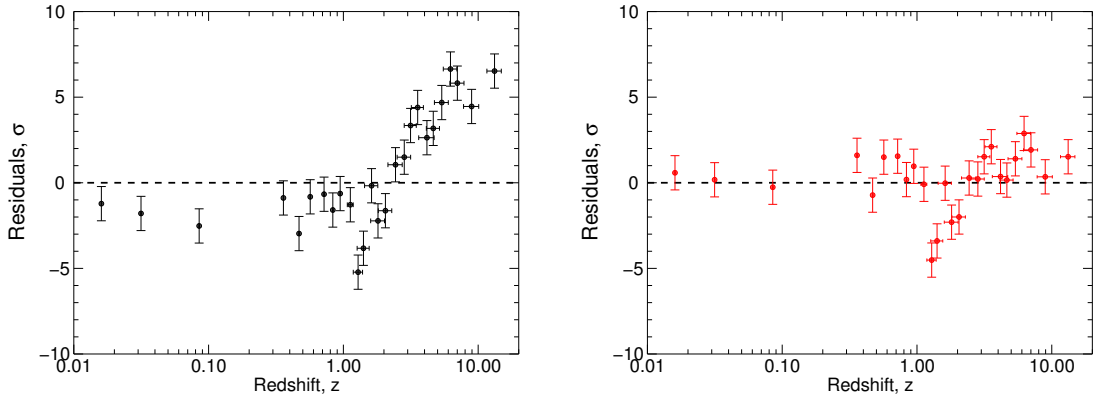

(a) ΛCDM

(b) Riess

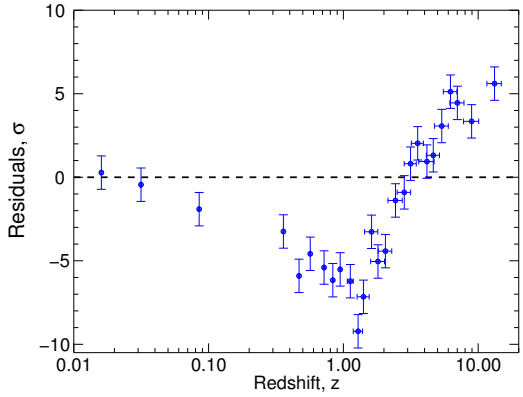

(c) Schaefer

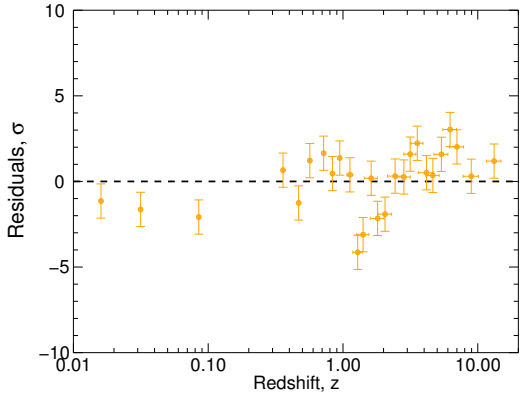

(d) $\Omega_k = 0.5, w = -1$

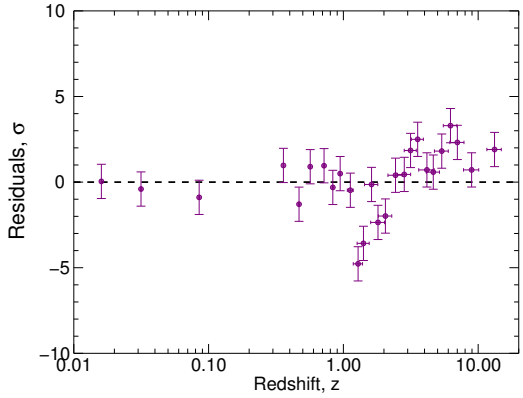

(e) $\Omega_k = 0, w_0 = -1.3, w' = 1.3$

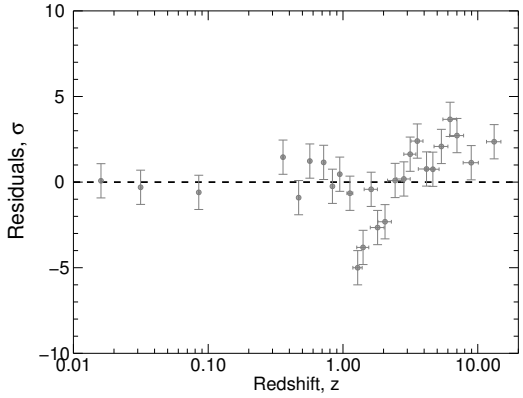

(f) $\Omega_k = 0, w_0 = -1.6, w_a = 3.8$

Figure 10.2: Residuals for the six models shown in Figure 10.1. The y-axis error bars display the 1σ standard deviation about the residuals.

of the GRB and therefore estimate the collimation-corrected luminosity and energy. I also discussed the use of the E_p–L_{iso} relation to estimate the redshift of GRBs without known redshift. Putting the two methods together leaves one final uncertain parameter needed to construct a Hubble diagram: the distance modulus. Therefore, I constructed a method to estimate the redshift, distance modulus, and jet opening angle based on three different luminosity relations. These luminosity relations were calibrated using Type Ia Supernovae to determine the distance modulus to GRBs at $z < 1.5$.

Once calibrated, the luminosity relations represent a cosmological model-independent method to estimating the redshift and distance modulus in order to enable the use of a large number of GRBs over a wide range of redshift to study cosmology. The resulting SN Ia + GRB Hubble diagram was then used in two different methods to investigate the standard model of cosmology, the ΛCDM model, as well as models that require a dynamic dark energy density. I have found from these results that the if the systematic shift away from the nominal H_0 is accounted for in the GRB Hubble diagram, the GRB Hubble diagram is still consistent with the ΛCDM model at the 1σ confidence level if $w(z) = w_0$ is assumed. If a dynamic equation of state index is assumed, however, the ΛCDM model is rejected at the 1σ confidence level and the data prefer a dynamic equation of state index, $w(z) \approx -1.28 + 1.28z$ following the Riess parameterization or $w(z) \approx -1.64 + 3.76z(1+z)^{-1}$ following the CPL parametrization. These results indicate a dynamical Ω_Λ which became dominant at $z \sim 0.55 - 0.71$. This and previous findings using SNe and GRBs as standard candles add to the mounting evidence that the cosmological constant may not be

representative of dark energy. Certainly there are improvements to be made, such as refining the estimation of redshifts and distance moduli, as well as gathering more GRBs with known redshift. These improvements will lead to improvements in further constraining the behavior of dark energy and the evolution of the universe.

APPENDICES

APPENDIX A

TABULATED K-CORRECTION FOR GRBS WITH KNOWN REDSHIFT

Table A.1: K-Correction to 1 keV–10 MeV comoving band for GRB fluence spectra (K_S) and peak flux spectra (K_F)

GRB	z	K_S	K_F	Band (keV)
970508000	0.84	1.48±0.07	1.30±0.08	20–2000
971214000	3.42	0.85±0.12	1.12±0.16	20–2000
980329000	3.00	1.18±0.03	1.08±0.03	20–2000
980425000	0.01	1.43±0.04	–	20–2000
980703000	0.97	1.98±0.02	1.23±0.01	20–2000
990123000	1.60	1.02±0.03	1.23±0.09	20–2000
990506000	1.30	1.46±0.02	0.56±0.04	20–2000
990510000	1.62	1.39±0.03	1.13±0.04	20–2000
991216000	1.02	1.64±0.01	1.18±0.02	20–2000
080804972	2.20	0.70±0.59	0.13±0.24	8–1000
080810549	3.35	1.85±0.08	–	8–1000
080905705	2.37	0.86±0.06	–	8–1000
080916009	4.35	1.90±0.09	1.09±0.05	8–1000
080916406	0.69	2.19±0.14	0.95±0.02	8–1000
081007224	0.53	1.35±0.17	–	8–1000
081008832	1.97	1.24±0.02	0.99±0.02	8–1000
081121858	2.51	0.40±0.56	1.00±2.86	8–1000

Table A.1 (continued)

GRB	z	K_S	K_F	Band (keV)
081222204	2.77	1.20±0.17	1.10±0.26	8–1000
090102122	1.55	1.02±0.01	1.03±0.02	8–1000
090323002	3.57	1.63±0.03	1.02±0.04	8–1000
090328401	0.74	1.32±0.01	1.00±0.21	8–1000
090424592	0.54	1.14±0.04	0.93±0.05	8–1000
090516353	4.11	1.22±0.02	–	8–1000
090519881	3.85	2.16±0.85	–	8–1000
090618353	0.54	1.24±0.00	1.15±0.01	8–1000
090902462	1.82	0.98±0.00	2.54±0.07	8–1000
090926181	2.11	0.99±0.04	0.34±0.10	8–1000
090926914	1.24	0.10±0.02	1.02±0.22	8–1000
091003191	0.90	1.48±0.13	0.45±0.25	8–1000
091020900	1.71	1.19±0.02	–	8–1000
091024372	1.10	2.87±0.36	–	8–1000
091127976	0.49	1.47±0.03	0.98±0.04	8–1000
091208410	1.06	1.20±0.02	1.38±0.20	8–1000
100117879	0.92	1.01±0.05	–	8–1000
100414097	1.37	1.07±0.07	1.03±0.21	8–1000
100724029	1.29	1.26±0.06	1.06±0.27	8–1000
100814160	1.44	0.08±0.69	0.37±9.81	8–1000
100816026	0.81	1.13±0.24	0.24±0.60	8–1000
100906576	1.73	2.63±0.03	0.75±0.42	8–1000
101219686	0.55	0.86±0.11	1.01±0.02	8–1000
110106893	0.62	0.98±0.04	–	8–1000
110213220	1.46	1.85±0.04	1.24±0.02	8–1000
110731465	2.83	1.24±0.14	0.89±0.02	8–1000
110818860	3.36	1.30±0.03	–	8–1000
111107035	2.89	1.28±0.85	–	8–1000
111228657	0.48	1.37±0.06	1.41±0.09	8–1000
120119170	1.73	1.61±0.07	0.01±3.40	8–1000
120711115	1.41	1.85±0.05	1.59±0.34	8–1000
120712571	4.17	0.82±0.65	–	8–1000
120716712	2.49	1.26±0.13	0.92±0.03	8–1000

APPENDIX B

DERIVATION OF JET OPENING ANGLE FROM THE E_P–E_γ RELATION

The E_p–E_γ relation can be written as

$$E_p(1+z) = \xi\left(\frac{E_\gamma}{E_0}\right)^\eta, \tag{B.1}$$

where E_0 is a normalization constant fixed to a value within the range of the data (for example 10^{51} erg), and ξ and η are the best fit power law parameters. The E_γ parameter represents the collimation-corrected energy in gamma-rays, $E_\gamma = E_{iso} f_b$, where $f_b \leq 1$ is the beaming fraction due to collimation. The E_{iso} parameter is a function of redshift, the fluence S_γ, and the luminosity distance d_L:

$$E_\gamma = E_{iso} f_b = \frac{4\pi d_L^2 S_\gamma K_S}{E_0(1+z)} f_b, \tag{B.2}$$

where K_S is the K-correction of the spectrum over which the fluence was calculated. The beaming fraction is expressed in terms of the half-opening angle of the jet, $f_b = 1 - \cos\theta_j$, therefore the E_p–E_γ relation can be inverted to solve for the jet

opening angle,

$$\theta_j = \cos^{-1}\left\{1 - \left[\frac{E_p(1+z)}{\xi}\right]^{1/\eta}\left[\frac{E_0(1+z)}{4\pi d_L^2 S_\gamma K_S}.\right]\right\} \tag{B.3}$$

Because there exists non-negligible uncertainties in the E_p and fluence of a GRB spectrum, as well as the E_p–E_γ best fit parameters, the uncertainties from each parameter needs to be properly propagated. For simplicity, all second-order contributions to the uncertainty are neglected, and the uncertainties in the redshift, luminosity distance, and K-correction will also be considered. Redefining terms in Equation B.3,

$$\begin{aligned} A &= \frac{E_0}{4\pi}; \\ B &= \frac{E_p(1+z)}{\xi}; \\ C &= \frac{A(1+z)}{d_L^2 S_\gamma K_S}; \\ D &= \sqrt{1-(CB^{1/\eta}-1)^2}; \end{aligned} \tag{B.4}$$

the partial derivatives for each parameter can be calculated:

$$\begin{aligned}
\frac{\partial\theta_j}{\partial E_p} &= \frac{CB^{1/\eta}}{E_p\eta D};\\
\frac{\partial\theta_j}{\partial S_\gamma} &= \frac{-CB^{1/\eta}}{S_\gamma D};\\
\frac{\partial\theta_j}{\partial z} &= \frac{-(1+\eta)CB^{1/\eta}}{(1+z)\eta D};\\
\frac{\partial\theta_j}{\partial d_L} &= \frac{-2CB^{1/\eta}}{d_L D};\\
\frac{\partial\theta_j}{\partial K_S} &= \frac{-CB^{1/\eta}}{K_S D};\\
\frac{\partial\theta_j}{\partial \xi} &= \frac{-CB^{1+1/\eta}}{(1+z)\eta E_p D};\\
\frac{\partial\theta_j}{\partial \eta} &= \frac{-CB^{1/\eta}\ln B}{\eta^2 D}.
\end{aligned} \tag{B.5}$$

Finally, the uncertainty in the jet opening angle can be determined as

$$\sigma^2_{\theta_j} = \left|\frac{\partial\theta_j}{\partial E_p}\right|^2\sigma^2_{E_p}+\left|\frac{\partial\theta_j}{\partial S_\gamma}\right|^2\sigma^2_{S_\gamma}+\left|\frac{\partial\theta_j}{\partial z}\right|^2\sigma^2_z+\left|\frac{\partial\theta_j}{\partial d_L}\right|^2\sigma^2_{d_L}+\left|\frac{\partial\theta_j}{\partial K_S}\right|^2\sigma^2_{K_S}+\left|\frac{\partial\theta_j}{\partial \xi}\right|^2\sigma^2_{\xi}+\left|\frac{\partial\theta_j}{\partial \eta}\right|^2\sigma^2_{\eta}. \tag{B.6}$$

APPENDIX C

DERIVATION OF REDSHIFT FROM THE E_P–L_{ISO} RELATION

The E_p–L_{iso} relation can be written as

$$E_p(1+z) = \xi\left(\frac{L_{iso}}{L_0}\right)^{\eta}, \tag{C.1}$$

where L_0 is a normalization constant fixed to a value within the range of the data, and ξ and η are the best fit power law parameters. The L_{iso} parameter is the isotropic peak luminosity and is a function of the peak flux F_γ and the luminosity distance d_L,

$$L_{iso} = 4\pi d_L^2 F_\gamma K_F, \tag{C.2}$$

where K_F is the K-correction of the spectrum measured at the peak brightness of the burst. Since E_p and F_γ are the only observables in the relation, all other non-constant terms can be moved to one side of the equation as:

$$\frac{d_L^2(z,\Omega)K_F(z,\phi(E))}{(1+z)^{1/\eta}} = \left(\frac{E_p}{\xi}\right)^{1/\eta}\frac{L_0}{4\pi F_\gamma}. \tag{C.3}$$

The redshift can then be solved by a numerical method such as Newton's method or a bisection method. In the case of a recursive root-finding algorithm, d_L and K_F must be calculated at each recursion so that the redshift can be successfully found. To find the associated uncertainty, let

$$C = \left(\frac{E_p}{\xi}\right)^{1/\eta} \frac{L_0}{4\pi F_\gamma} \tag{C.4}$$

and then the partial derivatives of C are

$$\begin{aligned}
\frac{\partial C}{\partial E_p} &= \frac{C}{\eta E_p}; \\
\frac{\partial C}{\partial F_\gamma} &= -\frac{C}{F_\gamma}; \\
\frac{\partial C}{\partial \xi} &= -\frac{C}{\eta \xi}; \\
\frac{\partial C}{\partial \eta} &= -\frac{C \ln(\frac{E_p}{\xi})}{\eta^2}.
\end{aligned} \tag{C.5}$$

The propagated uncertainty of the pseudo-redshift can then be determined as

$$\sigma_z^2 = \left|\frac{\partial C}{\partial E_p}\right| \sigma_{E_p}^2 + \left|\frac{\partial C}{\partial F_\gamma}\right| \sigma_{F_\gamma}^2 + \left|\frac{\partial C}{\partial \xi}\right| \sigma_\xi^2 + \left|\frac{\partial C}{\partial \eta}\right| \sigma_\eta^2. \tag{C.6}$$

APPENDIX D

SIMULTANEOUS SOLUTIONS OF REDSHIFT, DISTANCE MODULUS, AND JET OPENING ANGLE

Since the luminosity relations under discussion were independently calibrated without regard to a specific cosmological model, and the assumption is that the relations do not change appreciably with redshift, then we have three resulting equations for three unknown quantities: the redshift z, distance modulus μ, and jet opening angle θ_j. Since the correlations all take the form of a power law, we can take the logarithm of each relation such that they become linear equations in logarithmic space. For clarity and brevity, we use the following notation: $\hat{x} = \log_{10}(x)$. Let $A = 4\pi/E_0$ or $A = 4\pi/L_0$ depending on the relation and let $Z = (1+z)$, and then each relation can be written as

$$\begin{aligned}
\hat{E}_{p,f} + \hat{Z} &= \hat{\xi}_1 + \eta_1(\hat{A}_1 + 2\hat{d}_L + \hat{S}_\gamma + \hat{K}_S + \hat{f}_b - \hat{Z}), \\
\hat{E}_{p,p} + \hat{Z} &= \hat{\xi}_2 + \eta_2(\hat{A}_2 + 2\hat{d}_L + \hat{F}_\gamma + \hat{K}_F), \\
\hat{E}_{p,p} + \hat{Z} &= \hat{\xi}_3 + \eta_3(\hat{A}_3 + 2\hat{d}_L + \hat{F}_\gamma + \hat{K}_F + \hat{f}_b),
\end{aligned} \tag{D.1}$$

where the ξ_i and η_i are the corresponding correlation parameters, d_L is the luminosity distance, S_γ is the gamma-ray fluence, F_γ is the gamma-ray peak flux, $E_{p,f}$ is the E_p

of the time-integrated spectrum, $E_{p,p}$ is the E_p of the peak flux spectrum, K_S and K_F are the K-corrections for the time-integrated and peak spectra respectively, and f_b is the beaming fraction. The equations can be rearranged so that all of the unknown quantities are on one side of the equation:

$$\begin{aligned}
(1+\eta_1)\hat{Z} - 2\eta_1\hat{d}_L - \eta_1\hat{K}_S - \eta_1\hat{f}_b &= \hat{\xi}_1 + \eta_1(\hat{A}_1 + \hat{S}_\gamma) - \hat{E}_{p,f}, \\
\hat{Z} - 2\eta_2\hat{d}_L - \eta_2\hat{K}_F &= \hat{\xi}_2 + \eta_2(\hat{A}_2 + \hat{F}_\gamma) - \hat{E}_{p,p}, \\
\hat{Z} - 2\eta_3\hat{d}_L - \eta_3\hat{K}_F - \eta_3\hat{f}_b &= \hat{\xi}_3 + \eta_3(\hat{A}_3 + \hat{F}_\gamma) - \hat{E}_{p,p}.
\end{aligned} \tag{D.2}$$

The K-corrections are functions of the redshift and the photon model parameters and introduce nonlinearity into Equation D.2. If the K-corrections are neglected, then the equations can be written in matrix form as a set of linear equations:

$$\begin{bmatrix} 1+\eta_1 & -2\eta_1 & -\eta_1 \\ 1 & -2\eta_2 & 0 \\ 1 & -2\eta_3 & -\eta_3 \end{bmatrix} \begin{bmatrix} \hat{z} \\ \hat{d}_L \\ \hat{f}_b \end{bmatrix} = \begin{bmatrix} \hat{C}_1 \\ \hat{C}_2 \\ \hat{C}_3 \end{bmatrix}, \tag{D.3}$$

where the $\hat{C}_i$ are the right hand side of Equation D.2. The solution vector can then be found by any number of algorithms such as Gaussian elimination or LU decomposition. Once the solution vector is found, it can be mapped back into linear space. The linearization of the relations in Equation D.3 results in an efficient and effective procedure to estimate the pertinent unknown quantities.

If, however, the K-corrections are incorporated into the relations, the linear solution is no longer an option. In this case the relations again take the form of

Equation D.2 and moving the $\hat{C}_i$ to the left hand side of the equation creates an opportunity to use a root-finding algorithm such as Newton-Raphson. The difficulty with root-finding algorithms is that they require an initial guess vector sufficiently close to a root. The accuracy of such methods are increased by testing convergence to a solution vector by initializing at different guess vectors. An alternative method is to solve the exact equation by excluding the K-correction and then using the result as the initial guess vector for the root-finding algorithm. For each iteration of the root-finding algorithm, the K-corrections for both spectra must be calculated and applied to the corresponding equations. One important point to note is that while the linear solution is exact, the nonlinear case will only converge to a certain specified tolerance of the actual value. It is important to be sure that the tolerance is much less than the total propagated error.

For both cases, the error propagation is straightforward. Note that the partial derivates with respect to the K-corrections are not needed if the linear case is desired. Working in logarithmic space, the partial derivatives are simply

$$\begin{aligned}
&\frac{\partial \hat{C}_i}{\partial \hat{E}_{p,i}} = -1; \quad \frac{\partial \hat{C}_1}{\partial \hat{S}_\gamma} = \eta_1; \quad \frac{\partial \hat{C}_{2,3}}{\partial \hat{F}_\gamma} = \eta_{2,3}; \\
&\frac{\partial \hat{C}_i}{\partial \hat{K}_{S,F}} = -\eta_i; \quad \frac{\partial \hat{C}_i}{\partial \hat{\xi}_i} = 1; \\
&\frac{\partial \hat{C}_1}{\partial \eta_1} = \hat{Z} - (\hat{A}_1 + 2\hat{d}_L + \hat{S}_\gamma + \hat{K}_S + \hat{f}_b); \\
&\frac{\partial \hat{C}_2}{\partial \eta_2} = -(\hat{A}_2 + 2\hat{d}_L + \hat{F}_\gamma + \hat{K}_F); \\
&\frac{\partial \hat{C}_3}{\partial \eta_3} = -(\hat{A}_3 + 2\hat{d}_L + \hat{F}_\gamma + \hat{K}_F + \hat{f}_b).
\end{aligned} \tag{D.4}$$

Since all three equations are required to solve for each unknown, the propagated uncertainty for each unknown is the sum of the uncertainty from all equations in quadrature:

$$\sigma_{\hat{Z}}^2 = \sigma_{\hat{d}_L}^2 = \sigma_{\hat{f}_b}^2 = \sum_j \left| \frac{\partial C_j}{\partial \hat{\Theta}_j} \right|^2 \sigma_{\hat{\Theta}_j}^2, \tag{D.5}$$

where the Θ_j are the known quantities which have uncertainties to be propagated. Once the values and uncertainties have been determined in logarithmic space, they can be mapped back into linear space (e.g. $Z = 10^{\hat{Z}}$ and $\sigma_Z = Z \ln(10) \sigma_{\hat{Z}}$).

APPENDIX E

DERIVED Z, μ, AND θ_J VALUES

Table E.1: Derived z, μ, and θ_j used in the GBM silver sample

GBM Trigger #	z	μ	$\theta_j(^\circ)$
080714745	6.18 ± 3.07	48.08 ± 0.93	9.31 ± 2.00
080723557	1.85 ± 0.47	44.33 ± 0.36	7.89 ± 0.65
080723985	1.88 ± 0.82	46.57 ± 0.62	8.80 ± 1.25
080724401	1.62 ± 0.59	45.00 ± 0.49	7.48 ± 0.84
080727964	5.89 ± 3.30	48.65 ± 1.04	9.37 ± 2.25
080730520	2.24 ± 1.10	45.84 ± 0.74	7.50 ± 1.28
080804972	1.42 ± 0.86	46.28 ± 0.77	7.57 ± 1.35
080806896	13.13 ± 3.58	48.23 ± 0.55	9.08 ± 1.15
080808565	1.37 ± 0.66	45.23 ± 0.61	6.83 ± 0.95
080816503	2.17 ± 0.82	45.74 ± 0.57	7.47 ± 0.97
080817161	2.17 ± 0.78	46.07 ± 0.53	8.65 ± 1.06
080825593	1.56 ± 0.47	44.57 ± 0.40	7.95 ± 0.73
080829790	1.63 ± 0.85	46.29 ± 0.70	7.25 ± 1.18
080830368	1.18 ± 1.07	46.97 ± 1.06	8.38 ± 2.06
080831921	5.68 ± 4.08	48.18 ± 1.33	8.41 ± 2.57
080904886	2.96 ± 0.78	44.87 ± 0.43	6.98 ± 0.69
080905570	1.78 ± 1.30	45.88 ± 1.02	7.05 ± 1.65
080913735	1.24 ± 0.96	46.37 ± 0.93	7.15 ± 1.54
080916406	8.26 ± 3.18	48.40 ± 0.74	9.31 ± 1.60
080927480	12.46 ± 9.42	49.77 ± 1.52	9.38 ± 3.29

Table E.1 (continued)

GBM Trigger #	z	μ	$\theta_j(^\circ)$
081008832	3.49 ± 2.32	47.85 ± 1.12	8.20 ± 2.12
081009140	4.21 ± 0.64	43.31 ± 0.27	7.54 ± 0.46
081009690	4.53 ± 2.99	46.32 ± 1.18	8.06 ± 2.19
081021398	1.59 ± 0.91	46.48 ± 0.77	7.50 ± 1.32
081024851	5.83 ± 3.87	48.13 ± 1.23	7.93 ± 2.25
081025349	1.40 ± 1.15	46.89 ± 1.04	8.42 ± 2.02
081102739	1.50 ± 1.22	46.74 ± 1.06	7.24 ± 1.77
081118876	2.60 ± 0.98	45.77 ± 0.59	7.40 ± 1.01
081120618	5.61 ± 0.85	48.22 ± 0.28	8.52 ± 0.55
081121858	1.67 ± 1.37	45.58 ± 1.12	7.82 ± 2.02
081204004	3.20 ± 2.59	48.05 ± 1.34	8.79 ± 2.72
081207680	13.99 ± 9.37	50.44 ± 1.36	11.64 ± 3.65
081221681	3.21 ± 0.56	44.98 ± 0.29	7.76 ± 0.52
081226156	1.39 ± 0.57	45.67 ± 0.52	7.97 ± 0.95
081231140	2.16 ± 0.60	45.57 ± 0.42	7.69 ± 0.74
090101758	2.48 ± 1.05	45.26 ± 0.66	7.86 ± 1.19
090112729	2.10 ± 1.97	47.40 ± 1.38	8.26 ± 2.63
090117632	2.70 ± 2.12	47.54 ± 1.24	8.82 ± 2.53
090129880	2.02 ± 1.56	46.59 ± 1.12	7.63 ± 1.98
090222179	1.44 ± 0.58	47.28 ± 0.52	7.25 ± 0.86
090306245	2.62 ± 2.30	49.62 ± 1.38	9.65 ± 3.07
090309767	4.52 ± 2.23	48.01 ± 0.88	8.82 ± 1.78
090310189	2.32 ± 0.72	46.40 ± 0.47	8.92 ± 0.98
090323002	5.49 ± 4.05	47.71 ± 1.36	7.99 ± 2.50
090326633	3.10 ± 1.36	47.20 ± 0.72	7.56 ± 1.25
090327404	6.19 ± 3.29	48.63 ± 0.99	9.69 ± 2.23
090330279	1.82 ± 1.13	45.87 ± 0.87	7.65 ± 1.53
090411838	3.85 ± 2.50	47.95 ± 1.12	8.86 ± 2.29
090411991	1.80 ± 1.69	46.78 ± 1.31	7.02 ± 2.13
090422150	3.93 ± 1.71	47.50 ± 0.75	7.60 ± 1.32
090425377	4.97 ± 2.10	47.02 ± 0.76	7.79 ± 1.37
090427688	8.43 ± 5.57	49.68 ± 1.28	10.13 ± 3.00
090502777	3.53 ± 0.76	45.74 ± 0.36	7.22 ± 0.60
090514734	6.56 ± 4.14	48.43 ± 1.19	8.65 ± 2.38
090516137	3.07 ± 0.70	45.71 ± 0.37	7.90 ± 0.68

Table E.1 (continued)

GBM Trigger #	z	μ	$\theta_j(^\circ)$
090520876	5.75 ± 5.55	46.47 ± 1.78	7.43 ± 3.06
090522344	3.90 ± 1.47	46.57 ± 0.65	8.66 ± 1.30
090524346	14.68 ± 2.98	47.41 ± 0.41	8.85 ± 0.84
090528173	3.41 ± 2.86	48.23 ± 1.41	8.18 ± 2.65
090528516	16.57 ± 7.89	48.99 ± 0.98	8.90 ± 2.00
090530760	3.97 ± 3.54	47.23 ± 1.55	7.39 ± 2.63
090610723	1.54 ± 1.07	46.27 ± 0.91	7.28 ± 1.53
090618353	7.27 ± 2.63	48.33 ± 0.69	8.54 ± 1.36
090621185	5.00 ± 1.42	46.29 ± 0.51	8.51 ± 1.01
090621447	5.12 ± 1.90	46.09 ± 0.68	7.20 ± 1.12
090709630	12.62 ± 7.25	49.04 ± 1.16	8.72 ± 2.32
090713020	1.36 ± 0.77	45.68 ± 0.71	7.53 ± 1.23
090717034	1.40 ± 1.26	46.90 ± 1.14	8.16 ± 2.14
090810659	2.34 ± 0.77	44.82 ± 0.50	6.84 ± 0.79
090810781	3.85 ± 1.44	46.63 ± 0.65	6.93 ± 1.03
090813174	5.09 ± 3.09	48.30 ± 1.10	8.74 ± 2.22
090814950	3.09 ± 1.08	46.84 ± 0.57	10.81 ± 1.43
090815438	11.99 ± 6.51	48.85 ± 1.09	9.77 ± 2.45
090824918	4.23 ± 2.17	48.10 ± 0.90	9.29 ± 1.93
090829702	1.61 ± 1.44	47.33 ± 1.20	9.00 ± 2.50
090902462	2.18 ± 1.24	45.89 ± 0.85	7.24 ± 1.41
090904058	5.89 ± 2.12	47.66 ± 0.67	8.19 ± 1.26
090910812	2.68 ± 1.15	47.39 ± 0.68	8.31 ± 1.30
090920035	3.40 ± 1.45	48.03 ± 0.72	10.19 ± 1.69
090922605	1.28 ± 0.90	46.70 ± 0.85	8.56 ± 1.69
090925389	4.65 ± 4.38	47.93 ± 1.68	7.62 ± 2.96
090926914	2.48 ± 0.58	45.28 ± 0.36	7.65 ± 0.64
091030613	3.19 ± 2.03	46.69 ± 1.05	7.94 ± 1.93
091030828	5.10 ± 1.39	47.14 ± 0.49	8.98 ± 1.02
091031500	2.86 ± 1.90	47.45 ± 1.07	8.32 ± 2.05
091117080	3.82 ± 1.35	45.41 ± 0.61	8.11 ± 1.13
091120191	2.41 ± 1.24	45.54 ± 0.79	6.89 ± 1.26
091123298	2.64 ± 1.07	46.23 ± 0.64	7.76 ± 1.14
091128285	15.87 ± 9.46	50.60 ± 1.22	11.46 ± 3.22
091207333	4.62 ± 3.68	47.99 ± 1.42	8.13 ± 2.67

Table E.1 (continued)

GBM Trigger #	z	μ	$\theta_j(^\circ)$
091208410	2.41 ± 1.66	47.90 ± 1.05	9.07 ± 2.21
091209001	2.80 ± 1.18	46.89 ± 0.68	7.91 ± 1.24
091220442	1.33 ± 0.70	47.44 ± 0.65	10.03 ± 1.51
091221870	1.58 ± 0.50	43.16 ± 0.42	6.86 ± 0.67
091223511	6.61 ± 6.50	48.75 ± 1.85	9.72 ± 4.16
091227294	7.41 ± 6.03	48.95 ± 1.56	9.11 ± 3.27
091231206	5.18 ± 4.18	48.43 ± 1.47	9.08 ± 3.08
100116897	3.45 ± 2.46	47.89 ± 1.20	7.93 ± 2.19
100122616	2.69 ± 1.84	45.87 ± 1.08	7.85 ± 1.96
100130729	5.43 ± 5.33	49.21 ± 1.80	8.76 ± 3.64
100130777	1.65 ± 1.13	46.84 ± 0.93	7.58 ± 1.62
100204024	8.45 ± 4.06	48.21 ± 0.93	8.59 ± 1.85
100204566	8.10 ± 7.43	48.27 ± 1.77	8.25 ± 3.38
100211440	1.88 ± 0.41	45.17 ± 0.31	7.78 ± 0.56
100221368	4.22 ± 2.77	47.15 ± 1.15	7.72 ± 2.05
100301223	1.56 ± 0.68	45.83 ± 0.58	7.50 ± 1.00
100304534	1.18 ± 1.09	45.68 ± 1.09	6.98 ± 1.75
100307928	12.04 ± 6.17	51.70 ± 1.03	11.07 ± 2.63
100322045	3.07 ± 2.10	47.08 ± 1.12	7.85 ± 2.03
100325246	3.89 ± 2.07	48.13 ± 0.92	9.01 ± 1.91
100330309	1.39 ± 0.96	46.11 ± 0.87	7.71 ± 1.56
100406758	2.66 ± 0.96	46.90 ± 0.57	7.78 ± 1.03
100410356	4.78 ± 2.15	46.08 ± 0.81	7.90 ± 1.47
100421917	7.07 ± 6.14	48.13 ± 1.65	8.42 ± 3.21
100424876	4.02 ± 0.96	46.63 ± 0.42	7.70 ± 0.74
100503554	10.87 ± 5.51	48.07 ± 1.01	9.35 ± 2.17
100507577	1.71 ± 0.72	45.91 ± 0.58	8.37 ± 1.12
100517072	2.33 ± 1.61	47.06 ± 1.05	8.67 ± 2.10
100517243	5.54 ± 2.39	48.32 ± 0.79	8.52 ± 1.56
100519204	2.52 ± 1.11	44.62 ± 0.69	6.82 ± 1.08
100527795	1.29 ± 0.82	45.52 ± 0.78	7.08 ± 1.28
100528075	5.66 ± 3.15	48.50 ± 1.03	8.97 ± 2.12
100604287	1.76 ± 0.92	46.20 ± 0.72	8.07 ± 1.35
100609783	5.71 ± 4.70	48.78 ± 1.52	9.71 ± 3.41

Table E.2: Derived z, μ, and θ_j used in the GBM gold sample

GBM Trigger #	z	μ	$\theta_j(^\circ)$
080808565	2.28 ± 1.75	45.85 ± 1.16	7.11 ± 1.90
080818945	2.73 ± 2.55	47.20 ± 1.49	6.99 ± 2.40
080829790	1.32 ± 0.97	46.10 ± 0.91	7.15 ± 1.50
080904886	2.62 ± 1.43	44.36 ± 0.86	6.91 ± 1.36
080916406	17.27 ± 13.67	49.46 ± 1.63	10.12 ± 3.80
081009140	6.47 ± 1.36	43.92 ± 0.39	7.88 ± 0.72
081021398	1.84 ± 1.63	46.58 ± 1.25	7.58 ± 2.18
081024851	6.27 ± 4.38	48.18 ± 1.31	7.99 ± 2.42
081118876	2.64 ± 2.22	45.65 ± 1.32	7.41 ± 2.26
081221681	3.07 ± 0.83	44.90 ± 0.44	7.73 ± 0.79
081231140	4.40 ± 3.10	46.94 ± 1.25	8.81 ± 2.53
090101758	4.34 ± 3.60	46.92 ± 1.46	8.20 ± 2.77
090112729	5.88 ± 4.25	46.18 ± 1.34	8.54 ± 2.64
090131090	3.55 ± 1.01	44.49 ± 0.48	6.94 ± 0.77
090323002	3.53 ± 3.13	46.86 ± 1.50	9.27 ± 3.21
090502777	6.71 ± 5.19	47.53 ± 1.46	8.04 ± 2.71
090520876	4.97 ± 1.86	46.47 ± 0.68	7.46 ± 1.16
090524346	4.08 ± 1.50	46.04 ± 0.64	8.11 ± 1.20
090618353	3.55 ± 1.99	44.94 ± 0.95	7.87 ± 1.72
090621185	7.18 ± 3.08	48.29 ± 0.82	8.53 ± 1.61
090626189	7.20 ± 5.27	46.57 ± 1.39	8.84 ± 2.85
090713020	2.97 ± 2.18	45.86 ± 1.19	8.25 ± 2.27
090717034	5.20 ± 3.85	45.87 ± 1.35	7.21 ± 2.24
090718762	2.39 ± 1.51	44.53 ± 0.97	6.86 ± 1.53
090810659	2.34 ± 0.82	44.07 ± 0.53	8.29 ± 1.02
090815438	1.66 ± 0.85	42.91 ± 0.70	7.65 ± 1.23
090820027	1.87 ± 1.41	45.29 ± 1.07	10.35 ± 2.55
090829672	13.10 ± 13.03	48.78 ± 2.01	9.86 ± 4.57
090902462	3.06 ± 1.36	45.58 ± 0.72	8.84 ± 1.48
090904058	6.62 ± 2.78	47.83 ± 0.79	8.29 ± 1.52

Table E.2 (continued)

GBM Trigger #	z	μ	$\theta_j(^\circ)$
090926181	9.40 ± 7.53	49.50 ± 1.57	9.15 ± 3.32
090926914	3.04 ± 1.00	45.53 ± 0.54	7.80 ± 0.96
091101143	2.01 ± 0.52	42.52 ± 0.38	6.81 ± 0.59
091120191	5.66 ± 4.24	47.31 ± 1.38	9.08 ± 2.90
091127976	4.12 ± 3.57	45.15 ± 1.51	8.17 ± 2.85
091128285	2.53 ± 1.93	45.49 ± 1.19	6.92 ± 1.90
091208410	1.51 ± 0.65	42.80 ± 0.56	6.83 ± 0.89
091209001	1.64 ± 1.50	46.87 ± 1.23	7.58 ± 2.16
100122616	2.94 ± 1.55	45.64 ± 0.86	8.08 ± 1.59
100301223	1.76 ± 1.32	45.94 ± 1.04	7.57 ± 1.81
100322045	2.64 ± 1.93	47.02 ± 1.15	7.78 ± 2.06
100330309	7.13 ± 4.61	46.38 ± 1.23	8.23 ± 2.34
100507577	1.44 ± 1.40	44.92 ± 1.25	6.91 ± 1.98
100517072	4.88 ± 4.69	46.91 ± 1.73	9.20 ± 3.68
100517154	6.62 ± 4.65	45.98 ± 1.32	7.49 ± 2.29

Table E.3: Derived z, μ, and θ_j used in the BATSE silver sample

BATSE Trigger #	z	μ	$\theta_j(^\circ)$
1009	6.11 ± 2.25	49.06 ± 0.69	9.35 ± 1.48
1036	5.58 ± 2.38	49.17 ± 0.79	8.80 ± 1.60
1039	2.33 ± 0.45	46.76 ± 0.29	7.42 ± 0.50
1046	7.57 ± 3.28	48.91 ± 0.83	9.05 ± 1.74
1086	15.67 ± 4.94	53.74 ± 0.64	11.91 ± 1.77
1087	4.30 ± 2.27	48.98 ± 0.93	7.93 ± 1.70
1122	1.74 ± 0.34	44.91 ± 0.27	7.91 ± 0.49
1148	1.79 ± 0.63	47.69 ± 0.49	8.55 ± 0.96
1150	2.04 ± 0.66	45.42 ± 0.47	6.96 ± 0.75
1156	8.01 ± 6.13	49.23 ± 1.48	9.44 ± 3.22
1192	3.15 ± 0.86	48.55 ± 0.45	7.68 ± 0.80
1196	6.25 ± 3.26	49.62 ± 0.98	9.03 ± 2.03
1197	3.63 ± 0.80	47.88 ± 0.38	8.15 ± 0.71
1200	1.64 ± 0.41	46.18 ± 0.34	7.17 ± 0.56
1218	1.23 ± 0.62	46.61 ± 0.60	7.27 ± 1.01
1221	4.68 ± 0.91	47.34 ± 0.35	8.52 ± 0.68
1235	5.33 ± 1.22	47.16 ± 0.42	9.30 ± 0.90
1279	1.96 ± 0.96	47.36 ± 0.71	7.86 ± 1.28
1288	1.94 ± 0.51	46.56 ± 0.38	8.98 ± 0.78
1384	7.77 ± 7.13	50.09 ± 1.76	9.79 ± 3.98
1385	1.65 ± 0.45	45.71 ± 0.36	7.37 ± 0.62
1396	3.88 ± 0.79	46.57 ± 0.35	8.61 ± 0.70
1406	1.48 ± 0.36	46.65 ± 0.32	8.17 ± 0.60
1419	1.72 ± 0.85	47.65 ± 0.67	8.38 ± 1.31
1447	5.45 ± 1.77	48.92 ± 0.60	8.39 ± 1.15
1449	1.56 ± 0.50	45.81 ± 0.43	7.64 ± 0.75
1458	1.81 ± 0.55	46.75 ± 0.43	7.76 ± 0.77
1467	4.03 ± 1.64	48.40 ± 0.71	8.30 ± 1.36
1468	2.98 ± 0.57	46.82 ± 0.31	8.00 ± 0.57
1472	6.19 ± 1.64	49.25 ± 0.50	8.57 ± 0.98

Table E.3 (continued)

BATSE Trigger #	z	μ	$\theta_j(^\circ)$
1515	4.09 ± 1.25	48.74 ± 0.53	8.80 ± 1.08
1524	5.36 ± 1.60	49.02 ± 0.55	8.50 ± 1.07
1533	1.28 ± 0.60	46.03 ± 0.57	6.55 ± 0.86
1540	8.47 ± 3.46	49.77 ± 0.79	9.12 ± 1.67
1559	1.29 ± 0.29	45.72 ± 0.28	7.70 ± 0.49
1561	1.91 ± 0.76	48.61 ± 0.57	8.99 ± 1.17
1567	5.99 ± 1.16	48.42 ± 0.36	8.22 ± 0.68
1574	9.76 ± 2.47	51.68 ± 0.50	10.45 ± 1.20
1578	4.93 ± 3.28	49.11 ± 1.20	8.45 ± 2.34
1580	6.77 ± 1.37	47.34 ± 0.38	9.23 ± 0.81
1586	2.78 ± 1.21	48.07 ± 0.70	8.01 ± 1.29
1590	2.66 ± 0.89	47.82 ± 0.53	9.17 ± 1.12
1603	3.17 ± 1.32	47.93 ± 0.69	8.16 ± 1.29
1604	1.50 ± 0.41	45.49 ± 0.36	9.04 ± 0.75
1606	5.24 ± 1.70	47.86 ± 0.59	8.29 ± 1.13
1614	2.96 ± 1.59	48.55 ± 0.87	8.15 ± 1.64
1623	2.77 ± 1.26	48.45 ± 0.73	7.55 ± 1.26
1624	4.88 ± 0.85	46.78 ± 0.31	8.46 ± 0.61
1625	7.80 ± 3.35	48.42 ± 0.83	8.05 ± 1.54
1628	4.37 ± 1.63	48.91 ± 0.66	7.77 ± 1.18
1642	2.30 ± 0.54	50.31 ± 0.36	9.29 ± 0.76
1648	3.23 ± 0.64	47.32 ± 0.33	8.01 ± 0.61
1652	1.43 ± 0.41	45.33 ± 0.36	9.01 ± 0.76
1653	3.64 ± 0.68	46.40 ± 0.32	8.65 ± 0.64
1655	3.45 ± 2.05	48.83 ± 1.00	7.72 ± 1.78
1657	7.40 ± 2.47	53.00 ± 0.64	11.88 ± 1.75
1660	1.76 ± 0.33	45.19 ± 0.26	7.79 ± 0.46
1663	11.64 ± 2.84	49.11 ± 0.49	9.89 ± 1.12
1676	9.59 ± 4.88	49.96 ± 1.00	9.00 ± 2.08
1687	1.44 ± 0.51	47.17 ± 0.45	8.47 ± 0.89
1693	1.69 ± 0.54	46.48 ± 0.43	7.16 ± 0.72
1698	2.02 ± 0.92	46.70 ± 0.66	7.16 ± 1.09
1712	5.38 ± 1.11	49.53 ± 0.38	8.41 ± 0.73
1730	5.32 ± 1.21	47.91 ± 0.42	8.78 ± 0.84
1731	1.93 ± 1.18	48.04 ± 0.87	7.75 ± 1.56

Table E.3 (continued)

BATSE Trigger #	z	μ	$\theta_j(^\circ)$
1734	7.23 ± 1.25	49.55 ± 0.33	8.86 ± 0.68
1742	2.40 ± 0.52	47.03 ± 0.33	7.97 ± 0.61
1806	3.09 ± 1.02	47.22 ± 0.54	8.62 ± 1.08
1807	11.27 ± 4.25	48.48 ± 0.75	9.40 ± 1.63
1830	7.92 ± 2.36	49.34 ± 0.57	10.00 ± 1.33
1885	2.86 ± 2.46	49.40 ± 1.38	9.86 ± 3.15
1967	15.58 ± 5.65	49.82 ± 0.74	10.93 ± 1.87
1982	2.10 ± 0.40	44.63 ± 0.28	8.38 ± 0.54
1997	3.52 ± 1.68	49.33 ± 0.81	8.83 ± 1.64
2019	8.01 ± 1.76	48.94 ± 0.42	9.09 ± 0.89
2041	10.32 ± 3.67	49.94 ± 0.70	8.65 ± 1.41
2061	1.73 ± 1.17	48.22 ± 0.93	8.08 ± 1.73
2067	4.43 ± 1.08	47.47 ± 0.43	9.05 ± 0.90
2070	1.83 ± 0.39	45.99 ± 0.30	8.30 ± 0.57
2074	9.42 ± 3.14	52.76 ± 0.65	11.89 ± 1.80
2077	2.28 ± 0.64	47.37 ± 0.42	8.27 ± 0.81
2079	3.70 ± 0.67	47.82 ± 0.31	7.97 ± 0.57
2080	3.30 ± 0.63	46.51 ± 0.32	7.74 ± 0.57
2090	2.82 ± 0.50	45.35 ± 0.28	8.12 ± 0.53
2101	3.13 ± 0.83	47.18 ± 0.44	7.17 ± 0.72
2106	2.42 ± 1.37	47.81 ± 0.87	8.23 ± 1.66
2111	5.75 ± 1.33	46.52 ± 0.43	9.71 ± 0.96
2123	2.53 ± 1.09	47.51 ± 0.67	7.79 ± 1.20
2138	1.43 ± 0.91	48.14 ± 0.81	8.18 ± 1.53
2140	3.86 ± 0.90	48.00 ± 0.40	7.72 ± 0.72
2148	2.68 ± 1.04	48.77 ± 0.61	7.92 ± 1.12
2156	9.43 ± 2.32	49.22 ± 0.48	9.83 ± 1.09
2160	2.83 ± 0.50	47.95 ± 0.29	8.07 ± 0.53
2169	2.78 ± 2.02	47.93 ± 1.16	7.53 ± 2.02
2188	3.74 ± 1.24	48.60 ± 0.57	9.18 ± 1.21
2189	2.42 ± 0.65	46.88 ± 0.41	8.77 ± 0.83
2193	5.89 ± 1.14	47.23 ± 0.36	8.94 ± 0.74
2197	1.80 ± 1.39	49.22 ± 1.08	7.94 ± 1.97
2202	6.51 ± 5.26	49.29 ± 1.52	8.76 ± 3.07
2204	3.77 ± 1.99	48.48 ± 0.90	7.85 ± 1.64

Table E.3 (continued)

BATSE Trigger #	z	μ	$\theta_j(^\circ)$
2211	5.33 ± 1.01	49.16 ± 0.35	8.52 ± 0.68
2213	2.75 ± 2.58	48.64 ± 1.50	9.12 ± 3.15
2228	3.98 ± 1.36	51.74 ± 0.59	11.15 ± 1.52
2233	1.36 ± 0.69	47.35 ± 0.63	7.83 ± 1.14
2240	10.59 ± 2.60	48.74 ± 0.49	9.57 ± 1.07
2244	1.84 ± 1.66	47.09 ± 1.27	7.33 ± 2.15
2252	6.74 ± 2.80	49.12 ± 0.79	8.72 ± 1.58
2267	3.19 ± 2.59	47.71 ± 1.34	7.42 ± 2.30
2276	1.85 ± 1.38	47.02 ± 1.05	7.03 ± 1.71
2277	2.20 ± 0.53	47.11 ± 0.36	7.99 ± 0.66
2287	3.72 ± 0.92	46.36 ± 0.42	8.40 ± 0.82
2298	4.83 ± 1.45	48.67 ± 0.54	8.43 ± 1.05
2304	7.30 ± 2.36	48.78 ± 0.62	9.10 ± 1.30
2310	1.53 ± 0.39	46.54 ± 0.33	7.31 ± 0.56
2311	1.41 ± 0.33	49.64 ± 0.29	8.70 ± 0.59
2315	2.15 ± 1.59	48.92 ± 1.10	9.20 ± 2.33
2316	3.25 ± 1.40	49.30 ± 0.72	9.26 ± 1.53
2324	2.89 ± 0.52	46.18 ± 0.29	8.15 ± 0.54
2328	5.42 ± 1.96	49.01 ± 0.66	9.06 ± 1.38
2340	3.66 ± 0.99	49.88 ± 0.46	9.22 ± 0.98
2347	3.52 ± 1.52	48.07 ± 0.73	9.13 ± 1.54
2373	10.55 ± 2.72	49.19 ± 0.51	9.39 ± 1.11
2375	1.60 ± 0.51	46.77 ± 0.43	7.27 ± 0.72
2380	5.35 ± 1.51	48.13 ± 0.51	8.36 ± 0.99
2387	4.39 ± 1.26	48.30 ± 0.51	8.10 ± 0.95
2394	2.39 ± 0.94	47.58 ± 0.60	8.58 ± 1.19
2419	2.77 ± 0.55	46.24 ± 0.32	8.52 ± 0.63
2428	6.01 ± 1.79	48.99 ± 0.55	8.64 ± 1.11
2429	3.04 ± 0.54	46.78 ± 0.29	7.36 ± 0.50
2430	4.36 ± 4.25	50.29 ± 1.72	9.07 ± 3.60
2435	5.34 ± 0.79	46.95 ± 0.27	7.87 ± 0.49
2440	3.95 ± 0.96	47.57 ± 0.42	8.14 ± 0.79
2443	1.89 ± 1.24	48.47 ± 0.93	8.59 ± 1.85
2447	10.40 ± 3.05	49.64 ± 0.58	9.58 ± 1.29
2450	2.95 ± 1.44	48.86 ± 0.79	8.26 ± 1.51

Table E.3 (continued)

BATSE Trigger #	z	μ	$\theta_j(^\circ)$
2451	1.51 ± 1.22	47.44 ± 1.06	7.52 ± 1.83
2452	4.43 ± 1.53	48.14 ± 0.61	8.36 ± 1.18
2472	4.59 ± 1.12	48.16 ± 0.44	9.16 ± 0.92
2476	11.79 ± 2.55	48.49 ± 0.43	9.09 ± 0.91
2482	4.38 ± 1.13	46.89 ± 0.46	9.71 ± 1.02
2495	7.84 ± 3.62	49.54 ± 0.89	9.33 ± 1.91
2500	3.08 ± 0.73	47.68 ± 0.39	8.51 ± 0.77
2505	1.76 ± 0.55	48.59 ± 0.43	8.85 ± 0.88
2515	6.91 ± 4.72	50.18 ± 1.30	10.09 ± 3.02
2519	2.27 ± 0.47	46.83 ± 0.31	7.45 ± 0.53
2522	3.52 ± 0.55	45.75 ± 0.26	7.45 ± 0.45
2530	5.09 ± 1.71	48.02 ± 0.61	9.23 ± 1.30
2533	2.69 ± 0.89	47.05 ± 0.52	7.17 ± 0.87
2541	2.24 ± 0.54	49.51 ± 0.36	9.10 ± 0.77
2542	2.60 ± 1.17	47.30 ± 0.70	7.73 ± 1.26
2560	4.03 ± 3.74	49.00 ± 1.61	8.36 ± 3.11
2581	1.20 ± 0.44	46.74 ± 0.44	7.05 ± 0.71
2593	4.16 ± 1.63	48.75 ± 0.69	7.94 ± 1.26
2600	2.27 ± 0.53	46.58 ± 0.35	7.68 ± 0.62
2603	2.51 ± 1.04	48.02 ± 0.64	8.92 ± 1.32
2606	2.26 ± 0.73	47.53 ± 0.49	7.93 ± 0.89
2608	7.90 ± 4.20	49.84 ± 1.02	8.80 ± 2.08
2619	5.39 ± 1.17	47.72 ± 0.40	8.13 ± 0.74
2620	1.68 ± 0.46	45.83 ± 0.38	8.01 ± 0.69
2634	4.44 ± 1.95	48.80 ± 0.78	9.60 ± 1.72
2636	2.15 ± 0.62	47.48 ± 0.43	8.75 ± 0.87
2640	1.52 ± 0.95	47.64 ± 0.82	7.91 ± 1.49
2663	1.93 ± 0.51	47.47 ± 0.37	8.41 ± 0.73
2665	5.03 ± 1.13	47.87 ± 0.41	9.22 ± 0.87
2681	1.30 ± 0.33	44.39 ± 0.31	8.67 ± 0.62
2688	2.20 ± 0.50	45.91 ± 0.34	8.44 ± 0.66
2695	10.98 ± 2.62	48.42 ± 0.47	8.54 ± 0.93
2696	5.72 ± 5.51	49.87 ± 1.78	8.25 ± 3.39
2700	1.86 ± 0.57	51.22 ± 0.43	9.97 ± 0.99
2703	2.00 ± 0.45	46.10 ± 0.33	8.44 ± 0.64

Table E.3 (continued)

BATSE Trigger #	z	μ	$\theta_j(^\circ)$
2709	2.58 ± 0.56	46.04 ± 0.34	8.67 ± 0.68
2753	3.07 ± 0.71	45.68 ± 0.38	9.15 ± 0.80
2775	3.50 ± 1.01	48.00 ± 0.49	8.99 ± 1.01
2780	3.27 ± 0.83	47.07 ± 0.42	8.27 ± 0.81
2790	1.87 ± 0.76	47.72 ± 0.58	9.09 ± 1.21
2798	2.94 ± 0.66	47.09 ± 0.37	8.92 ± 0.75
2812	1.49 ± 0.91	47.89 ± 0.79	8.90 ± 1.63
2815	3.97 ± 0.66	45.21 ± 0.29	7.19 ± 0.48
2825	3.04 ± 2.23	48.81 ± 1.20	7.69 ± 2.13
2830	2.20 ± 1.64	48.54 ± 1.12	7.87 ± 2.03
2848	3.49 ± 0.74	46.85 ± 0.36	8.15 ± 0.67
2852	7.13 ± 2.59	49.27 ± 0.69	8.62 ± 1.37
2855	7.67 ± 3.67	49.91 ± 0.92	9.47 ± 2.01
2856	1.95 ± 1.09	48.01 ± 0.80	7.96 ± 1.47
2863	1.69 ± 1.41	48.16 ± 1.14	8.03 ± 2.11
2877	1.30 ± 0.51	45.19 ± 0.48	7.05 ± 0.79
2881	3.92 ± 1.84	48.83 ± 0.81	8.00 ± 1.50
2889	1.72 ± 0.50	46.68 ± 0.40	7.28 ± 0.67
2890	2.26 ± 0.52	46.11 ± 0.35	7.79 ± 0.63
2897	2.63 ± 1.67	48.93 ± 1.00	8.82 ± 2.03
2916	1.85 ± 1.03	47.28 ± 0.78	9.25 ± 1.67
2917	4.11 ± 1.21	48.83 ± 0.51	8.19 ± 0.97
2922	1.52 ± 0.29	47.85 ± 0.25	7.31 ± 0.43
2924	1.61 ± 0.46	46.07 ± 0.38	6.88 ± 0.60
2925	1.34 ± 0.60	47.06 ± 0.56	7.56 ± 0.98
2931	1.86 ± 0.69	47.98 ± 0.52	8.60 ± 1.04
2932	3.59 ± 2.86	48.88 ± 1.36	8.25 ± 2.58
2939	4.30 ± 2.75	48.33 ± 1.13	8.22 ± 2.13
2947	1.22 ± 0.43	46.51 ± 0.42	7.37 ± 0.71
2950	7.80 ± 1.91	48.00 ± 0.47	9.76 ± 1.06
2958	1.47 ± 0.75	47.07 ± 0.66	7.81 ± 1.19
2961	6.52 ± 1.68	47.63 ± 0.48	9.77 ± 1.09
2984	2.55 ± 0.47	46.12 ± 0.29	7.16 ± 0.47
2985	3.72 ± 0.93	47.14 ± 0.43	8.46 ± 0.83
2990	1.34 ± 0.36	44.38 ± 0.34	8.86 ± 0.69

Table E.3 (continued)

BATSE Trigger #	z	μ	$\theta_j(^\circ)$
2996	10.59 ± 4.46	50.04 ± 0.84	9.88 ± 1.90
2998	2.03 ± 0.41	48.69 ± 0.29	7.66 ± 0.52
3005	7.03 ± 2.25	48.41 ± 0.61	8.87 ± 1.25
3011	3.94 ± 2.48	48.13 ± 1.09	8.03 ± 2.02
3012	2.72 ± 1.04	47.29 ± 0.60	7.99 ± 1.11
3017	4.22 ± 0.76	46.13 ± 0.32	7.24 ± 0.53
3032	1.47 ± 0.60	45.87 ± 0.53	7.18 ± 0.88
3035	4.25 ± 2.10	49.10 ± 0.87	9.21 ± 1.85
3040	2.27 ± 0.72	47.32 ± 0.48	7.25 ± 0.80
3042	1.86 ± 0.50	47.06 ± 0.38	8.35 ± 0.74
3055	4.72 ± 0.84	48.13 ± 0.32	8.22 ± 0.60
3056	1.20 ± 0.77	46.35 ± 0.76	7.09 ± 1.23
3057	2.20 ± 0.50	46.29 ± 0.34	7.28 ± 0.58
3071	12.47 ± 4.70	50.09 ± 0.76	8.63 ± 1.51
3074	1.85 ± 0.41	45.39 ± 0.31	8.68 ± 0.63
3075	4.43 ± 2.54	49.34 ± 1.02	8.27 ± 1.94
3085	3.76 ± 0.63	46.23 ± 0.29	7.33 ± 0.48
3093	1.52 ± 0.59	46.37 ± 0.51	7.02 ± 0.83
3100	1.53 ± 1.45	48.44 ± 1.25	7.38 ± 2.12
3101	2.88 ± 1.55	47.60 ± 0.87	8.58 ± 1.72
3102	5.31 ± 1.58	47.64 ± 0.54	7.44 ± 0.93
3103	1.23 ± 0.39	46.05 ± 0.38	8.20 ± 0.72
3105	1.47 ± 1.21	47.78 ± 1.07	7.62 ± 1.88
3109	1.71 ± 0.49	49.21 ± 0.39	9.50 ± 0.86
3120	5.18 ± 2.88	49.18 ± 1.01	8.38 ± 1.96
3125	6.76 ± 6.46	50.30 ± 1.81	10.00 ± 4.17
3127	9.44 ± 2.53	48.62 ± 0.53	9.25 ± 1.12
3128	16.37 ± 7.83	50.54 ± 0.98	10.09 ± 2.28
3129	2.79 ± 0.64	45.74 ± 0.37	9.16 ± 0.78
3130	1.72 ± 0.62	46.18 ± 0.49	7.72 ± 0.88
3131	3.15 ± 1.04	47.94 ± 0.55	7.89 ± 1.00
3132	3.69 ± 0.81	46.36 ± 0.37	9.17 ± 0.79
3136	6.21 ± 1.27	46.56 ± 0.38	9.39 ± 0.83
3143	7.29 ± 2.11	49.11 ± 0.55	9.31 ± 1.19
3156	3.37 ± 0.65	45.58 ± 0.32	8.90 ± 0.66

Table E.3 (continued)

BATSE Trigger #	z	μ	$\theta_j(^\circ)$
3163	3.68 ± 0.72	47.56 ± 0.33	8.17 ± 0.63
3168	3.26 ± 0.66	47.05 ± 0.33	8.45 ± 0.65
3171	1.30 ± 0.52	46.35 ± 0.49	7.91 ± 0.89
3174	1.92 ± 0.82	48.47 ± 0.61	7.76 ± 1.09
3193	4.15 ± 0.86	47.41 ± 0.36	7.68 ± 0.64
3212	1.37 ± 0.65	46.86 ± 0.60	7.77 ± 1.08
3220	1.36 ± 0.28	44.29 ± 0.26	7.47 ± 0.45
3227	6.27 ± 1.39	47.67 ± 0.41	8.65 ± 0.83
3237	5.41 ± 1.41	48.40 ± 0.48	8.37 ± 0.92
3238	1.86 ± 1.27	48.51 ± 0.96	7.83 ± 1.74
3241	1.53 ± 0.99	48.32 ± 0.85	7.63 ± 1.50
3245	5.14 ± 1.37	48.19 ± 0.48	8.74 ± 0.97
3247	2.86 ± 2.45	47.78 ± 1.38	7.87 ± 2.51
3253	7.34 ± 1.46	47.83 ± 0.38	9.23 ± 0.81
3256	3.02 ± 1.06	48.10 ± 0.57	8.09 ± 1.07
3257	2.54 ± 1.32	46.44 ± 0.81	7.31 ± 1.36
3259	6.79 ± 2.64	48.63 ± 0.74	8.13 ± 1.38
3267	1.51 ± 1.45	47.18 ± 1.26	7.30 ± 2.11
3279	4.17 ± 0.86	46.11 ± 0.36	9.09 ± 0.75
3283	2.36 ± 0.45	45.61 ± 0.29	7.87 ± 0.52
3290	3.42 ± 1.09	47.69 ± 0.54	8.72 ± 1.08
3306	9.13 ± 2.45	48.67 ± 0.53	9.32 ± 1.13
3320	2.38 ± 0.51	45.91 ± 0.33	8.78 ± 0.66
3322	1.23 ± 0.54	46.05 ± 0.52	7.11 ± 0.86
3324	9.53 ± 1.61	49.48 ± 0.33	8.94 ± 0.68
3336	4.05 ± 1.59	48.53 ± 0.68	9.04 ± 1.42
3347	2.55 ± 0.59	46.67 ± 0.36	8.93 ± 0.75
3352	2.93 ± 0.98	51.42 ± 0.54	10.83 ± 1.35
3358	1.43 ± 0.67	47.67 ± 0.60	7.58 ± 1.04
3364	10.78 ± 1.91	50.41 ± 0.35	9.03 ± 0.73
3369	2.08 ± 0.35	48.01 ± 0.25	7.91 ± 0.45
3403	7.37 ± 2.54	48.52 ± 0.66	8.67 ± 1.32
3408	3.11 ± 2.43	47.85 ± 1.29	7.84 ± 2.32
3415	2.69 ± 0.60	47.30 ± 0.35	8.83 ± 0.71
3436	1.92 ± 0.67	46.45 ± 0.50	8.08 ± 0.93

Table E.3 (continued)

BATSE Trigger #	z	μ	$\theta_j(^\circ)$
3448	5.69 ± 1.14	47.21 ± 0.37	9.23 ± 0.79
3458	1.23 ± 0.34	46.02 ± 0.33	8.02 ± 0.61
3472	1.35 ± 1.10	46.48 ± 1.02	7.04 ± 1.65
3485	3.21 ± 0.88	47.10 ± 0.46	8.56 ± 0.90
3486	4.92 ± 1.14	47.42 ± 0.42	7.96 ± 0.77
3489	4.43 ± 1.64	47.90 ± 0.66	8.34 ± 1.27
3511	1.28 ± 0.28	44.17 ± 0.27	8.21 ± 0.51
3515	2.75 ± 1.38	47.83 ± 0.80	8.42 ± 1.55
3528	2.24 ± 0.53	47.07 ± 0.36	7.28 ± 0.60
3552	8.17 ± 6.14	49.77 ± 1.45	9.47 ± 3.18
3567	6.30 ± 2.58	48.40 ± 0.77	7.50 ± 1.33
3611	2.66 ± 0.46	46.34 ± 0.27	8.09 ± 0.51
3618	7.44 ± 1.69	47.72 ± 0.43	9.79 ± 0.98
3634	1.65 ± 0.77	47.88 ± 0.63	7.89 ± 1.15
3648	3.50 ± 1.25	48.22 ± 0.60	8.11 ± 1.13
3649	2.03 ± 0.46	46.79 ± 0.33	8.08 ± 0.61
3655	1.40 ± 0.43	46.45 ± 0.39	8.76 ± 0.78
3663	1.83 ± 0.36	46.91 ± 0.27	7.74 ± 0.49
3664	3.19 ± 0.57	46.59 ± 0.30	8.30 ± 0.57
3740	8.77 ± 7.90	49.92 ± 1.76	8.84 ± 3.58
3745	3.63 ± 1.16	47.96 ± 0.54	7.85 ± 0.98
3765	4.27 ± 0.75	49.89 ± 0.31	8.80 ± 0.63
3766	1.66 ± 0.42	45.63 ± 0.34	7.94 ± 0.62
3768	1.30 ± 0.39	45.82 ± 0.37	7.22 ± 0.61
3771	3.38 ± 2.41	49.73 ± 1.19	8.46 ± 2.33
3773	4.36 ± 1.03	47.29 ± 0.42	7.89 ± 0.76
3776	8.16 ± 2.56	50.71 ± 0.61	10.83 ± 1.52
3788	10.69 ± 3.42	49.30 ± 0.64	9.99 ± 1.46
3805	5.08 ± 2.21	48.45 ± 0.79	8.26 ± 1.50
3819	1.22 ± 0.57	44.98 ± 0.55	7.99 ± 1.02
3843	3.13 ± 0.89	47.54 ± 0.47	7.51 ± 0.81
3860	2.11 ± 0.41	46.11 ± 0.28	7.32 ± 0.48
3879	12.38 ± 3.22	51.77 ± 0.52	10.03 ± 1.21
3893	2.94 ± 0.46	43.49 ± 0.25	8.05 ± 0.47
3899	3.56 ± 1.03	47.37 ± 0.49	7.72 ± 0.87

Table E.3 (continued)

BATSE Trigger #	z	μ	$\theta_j(^\circ)$
3900	2.73 ± 0.50	46.39 ± 0.29	8.58 ± 0.57
3901	3.61 ± 0.75	48.54 ± 0.35	8.37 ± 0.68
3905	3.03 ± 0.61	46.37 ± 0.33	7.25 ± 0.55
3906	1.42 ± 0.35	45.13 ± 0.31	8.60 ± 0.62
3914	7.56 ± 7.46	49.74 ± 1.89	8.69 ± 3.80
3916	2.55 ± 0.62	47.80 ± 0.38	8.13 ± 0.72
3917	3.41 ± 1.42	48.36 ± 0.70	8.23 ± 1.32
3918	11.05 ± 5.38	51.02 ± 0.97	10.39 ± 2.33
3938	10.44 ± 4.19	49.06 ± 0.79	9.22 ± 1.69
3954	1.39 ± 0.44	46.43 ± 0.40	7.46 ± 0.68
4146	2.12 ± 0.69	46.88 ± 0.48	7.61 ± 0.84
4157	2.00 ± 0.64	46.35 ± 0.46	7.37 ± 0.79
4251	6.41 ± 1.22	48.82 ± 0.36	9.17 ± 0.76
4368	2.68 ± 0.91	47.93 ± 0.54	8.71 ± 1.08
4388	17.79 ± 11.74	53.38 ± 1.36	12.94 ± 4.06
4653	1.25 ± 0.36	46.70 ± 0.35	8.24 ± 0.66
4701	1.28 ± 0.29	45.86 ± 0.28	7.77 ± 0.50
4939	11.61 ± 9.94	49.58 ± 1.71	9.28 ± 3.66
5080	4.69 ± 2.59	49.13 ± 0.99	8.77 ± 2.00
5304	3.22 ± 2.24	46.52 ± 1.16	7.09 ± 1.89
5305	5.71 ± 1.37	49.01 ± 0.44	9.03 ± 0.92
5387	2.23 ± 0.46	47.48 ± 0.31	8.79 ± 0.63
5407	2.24 ± 0.76	46.65 ± 0.51	7.66 ± 0.90
5409	4.53 ± 0.84	47.39 ± 0.33	8.48 ± 0.65
5412	3.74 ± 1.04	47.32 ± 0.48	8.66 ± 0.95
5415	8.98 ± 4.46	49.78 ± 0.97	9.23 ± 2.07
5416	1.96 ± 0.47	45.24 ± 0.34	8.45 ± 0.67
5419	2.08 ± 0.42	45.68 ± 0.30	8.43 ± 0.58
5421	2.10 ± 0.78	48.05 ± 0.54	7.69 ± 0.96
5429	1.72 ± 1.08	48.10 ± 0.86	8.50 ± 1.69
5434	7.73 ± 6.00	48.33 ± 1.49	8.28 ± 2.85
5450	5.22 ± 1.49	52.23 ± 0.52	10.58 ± 1.27
5451	3.84 ± 2.17	48.01 ± 0.97	7.31 ± 1.64
5454	6.76 ± 1.44	51.07 ± 0.40	9.67 ± 0.90
5463	5.41 ± 1.47	47.75 ± 0.50	9.22 ± 1.06

Table E.3 (continued)

BATSE Trigger #	z	μ	$\theta_j(^\circ)$
5466	5.36 ± 2.11	48.78 ± 0.72	8.52 ± 1.41
5472	2.78 ± 1.25	49.23 ± 0.72	8.41 ± 1.40
5473	1.50 ± 0.39	46.39 ± 0.34	7.85 ± 0.61
5476	4.74 ± 1.41	48.73 ± 0.53	9.23 ± 1.13
5478	2.01 ± 0.57	46.69 ± 0.41	7.70 ± 0.73
5479	1.74 ± 1.50	48.73 ± 1.19	8.65 ± 2.38
5482	2.69 ± 0.93	47.46 ± 0.55	7.56 ± 0.95
5486	1.54 ± 0.65	47.59 ± 0.55	8.16 ± 1.04
5489	13.92 ± 5.77	49.47 ± 0.84	9.08 ± 1.76
5490	1.19 ± 1.10	47.60 ± 1.09	8.72 ± 2.20
5492	5.17 ± 1.94	49.09 ± 0.68	8.45 ± 1.33
5493	12.59 ± 4.02	51.48 ± 0.64	11.16 ± 1.66
5497	3.98 ± 1.11	48.64 ± 0.49	8.08 ± 0.91
5503	4.89 ± 2.67	48.50 ± 0.99	8.33 ± 1.89
5510	14.84 ± 7.18	50.30 ± 0.98	10.31 ± 2.34
5512	5.77 ± 1.55	48.62 ± 0.50	8.05 ± 0.92
5515	2.02 ± 1.00	46.61 ± 0.72	8.71 ± 1.45
5516	1.37 ± 0.41	47.06 ± 0.37	8.37 ± 0.72
5518	1.65 ± 0.51	47.05 ± 0.42	8.53 ± 0.82
5526	10.22 ± 5.36	50.24 ± 1.04	8.73 ± 2.09
5531	1.97 ± 1.90	47.11 ± 1.39	8.12 ± 2.61
5538	1.26 ± 0.98	47.40 ± 0.94	7.71 ± 1.67
5540	2.06 ± 1.41	48.43 ± 1.00	8.17 ± 1.89
5542	5.64 ± 1.06	47.06 ± 0.35	9.00 ± 0.72
5551	9.31 ± 2.51	48.61 ± 0.53	8.53 ± 1.04
5554	1.20 ± 0.30	44.36 ± 0.30	7.56 ± 0.52
5555	4.31 ± 2.07	48.85 ± 0.85	9.27 ± 1.81
5566	1.46 ± 0.53	50.67 ± 0.46	10.16 ± 1.09
5569	1.54 ± 0.48	50.65 ± 0.41	9.65 ± 0.90
5574	1.91 ± 1.47	46.27 ± 1.10	6.82 ± 1.73
5585	1.30 ± 0.59	47.75 ± 0.56	8.34 ± 1.07
5589	5.17 ± 2.21	48.83 ± 0.78	8.01 ± 1.44
5591	6.68 ± 2.00	47.09 ± 0.57	8.35 ± 1.09
5604	2.87 ± 0.61	45.63 ± 0.34	7.43 ± 0.59
5617	2.42 ± 2.24	48.95 ± 1.42	8.67 ± 2.84

Table E.3 (continued)

BATSE Trigger #	z	μ	$\theta_j(^\circ)$
5622	3.25 ± 0.99	46.98 ± 0.51	8.20 ± 0.96
5637	9.70 ± 5.05	50.33 ± 1.02	9.23 ± 2.18
5645	2.02 ± 0.35	44.69 ± 0.25	7.86 ± 0.45
5648	2.23 ± 1.09	45.83 ± 0.74	9.70 ± 1.65
5654	5.32 ± 1.42	47.68 ± 0.49	8.36 ± 0.94
5693	1.25 ± 0.46	45.90 ± 0.44	6.90 ± 0.70
5704	1.27 ± 0.46	46.03 ± 0.44	7.65 ± 0.78
5706	1.85 ± 1.11	47.41 ± 0.85	7.98 ± 1.56
5713	6.90 ± 2.51	49.26 ± 0.69	9.72 ± 1.55
5715	2.42 ± 0.49	46.99 ± 0.31	7.11 ± 0.51
5716	3.80 ± 2.63	49.67 ± 1.19	8.30 ± 2.27
5721	2.47 ± 0.83	50.53 ± 0.52	10.66 ± 1.29
5723	7.82 ± 3.69	49.18 ± 0.91	9.88 ± 2.07
5726	5.54 ± 1.08	49.80 ± 0.36	8.65 ± 0.71
5729	8.94 ± 2.34	50.36 ± 0.51	10.15 ± 1.20
5730	3.83 ± 0.77	47.00 ± 0.34	7.27 ± 0.58
5731	4.23 ± 0.79	47.89 ± 0.33	7.98 ± 0.60
5736	4.44 ± 0.93	48.01 ± 0.37	8.22 ± 0.70
5773	1.49 ± 0.43	45.23 ± 0.37	8.69 ± 0.75
5995	4.48 ± 1.92	48.32 ± 0.76	8.18 ± 1.44
6004	3.26 ± 0.60	46.59 ± 0.31	7.68 ± 0.54
6083	1.88 ± 0.49	46.18 ± 0.37	7.79 ± 0.66
6090	6.69 ± 2.49	47.48 ± 0.70	9.06 ± 1.47
6101	8.52 ± 2.97	49.83 ± 0.68	8.95 ± 1.40
6103	3.13 ± 1.95	48.14 ± 1.03	8.96 ± 2.12
6104	1.81 ± 0.46	46.50 ± 0.36	8.51 ± 0.70
6109	11.57 ± 6.75	52.81 ± 1.17	11.61 ± 3.13
6111	9.37 ± 1.38	47.56 ± 0.29	8.25 ± 0.55
6115	6.30 ± 2.86	49.32 ± 0.85	9.02 ± 1.77
6118	2.99 ± 0.63	45.64 ± 0.34	8.33 ± 0.66
6125	4.83 ± 0.91	47.33 ± 0.34	7.60 ± 0.59
6128	10.54 ± 5.80	49.48 ± 1.09	9.73 ± 2.45
6147	2.17 ± 0.36	47.59 ± 0.24	7.59 ± 0.43
6154	7.13 ± 3.02	48.50 ± 0.81	8.94 ± 1.66
6168	1.37 ± 0.41	45.44 ± 0.38	7.69 ± 0.67

Table E.3 (continued)

BATSE Trigger #	z	μ	$\theta_j(^\circ)$
6190	1.61 ± 0.43	45.37 ± 0.36	7.14 ± 0.60
6194	1.82 ± 0.94	47.03 ± 0.73	7.26 ± 1.22
6226	3.12 ± 1.18	47.51 ± 0.62	7.84 ± 1.12
6242	3.90 ± 2.63	47.45 ± 1.17	8.21 ± 2.21
6244	1.22 ± 0.74	46.63 ± 0.72	6.95 ± 1.15
6249	11.43 ± 3.55	50.59 ± 0.62	9.20 ± 1.32
6266	2.69 ± 0.55	45.94 ± 0.32	8.46 ± 0.63
6271	4.91 ± 1.60	53.12 ± 0.59	11.38 ± 1.55
6272	4.58 ± 0.89	47.08 ± 0.35	8.61 ± 0.69
6273	1.19 ± 0.91	47.26 ± 0.91	8.12 ± 1.70
6274	5.38 ± 1.77	48.93 ± 0.60	8.34 ± 1.16
6279	1.85 ± 0.81	46.89 ± 0.62	8.10 ± 1.16
6280	1.81 ± 1.04	47.06 ± 0.80	7.45 ± 1.37
6285	12.17 ± 3.08	48.80 ± 0.51	9.77 ± 1.14
6295	2.84 ± 1.76	48.36 ± 0.99	7.78 ± 1.79
6303	1.71 ± 1.35	46.83 ± 1.08	7.27 ± 1.81
6315	2.02 ± 1.06	47.68 ± 0.76	8.83 ± 1.56
6317	2.67 ± 2.05	48.72 ± 1.21	8.63 ± 2.42
6319	3.82 ± 2.57	49.26 ± 1.16	8.79 ± 2.35
6320	1.61 ± 0.35	45.28 ± 0.29	7.93 ± 0.53
6323	2.54 ± 1.59	47.18 ± 0.98	7.59 ± 1.71
6328	1.95 ± 1.12	49.74 ± 0.82	9.03 ± 1.72
6329	13.66 ± 11.18	50.73 ± 1.66	9.47 ± 3.62
6330	1.70 ± 0.89	46.90 ± 0.72	6.60 ± 1.09
6335	1.49 ± 0.47	45.97 ± 0.41	7.71 ± 0.73
6337	9.55 ± 1.67	47.24 ± 0.34	8.75 ± 0.69
6344	7.70 ± 2.09	48.90 ± 0.52	9.54 ± 1.15
6349	8.19 ± 2.02	47.38 ± 0.48	10.15 ± 1.12
6351	4.26 ± 0.70	47.04 ± 0.29	8.14 ± 0.54
6353	5.46 ± 4.86	49.29 ± 1.64	8.51 ± 3.21
6355	2.80 ± 0.61	46.83 ± 0.35	8.30 ± 0.67
6369	4.40 ± 1.37	48.66 ± 0.55	8.23 ± 1.05
6380	3.30 ± 0.54	47.65 ± 0.27	8.01 ± 0.50
6388	3.28 ± 0.75	46.95 ± 0.38	8.81 ± 0.78
6396	2.41 ± 1.47	46.97 ± 0.94	7.25 ± 1.56

Table E.3 (continued)

BATSE Trigger #	z	μ	$\theta_j(^\circ)$
6397	2.09 ± 0.53	46.62 ± 0.37	7.94 ± 0.69
6405	1.82 ± 1.38	47.01 ± 1.06	7.54 ± 1.85
6408	2.47 ± 2.28	47.83 ± 1.43	8.42 ± 2.77
6440	4.47 ± 3.15	48.89 ± 1.25	8.19 ± 2.36
6448	3.59 ± 0.57	47.52 ± 0.27	7.88 ± 0.49
6450	1.58 ± 0.33	45.34 ± 0.27	7.80 ± 0.49
6451	2.24 ± 0.75	46.97 ± 0.50	7.79 ± 0.91
6453	16.23 ± 5.50	49.85 ± 0.69	9.42 ± 1.51
6454	1.88 ± 0.58	46.07 ± 0.43	9.39 ± 0.94
6472	1.45 ± 0.99	47.36 ± 0.88	7.77 ± 1.57
6489	4.49 ± 2.35	48.48 ± 0.93	8.30 ± 1.78
6490	1.35 ± 0.64	45.92 ± 0.59	6.90 ± 0.94
6498	1.74 ± 0.96	47.23 ± 0.76	7.78 ± 1.36
6504	1.44 ± 0.32	44.16 ± 0.29	8.43 ± 0.56
6521	5.37 ± 4.84	49.71 ± 1.65	8.65 ± 3.29
6523	2.74 ± 1.14	47.65 ± 0.66	8.43 ± 1.28
6525	2.82 ± 0.57	46.12 ± 0.32	8.52 ± 0.63
6531	1.55 ± 0.53	45.50 ± 0.45	6.90 ± 0.72
6533	3.43 ± 1.34	48.12 ± 0.65	8.57 ± 1.29
6538	1.53 ± 0.39	45.73 ± 0.33	7.39 ± 0.57
6544	2.61 ± 0.60	47.08 ± 0.36	7.34 ± 0.61
6551	5.37 ± 1.68	47.95 ± 0.57	9.35 ± 1.24
6554	2.64 ± 2.24	47.69 ± 1.34	8.19 ± 2.52
6560	11.40 ± 7.62	49.78 ± 1.33	9.22 ± 2.84
6564	3.08 ± 0.64	45.34 ± 0.34	7.93 ± 0.63
6566	2.91 ± 1.35	48.34 ± 0.75	8.23 ± 1.42
6576	4.31 ± 0.94	46.71 ± 0.38	7.96 ± 0.71
6577	1.43 ± 0.51	45.71 ± 0.46	8.46 ± 0.89
6578	4.75 ± 1.72	48.70 ± 0.65	9.43 ± 1.41
6582	4.43 ± 3.05	49.77 ± 1.22	9.29 ± 2.62
6583	5.06 ± 1.28	51.69 ± 0.46	10.21 ± 1.08
6587	4.26 ± 1.44	48.17 ± 0.59	8.36 ± 1.14
6589	2.74 ± 0.62	45.75 ± 0.36	7.75 ± 0.64
6590	2.07 ± 0.85	47.51 ± 0.60	7.54 ± 1.04
6593	5.32 ± 4.15	48.81 ± 1.43	8.51 ± 2.80

Table E.3 (continued)

BATSE Trigger #	z	μ	$\theta_j(^\circ)$
6598	1.96 ± 0.52	46.84 ± 0.38	8.90 ± 0.79
6601	2.89 ± 2.68	49.30 ± 1.49	8.65 ± 2.98
6605	2.52 ± 0.95	47.39 ± 0.58	7.84 ± 1.06
6610	1.38 ± 0.97	46.57 ± 0.89	7.12 ± 1.45
6615	2.47 ± 1.06	46.20 ± 0.66	7.78 ± 1.19
6619	1.41 ± 0.61	46.19 ± 0.55	8.19 ± 1.04
6620	8.21 ± 4.37	49.44 ± 1.03	8.86 ± 2.11
6621	3.56 ± 3.17	49.63 ± 1.51	8.57 ± 2.99
6622	3.19 ± 0.78	46.47 ± 0.41	7.84 ± 0.73
6625	1.91 ± 0.47	46.70 ± 0.35	7.59 ± 0.62
6629	15.36 ± 4.81	52.41 ± 0.64	11.89 ± 1.75
6642	5.94 ± 2.51	48.15 ± 0.79	9.57 ± 1.74
6648	9.65 ± 3.94	48.82 ± 0.80	9.54 ± 1.77
6649	6.43 ± 2.55	48.71 ± 0.75	8.83 ± 1.52
6657	2.17 ± 1.45	47.21 ± 0.99	7.30 ± 1.67
6672	10.69 ± 3.04	49.45 ± 0.57	9.00 ± 1.17
6673	1.43 ± 0.58	47.00 ± 0.52	7.88 ± 0.94
6674	2.73 ± 0.61	44.56 ± 0.35	9.19 ± 0.75
6694	4.15 ± 3.39	48.43 ± 1.43	7.60 ± 2.51
6695	2.29 ± 1.01	46.93 ± 0.67	7.45 ± 1.14
6707	2.41 ± 1.92	47.15 ± 1.22	6.94 ± 1.95
6745	5.96 ± 0.95	46.21 ± 0.30	7.98 ± 0.55
6763	1.59 ± 0.61	46.94 ± 0.51	7.82 ± 0.92
6764	1.27 ± 0.62	47.03 ± 0.60	7.58 ± 1.05
6767	3.84 ± 2.11	48.08 ± 0.95	8.05 ± 1.76
6796	5.37 ± 1.99	48.85 ± 0.68	8.93 ± 1.40
6816	4.59 ± 1.55	47.76 ± 0.60	8.70 ± 1.21
6877	1.55 ± 0.56	46.73 ± 0.47	8.05 ± 0.88
6882	3.31 ± 0.68	46.40 ± 0.34	7.89 ± 0.63
6884	6.06 ± 1.88	47.79 ± 0.58	8.51 ± 1.14
6891	3.44 ± 0.65	46.91 ± 0.32	8.44 ± 0.62
6892	8.16 ± 3.02	49.41 ± 0.72	9.89 ± 1.64
6903	3.26 ± 1.14	47.60 ± 0.58	8.36 ± 1.12
6935	2.57 ± 1.69	47.75 ± 1.03	8.34 ± 1.98
6938	6.71 ± 1.45	48.12 ± 0.41	8.35 ± 0.79

Table E.3 (continued)

BATSE Trigger #	z	μ	$\theta_j(^\circ)$
6989	6.90 ± 2.87	50.76 ± 0.79	10.94 ± 2.00
7000	2.48 ± 0.68	45.47 ± 0.42	9.74 ± 0.95
7087	1.81 ± 1.48	48.30 ± 1.14	8.09 ± 2.13
7113	4.89 ± 1.02	46.73 ± 0.37	8.90 ± 0.77
7164	1.93 ± 0.87	47.34 ± 0.65	8.17 ± 1.22
7178	5.08 ± 2.77	49.08 ± 0.99	9.10 ± 2.07
7183	2.25 ± 0.70	47.37 ± 0.47	7.82 ± 0.84
7185	5.88 ± 1.68	48.18 ± 0.53	9.25 ± 1.13
7207	4.24 ± 1.13	48.13 ± 0.47	8.49 ± 0.92
7209	1.53 ± 0.44	47.91 ± 0.37	7.89 ± 0.68
7213	1.31 ± 0.32	46.20 ± 0.30	7.91 ± 0.54
7219	1.80 ± 1.07	45.94 ± 0.83	6.66 ± 1.28
7228	1.40 ± 0.92	46.96 ± 0.83	7.99 ± 1.54
7230	2.24 ± 0.54	46.33 ± 0.36	8.81 ± 0.73
7250	3.46 ± 0.78	46.31 ± 0.38	8.32 ± 0.72
7285	2.48 ± 0.84	46.53 ± 0.53	8.35 ± 1.01
7293	7.67 ± 3.09	49.01 ± 0.77	8.17 ± 1.46
7310	4.15 ± 0.95	47.54 ± 0.40	8.16 ± 0.76
7319	7.43 ± 2.17	48.18 ± 0.56	8.71 ± 1.12
7322	6.51 ± 2.03	47.50 ± 0.59	9.27 ± 1.26
7328	1.37 ± 0.51	46.18 ± 0.47	7.91 ± 0.86
7335	5.39 ± 1.32	48.26 ± 0.45	9.15 ± 0.94
7343	5.70 ± 2.53	48.69 ± 0.82	8.48 ± 1.61
7357	3.18 ± 0.63	46.20 ± 0.33	8.67 ± 0.65
7360	1.51 ± 0.47	50.21 ± 0.41	9.64 ± 0.91
7369	2.16 ± 0.49	45.02 ± 0.34	8.92 ± 0.70
7379	1.92 ± 1.81	46.92 ± 1.34	7.18 ± 2.22
7387	1.92 ± 0.48	46.32 ± 0.36	7.55 ± 0.62
7390	2.28 ± 1.18	48.09 ± 0.78	7.70 ± 1.39
7403	1.88 ± 0.37	46.28 ± 0.28	7.70 ± 0.50
7404	9.82 ± 1.87	48.13 ± 0.37	8.85 ± 0.76
7429	3.84 ± 1.28	48.68 ± 0.57	8.20 ± 1.08
7433	3.62 ± 1.25	47.79 ± 0.59	7.57 ± 1.02
7451	1.90 ± 0.62	47.62 ± 0.46	8.17 ± 0.87
7457	2.03 ± 1.05	47.93 ± 0.75	7.62 ± 1.33

Table E.3 (continued)

BATSE Trigger #	z	μ	$\theta_j(^\circ)$
7464	2.16 ± 1.27	47.56 ± 0.87	8.44 ± 1.70
7475	2.57 ± 1.88	47.20 ± 1.14	7.26 ± 1.91
7477	1.21 ± 0.95	47.20 ± 0.94	7.42 ± 1.60
7493	10.25 ± 3.59	51.19 ± 0.69	10.78 ± 1.73
7497	2.26 ± 2.01	49.27 ± 1.34	9.17 ± 2.83
7502	1.45 ± 1.24	45.97 ± 1.10	7.03 ± 1.79
7503	6.39 ± 4.15	49.18 ± 1.22	8.31 ± 2.34
7515	1.82 ± 0.58	47.27 ± 0.45	8.22 ± 0.85
7520	4.44 ± 1.76	48.33 ± 0.70	8.20 ± 1.33
7528	16.32 ± 5.47	51.65 ± 0.69	11.79 ± 1.87
7552	4.40 ± 1.95	48.92 ± 0.78	8.58 ± 1.55
7560	3.22 ± 0.72	46.58 ± 0.37	9.11 ± 0.78
7566	2.73 ± 2.55	48.83 ± 1.48	9.62 ± 3.29
7575	1.92 ± 0.49	46.12 ± 0.37	8.24 ± 0.70
7580	3.24 ± 1.56	47.75 ± 0.80	8.30 ± 1.53
7598	6.54 ± 2.90	48.95 ± 0.84	8.59 ± 1.65
7604	2.17 ± 0.37	46.72 ± 0.26	7.80 ± 0.46
7605	4.89 ± 3.28	49.36 ± 1.21	8.79 ± 2.45
7607	9.95 ± 5.24	49.99 ± 1.04	8.67 ± 2.08
7608	2.05 ± 0.60	46.71 ± 0.43	7.52 ± 0.74
7609	4.05 ± 0.81	47.22 ± 0.35	8.43 ± 0.68
7614	2.54 ± 1.05	46.79 ± 0.64	7.65 ± 1.13
7615	4.18 ± 0.97	47.16 ± 0.41	8.73 ± 0.82
7617	13.49 ± 3.33	48.81 ± 0.50	8.46 ± 0.97
7619	14.07 ± 5.08	50.30 ± 0.73	10.68 ± 1.80
7625	1.34 ± 0.37	47.69 ± 0.35	7.42 ± 0.59
7630	1.94 ± 0.46	48.00 ± 0.34	8.09 ± 0.63
7635	10.60 ± 1.40	48.43 ± 0.26	8.11 ± 0.49
7642	1.76 ± 1.18	47.57 ± 0.93	7.97 ± 1.71
7645	3.08 ± 0.65	46.87 ± 0.34	8.22 ± 0.65
7648	4.36 ± 0.76	46.50 ± 0.31	8.41 ± 0.60
7654	2.29 ± 0.44	45.90 ± 0.29	7.48 ± 0.50
7660	6.82 ± 1.33	47.87 ± 0.37	8.81 ± 0.75
7677	2.38 ± 0.77	46.71 ± 0.49	9.51 ± 1.09
7678	1.20 ± 0.70	47.43 ± 0.69	8.05 ± 1.28

Table E.3 (continued)

BATSE Trigger #	z	μ	$\theta_j(^\circ)$
7683	2.00 ± 1.16	47.66 ± 0.84	7.31 ± 1.41
7684	1.40 ± 0.42	50.29 ± 0.38	9.41 ± 0.82
7688	1.36 ± 0.43	45.59 ± 0.40	8.93 ± 0.82
7703	6.20 ± 1.37	47.69 ± 0.41	8.80 ± 0.84
7707	4.31 ± 0.80	48.36 ± 0.33	8.73 ± 0.66
7727	12.65 ± 3.75	52.57 ± 0.60	11.21 ± 1.54
7729	4.03 ± 1.87	47.85 ± 0.81	7.77 ± 1.45
7741	2.82 ± 0.46	45.80 ± 0.26	7.34 ± 0.44
7750	6.12 ± 1.82	48.24 ± 0.55	9.42 ± 1.20
7785	1.45 ± 0.32	45.85 ± 0.28	8.07 ± 0.52
7786	6.66 ± 2.49	49.11 ± 0.71	9.23 ± 1.51
7788	2.43 ± 0.73	47.26 ± 0.46	7.55 ± 0.80
7790	1.86 ± 0.59	45.43 ± 0.45	6.94 ± 0.72
7794	3.41 ± 0.69	46.66 ± 0.34	8.41 ± 0.66
7795	1.79 ± 0.66	46.19 ± 0.51	7.25 ± 0.86
7818	2.01 ± 0.51	46.19 ± 0.37	7.90 ± 0.67
7831	4.02 ± 1.24	47.72 ± 0.53	8.32 ± 1.03
7835	1.48 ± 1.11	47.34 ± 0.97	7.50 ± 1.67
7838	5.32 ± 1.00	47.94 ± 0.34	8.49 ± 0.67
7840	6.60 ± 1.03	47.94 ± 0.29	7.86 ± 0.53
7854	1.64 ± 0.40	45.84 ± 0.33	7.57 ± 0.57
7858	7.77 ± 1.32	47.81 ± 0.33	8.57 ± 0.65
7868	2.53 ± 1.63	47.37 ± 1.00	8.83 ± 2.05
7884	5.32 ± 1.33	47.46 ± 0.46	9.50 ± 1.00
7900	6.18 ± 1.20	47.55 ± 0.36	8.86 ± 0.75
7902	6.66 ± 1.97	48.86 ± 0.56	9.48 ± 1.22
7923	4.29 ± 0.94	49.17 ± 0.39	8.72 ± 0.78
7929	4.77 ± 0.93	47.61 ± 0.35	8.07 ± 0.65

Table E.4: Derived z, μ, and θ_j used in the BATSE gold sample

BATSE Trigger #	z	μ	$\theta_j(^\circ)$
1009	5.08 ± 3.61	48.37 ± 1.29	9.18 ± 2.73
1039	2.68 ± 0.73	46.83 ± 0.43	7.51 ± 0.75
1046	8.50 ± 6.17	48.71 ± 1.41	9.16 ± 2.98
1085	11.11 ± 3.69	48.43 ± 0.66	9.27 ± 1.42
1122	1.63 ± 0.54	44.78 ± 0.45	7.87 ± 0.81
1157	1.34 ± 0.63	45.04 ± 0.58	7.86 ± 1.05
1200	1.80 ± 0.73	46.21 ± 0.57	7.22 ± 0.94
1218	1.97 ± 0.96	47.42 ± 0.70	7.53 ± 1.22
1235	6.25 ± 2.11	47.47 ± 0.63	8.78 ± 1.28
1288	6.52 ± 2.93	47.41 ± 0.85	9.50 ± 1.86
1385	1.94 ± 1.19	46.67 ± 0.88	8.98 ± 1.82
1406	8.35 ± 5.41	48.81 ± 1.26	8.60 ± 2.49
1419	4.28 ± 1.55	46.35 ± 0.64	8.69 ± 1.28
1447	1.89 ± 1.02	47.06 ± 0.77	8.33 ± 1.48
1458	5.62 ± 3.66	48.82 ± 1.20	8.42 ± 2.34
1467	2.26 ± 1.11	46.04 ± 0.74	7.87 ± 1.34
1472	2.48 ± 1.25	46.76 ± 0.78	7.96 ± 1.44
1524	4.36 ± 4.24	48.30 ± 1.72	8.36 ± 3.31
1533	2.97 ± 0.89	46.77 ± 0.49	7.99 ± 0.89
1540	6.55 ± 2.52	49.23 ± 0.72	8.63 ± 1.44
1541	1.75 ± 0.64	44.37 ± 0.50	8.41 ± 0.97
1559	4.36 ± 2.59	48.74 ± 1.05	8.85 ± 2.14
1561	8.47 ± 6.91	49.57 ± 1.58	8.92 ± 3.26
1574	11.82 ± 6.39	50.45 ± 1.08	9.47 ± 2.36
1578	1.66 ± 0.55	46.08 ± 0.45	7.84 ± 0.81
1586	5.45 ± 1.71	48.18 ± 0.58	8.14 ± 1.08
1606	7.75 ± 2.71	47.40 ± 0.67	9.37 ± 1.45
1614	2.62 ± 2.37	47.89 ± 1.42	7.97 ± 2.61
1624	6.83 ± 6.78	48.90 ± 1.88	8.81 ± 3.82
1628	6.36 ± 3.57	47.81 ± 1.05	8.45 ± 2.05

Table E.4 (continued)

BATSE Trigger #	z	μ	$\theta_j(^\circ)$
1650	6.15 ± 1.96	46.95 ± 0.59	8.66 ± 1.19
1652	4.84 ± 3.03	49.00 ± 1.13	7.85 ± 2.04
1655	1.98 ± 0.85	45.62 ± 0.62	9.24 ± 1.33
1663	4.58 ± 1.49	46.60 ± 0.58	8.85 ± 1.19
1676	1.66 ± 0.50	45.04 ± 0.41	7.75 ± 0.74
1698	14.70 ± 6.05	49.43 ± 0.84	10.15 ± 1.96
1712	1.37 ± 1.22	47.27 ± 1.12	8.44 ± 2.18
1731	2.34 ± 1.79	46.78 ± 1.16	7.35 ± 1.97
1734	2.36 ± 2.19	46.50 ± 1.41	7.25 ± 2.37
1742	2.50 ± 2.00	48.21 ± 1.24	7.92 ± 2.27
1830	1.33 ± 0.62	45.58 ± 0.58	7.58 ± 1.01
1956	2.31 ± 0.74	46.90 ± 0.49	7.94 ± 0.89
1967	12.43 ± 2.99	48.67 ± 0.48	8.06 ± 0.90
1974	11.95 ± 7.13	48.09 ± 1.20	9.46 ± 2.61
1997	9.23 ± 8.24	49.55 ± 1.75	10.17 ± 4.10
2019	1.59 ± 1.20	46.64 ± 1.01	7.37 ± 1.71
2047	2.61 ± 0.85	45.02 ± 0.51	8.54 ± 1.01
2067	3.97 ± 2.55	49.49 ± 1.12	8.93 ± 2.30
2070	12.62 ± 6.53	49.70 ± 1.04	9.56 ± 2.30
2074	5.53 ± 2.74	47.61 ± 0.91	9.25 ± 1.95
2077	9.41 ± 3.32	47.87 ± 0.69	9.80 ± 1.57
2080	3.26 ± 1.30	46.79 ± 0.66	8.72 ± 1.34
2083	3.17 ± 1.98	47.90 ± 1.03	8.51 ± 2.03
2090	6.85 ± 6.20	50.12 ± 1.72	9.87 ± 3.91
2106	4.57 ± 1.45	48.18 ± 0.57	8.14 ± 1.06
2110	3.05 ± 1.27	45.97 ± 0.68	7.69 ± 1.21
2111	3.03 ± 1.01	45.03 ± 0.54	8.18 ± 1.02
2123	11.64 ± 4.93	47.78 ± 0.85	10.48 ± 2.05
2138	4.36 ± 3.59	48.17 ± 1.46	8.19 ± 2.75
2156	4.51 ± 1.94	48.03 ± 0.77	7.84 ± 1.39
2160	2.25 ± 1.25	48.53 ± 0.83	7.80 ± 1.50
2188	9.46 ± 5.21	49.27 ± 1.08	9.83 ± 2.45
2189	3.44 ± 2.03	48.53 ± 0.99	9.11 ± 2.09
2193	3.30 ± 1.69	47.20 ± 0.85	9.02 ± 1.78
2211	7.16 ± 2.63	47.41 ± 0.70	9.12 ± 1.47

Table E.4 (continued)

BATSE Trigger #	z	μ	$\theta_j(^\circ)$
2213	1.37 ± 0.58	45.56 ± 0.53	7.74 ± 0.95
2228	9.08 ± 6.47	48.53 ± 1.39	9.41 ± 3.03
2232	8.43 ± 6.65	49.08 ± 1.53	8.93 ± 3.16
2287	3.03 ± 1.11	47.59 ± 0.60	8.22 ± 1.13
2304	3.88 ± 1.53	45.94 ± 0.68	8.44 ± 1.32
2315	4.78 ± 2.55	48.55 ± 0.96	8.43 ± 1.86
2316	8.92 ± 5.46	48.86 ± 1.20	9.30 ± 2.56
2324	1.97 ± 0.73	46.88 ± 0.54	7.45 ± 0.92
2328	1.20 ± 0.59	45.17 ± 0.58	7.87 ± 1.06
2340	2.92 ± 1.01	46.07 ± 0.56	8.16 ± 1.05
2371	8.48 ± 7.99	49.75 ± 1.83	9.50 ± 4.01
2387	4.03 ± 3.44	48.02 ± 1.48	9.25 ± 3.17
2394	9.46 ± 3.71	48.87 ± 0.77	9.28 ± 1.65
2428	6.63 ± 2.77	48.21 ± 0.79	8.54 ± 1.55
2429	4.62 ± 1.73	48.29 ± 0.67	8.14 ± 1.26
2435	2.72 ± 2.20	47.52 ± 1.28	8.68 ± 2.57
2440	3.63 ± 1.35	46.68 ± 0.64	8.73 ± 1.28
2443	6.83 ± 2.85	49.26 ± 0.79	8.76 ± 1.60
2450	3.35 ± 1.42	46.76 ± 0.71	7.43 ± 1.21
2451	6.42 ± 1.79	47.14 ± 0.52	8.02 ± 0.97
2452	5.32 ± 2.86	48.11 ± 0.98	8.39 ± 1.90
2476	11.62 ± 4.66	49.74 ± 0.80	9.70 ± 1.80
2482	5.77 ± 2.43	48.57 ± 0.78	8.59 ± 1.54
2500	5.98 ± 2.46	48.47 ± 0.77	9.41 ± 1.66
2519	13.15 ± 5.19	48.32 ± 0.80	9.21 ± 1.69
2522	5.78 ± 3.17	47.41 ± 1.02	9.99 ± 2.34
2530	6.00 ± 5.94	48.82 ± 1.84	9.06 ± 3.85
2533	1.82 ± 0.57	46.49 ± 0.44	7.31 ± 0.74
2541	3.73 ± 0.95	45.67 ± 0.44	7.50 ± 0.76
2600	3.28 ± 2.14	47.08 ± 1.09	8.84 ± 2.22
2603	4.04 ± 3.96	47.34 ± 1.70	7.45 ± 2.93
2606	8.23 ± 8.04	49.78 ± 1.89	8.84 ± 3.86
2608	6.15 ± 2.69	47.54 ± 0.82	8.24 ± 1.56
2695	1.49 ± 1.34	46.03 ± 1.17	7.32 ± 1.98
2696	1.61 ± 0.81	45.34 ± 0.67	7.98 ± 1.23

Table E.4 (continued)

BATSE Trigger #	z	μ	$\theta_j(^\circ)$
2697	2.70 ± 1.59	47.85 ± 0.93	8.92 ± 1.92
2700	1.28 ± 1.09	46.76 ± 1.04	7.64 ± 1.83
2709	1.69 ± 1.12	47.21 ± 0.91	8.33 ± 1.75
2732	1.56 ± 0.67	44.43 ± 0.57	8.78 ± 1.16
2780	3.25 ± 1.72	46.48 ± 0.88	8.74 ± 1.77
2798	1.85 ± 0.83	45.94 ± 0.63	8.39 ± 1.23
2812	2.94 ± 1.31	46.32 ± 0.72	8.77 ± 1.46
2852	5.37 ± 2.63	47.02 ± 0.90	9.66 ± 2.00
2855	4.85 ± 4.84	48.39 ± 1.80	9.28 ± 3.85
2856	3.10 ± 1.50	46.69 ± 0.79	8.23 ± 1.50
2863	3.12 ± 1.90	47.34 ± 1.00	8.97 ± 2.07
2877	6.21 ± 2.51	45.61 ± 0.76	7.52 ± 1.31
2889	2.88 ± 2.55	49.00 ± 1.43	8.06 ± 2.65
2897	3.37 ± 1.30	46.44 ± 0.65	8.12 ± 1.21
2917	1.89 ± 1.58	46.21 ± 1.19	9.19 ± 2.52
2922	1.81 ± 1.73	47.90 ± 1.34	7.92 ± 2.44
2929	1.73 ± 0.80	46.58 ± 0.64	7.28 ± 1.08
2931	3.19 ± 1.19	46.34 ± 0.62	8.03 ± 1.15
2950	1.58 ± 1.39	46.08 ± 1.17	9.14 ± 2.48
2958	1.46 ± 1.28	45.65 ± 1.13	6.83 ± 1.77
2984	6.46 ± 4.49	48.90 ± 1.31	8.57 ± 2.58
2998	1.47 ± 1.00	46.69 ± 0.88	7.47 ± 1.51
3017	10.34 ± 4.51	48.24 ± 0.86	10.06 ± 2.01
3032	8.11 ± 3.80	47.75 ± 0.91	10.00 ± 2.09
3035	2.21 ± 0.65	45.81 ± 0.44	7.07 ± 0.72
3042	1.67 ± 0.77	44.51 ± 0.63	9.00 ± 1.31
3055	15.31 ± 11.58	50.55 ± 1.54	10.29 ± 3.66
3057	6.92 ± 4.03	48.08 ± 1.11	8.86 ± 2.26
3071	3.55 ± 2.36	47.41 ± 1.13	8.18 ± 2.13
3075	1.70 ± 1.08	46.21 ± 0.87	7.85 ± 1.57
3093	5.01 ± 3.44	45.99 ± 1.24	7.37 ± 2.11
3099	1.56 ± 1.22	45.72 ± 1.04	7.21 ± 1.73
3100	1.97 ± 0.90	47.16 ± 0.66	8.39 ± 1.28
3101	4.85 ± 1.45	48.09 ± 0.54	8.24 ± 1.02
3105	1.62 ± 0.79	46.26 ± 0.66	8.22 ± 1.25

Table E.4 (continued)

BATSE Trigger #	z	μ	$\theta_j(^\circ)$
3109	1.78 ± 1.58	46.54 ± 1.23	7.29 ± 2.07
3115	2.00 ± 1.16	45.66 ± 0.84	7.23 ± 1.40
3120	1.75 ± 0.72	45.27 ± 0.57	8.64 ± 1.14
3125	4.48 ± 1.50	46.17 ± 0.59	7.46 ± 1.02
3128	3.75 ± 3.11	47.63 ± 1.42	8.80 ± 2.89
3131	2.01 ± 1.28	46.39 ± 0.93	8.51 ± 1.82
3143	7.39 ± 5.09	47.85 ± 1.32	9.01 ± 2.74
3163	4.60 ± 1.86	46.30 ± 0.72	9.61 ± 1.60
3212	2.02 ± 1.35	46.22 ± 0.97	7.82 ± 1.75
3227	3.88 ± 2.90	48.11 ± 1.29	8.04 ± 2.39
3237	4.31 ± 2.02	46.41 ± 0.83	9.31 ± 1.78
3238	9.18 ± 7.58	49.58 ± 1.62	9.55 ± 3.56
3241	1.29 ± 0.58	46.82 ± 0.55	7.39 ± 0.94
3245	5.37 ± 1.75	46.30 ± 0.60	9.31 ± 1.28
3247	3.91 ± 1.38	47.70 ± 0.61	8.21 ± 1.16
3251	3.01 ± 1.07	46.79 ± 0.58	8.39 ± 1.12
3253	4.43 ± 2.51	47.43 ± 1.00	7.73 ± 1.79
3256	1.71 ± 0.49	44.38 ± 0.39	7.60 ± 0.68
3257	6.46 ± 2.69	47.27 ± 0.78	8.67 ± 1.57
3279	4.52 ± 1.61	48.11 ± 0.63	8.22 ± 1.20
3290	1.83 ± 1.60	48.48 ± 1.23	7.82 ± 2.21
3306	1.21 ± 0.67	44.92 ± 0.66	7.80 ± 1.19
3320	11.90 ± 4.37	48.65 ± 0.74	9.74 ± 1.65
3322	3.19 ± 1.72	48.07 ± 0.89	8.13 ± 1.68
3345	4.21 ± 1.55	45.98 ± 0.65	9.10 ± 1.36
3352	2.66 ± 0.86	45.54 ± 0.51	7.95 ± 0.94
3358	4.50 ± 2.56	47.95 ± 1.01	8.95 ± 2.09
3369	12.61 ± 7.39	49.04 ± 1.18	9.66 ± 2.63
3408	3.07 ± 1.15	46.28 ± 0.61	8.98 ± 1.27
3415	1.84 ± 1.28	46.26 ± 0.98	7.32 ± 1.65
3436	1.80 ± 1.32	46.59 ± 1.02	8.32 ± 1.96
3448	2.76 ± 1.21	46.88 ± 0.70	8.99 ± 1.45
3458	7.16 ± 4.35	47.97 ± 1.16	8.65 ± 2.31
3472	2.38 ± 2.14	46.61 ± 1.37	8.23 ± 2.61
3488	5.93 ± 2.11	47.18 ± 0.66	9.27 ± 1.41

Table E.4 (continued)

BATSE Trigger #	z	μ	$\theta_j(^\circ)$
3489	1.93 ± 1.27	46.41 ± 0.94	8.30 ± 1.79
3567	1.35 ± 0.88	46.88 ± 0.81	8.09 ± 1.51
3634	3.10 ± 1.88	46.78 ± 1.00	8.53 ± 1.96
3648	7.45 ± 3.99	47.88 ± 1.02	8.32 ± 1.97
3649	1.22 ± 0.94	46.56 ± 0.92	7.18 ± 1.53
3654	6.08 ± 3.76	48.04 ± 1.15	8.62 ± 2.29
3663	1.84 ± 0.65	44.46 ± 0.50	8.43 ± 0.97
3664	2.87 ± 1.72	47.41 ± 0.97	7.44 ± 1.66
3711	3.62 ± 1.04	46.66 ± 0.49	8.32 ± 0.94
3745	6.26 ± 2.67	47.37 ± 0.80	9.62 ± 1.77
3765	1.85 ± 1.31	47.86 ± 1.00	7.96 ± 1.83
3768	1.89 ± 0.86	46.61 ± 0.64	8.03 ± 1.19
3776	1.35 ± 1.25	46.48 ± 1.16	8.74 ± 2.33
3788	3.32 ± 1.01	46.58 ± 0.51	8.33 ± 0.98
3805	3.70 ± 1.91	47.90 ± 0.88	7.86 ± 1.60
3843	1.42 ± 0.67	45.48 ± 0.60	7.27 ± 1.01
3860	1.22 ± 0.55	45.32 ± 0.54	7.62 ± 0.94
3893	5.08 ± 2.42	47.21 ± 0.86	8.01 ± 1.60
3900	19.46 ± 13.63	50.29 ± 1.45	10.70 ± 3.58
3906	5.60 ± 3.60	48.27 ± 1.18	8.34 ± 2.28
3912	1.67 ± 1.19	44.74 ± 0.97	8.17 ± 1.82
3916	3.19 ± 1.82	47.49 ± 0.95	7.52 ± 1.64
3918	2.31 ± 0.59	46.12 ± 0.39	7.37 ± 0.66
3938	4.40 ± 2.99	47.49 ± 1.20	7.88 ± 2.19
3954	3.14 ± 1.91	46.20 ± 1.00	7.28 ± 1.68
4146	2.80 ± 1.02	47.90 ± 0.58	8.20 ± 1.10
4157	13.90 ± 11.24	49.32 ± 1.64	9.53 ± 3.60
4653	2.03 ± 1.14	46.95 ± 0.82	7.68 ± 1.45
5080	2.99 ± 1.62	47.31 ± 0.88	7.84 ± 1.60
5387	2.30 ± 1.39	46.09 ± 0.92	7.46 ± 1.57
5412	1.38 ± 1.16	46.14 ± 1.06	7.17 ± 1.75
5415	1.41 ± 0.73	46.85 ± 0.66	8.31 ± 1.26
5416	1.23 ± 0.42	45.79 ± 0.41	7.75 ± 0.73
5419	2.54 ± 1.51	46.41 ± 0.93	7.74 ± 1.66
5428	4.88 ± 1.58	47.42 ± 0.58	8.55 ± 1.15

Table E.4 (continued)

BATSE Trigger #	z	μ	$\theta_j(^\circ)$
5450	4.24 ± 2.15	47.08 ± 0.89	8.77 ± 1.80
5451	1.97 ± 0.87	44.82 ± 0.64	8.46 ± 1.24
5476	2.61 ± 1.05	45.84 ± 0.63	8.59 ± 1.25
5478	7.96 ± 4.76	48.32 ± 1.16	9.60 ± 2.56
5479	4.89 ± 3.67	48.57 ± 1.35	8.44 ± 2.63
5486	3.11 ± 2.84	49.33 ± 1.50	8.50 ± 2.95
5489	2.07 ± 0.94	46.38 ± 0.66	7.72 ± 1.18
5512	3.01 ± 2.67	47.26 ± 1.45	7.64 ± 2.55
5515	3.67 ± 1.44	48.50 ± 0.67	8.02 ± 1.24
5516	5.30 ± 5.14	48.12 ± 1.77	8.40 ± 3.43
5531	17.03 ± 16.10	50.25 ± 1.94	10.47 ± 4.69
5540	1.79 ± 1.13	47.42 ± 0.88	8.53 ± 1.72
5569	12.13 ± 7.41	48.88 ± 1.23	8.78 ± 2.48
5574	1.45 ± 0.46	44.60 ± 0.41	6.72 ± 0.63
5585	3.38 ± 1.43	45.50 ± 0.71	7.54 ± 1.23
5604	3.14 ± 1.75	46.58 ± 0.92	8.17 ± 1.73
5654	11.90 ± 8.28	50.56 ± 1.39	9.45 ± 3.04
5693	8.18 ± 3.04	48.12 ± 0.72	9.00 ± 1.49
5697	5.15 ± 2.67	47.20 ± 0.94	8.34 ± 1.81
5729	2.44 ± 1.60	46.35 ± 1.01	7.26 ± 1.70
5731	2.12 ± 1.18	46.46 ± 0.82	7.96 ± 1.50
5736	8.68 ± 6.35	48.61 ± 1.43	7.91 ± 2.60
5773	4.92 ± 1.34	48.01 ± 0.49	8.10 ± 0.92
6004	4.58 ± 1.59	47.95 ± 0.62	8.25 ± 1.17
6083	2.39 ± 1.17	45.29 ± 0.75	9.02 ± 1.56
6090	6.44 ± 4.67	48.61 ± 1.36	8.49 ± 2.67
6128	2.83 ± 1.57	46.72 ± 0.89	8.06 ± 1.66
6147	6.46 ± 4.69	46.84 ± 1.37	9.03 ± 2.85
6154	8.77 ± 7.75	49.75 ± 1.72	8.98 ± 3.57
6168	1.64 ± 1.07	46.39 ± 0.88	8.44 ± 1.72
6190	12.32 ± 4.13	47.69 ± 0.67	8.51 ± 1.32
6226	3.44 ± 1.28	45.52 ± 0.63	8.44 ± 1.22
6242	11.44 ± 6.26	48.72 ± 1.09	8.33 ± 2.10
6244	11.92 ± 10.72	49.24 ± 1.80	9.87 ± 4.10
6266	6.37 ± 4.83	47.91 ± 1.42	8.83 ± 2.90

Table E.4 (continued)

BATSE Trigger #	z	μ	$\theta_j(^\circ)$
6272	6.10 ± 5.27	48.21 ± 1.61	8.79 ± 3.27
6274	1.74 ± 0.76	45.24 ± 0.60	7.18 ± 1.00
6279	6.02 ± 3.90	48.47 ± 1.21	8.37 ± 2.33
6280	1.30 ± 0.72	45.42 ± 0.68	7.64 ± 1.20
6295	4.08 ± 1.54	46.27 ± 0.66	8.79 ± 1.33
6303	4.04 ± 3.57	47.60 ± 1.54	8.68 ± 3.08
6315	2.08 ± 1.81	46.86 ± 1.27	7.54 ± 2.21
6319	14.52 ± 6.88	48.93 ± 0.96	9.97 ± 2.21
6321	4.29 ± 2.90	48.80 ± 1.19	8.09 ± 2.22
6329	13.33 ± 8.77	49.91 ± 1.33	9.76 ± 2.99
6349	1.78 ± 0.90	45.87 ± 0.70	7.82 ± 1.27
6351	8.53 ± 2.79	46.73 ± 0.64	8.64 ± 1.27
6353	16.22 ± 6.97	48.80 ± 0.88	10.96 ± 2.23
6355	4.35 ± 1.17	47.02 ± 0.47	8.16 ± 0.89
6397	1.25 ± 0.74	46.11 ± 0.72	7.82 ± 1.29
6451	1.48 ± 1.09	46.16 ± 0.96	7.73 ± 1.71
6453	6.49 ± 6.21	49.51 ± 1.80	8.51 ± 3.53
6472	1.79 ± 0.62	45.42 ± 0.48	7.87 ± 0.87
6489	2.19 ± 1.33	46.83 ± 0.90	7.77 ± 1.62
6528	3.49 ± 2.14	46.53 ± 1.04	9.91 ± 2.37
6533	4.75 ± 1.74	46.43 ± 0.66	9.36 ± 1.41
6551	3.56 ± 2.44	47.78 ± 1.16	8.63 ± 2.31
6560	2.73 ± 1.14	45.93 ± 0.66	8.49 ± 1.30
6564	2.44 ± 0.89	46.17 ± 0.56	7.67 ± 1.00
6566	2.51 ± 1.03	46.80 ± 0.64	7.31 ± 1.07
6576	3.50 ± 2.44	48.50 ± 1.18	8.37 ± 2.28
6587	4.78 ± 1.94	46.68 ± 0.73	8.04 ± 1.35
6590	1.77 ± 0.97	45.32 ± 0.76	8.60 ± 1.51
6593	5.13 ± 3.44	48.36 ± 1.22	8.52 ± 2.40
6605	1.20 ± 0.45	44.02 ± 0.44	7.79 ± 0.80
6610	3.29 ± 1.23	45.47 ± 0.62	7.88 ± 1.14
6622	2.36 ± 2.01	46.99 ± 1.30	9.03 ± 2.70
6625	3.86 ± 2.00	47.80 ± 0.89	8.15 ± 1.68
6629	4.32 ± 3.96	46.59 ± 1.62	8.19 ± 3.06
6657	2.44 ± 1.63	46.56 ± 1.03	8.55 ± 2.03

Table E.4 (continued)

BATSE Trigger #	z	μ	$\theta_j(^\circ)$
6665	9.16 ± 7.07	49.28 ± 1.51	8.97 ± 3.13
6672	4.06 ± 3.94	49.78 ± 1.69	8.68 ± 3.39
6694	3.43 ± 1.47	46.27 ± 0.72	7.89 ± 1.31
6707	1.87 ± 0.62	46.58 ± 0.47	7.58 ± 0.82
6763	6.99 ± 4.62	47.81 ± 1.26	9.74 ± 2.82
6764	3.22 ± 2.15	46.41 ± 1.11	7.56 ± 1.93
6767	2.12 ± 1.78	46.51 ± 1.24	7.40 ± 2.12
6796	6.97 ± 2.54	46.00 ± 0.69	8.12 ± 1.30
6816	2.15 ± 1.54	47.20 ± 1.06	8.00 ± 1.96
6877	1.34 ± 1.03	47.05 ± 0.96	7.61 ± 1.69
6891	4.57 ± 4.20	47.93 ± 1.64	8.19 ± 3.09
6930	4.37 ± 2.75	48.36 ± 1.11	8.75 ± 2.25
7178	2.50 ± 1.81	47.13 ± 1.12	8.22 ± 2.13
7185	1.66 ± 1.10	45.47 ± 0.90	8.31 ± 1.73
7207	3.55 ± 1.35	46.31 ± 0.64	7.94 ± 1.18
7209	5.85 ± 3.77	47.53 ± 1.20	8.47 ± 2.34
7213	7.34 ± 4.30	48.68 ± 1.12	9.07 ± 2.34
7219	7.05 ± 2.68	48.05 ± 0.72	8.39 ± 1.40
7228	1.99 ± 1.09	45.02 ± 0.79	9.56 ± 1.75
7247	5.29 ± 2.25	46.67 ± 0.78	8.98 ± 1.61
7250	5.36 ± 4.77	47.94 ± 1.63	9.16 ± 3.44
7285	4.63 ± 1.88	48.16 ± 0.73	8.57 ± 1.44
7319	1.79 ± 1.01	46.08 ± 0.78	8.65 ± 1.57
7328	3.43 ± 1.38	45.86 ± 0.68	8.31 ± 1.30
7343	4.45 ± 3.20	47.12 ± 1.28	8.82 ± 2.60
7360	1.67 ± 0.71	44.70 ± 0.58	8.60 ± 1.15
7390	4.09 ± 1.92	47.39 ± 0.82	8.15 ± 1.54
7403	11.49 ± 6.81	48.75 ± 1.19	9.14 ± 2.50
7464	6.19 ± 2.92	46.81 ± 0.88	9.22 ± 1.88
7475	3.17 ± 1.71	46.94 ± 0.89	8.47 ± 1.74
7477	9.60 ± 5.03	49.28 ± 1.03	9.73 ± 2.31
7491	2.99 ± 0.91	45.17 ± 0.50	8.26 ± 0.94
7497	3.93 ± 1.38	46.31 ± 0.61	8.85 ± 1.24
7502	6.69 ± 3.31	47.51 ± 0.93	9.94 ± 2.15
7503	2.40 ± 0.96	46.20 ± 0.61	7.69 ± 1.09

Table E.4 (continued)

BATSE Trigger #	z	μ	$\theta_j(^\circ)$
7515	10.24 ± 4.14	47.99 ± 0.80	8.89 ± 1.64
7520	2.52 ± 1.47	48.12 ± 0.91	7.89 ± 1.65
7549	1.58 ± 1.30	46.77 ± 1.09	7.05 ± 1.77
7560	2.10 ± 1.69	47.42 ± 1.19	8.32 ± 2.27
7575	5.63 ± 4.77	48.77 ± 1.56	8.40 ± 3.03
7598	4.22 ± 1.67	46.97 ± 0.69	9.35 ± 1.49
7607	4.70 ± 3.27	48.35 ± 1.24	8.61 ± 2.47
7608	11.89 ± 8.50	50.13 ± 1.43	8.84 ± 2.92
7609	3.46 ± 1.47	47.02 ± 0.71	8.31 ± 1.37
7648	5.14 ± 2.26	47.14 ± 0.80	8.91 ± 1.65
7654	1.18 ± 0.56	45.00 ± 0.55	7.21 ± 0.92
7678	3.08 ± 1.44	46.73 ± 0.77	8.22 ± 1.46
7703	4.76 ± 1.56	46.49 ± 0.59	8.48 ± 1.15
7741	2.28 ± 0.73	45.81 ± 0.48	7.47 ± 0.83
7785	5.33 ± 1.93	47.44 ± 0.66	8.58 ± 1.31
7788	2.52 ± 1.69	46.38 ± 1.04	9.56 ± 2.30
7822	1.31 ± 1.29	47.50 ± 1.21	8.10 ± 2.26
7840	7.42 ± 7.09	50.30 ± 1.83	8.29 ± 3.50
7854	2.85 ± 1.56	46.08 ± 0.88	9.49 ± 1.93
7858	7.12 ± 2.86	47.60 ± 0.77	8.93 ± 1.58
7868	7.35 ± 6.12	48.56 ± 1.59	9.60 ± 3.53
7884	1.58 ± 0.56	45.93 ± 0.47	8.13 ± 0.88
7900	3.15 ± 1.53	47.43 ± 0.80	7.72 ± 1.43
7902	4.12 ± 1.64	46.82 ± 0.69	8.57 ± 1.37
7929	2.75 ± 1.77	46.63 ± 1.02	7.52 ± 1.77
7932	3.17 ± 1.43	46.57 ± 0.75	8.22 ± 1.41
7969	1.85 ± 0.75	45.78 ± 0.57	7.65 ± 1.00
7976	8.04 ± 2.44	47.73 ± 0.59	8.60 ± 1.16
7994	3.93 ± 3.43	47.47 ± 1.51	9.20 ± 3.21
8012	6.34 ± 3.36	47.66 ± 0.99	9.68 ± 2.22
8022	5.99 ± 2.19	47.47 ± 0.68	8.84 ± 1.38
8026	5.87 ± 4.10	48.69 ± 1.29	9.36 ± 2.79
8030	1.54 ± 1.21	46.15 ± 1.04	8.09 ± 1.94
8075	6.35 ± 2.30	47.90 ± 0.68	8.31 ± 1.30

REFERENCES

[1] C. Meegan et al., Astrophysical Journal **702**, 791 (2009).

[2] D. Fox and P. Mészáros, New Journal of Physics **8**, 199 (2006).

[3] R. Klebesadel, I. Strong, and R. Olson, Astrophysical Journal **182**, L85 (1973).

[4] G. Fishman et al., The BATSE experiment on the Compton Gamma Ray Observatory: Status and some early results, in *GRO Science Workshop Proceedings*, volume 1, page 2, NASA: Greenbelt, MD, 1989.

[5] G. Boella, R. Butler, and G. Perola, Astrophysical Journal Supplements **122**, 299 (1997).

[6] D. Reichart, Astrophysical Journal Letters **495**, L99 (1998).

[7] C. Tinney, R. Stathakis, and R. Cannon, GRB 980425, 1998.

[8] N. Tanvir et al., GCN Circular #9219: GRB 090423: VLT/ISAAC spectroscopy, 2009.

[9] R. Aptekar et al., Space Science Reviews **71**, 265 (1995).

[10] K. Mitsuda et al., Publications of the Astronomical Society of Japan **59**, S1 (2007).

[11] S. Barthelmy et al., Space Science Reviews **120**, 143 (2005).

[12] C. Meegan et al., Nature **355**, 14 (1992).

[13] W. Paciesas et al., Astrophysical Journal Supplements **122**, 465 (1999).

[14] S. Barthelmy et al., BACODINE the real-time BATSE gamma-ray burst coordinates distribution network, in *Gamma-ray bursts: Second workshop*, volume 307, AIP Conference Proceedings, 1994.

[15] J. Horack, *Development of the Burst and Transient Source Experiment (BATSE)*, NASA, Washington, D.C., 1991.

[16] W. Atwood et al., Astrophysical Journal **697**, 1071 (2009).

[17] G. Pendleton et al., Nuclear Instruments and Methods **364**, 567 (1995).

[18] A. Hoover, M. Kippen, and M. Wallace, General Response Simulation System (GRESS) software user's guide, Manual GRESS-SUG-001-21, LANL, Los Alamos, NM, 2010.

[19] M. Briggs et al., Astrophysical Journal **524**, 82 (1999).

[20] S. Guiriec et al., Astrophysical Journal **725**, 225 (2010).

[21] R. Kippen et al., Comparing prompt emission from X-ray flashes and gamma-ray bursts, in *Gamma-Ray Bursts: 30 Years of Discovery*, volume 727, page 119, AIP Conference Proceedings, 2004.

[22] T. Sakamoto et al., Astrophysical Journal **602**, 875 (2004).

[23] G. Hrabovsky, H. Ogelman, C. Kouveliotou, and J. van Paradijs, Bulletin of the American Astronomical Society **28**, 1198 (1996).

[24] P. Bhat et al., Nature **359**, 217 (1992).

[25] C. Kouveliotou et al., Astrophysical Journal **413**, L101 (1993).

[26] J. Dezalay et al., Short cosmic events: A subset of classical GRBs?, in *Gamma-ray Bursts*, volume 265, page 304, AIP Conference Proceedings, 1992.

[27] T. Cline, U. Desal, R. Klebesadel, and I. Strong, Astrophysical Journal **185**, L1 (1973).

[28] E. Mazets et al., Astrophysical and Space Science **80**, 3 (1981).

[29] S. Matz et al., Astrophysical Journal **288**, L37 (1985).

[30] J. Norris et al., Spectral evolution in gamma-ray bursts, in *26th COSPAR meeting*, volume 6, page 19, Advances in Space Research: Elsevier, 1986.

[31] D. Band et al., Astrophysical Journal **413**, 218 (1993).

[32] B. Dingus et al., EGRET observations of three gamma-ray bursts at energies < 30 MeV, in *Gamma-Ray Bursts: Proceedings of the 2nd Workshop*, volume 307, page 22, AIP Conference Proceedings, 1994.

[33] M. Ackermann et al., Astrophysical Journal **729**, 114 (2011).

[34] E. Costa et al., Nature **387**, 783 (1997).

[35] V. Connaughton, Astrophysical Journal **567**, 1028 (2002).

[36] T. Giblin et al., Astrophysical Journal **570**, 573 (2002).

[37] B. Zhang and P. Mészáos, International Journal of Modern Physics A **19**, 2385 (2004).

[38] D. Wei and T. Lu, Astronomy & Astrophysics **381**, 731 (2002).

[39] S. Yost et al., Astrophysical Journal **636**, 959 (2006).

[40] J. Rhoads, Astrophysical Journal **525**, 737 (1999).

[41] T. Galama et al., Astrophysical Journal **536**, 185 (2000).

[42] G. Björnsson, J. Hjorth, P. Jakobsson, L. Christensen, and S. Holland, Astrophysical Journal **552**, L121 (2001).

[43] A. Zeh, S. Klose, and D. Hartmann, Astrophysical Journal **609**, 952 (2004).

[44] R. Sari and T. Piran, Astrophysical Journal **517**, L109 (1999).

[45] D. Frail et al., Astrophysical Journal Letters **562**, L55 (2001).

[46] C. Akerlof et al., Nature **398**, 400 (1999).

[47] E. Nakar and T. Piran, Astrophysical Journal **619**, L147 (2004).

[48] E. Rol et al., Astrophysical Journal **624**, 868 (2005).

[49] D. Frail et al., Astronomical Journal **125**, 2299 (2003).

[50] J. Goodman, New Astronomy **2**, 449 (1997).

[51] D. Frail et al., Nature **389**, 261 (1997).

[52] J. Fynbo et al., Astrophysical Journal Supplements **185**, 526 (2009).

[53] D. Koo, Astronomical Journal **90**, 418 (1985).

[54] M. Bolzonella, J. Miralles, and R. Pelló, Astronomy & Astrophysics **363**, 476 (2000).

[55] T. Krühler et al., Astronomy & Astrophyiscs **526**, A153 (2011).

[56] B. Paczyński et al., Astrophysical Journal Letters **308**, L43 (1986).

[57] E. Fenimore et al., Astronomy & Astrophysics **97**, 59 (1993).

[58] M. Rees and P. Mészáros, Monthly Notices of the Royal Astronomical Society **258**, 41P (1992).

[59] P. Mészáros and M. Rees, Astrophysical Journal **405**, 278 (1993).

[60] E. Waxman, Plasma Physics and Controlled Fusion **48**, B137 (2006).

[61] E. Fenimore et al., Astrophysical Journal **473**, 998 (1996).

[62] R. Sari and T. Piran, Astrophysical Journal **485**, 270 (1997).

[63] A. Panaitescu and P. Mészáros, Astrophysical Journal **492**, 683 (1998).

[64] M. Rees and P. Mészáros, Astrophysical Journal Letters **430**, L93 (1994).

[65] P. Mészáros and M. Rees, Astrophysical Journal Letters **418**, L59 (1993).

[66] R. Sari and T. Piran, Astrophysical Journal **520**, 641 (1999).

[67] M. Tavani, Astrophysical Journal **466**, 768 (1996).

[68] M. Tavani, Physical Review Letters **76**, 3478 (1996).

[69] G. Rybicki and A. Lightman, *Radiative Processes in Astrophysics*, Wiley-VCH, Weinheim, Germany, 2004.

[70] M. Baring and M. Braby, Astrophysical Journal **613**, 460 (2004).

[71] S. Woosley, Astrophysical Journal **405**, 273 (1993).

[72] S. Woosley and A. MacFadyen, Astronomy & Astrophysics **138**, 499 (1999).

[73] A. MacFadyen and S. Woosley, Astrophysical Journal **524**, 262 (1999).

[74] A. MacFadyen, S. Woosley, and A. Heger, Astrophysical Journal **550**, 410 (2001).

[75] R. Blandford and C. McKee, Physics of Fluids **19**, 1130 (1976).

[76] W. Zhang, S. Woosley, and A. MacFadyen, Astrophysical Journal **586**, 356 (2003).

[77] S. Yoon and N. Langer, Astronomy & Astrophysics **443**, 648 (2005).

[78] S. Woosley and H. A., Astrophysical Journal **637**, 914 (2006).

[79] N. Langer and C. Norman, Astrophysical Journal **638**, L63 (2006).

[80] P. Jakobbson, D. Malesani, J. Fynbo, J. Hjorth, and B. Milvang-Jensen, GRB redshifts & host galaxies: An unbiased sample, in *Gamma-Ray Bursts: Sixth Huntsville Symposium*, volume 1133, page 455, AIP Conference Proceedings, 2009.

[81] P. Jakobsson, Astrophysical Journal **752**, 62 (2012).

[82] A. Fruchter et al., Nature **441**, 463 (2006).

[83] X. Han et al., Astronomy & Astrophysics **514**, A24 (2010).

[84] E. Levesque, L. Kewley, E. Berger, and H. Jabran Zahid, Astrophysical Journal **140**, 1557 (2010).

[85] D. Kocevski and A. West, Astrophysical Journal **735**, L8 (2011).

[86] J. Bloom, S. Kulkarni, and S. Djorgovski, Astronomical Journal **123**, 1111 (2002).

[87] S. Kulkarni et al., Nature **395**, 663 (1998).

[88] P. Mazzali et al., Astrophysical Journal Letters **599**, L95 (2003).

[89] J. Sollerman et al., Astronomy & Astrophysics **454**, 503S (2006).

[90] J. Fynbo et al., Nature **444**, 1047 (2006).

[91] S. Blinnikov et al., Soviet Astronomy Letters **10**, 177 (1984).

[92] J. Lattimer and D. Schramm, Astrophysical Journal **210**, 549 (1976).

[93] J. Goodman, Astrophysical Journal Letters **308**, L47 (1986).

[94] D. Eichler et al., Nature **340**, 126 (1989).

[95] P. Mészáros and M. Rees, Astrophysical Journal Letters **482**, L29 (1997).

[96] J. Prochaska et al., Astrophysical Journal **642**, 989 (2006).

[97] R. O'Shaughnessy, K. Belczynski, and V. Kalogera, Astrophysical Journal **675**, 566 (2008).

[98] W. Fong, E. Berger, and D. Fox, Astrophysical Journal **708**, 9 (2010).

[99] D. Burrows et al., Science **309**, 1833 (2005).

[100] R. Duncan and C. Thompson, Astrophysical Journal Letters **392**, L9 (1992).

[101] K. Hurley et al., Nature **434**, 1098 (2005).

[102] A. Goldstein et al., Astrophysical Journal Supplements **to be published** (2012).

[103] A. Goldstein et al., Astrophysical Journal Supplements **199**, 19 (2012).

[104] *Fermi* Science Support Center >> Data Analysis >> User Contributions, http://fermi.gsfc.nasa.gov/ssc/data/analysis/user/, 2012.

[105] W. Cash, Astrophysical Journal **228**, 939 (1979).

[106] F. Ryde, Astronomy Letters and Communications **39**, 281 (1999).

[107] Y. Kaneko et al., Astrophysical Journal Supplements **166**, 298 (2006).

[108] F. Massaro, J. Grindlay, and A. Paggi, Astrophysical Journal Letters **714**, L299 (2010).

[109] P. Bhat et al., Astrophysical Journal **426**, 604 (1994).

[110] J. Norris et al., Astrophysical Journal **459**, 393 (1996).

[111] H. Lee, R. Wijers, and G. Brown, Physics Reports **325**, 83 (2000).

[112] R. Sari, T. Piran, and R. Narayan, Astrophysical Journal Letters **497**, L17 (1998).

[113] R. Preece et al., Astrophysical Journal **581**, 1248 (2002).

[114] K. Asano, S. Guiriec, and P. Mészáros, Astrophysical Journal **705**, L191 (2009).

[115] J. Burgess et al., Astrophysical Journal **741**, 24 (2011).

[116] A. Pe'er et al., Monthly Notices of the Royal Astronomical Society **420**, 468 (2012).

[117] L. Amati et al., Astronomy & Astrophysics **390**, 81 (2002).

[118] G. Ghirlanda, G. Ghisellini, and D. Lazzati, Astrophysical Journal **616**, 331 (2004).

[119] D. Yonetoku et al., Astrophysical Journal **609**, 935 (2004).

[120] B. Schaefer and A. Collazzi, Astrophysical Journal **656**, L54 (2007).

[121] W. Paciesas et al., Astrophysical Journal Supplements **199**, 18 (2012).

[122] A. Goldstein, R. Preece, and M. Briggs, Astrophysical Journal **721**, 1329 (2010).

[123] E. Fenimore and E. Ramirez-Ruiz, astro-ph/0004176, 2000.

[124] J. Norris, G. Marani, and J. Bonnell, Astrophysical Journal **534**, 248 (2000).

[125] J. Norris, Astrophysical Journal **579**, 386 (2002).

[126] T. Murakami and D. Yonetoku, Publications of the Astronomical Society of Japan **55**, 65 (2003).

[127] J. Bloom, D. Frail, and R. Sari, Astronomical Journal **121**, 2879 (2001).

[128] N. Lloyd-Ronning and E. Ramirez-Ruiz, Astrophysical Journal **576**, 101 (2002).

[129] A. Friedman and J. Bloom, Astrophysical Journal **627**, 1 (2005).

[130] E. Nakar and T. Piran, Monthly Notices of the Royal Astronomical Society **360**, L73 (2005).

[131] D. Band and R. Preece, Astrophysical Journal **627**, 319 (2005).

[132] N. Butler, D. Kocevski, J. Bloom, and J. Curtis, Astrophysical Journal **671**, 656 (2007).

[133] E. Nakar, Physics Reports **442**, 166 (2007).

[134] A. Panaitescu and P. Kumar, Astrophysical Journal **571**, 779 (2002).

[135] M. Livio and E. Waxman, Astrophysical Journal **538**, 187 (2000).

[136] B. Watson et al., Astronomy & Astrophysics **454**, L123 (2006).

[137] S. Cenko et al., Astrophysical Journal **732**, 29 (2011).

[138] S. McBreen et al., Astronomy & Astrophysics **516**, A71 (2010).

[139] A. Rau et al., Astrophysical Journal **720**, 862 (2010).

[140] D. Frail et al., Astrophysical Journal **590**, 992 (2003).

[141] K. Page et al., Monthly Notices of the Royal Astronomical Society **416**, 2078 (2011).

[142] R. Filgas et al., Astronomy & Astrophysics **535**, A57 (2011).

[143] E. Troja et al., astro-ph/1201.4181v1 **to be published** (2012).

[144] J. Greiner, http://www.mpe.mpg.de/∼jcg/grbgen.html, 2012.

[145] R. Yamazaki, D. Yonetoku, and T. Nakamura, Astrophysical Journal **594**, L79 (2003).

[146] A. Einstein, Annalen der Physik **354**, 769 (1916).

[147] J. Peacock, *Cosmological Physics*, Cambridge University Press, New York., 2007.

[148] A. Friedman, Zeitschrift für Physik **10**, 377 (1922).

[149] A. Friedman, General Relativity and Gravitation **31**, 1991 (1999).

[150] G. Lemaître, Annales de la Societe Scientifique de Bruxelles **A47**, 49 (1927).

[151] P. Peebles, Astrophysical Journal **263**, L1 (1982).

[152] A. Jenkins and C. Frenk, Astrophysical Journal **499**, 20 (1998).

[153] A. Riess et al., Astrophysical Journal **607**, 665 (2004).

[154] A. Riess et al., Astrophysical Journal **659**, 98 (2007).

[155] M. Chevallier and D. Polarski, International Journal of Modern Physics D **10**, 213 (2001).

[156] E. Linder, Physical Review Letters **90**, 091301 (2003).

[157] H. Leavitt, Annals of Harvard College **60**, 87 (1908).

[158] E. Hubble and M. Humason, Astrophysical Journal **74**, 43 (1931).

[159] C. Bennett et al., Astrophysical Journal Supplements **148**, 97 (2003).

[160] Y. Sunyaev, R.A. an Zeldovich, Astrophysics and Space Science **7**, 3 (1970).

[161] P. Peebles and J. Yu, Astrophysical Journal **162**, 815 (1970).

[162] B. Bassett and R. Hlozek, *Dark Energy*, Cambridge University Press, Cambridge, UK, 2010.

[163] C. Ahn et al., arXiv:1207.7137 **to be published** (2012).

[164] D. Eisenstein et al., Astrophysical Journal **633**, 560 (2005).

[165] S. Cole et al., Monthly Notices of the Royal Astronomical Society **362**, 505 (2005).

[166] A. Soderberg et al., Nature **430**, 648 (2004).

[167] D. Guetta, R. Perna, L. Stella, and M. Vietri, Astrophysical Journal Letters **615**, L73 (2004).

[168] E. Liang and B. Zhang, Astrophysical Journal Letters **638**, L67 (2006).

[169] H. Li, X. Jun-Qing, J. Liu, G. Zhao, and X. Fan, Z. Zhang, Astrophysical Journal **680**, 92 (2008).

[170] C. Firmani, G. Ghisellini, G. Ghirlanda, and V. Avila-Reese, Monthly Notices of the Royal Astronomical Society **360**, L1 (2005).

[171] G. Ghirlanda, G. Ghisellini, and C. Firmani, New Journal of Physics **8**, 123 (2006).

[172] G. Ghirlanda et al., Astronomy and Astrophysics **452**, 839 (2006).

[173] E. Liang and B. Zhang, Monthly Notices of the Royal Astronomical Society **369**, L37 (2006).

[174] N. Liang, W. Xiao, Y. Liu, and S. Zhang, Astrophysical Journal **685**, 354 (2008).

[175] S. Djorgovski et al., Astrophysical Journal **562**, 654 (2001).

[176] S. Djorgovski et al., Astrophysical Journal **508**, L17 (1998).

[177] E. Berger et al., Astrophysical Journal **556**, 556 (2001).

[178] S. Kulkarni et al., Nature **398**, 389 (1999).

[179] P. Vreeswijk et al., Astrophysical Journal **546**, 672 (2001).

[180] F. Harrison et al., Astrophysical Journal **523**, L121 (1999).

[181] E. Le Floc'h et al., Astrophysical Journal **581**, L81 (2002).

[182] N. Masetti et al., Astronomy & Astrophysics **354**, 473 (1999).

[183] P. Vreeswijk et al., GCN Circular #496: VLT spectra of GRB 991216, 1999.

[184] J. Halpern et al., Astrophysical Journal **543**, 697 (2000).

[185] J. Greiner et al., GCN Circular #2020: Redshift of GRB 030329, 2003.

[186] E. Berger et al., Nature **426**, 154 (2003).

[187] R. Chornock, D. Perley, S. Cenko, and J. Bloom, GCN Circular #9028: GRB 090323 Gemini-south redshift, 2009.

[188] S. Cenko, J. Bloom, A. Morgan, and D. Perley, GCN Circular #9053: GRB 090328: Gemini south redshift, 2009.

[189] S. Cenko, D. Perley, V. Junkkarinen, M. Burbridge, and K. Miller, GCN Circular #9518: GRB 090618: Lick/KAST spectroscopy, 2009.

[190] A. Cuchiarra, D. Fox, N. Tanvir, and E. Berger, GCN Circular #9873: GRB 090902B: Gemini-N absorption redshift, 2009.

[191] D. Malesani et al., GCN Circular #9942: GRB 090926A: VLT/X-shooter redshift, 2009.

[192] A. Cuchiarra, D. Fox, A. Levan, and N. Tanvir, GCN Circular #10202: GRB 091127: Gemini-N redshift, 2009.

[193] R. Wijers and T. Galama, Astrophysical Journal **523**, 177 (1999).

[194] G. Ghirlanda et al., Monthly Notices of the Royal Astronomical Society **420**, 483 (2012).

[195] A. Riess et al., Astrophysical Journal **730**, 119 (2011).

[196] E. Komatsu et al., Astrophysical Journal **192**, 18 (2011).

[197] L. Anderson et al., arXiv:1203.6594 **to be published** (2012).

[198] D. Lazzati, G. Ghisellini, and A. Celotti, Monthly Notices of the Royal Astronomical Society **309**, L13 (1999).

[199] D. Giannios, Monthly Notices of the Royal Astronomical Society **422**, 3092 (2012).

[200] F. Daigne and R. Mochkovitch, Monthly Notices of the Royal Astronomical Society **296**, 275 (1998).

[201] G. Ghisellini and A. Celotti, Astrophysical Journal **511**, L93 (1999).

[202] G. Ghisellini, A. Celotti, and D. Lazzati, Monthly Notices of the Royal Astronomical Society **313**, L1 (2000).

[203] J. Granot, T. Piran, and R. Sari, Astrophysical Journal **527**, 236 (1999).

[204] S. Kobayashi, Astrophysical Journal **545**, 807 (2000).

[205] V. Kargatis et al., Astrophysical Journal **422**, 260 (1994).

[206] E. Liang and V. Kargatis, Nature **381**, 49 (1996).

[207] C. Firmani et al., Monthly Notices of the Royal Astronomical Society **393**, 1209 (2009).

[208] M. Ohno et al., Publications of the Astronomical Society of Japan **61**, 201 (2009).

[209] R. Lu, S. Hou, and E. Liang, Astrophysical Journal **720**, 1146 (2010).

[210] K. Ioka and T. Nakamura, Astrophysical Journal Letters **554**, L163 (2001).

[211] D. Eichler and J. Granot, Astrophysical Journal Letters **641**, L5 (2006).

[212] Y. Lithwick and R. Sari, Astrophysical Journal **555**, 540 (2001).

[213] E. Molinari et al., Astronomy & Astrophysics **469**, L13 (2007).

[214] A. Abdo et al., Science **323**, 1688 (2009).

[215] M. Ackermann et al., Astrophysical Journal **716**, 1178 (2009).

[216] H. Spruit, F. Daigne, and G. Drenkhahn, Astronomy & Astrophysics **369**, 694 (2001).

[217] Z. Li and E. Waxman, Astrophysical Journal **651**, 328 (2006).

[218] B. Schaefer, Astrophysical Journal **660**, 16 (2007).